

DISS. ETH NO. 29840

EFFICIENT PHYSICAL AND DATA-DRIVEN
SIMULATION TECHNIQUES FOR
TEMPERATURE-DEPENDENT PLASTICITY IN
MAGNESIUM.

A thesis submitted to attain the degree of

DOCTOR OF SCIENCES
(Dr. sc. ETH Zurich)

presented by

YANNICK HOLLENWEGER
M. Sc. in Mechanical Engineering, ETH Zurich

born on 7 November 1995

Accepted on the recommendation of

Prof. Dr. D. M. Kochmann
Prof. Dr. B. Liu
Prof. Dr. S. P. Joshi
Prof. Dr. T. P. Weihs

2023

Yannick Hollenweger: *Efficient Physical and Data-Driven Simulation Techniques for Temperature-Dependent Plasticity in Magnesium*. © 2023

DOI: [10.3929/ethz-b-000661745](https://doi.org/10.3929/ethz-b-000661745)

ABSTRACT

Magnesium (Mg) has immense potential to replace aluminum and steel in certain lightweight structural applications in numerous industries. However, the material suffers from significant drawbacks, notably a low ductility at ambient temperatures and poor thermal hardening. The main goal of this thesis is to understand and model thermal effects on the microstructure of the material and the corresponding response of Mg in an efficient manner in a push toward an integrated, computational framework in a bid to accelerate the material design process for Mg. We further divide this broad goal into two aspects; first, to investigate the material's plastic behavior at elevated temperatures and find potential solutions to existing drawbacks, and second, to accelerate the process of designing novel Mg-based materials with enhanced properties by numerical means, within the framework of an integrated computational material-by-design approach.

Improving the understanding of Mg's microstructure development at elevated temperatures is imperative to alleviate the material's key drawbacks. We develop a novel, efficient crystal plasticity model seamlessly integrating the behavior on the temperature range from 25-250°C. Modeling Mg across this range is challenging and must account for the experimentally reported competition between compressive twins and pyramidal slip and the thermally introduced changes to the microstructure. Only a few temperature-aware models for pure Mg and Mg alloys currently exist and most either disregard compressive twins entirely or suffer from efficiency or calibration issues. Additionally, experimental evidence on the activity of the deformation modes has remained inconclusive. The presented model is thus meticulously calibrated with single-crystal experimental data to predict single- and polycrystal stress-strain responses accurately. By comparing two implementations of the model – with and without the compressive twins – we showcase their impact on the microstructure and texture evolution. Results highlight a transition in deformation modes from compressive twins at low temperatures to pyramidal II slip at elevated temperatures, confirming that the temperature dependence of pure Mg is primarily governed by non-basal slip.

The second part of the thesis is concerned with addressing the computational bottleneck of existing high-fidelity material models. We thus develop a neural network-based surrogate for the temperature-dependent

material model to reduce the overall computation time of simulations. The surrogate seamlessly maps the deformation and temperature history undergone by the material to its stress response, thus providing relief from explicitly computing plastic updates. This direct approach to mapping the temperature-dependent constitutive response of a highly anisotropic material poses a formidable challenge to data-driven methods in general and cannot be fulfilled in a satisfactory manner by existing recurrent network architectures. We, therefore, apply a novel architecture, based on recurrent neural operators, and learn the constitutive response of the material with great accuracy. The presented architecture outperforms state-of-the-art recurrent network architectures in terms of accuracy and training time and provides a self-consistent formulation that provides a time-step independent implementation of the surrogate model. The recurrent neural operator further shows the capability to generalize its predictions for varying temperature and strain paths with short stints of transfer learning. In addition, it was possible to identify a minimal number of state variables for the recurrent neural operator of the same order of magnitude as the underlying model, indicating the physical interpretability of the neural network's state space. Ultimately, the surrogate model was applied at the mesoscale for multiscale simulations of Mg with commercial FE software, leading to unprecedentedly quick computations of truly multiscale simulations.

Finally, as an outlook on ongoing and future work, we present an approach following the *material-by-design* paradigm to improve Mg's strength via *thermomechanical* hardening. Experimental work on binary Mg-Aluminium alloys suggests that this type of processing leads to the formation of nanoprecipitates in a process called deformation-induced precipitation. This leads to a high number-density of small precipitates that effectively oppose basal dislocation motion whilst also promoting pyramidal $\langle c + a \rangle$ dislocation climb, thus resulting in increased mobility on the pyramidal planes and reduced anisotropy and improved hardening on the basal planes. We perform full-field simulations of textured, polycrystalline Mg and investigate the distribution of key drivers of deformation-induced precipitation in the sample, and suggest a formulation of a fully-coupled thermomechanical hardening and precipitation framework.

ZUSAMMENFASSUNG

Magnesium (Mg) hat ein immenses Potenzial, um Aluminium und Stahl in zahlreichen Industrien als strukturelles Material für Leichtgewichtsanwendungen zu ersetzen. Allerdings leidet das Material unter signifikanten Nachteilen, insbesondere einer geringen Duktilität bei Umgebungstemperaturen sowie einer schlechten Verfestigung beim herkömmlichen (thermischen) Verfestigungsprozess. Das Ziel dieser Dissertation ist es die relevanten thermischen Plastizitätsprozesse in Magnesium zu identifizieren und effizient zu modellieren, mit dem Ziel näher an einen integrierten, rechnergestützten Entwicklungsprozess zu kommen. Wir unterteilen dieses weit gefasste Ziel weiter in zwei Unterkategorien. Erstens ist das Ziel, das plastische Verhalten des Materials bei erhöhten Temperaturen zu untersuchen und potenzielle Lösungen für die bestehenden Nachteile zu finden. Zweitens soll der Prozess der Entwicklung neuartiger Mg-basierter Materialien mit verbesserten Eigenschaften durch numerische Methoden im Rahmen eines integrierten rechnergestützten Materialdesign-Ansatzes beschleunigt werden. Dazu werden höchsteffiziente Rechen- und Simulationsmethoden benötigt, welche es zu entwickeln gilt.

Die Verbesserung unseres Verständnisses der Mikrostrukturbildung in Mg bei erhöhten Temperaturen ist entscheidend, um die Hauptnachteile des Materials zu mildern. Wir entwickeln ein neuartiges, effizientes Kristallplastizitätsmodell, welches nahtlos das Verhalten im Temperaturbereich von 25-250°C beschreibt, um die Mechanismen der plastischen Verformung in diesem Temperaturbereich besser zu verstehen. Die Modellierung von Mg in diesem Bereich ist anspruchsvoll und muss die experimentell beobachtete Konkurrenz zwischen kompressiver Zwillingsbildungen und pyramidalem Gleiten, sowie die thermisch induzierten Veränderungen der Mikrostruktur berücksichtigen. Derzeit existieren nur wenige solche temperaturabhängige Modelle für reines Mg und Mg-Legierungen, von denen die meisten die kompressive Zwillingsbildung entweder vollständig außer Acht lassen oder Effizienz- oder Kalibrierungsprobleme aufweisen. Darüber hinaus bleiben experimentelle Beweise für die Aktivität der Verformungsmodi uneindeutig. Das vorgestellte Modell wird daher sorgfältig mit experimentellen Daten an Einzelkristallen kalibriert, um die Spannungs-Dehnungs-Reaktionen sowie die Mikrostrukturevolution von Einzel- und Polykristallen präzise vorherzusagen. Durch den Vergleich von zwei Implementierungen des

Modells - mit und ohne die kompressive Zwillingsbildung - zeigen wir deren Auswirkungen auf die Mikrostruktur und die Texturentwicklung auf. Die Ergebnisse verdeutlichen einen Übergang der Verformungsmodi von kompressiven Zwillingsbildungen bei niedrigen Temperaturen zu pyramidalen II-Gleiten bei erhöhten Temperaturen und bestätigen, dass die Temperaturabhängigkeit von reinem Mg hauptsächlich durch nicht-basales Gleiten gesteuert wird.

Der zweite Teil der Arbeit befasst sich mit Möglichkeiten zur Bewältigung des rechnerischen Engpasses bestehender Materialmodelle und Simulationstechniken. Wir entwickeln ein neuronales Netzwerk-basiertes Ersatzmodell für das temperaturabhängige Kristallplastizitätsmodell, um die Gesamtberechnungszeit der Simulationen zu reduzieren. Das Ersatzmodell bildet nahtlos die Verformungs- und Temperaturhistorie des Materials auf seine Spannungsreaktion ab und bietet somit eine Alternative zur expliziten Berechnung plastischer Updates. Dieser direkte Ansatz zur Abbildung des temperaturabhängigen konstitutiven Verhaltens eines hochanisotropen Materials stellt eine enorme Herausforderung für datenbasierte Methoden dar und kann durch bestehende Netzwerkarchitekturen noch nicht gänzlich erfüllt werden. Daher wenden wir eine neuartige Architektur, basierend auf wiederkehrenden neuronalen Operatoren, an und bilden die konstitutive Antwort des Materials mit hoher Genauigkeit ab. Die vorgestellte Architektur übertrifft bestehende Netzwerkarchitekturen in Bezug auf die Genauigkeit und Trainingszeit und bietet eine selbstkonsistente Formulierung, die eine quasi zeitschrittunabhängige Implementierung des Ersatzmodells ermöglicht. Unser neuronaler Operator zeigt zudem die Fähigkeit, seine Vorhersagen für unterschiedliche Temperatur- und Dehnungspfade mit kurzen Phasen des Transferlernens zu verallgemeinern. Darüber hinaus war es möglich, eine minimale Anzahl von Zustandsvariablen für den wiederkehrenden neuronalen Operator in derselben Größenordnung wie das zugrunde liegende Plastizitätsmodell zu identifizieren, was auf die physikalische Interpretierbarkeit des Zustandsraums des neuronalen Netzwerks hinweist. Letztendlich wurde das Ersatzmodell auf der Mesoskala für Multiskalen-Simulationen von Mg mit kommerzieller FE-Software angewendet, was zu beispiellosen Beschleunigungen der Berechnungen von Multiskalen-Simulationen führte.

Abschließend präsentieren wir als Ausblick auf laufende und zukünftige Arbeiten einen Ansatz, der dem *Material-by-Design*-Paradigma folgt, um die Festigkeit von Mg durch *thermomechanische* Verfestigung zu verbessern. Experimentelle Arbeiten an binären Mg-Aluminium-Legierungen legen

nahe, dass diese Art der Verarbeitung zur Bildung von Nano-Ausfällungen in einem Prozess der Verformungsinduzierten Ausfällung. Dies führt zu einer hohen Dichte kleiner Seigerungen, die effektiv der Gleitbewegung von basalen Versetzungen entgegenwirken, gleichzeitig jedoch den Versetzungsaufstieg pyramidaler $\langle c + a \rangle$ -Versetzungen fördern, was zu einer erhöhten Beweglichkeit auf den pyramidalen Ebenen, einer reduzierten Anisotropie und einer verbesserten Verfestigung auf den Basalebene führt. Wir führen Simulationen von texturiertem, polykristallinem Mg durch und untersuchen die Verteilung der Haupttreiber der Verformungsinduzierten Ausfällung im Material und schlagen eine Formulierung eines vollständig gekoppelten thermomechanischen Verfestigungs- und Ausfällungsmodells vor.

ACKNOWLEDGEMENTS

Embarking on a Doctorate degree is a rigorous and demanding undertaking that is challenging personally and scientifically. But as they say, nothing worth having comes easy. Friends, family, and collaborators can, however, have a huge impact on the journey. I, for one, was blessed with great people in my life.

First and foremost, I wish to thank my supervisor and mentor, Dennis M. Kochmann. Over the course of the last four years, he has been the most valuable mentor and friend. He has helped me with so many of my questions and problems, and has been a steady supporter over the course of the past four years. I am also deeply thankful to him for offering me this position at a time where I wanted to leave ETH to pursue my Ph.D. elsewhere. He enabled me to stay at an amazing university in a group full of amazing collaborators and team members. Further, he has allowed me to work with the outstanding researchers at MEDE and the University of Cambridge, and for always encouraging my endeavors. I am deeply grateful.

Next, I wish to thank my co-supervisor, friend and mentor, Prof. Burigede Liu at the University of Cambridge and his Ph.D. Student, Rui Wu. Our collaborations and discussions have proven to be fruitful, motivating and rewarding, and I am grateful that I was given the chance to work with and visit your new and growing group at Cambridge. My time there and our joint project have been a blessing for me, personally and for the present thesis, and I am thankful for this opportunity.

Friends and family were my steady rock throughout the last four years and their support, love and belief has made this degree possible. I am deeply grateful for the people who have accompanied me throughout my life and fostered my curiosity. I thank my parents from the bottom of my heart. You have held me up and taught me to believe in myself, have always pushed me to achieve more and encouraged my endeavours. You have had my back throughout my life and I thank you, for I owe you everything. Besides them, an enormous amount of credit is due to my amazing and supportive partner, Abby, and her infinite patience and strength. She has lived every up and down of this degree in the front row and has been a rock, a sounding board, and a font of power throughout.

Additionally, my thanks go out to my numerous collaborators I had the chance to meet thanks to C-MEDE, notably Timothy P. Weihs, Michael L. Falk and their group members Suhas E. Prameela and Peng Yi at the Johns Hopkins University in Baltimore. Our collaboration was a gift that quickened the start of my thesis and has significantly impacted my journey and my learning. C-MEDE was an invaluable source of knowledge and collaboration and I am truly humbled and thankful to have been a part of this outstanding group of researchers.

I also wish to thank my colleagues, friends, office mates, and lovely people all around, Kaoutar , Jan-Hendrik and Roman, Hsu-Cheng and Dotan, Laurent and Bastian for their help, support (scientific and personal in nature) and for making my time in and around ETH a wonderful experience.

Finally, I would like to thank the people at OpenAI for making ChatGPT available just in time for me to write this thesis. Chat GPT was used (only!) to re-write and improve the quality of the language throughout the document, where it was deemed necessary. This saved me countless hours of painstaking revisional work.

CONTENTS

List of Figures	xiv
List of Tables	xxv
1 Introduction and Motivation	1
1.1 Motivation for the Use of Mg Alloys	1
1.2 Recent Challenges in Mg-Based Material Design	5
1.3 Towards an Integrated Material-by-Design Paradigm for Mg- Based Materials	8
1.4 Scope of the Present Thesis	12
2 Background	15
2.1 Multiscale Description of Materials	15
2.1.1 Lower-Scale Effects on Plasticity	20
2.2 Mechanical Processes During Plastic Deformation in Mg	21
2.2.1 Crystallography and Stacking Faults in Mg	23
2.2.2 Slip and Twin Systems in Mg	26
2.2.3 Mechanical Response and Microstructure in Mg Single- Crystals	34
2.2.4 Mechanical Response at Elevated Temperatures	37
2.2.5 Mechanical Characterization of Polycrystals	42
2.2.6 Hardening Mechanisms in Mg and its Alloys	44
2.3 Modeling Approaches for Mg	49
2.3.1 Sub-Micro Scale Modeling of Mg	50
2.3.2 Micro- and Mesoscale Modeling Techniques for Mg	51
2.3.3 Modeling at Elevated Temperatures	57
2.3.4 Homogenization Methods	58
2.3.5 Preliminary Conclusions	69
2.4 Data-Driven Methods	71
2.4.1 Introduction to Data-Driven Methods	71
2.4.2 Recurrent Neural Networks Applied to the Depen- dence in Plasticity	75
2.5 Outline of this Thesis	84
3 Efficient Temperature-Dependent Crystal Plasticity Model for Pure Mg	89
3.1 Introduction	89
3.1.1 Experimental Investigations	91
3.1.2 Numerical Studies	92

3.2	Kinematics	94
3.3	Constitutive Relation	95
3.4	Temperature Dependence	98
3.5	Parameter identification and model validation	100
3.6	Single Crystal Simulations	106
3.6.1	Room-Temperature Single-Crystal Response	108
3.6.2	Temperature Dependence of Monocrystalline Mg	117
3.7	Polycrystal Simulations	122
3.7.1	Taylor Model for Polycrystal Simulations	122
3.8	Model Validation	124
3.8.1	Textured Polycrystals at Room Temperature	124
3.8.2	Temperature-Dependent Response of Textured Polycrystals	127
3.9	Texture Evolution in Mg	129
3.10	Chapter Summary	131
4	Recurrent Neural Operator Describing Thermoplastic Behavior in Mg	135
4.1	Introduction	136
4.1.1	State of the Art	137
4.1.2	Proposed Solution	141
4.2	Background and Proposed Architecture	142
4.2.1	Recurrent Neural Operator	145
4.2.2	Time Discretization and Operator Architecture	146
4.2.3	Internal Variables and Markovian Description	148
4.2.4	Loss Function	148
4.3	Material and Methods	148
4.3.1	Data Generation	149
4.3.2	Training Methodology	157
4.4	Training Performance	163
4.4.1	Operator Training	163
4.4.2	Generalization for Various Temperature Paths via Transfer Learning	168
4.5	Results and Discussion	168
4.5.1	Validation of the RNO	168
4.5.2	Comparison with Traditional Recurrent Architectures	171
4.5.3	Behavior of State Variables	178
4.5.4	Application in Multiscale Simulations	185
4.5.5	Runtime Comparison	190
4.6	Chapter Summary	191

5	Conclusion and Outlook	193
5.1	Concluding Remarks	193
5.2	Outlook	196
	Bibliography	205

LIST OF FIGURES

Figure 1.1	Aging strength of select Mg-based alloys compared to Al-based alloys. Reproduced from [1]. Courtesy of Suhas E.P.	3
Figure 1.2	(a) (0002) pole figures measured from the surface and the center of a hot-rolled sheet of pure Mg. (b) Sheet specimens after Erichsen tests at room temperature and 150°C. From [2], reproduced with permission from SNCSC.	4
Figure 1.3	Engineering stress–strain curves of polycrystalline sheets of pure Mg in the temperature range 77 to 523 K, adapted from [2, 3], reproduced with permission from SNCSC.	7
Figure 1.4	Depiction of the conventional and inverse design of Mg alloys, courtesy of Suhas E.P.	9
Figure 2.1	Relevant length scales for Mg material-by-design frameworks, from the atomic to the continuum scale. On the macroscale, a hot-rolling simulation is schematically depicted, courtesy of Suhas E.P. At the mesoscale we show a representative volume element of multiple grains simulated with our self-developed full-field methods. The microscale shows the propagation of twin needles across a grain boundary, adapted from [4] with permission from Elsevier, whilst the nanoscale shows a micrograph of precipitates in alloy A9, courtesy of Suhas E.P. Finally, the depiction at the atomic scale is that of solute atoms embedded in a matrix, courtesy of P. Yi.	17
Figure 2.2	Main crystal axes in the hcp system are shown in (a), with the basal plane represented in blue. Only two independent a -directions are shown, a_3 can be constructed by a linear combination of a_1 and a_2 . A schematic representation of a stereographic projection is shown in (b).	18

Figure 2.3	Lattice defects in metals. (a) represents a perfect lattice, (b) shows point defects such as large and small interstitial atoms, a lattice vacancy and a substitutional atom. (c) shows a line defect known as edge dislocation.	19
Figure 2.4	(a) Stress-strain curves of AZ31B rolled sheet data loaded under compression and tension along the three main directions. (b) and (c) show the resulting texture after compression in the rolling direction and the transverse direction, respectively. Adapted from [5] with permission from Elsevier.	22
Figure 2.5	Hexagonal closest-packed unit cell with corresponding closest packed planes allowing for dislocation movement. The planes best suited for dislocation movement are shown in (a), while the planes best suited for twin-like stacking faults are shown in (b). Adapted from Nie, Shin, and Zeng [2], reproduced with permission from SNCSC.	24
Figure 2.6	I ₁ , I ₂ and E stacking faults in hcp crystal lattice.	25
Figure 2.7	Dissociation of a perfect dislocation into two partial dislocations in (a) and propagation of a screw dislocation via cross-slip onto another plane exemplified for an fcc crystal in (b).	26
Figure 2.8	Schematic depiction of the Schmid law.	27
Figure 2.9	Evolution of the CRSS values of distinct slip systems with temperature are shown for pure Mg in (a) and after the addition of 1 wt% of Al solute in (b). Reprinted from [2] with permission from SNCSC.	29
Figure 2.10	Schematic depiction of a twin in an hcp material following <i>A, B, . . . , A</i> stacking sequence. The twin planes (mirror planes) are indicated in red. The M and T labels denote the matrix and twin phase, respectively. We show the reorientation of a basal slip system with normal n_b to its new configuration with n_b^* during a twinning event.	30

Figure 2.11 Electron back scattered diffraction (EBSD) scans of (a) Mg strained to 3% in-plane compression at room temperature (standard stereographic triangle showing compression direction) and (b) Zr strained to 10% in-plane compression at 76K temperature (standard stereographic triangle showing plate normal direction) at a strain rate of 10^3 s. Several adjoining twin pairs can be seen; a few are marked by black arrows [6]. Reprinted under open access creative commons license from Arul Kumar et al. [6]. 31

Figure 2.12 Illustrative example of the transmission of a twin in a Mg bicrystal PFM simulation with varying grain misorientation angles. (a) 11.25° , (b) 22.5° , (c) 33.75° , and (d) 45° 32

Figure 2.13 Twinning shear and nature of a twin system in hcp materials in dependence of the c/a -ratio. Adapted from Yoo [7] with permission from SNSC. 33

Figure 2.14 True stress-true strain response under plane-strain compression of Mg single crystals at room temperature. Adapted from [2, 8], reproduced with permission from SNCSC. 35

Figure 2.15 Response of Mg single crystals under plane strain compression in (a), c -axis compression, (b), a -axis compression with *unconstrained* c -direction, (c) in a -axis compression with *constrained* c -direction, and (d) at an 45° angle to the c -axis such as to promote basal slip. Reprinted from Chapuis and Driver [9] with permission from Elsevier. 39

Figure 2.16 EBSD map and corresponding pole figure of single crystal after unconstrained a -axis compression at room temperature (a,b), $\epsilon = 0.04$, and at 350°C (c,d), $\epsilon = 0.096$. The parent grain is shown in blue, the twins in red. Note the presence of small recrystallized zones in (c) at the twin boundaries. Reproduced from Chapuis and Driver [9] with permission from Elsevier. 41

Figure 2.17	The texture of polycrystalline rolled Mg sheet, reported by [8], is shown in (a). The corresponding experimental stress-strain curves of the polycrystals under plane strain compression are shown in (b). The nomenclature chosen by Kelley and Hosford [8] is described in chapter 3 and in Kelley and Hosford [8].	43
Figure 2.18	FR dislocation source. (a): bulging of pinned dislocation, (b): looping of the dislocation around itself, (c): forming of a new dislocation loop. Reprinted from Gurrutxaga-Lerma et al. [10] via Open Commons License.	46
Figure 2.19	Hall-Petch hardening in rolled Mg polycrystals tested under tensile load. The direction of loading is unknown. Reprinted from [3], with permission from Elsevier.	47
Figure 2.20	The theoretical precipitate hardening effect of un-shearable, evenly distributed Mg-Al precipitates at 7% volume fraction is shown.	49
Figure 2.21	DDD simulations of pure Mg single crystals and polycrystals, performed in 3D ParaDiS code. Adapted from Fan et al. [11], with permission from Elsevier.	52
Figure 2.22	Double-well potential typically used in phase-field modeling with single twin variant.	54
Figure 2.23	We show the laminate pattern formation in bicrystals under shear. (a) depicts the geometric arrangement of the two grains within the bicrystal RVE along with the definition of angles in the blue and red grains, respectively. Results for varying angles are shown in (b) through (d). Reprinted from Vidyasagar, Tutcuoglu, and Kochmann [12] with permission from Elsevier.	67
Figure 2.24	Schematic depiction of the FE ² method.	68
Figure 2.25	Schematic depiction of the FExTaylor method.	69
Figure 2.26	Schematic depiction of the FExSurrogate model approach.	70
Figure 2.27	Schematic representation of a perceptron	73

Figure 2.28 Stress-strain response of the ANN-enhanced CP model presented by Ibragimova et al. [13]. Graphic adapted from Ibragimova et al. [13], with permission from Elsevier. 74

Figure 2.29 Schematic visualization of a simple RNN with two inputs and one of which being propagated through time. 76

Figure 2.30 Graphical representation of an LSTM cell. The LSTM cell has two memory vectors, the hidden vector $h(t)$ and the cell state $c(t)$, carrying information through time. These vectors are updated based on "gates", the forget gate, update gate, input gate, and output gates. The output of the cell is the new hidden state $h(t_i)$ 78

Figure 2.31 Sketch of a fully gated GRU cell with a reset and an update gate and a hidden state h 81

Figure 2.32 Test error of the trained model for elasto-viscoplastic material model in (a), and for the viscoelastic model in (b). Reprinted and adapted from Liu et al. [14] with permission from Elsevier. 84

Figure 2.33 Comparison of the test error of an RNO trained with training data at a resolution of 200 time-steps against test data various resolution, for both the elasto-viscoplastic RNO labeled "E-VP" and the alternate viscoelastic RNO labeled "VE". (a) One-dimensional elasto-viscoplastic composite (b). Reprinted from Liu et al. [14] with permission from Elsevier. 85

Figure 3.1 Main deformation modes occurring in Mg 90

Figure 3.2 Range of the experimentally reported CRSS values for the slip and twin systems. The shown ranges were obtained from Wang, Liu, and Soh [15] and expanded with experimental data from Chapuis and Driver [9](1), Kelley and Hosford [8](2), Yoshinaga and Horiuchi [16, 17](3,7), Akhtar and Teghtsoonian [18](4), Wonsiewicz and Backofen [19](5), and Kitahara et al. [20](6). The pyramidal II CRSS of the reduced model coincides with the experimental values of Obara, Yoshinga, and Morozumi [21] . . . 102

Figure 3.3	Experimentally measured CRSS values for the slip and TT systems in Mg in comparison with this model over the studied range of temperatures. The filled markers show experimentally reported data from Yoshinaga and Horiuchi [17], Akhtar and Teghtsoonian [18], Wonsiewicz and Backofen [19], and Obara, Yoshinga, and Morozumi [21]. The solid lines with markers represent the data for the reduced model, the dashed lines for the full model. The TT and basal CRSS values were constant for both models.	106
Figure 3.4	Stress-strain data for the channel-die experiments of Kelley and Hosford [8] (dotted line) and Wonsiewicz and Backofen [19] (solid line).	107
Figure 3.5	Stress-strain responses of cases A through G. Dots represent experimental data by Kelley and Hosford [8], solid lines are results simulated with the reduced model.	109
Figure 3.6	Relative twin and slip activities for cases A, B, C, D, E, and F. Case G shows only basal activity, as expected, and is hence omitted here.	110
Figure 3.7	Tension-compression asymmetry and the reorientation of the crystal: due to the imposed initial orientation of the crystal, the x -direction is unconstrained, and the loading direction corresponds to the y -direction in the pole figures (a,b). Case E leads to a reorientation by 86° (a), whereas case F leads to a reorientation by 30.3° (b) [15, 19]. (c) shows the tension-compression asymmetry of the TT system, which is active under c -axis extension but inactive under c -axis compression.	112
Figure 3.8	Stress-strain responses of cases A through G, as obtained from the full model including CT. Dots represent experimental data of Kelley and Hosford [8], lines are simulated results.	114
Figure 3.9	Relative activities of the deformation modes, as obtained from the full model including CT. Results are for a single-crystal under plane-strain compression, mimicking cases A, C, E, and F of the experiments by Kelley and Hosford [8]	116

Figure 3.10 Temperature-dependent stress-strain response of Mg single-crystals, corresponding to cases A (left) and C (right). Solid lines are predictions by the *reduced* model, whereas the scatter plot represents the experimental data obtained by Wonsiewicz and Backofen [19] 118

Figure 3.11 Temperature-dependent stress-strain response of Mg single-crystals, corresponding to cases A (left) and C (right). Solid lines are predictions by the *full* model, whereas the scatter plot represents the experimental data of Wonsiewicz and Backofen [19]. 119

Figure 3.12 Relative activities of the slip and twin systems in Mg single-crystals for cases A at 271°C and C at 270°C. Results on the left were obtained from the reduced model, and results on the right from the full model. . 121

Figure 3.13 Schematic view of the Taylor model used for the extraction of the polycrystal response during channel-die loading with the indicated loading, constraint, and unconstrained free directions. 123

Figure 3.14 True stress-true strain response of textured polycrystals of pure Mg from experiments (dashed line) and from simulations with 24, 50, 100, and 200 grains simulated with the reduced model. Experimental data are from Kelley and Hosford [8]. 124

Figure 3.15 True stress vs. true strain response of textured polycrystals of pure Mg from experiments (markers) and from simulations with the reduced model (solid lines) at room temperature. The experimental data was obtained by Kelley and Hosford [8]. The *representative* texture utilized for the simulations is shown on the left and was chosen such as to approximate the texture reported by Kelley and Hosford [8]. . . . 126

- Figure 3.16 True stress-true strain response as obtained from polycrystal simulations, using the full and reduced models. Markers correspond to experimental data from Wonsiewicz and Backofen [19], solid lines show the response predicted by the reduced model, and dotted lines by the full model. The shown texture (used in simulations) was obtained by assuming a normal distribution with expectation value at the basal pole and outliers as far as 50° from the normal direction. 128
- Figure 3.17 Texture of the undeformed (left) and deformed (right) polycrystal of pure Mg, simulated by the reduced model for the case of compression up to 30% true strain at 25°C . Initially a strong pole in the normal direction exists (left). After deformation, most grains are reoriented due to twinning, leading to a new, weaker texture with the pole in the transversal direction (TD) (right) 129
- Figure 3.18 We show the textures of a polycrystal with 1000 grains. In (a), we depict the initial random grain orientations, whereas in (b) we show the cold-rolled texture, simulated by the reduced model. In (c) we show the hot-rolled texture predicted by the full model including CT, and in (d), the hot-rolled texture as predicted by the reduced model. The simulations were performed up to a total of 60% strain at a strain rate of $\dot{\epsilon}_{\text{true}} = 10^{-4}\text{s}^{-1}$ at a temperature of 25°C for the cold case and 270°C for the hot case 132
- Figure 4.1 Graphical representation of the surrogate model in a multiscale setting. On the top, a graphical representation of a multiscale model with a FExTaylor Ansatz is shown, where the macroscopic BVP is solved via the FEM, and the mesoscopic representation is given by the Taylor mode, comprising the average of numerous grains. On the bottom, we show the same multiscale model, however, we have replaced the Taylor model with a data-driven surrogate. 143

Figure 4.2	From left to right we show the schematic of the RNO architecture, as well as the the GRU- and the LSTM-based networks that were used for comparison.	147
Figure 4.3	Depiction of the stress-strain response of the Taylor model that was chosen as the ground truth for the data generation. We show results in ND tension in (a) and in ND compression in (b). The strong basal texture we chose for our polycrystals is depicted in (c), and the deformation modes present in the reduced crystal plasticity model in (d).	150
Figure 4.4	Schematic representation of the data generation process.	152
Figure 4.5	Example of the randomized strain and temperature paths.	155
Figure 4.6	Distribution of the strains (a) and of the training vs. testing data sets (b).	158
Figure 4.7	The distribution of the hydrostatic component (a) and of the deviatoric component (b) of the TI vs. TD datasets is shown.	159
Figure 4.8	Training and testing error vs. the number of trainable parameters in the network.	161
Figure 4.9	Convergence of the training error with the number of state variables for TI, TD, and TV cases. The TD and TV cases show the same kind of slower convergence with larger numbers of IVs (35-40) compared to the TI case, which converges much more rapidly and saturates around 15 IVs.	162
Figure 4.10	Test error evolution with the number of training epochs for training on the random dataset in the TI case (a), the TD case (c), and the TV case (e). Cases (b),(d), and (f) showcase the fine-tuning results of the RNOs on the -D labeled datasets.	164
Figure 4.11	Stress evolution for a testing case in the TI-R (top) at 25°C and TD-R (bottom) at 241°C datasets, respectively. The ground truth is shown as solid and the predicted response from the RNO is shown in a dashed line.	166

Figure 4.12	RNO Response pre and post-50 epochs of transfer learning on the RD-D dataset The response prior to transfer learning is shown by the dotted lines, the response afterward by the solid line. The dashed line represents the ground truth.	167
Figure 4.13	Performance of the TV-trained RNO before fine-tuning (a) and (b) after.	169
Figure 4.14	Predicted (dashed) and true (solid) material response for different load cases at room temperature: shear in the 13 direction in (a) and cyclic loading along the 11 direction in (b). (c) and (d) show the response for elevated temperatures instead.	170
Figure 4.15	Bauschinger effect under uniaxial tension/compression (a) and shear (b) at varying temperature levels captured by the RNO.	171
Figure 4.16	Architecture of the FCNN learning the equation of state, relating J and T to the hydrostatic pressure σ^h in (a) and prediction of the network for a random sample in the testing data set (b).	172
Figure 4.17	(a)Best performing GRU and LSTM architectures vs. TI-RNO with 300 NPL, 15 IVs. Trained on 8500 samples for the temperature invariant case at 25°C. (b) shows the prediction of the best-trained GRU model vs. the ground truth.	175
Figure 4.18	Resolution dependent test error of the GRU, LSTM and RNO. The GRU and LSTM networks show a strong resolution dependence with the error increasing as soon as one moves away from the training resolution. The RNO's error at finer resolutions, however, remains bounded.	177
Figure 4.19	Evolution of a given set of internal variables depicted as a surface plot with the y -axis being the time increments and the x -axis depicting the state variable identifier (a). The color indicates intensity. In (b), we show the five state variables that were identified to follow the cyclic deformation closely.	179
Figure 4.20	Heat map showing the time evolution of the activity levels of the states in the TD-RNO at 25°C for four distinct loading cases.	180

- Figure 4.21 Prediction of the slip and twin activity for a single sample of the dataset via one linear layer. The solid lines are the results from the Taylor model, whereas the dotted lines are the predictions from the network. 182
- Figure 4.22 Variance of state variables with respect to temperature, denoted by Var_T , and mechanical deformation at room temperature, denoted by Var_F 183
- Figure 4.23 Depiction of the linear and varying temperature paths of a sample used for data generation in (a) – we show the maximal distance between the temperatures with d_T . (b) shows the distribution of the stress difference (in MPa) of linear v.s. varying temperature paths along the same deformation pathway. Here, 100 pairs of linear v.s. varying temperature paths are shown for the same deformation path. The dots represent the predictions from the RNO, whereas the red diamonds show the results from the Taylor model for comparison. Finally, the color indicates the temperature at the final time step. . . . 185
- Figure 4.24 Von Mises equivalent stress distribution in the Taylor anvil for impact along the (a) TD and (b) ND at 25, 115, and 205°C after $e \times 10^{-7}$ seconds. The corresponding reaction forces over the duration of the simulation are shown in (c). Observe the varying stress levels for both cases. (d) shows a set of the simulation setup and (e) exemplifies the anisotropic stress distribution on the impact face at 115°C under impact along the TD (configuration (a)). 187
- Figure 4.25 Depiction of the Von Mises Stress (a) and the temperature distribution (b) in the Mg plate during impact. Distribution of the stress showcasing the anisotropy in Mg (c) at 25°C during impact. The geometry of the plate impact test (d). 189
- Figure 4.26 Isentropic heating contributions vs. the hydrostatic pressure. Comparison of the experimental study by Ravindran et al. [22] and our present model. The model prediction coincides well with the observed trends in Ravindran et al. [22]. 190

Figure 5.1	Deformation pathways in thermal aging (left) and during thermo-mechanical aging (right).	198
Figure 5.2	Heterogeneity of the stresses, hydrostatic pressure, and plastic activity across the RVE in a rolled Mg sample.	200
Figure 5.3	Ground truth (a) and prediction of an FNO network (b) of a 2D full-field simulation of a Mg polycrystal. The network is based on the work of Li et al. [23] and Wu, Hollenweger, and Liu [24]. The training performance of the network is shown in (c). These results are courtesy of Ms Rui Wu and Prof. Burigede Liu at the University of Cambridge. The training error of a transfer learning attempt of the existing RNO to a different texture is shown in (d).	202

LIST OF TABLES

Table 3.1	The seven cases in the channel-die experiments of Kelley and Hosford [8]. Single-crystals were subjected to plane-strain compression, being compressed in the <i>Compression</i> direction with a rigid constraint imposed in the <i>Constraint</i> direction, while being unconstrained in the third (orthogonal) direction. Each case is designed to promote the activity of the denoted system (<i>Deform. Mode(s)</i>), including pyramidal (Py), prismatic (Pris) and basal slip as well as tension twins (TT) and compressive twins (CT).	101
Table 3.2	Model parameters for the slip systems at room temperature, calibrated based on the experimental data of Kelley and Hosford [8]. All values are for the reduced model, unless those marked by †, which are for the full model including the CT systems. Values marked by an asterisk (*) were calibrated based on data from Kelley and Hosford [8], Chapuis and Driver [9], Akhtar and Teghtsoonian [18], Lilleodden [25], and Ando et al. [26] The temperature dependence of the CRSS values was calibrated such as to lie in the range of experimentally reported data, see Fig. 3.3.	105
Table 3.3	Model parameters for the twin systems in full and reduced models, calibrated based on the data of Kelley and Hosford [8] and Wonsiewicz and Backofen [19]	105
Table 4.1	Nomenclature of the datasets as well as key characteristics.	154
Table 4.2	GRU and LSTM architectures tested against the present RNO	173
Table 4.3	Runtimes of the physical model vs. the RNO for multiple applications	191

INTRODUCTION AND MOTIVATION

1.1 MOTIVATION FOR THE USE OF MG ALLOYS

Mg is a lightweight and abundant metallic material that offers exceptional strength-to-weight ratios, comparable to aluminum (Al) and titanium (Ti). This makes it a promising candidate for lightweight structural applications [2, 27]. The use of lightweight materials has garnered attention as a means to reduce vehicle energy consumption, with potential fuel savings of approximately 0.38 L per 100 kilometers, for every 100 kg of weight reduction (equivalent to 9g CO₂ per 100 km) [27, 28]. Thanks to recent improvements, the production of Mg also requires lower energy consumption compared to Al, thus addressing one of the largest critical points for widespread use. It therefore constitutes one of the most promising candidates for a green transition in the transportation sector. This trend is evidenced by the amount of work produced around Mg in recent years [29]. Today, cast Mg alloys already find relatively broad usage [30], such as in engine casings and gearboxes, where high temperature and corrosion resistance are required. To this end, a number of alloys have been developed specifically for the automotive industry, e.g. the AS (Mg-Al-Si), AE (Mg-Al-RE), AJ (Mg-Al-Sr), and QE (Mg-Y-RE) series developed in part by Volkswagen, Norsk Hydro and BMW for their improved creep properties [30].

In addition to the automotive industry, Mg alloys have potential applications in aircraft fuselage frames and lightweight applications in bicycles, railroad, and aerospace, due to the immense weight reduction possibilities, as well as in bio-absorbable implants due to their excellent bio-compatibility [27, 31–33]. Additionally, there is a growing interest in utilizing Mg alloys for protective materials, such as body or vehicle armor, and as protective shields in rocketry, where extreme material performance is required [34–37]. Many of these applications, however, require improved performance compared to their cast counterparts. The ductility, strength, and toughness of the materials must be improved for these applications [38].

Hence, sheets, extruded profiles, and forged parts are investigated as they have advantages compared to cast parts in their ability to provide better mechanical properties and thin-walled, long structures for structural applications [30]. Today, however, these parts are only in limited use. This

stems from a number of radical drawbacks of the Mg alloys. First, a relatively small number of alloys is available for structural applications. These applications require different properties from the alloys designed for castings, such as an increased ductility for plastic forming, improved strength and toughness for structural parts, and improved spall strength, in more extreme environments of application. The most widely used alloys for sheet, forged, and extruded applications are the AZ (Mg-Al-Zn) series, with prominent representatives being the AZ31 and AZ91 alloys. This series of alloys, however, suffers from a few important drawbacks.

First, they exhibit poor thermal hardening (strengthening due to thermal treatment), leading to relatively low strength in comparison with Al-based materials [1, 39], as shown in Figure 1.1. The poor thermal aging of the AZ series was also recently investigated by Cepeda-Jiménez, Castillo-Rodríguez, and Pérez-Prado [39]. It is tied to the crystallography of the material, as well as the exhibited precipitate types of the Mg-Al phase that cause poor hardening behavior on certain deformation modes [1, 2, 39–43]. Rare-earth alloys fare much better in this regard, however, the cost of these materials as well as the scarcity of the solutes render their widespread use complicated. This is why non-rare-earth alternatives are sought [44]. The obvious approach is to look for the existing material series, e.g. the A (Mg-Al), Z(Mg-Zn), and AZ series. These materials already fulfill some of the criteria required, however, they suffer from certain drawbacks when it comes to formability during plastic deformation and hardening of the material.

Second, the AZ series (and most Mg alloys in general) also show poor forming capabilities at room temperature. The reasons are linked to their pronounced plastic anisotropy, a phenomenon rooted in the atomic crystal structure of the material, whose plastic behavior is the result of the collective activation of a variety of slip and twin mechanisms. A limited number of suitable plastic deformation modes is available and thus restricts the material's ability to accommodate plastic deformation at room temperature [45–47]. This leads to overall poor and highly directional ductility.

Many other materials are strongly anisotropic in single crystal form, such as Ti or Zr, however, for a number of reasons, Mg is more challenging to process. For one, during many forming processes, such as rolling or extrusion, Mg alloys tend to form a strong texture, see Figure 1.2 (a), thus leading to an accentuated polycrystalline anisotropy. Another reason lies in the microstructural details pertaining to each material's crystal structure which will be discussed in chapter 2.

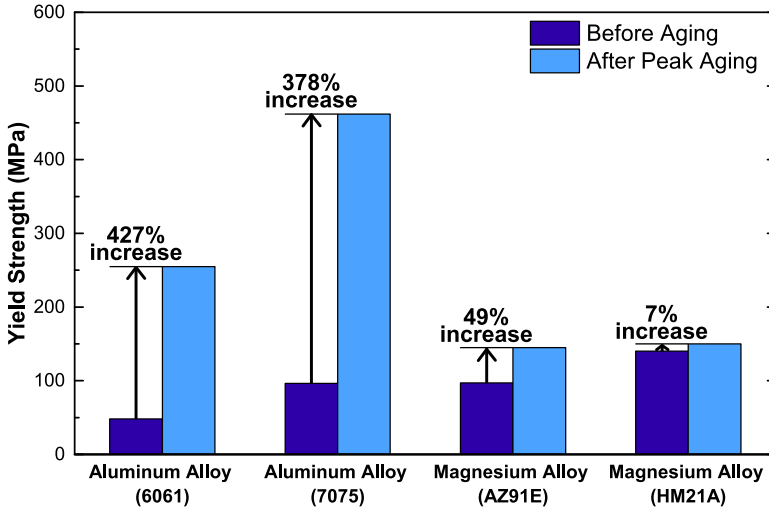


FIGURE 1.1: Aging strength of select Mg-based alloys compared to Al-based alloys. Reproduced from [1]. Courtesy of Suhas E.P.

These properties render sheet forming of rolled Mg a problematic task. One way of mitigating the issue lies in creating a very fine-grained material, as shown in [48], however, this requires additional processing steps beforehand, increasing the cost of production. Further, the process of creating ultra-fine-grained Mg is not applicable to arbitrary shapes and sizes, thus limiting this approach. Another approach consists of exploiting temperature as a process parameter. With increasing temperature, the material exhibits much more ductile behavior [9, 19, 45, 49–51], rendering sheet forming at elevated temperatures more reliable, see Figure 1.2 (b). Hence, heated tools and hot primary material are often required for processing Mg-based products, thus increasing the production cost and representing added difficulty in processing. The reasons and mechanisms for this increased ductility, however, are still debated and we still lack understanding of these processes [5, 52–56].

The goal of further effort now consists of addressing these drawbacks and designing materials with improved properties, facilitating processing at room temperature, and improving the hardening effect of AZ alloys.

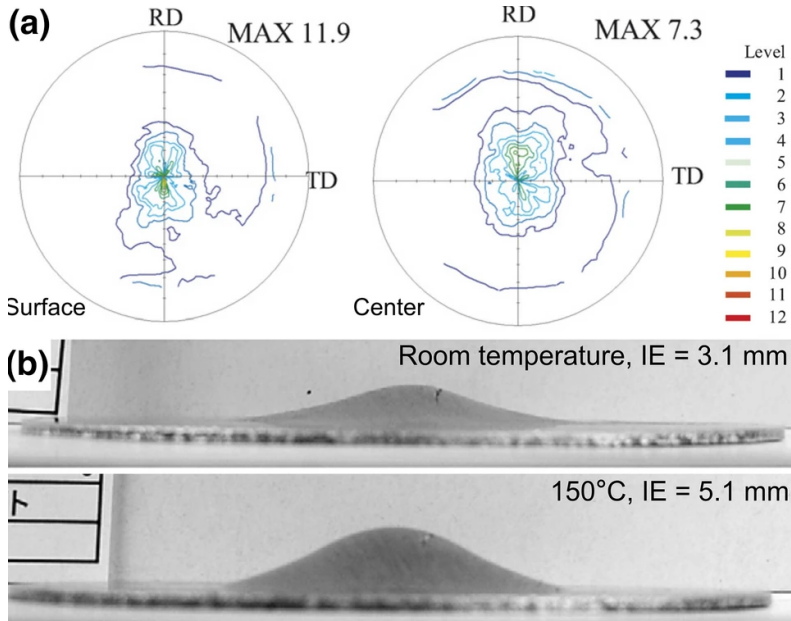


FIGURE 1.2: (a) (0002) pole figures measured from the surface and the center of a hot-rolled sheet of pure Mg. (b) Sheet specimens after Erichsen tests at room temperature and 150°C. From [2], reproduced with permission from SNCSC.

Extensive research has been conducted in the field of processing technology and material design, modeling, and industrial applications, all aiming to efficiently improve material performance [29]. These approaches encompass various strategies such as grain refinement [48, 57], thermomechanical processing [1, 58, 59] and texture weakening [60, 61]. The micro addition of alloying elements has the potential to be a highly effective approach in enhancing the mechanical properties of the material. Further, it was found that solutes contribute to improved ductility, and recent studies suggest that the hardening issues pertaining to the Mg-Al precipitate phase could be solved via thermomechanical processing and the targeted formation of small precipitates [1, 40, 62, 63]. This calls for a thorough investigation of the thermomechanical interplay of mechanisms in Mg.

1.2 RECENT CHALLENGES IN MG-BASED MATERIAL DESIGN

One of the primary challenges in designing Mg alloys is the complex interplay of mechanisms across multiple scales in the formation of the microstructure that governs material behavior. It is influenced dramatically by the presence of different deformation modes, recrystallization, as well as the formation of precipitates, and the presence of solutes [2]. This is a non-exhaustive list, so we refer the interested reader to specific literature available on the topic [1, 40, 49, 51, 58, 64, 65]. In addition, processing conditions play a large role in the formation of the microstructure and the resulting properties, examples including the strain rate, processing temperature, loading paths, degree of deformation, directional loading, and subsequent heat treatment, each of which can influence the texture, grain size, and size distribution of underlying precipitates. A complicating matter is that the influence of many of these processes is also not yet fully deciphered [44] and large gaps remain in our understanding of the interplay of these mechanisms. Therefore, a number of topics were identified by Pérez-Prado et al. [44] that are of notable interest in future investigations for the design of Mg alloys.

First, the texture development in Mg alloys in the presence of solutes, precipitates, and under the influence of strain rate, temperature, and recrystallization requires further investigation [44]. It has been observed that the presence of solutes, especially rare earths, lead to a weakening of the rolled texture poles [46, 66]. Additionally, the occurrence of static or dynamic recrystallization can result in a more diffuse texture due to randomization in the newly formed grains, thus improving the formability of sheets and wrought parts [44]. Experimental and numerical investigations have been conducted to understand texture formation in Mg alloys. However, the identification of temperature and recrystallization effects is challenging due to the mutual interplay of these factors and their interaction with dislocations and precipitates in the material [44, 49]. While modeling approaches can provide insights, most existing models are polycrystal-based plasticity models, sometimes relying on empirical understanding and suffering from challenges in calibration. Furthermore, the formulation of material models for Mg is complicated by the fact that deformation mechanisms in Mg vary over a wide temperature range, and their concurrent behavior and effects on texture are not fully understood. Exploiting high- and low-temperature material effects for material design remains challenging due to insufficient experimental data and the scarcity of temperature-aware models.

Second, the ductility and fracture mechanisms in Mg alloys continue to present perplexing questions. An intriguing anomaly in Mg, in contrast to materials like Al and steel, is that the ductility increases with reduced grain sizes [67] instead of deteriorating. It has been observed that super-formable Mg can be achieved in the presence of high degrees of recrystallization throughout the material, leading to extremely small grain sizes [48]. The improved ductility is primarily attributed to the suppression of the twin deformation mode, which is often considered a contributor to low ductility, below a certain grain size. Further studies indicate that recrystallization occurring inside twins has a beneficial effect on the ductility of the material [50]. However, there is conflicting evidence, with some observations suggesting rapid fracture despite recrystallization [19]. The complexity of the recrystallization mechanisms in Mg, occurring under different conditions, likely contributes to this confusion. Existing models aiming to capture recrystallization often rely on strong empirical assumptions and overlook certain recrystallization pathways [68, 69], or struggle to incorporate the temperature effects [59].

Third, temperature exerts a significant influence on Mg, both in single crystals and polycrystals. Stress levels decrease, and the ductility of Mg rapidly increases with rising temperature, as illustrated in Figure 1.3. These effects are often accompanied by recrystallization above a certain temperature. However, distinguishing and identifying the specific contributions of thermal softening and recrystallization can be challenging. The underlying thermal mechanisms responsible for the improved ductility at elevated temperatures are not yet fully understood, and multiple factors could potentially contribute to this behavior.

Further, a significant challenge in the hardening of Mg alloys lies in their relatively poor thermal aging behavior. Studies have revealed that the relatively large-spaced particles formed in the AZ alloy series are ineffective in strengthening the material [39]. However, recent investigations by Eswarappa Prameela et al. [1] suggest that smaller, finely scattered precipitates could hold the key to improving the hardening of Mg-Al(-Zn) alloys. Achieving such a microstructure with finely dispersed precipitates may be facilitated by thermo-mechanical aging, which involves the deformation-induced formation of precipitates at multiple temperatures. Nevertheless, the understanding of precipitation behavior in Mg alloys, particularly in the presence of deformation, remains limited, as calibrated models specific to this application and sufficient experimental data are currently lacking.

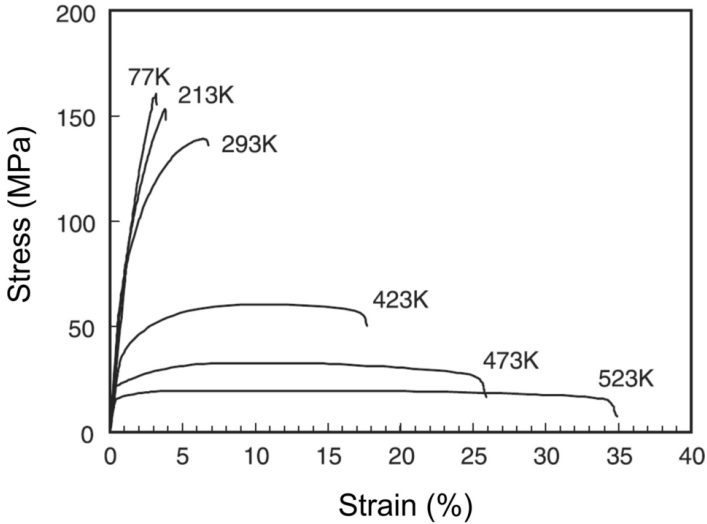


FIGURE 1.3: Engineering stress–strain curves of polycrystalline sheets of pure Mg in the temperature range 77 to 523 K, adapted from [2, 3], reproduced with permission from SNCSC.

Lastly, Pérez-Prado et al. [44] highlighted the emergence of advanced computational techniques as a significant area of interest for Mg alloys. The use of computational methods has already resulted in notable advancements and insights into the interaction of solutes with dislocations, hardening mechanisms, the interaction of precipitates with deformation modes, and the formation of twins [4, 62, 63, 70–72]. Further research employing increasingly accurate models and computer-aided experimental methods holds the potential to illuminate remaining questions concerning the behavior of Mg at various length scales. Additionally, computational methods are being increasingly utilized in materials design.

In conclusion, it is evident that the precise nature of thermal effects on plasticity in Mg remains a topic of ongoing discussion and thermal effects strongly affect all of the aforementioned mechanisms, such as precipitation, recrystallization, fracture, and even the microstructure evolution. As such, they warrant further investigation and are at the core of this Thesis' work. For a detailed discussion, see Chapters 2 and 3. In addition, the development of high-efficiency modeling methodologies play an important role in the development and the exploration of novel potential Mg-based materials.

1.3 TOWARDS AN INTEGRATED MATERIAL-BY-DESIGN PARADIGM FOR MG-BASED MATERIALS

Owing to the large appeal of Mg as a lightweight material, a number of research institutes across the U.S. and Europe formed a consortium, called the Center for Materials in Extreme Dynamic Environments, CMEDE, to further the understanding and development of Mg-based materials. CMEDE, which operated from 2012 to 2022 under the auspices of the Hopkins Extreme Materials Institute (HEMI) at Johns Hopkins University, was a collaborative initiative involving renowned academic institutions, national laboratories, the U.S. Army Research Laboratories, and industry partners. The primary objective of CMEDE was to advance the development of materials capable of withstanding dynamic loads and impacts, addressing critical needs in the field of materials science and engineering. During its operation, extensive investigations were carried out on Mg, which showed great promise as a model material. CMEDE fostered a strong collaboration between experimentalists and numerical scientists to study material mechanisms at different length- and time scales. This multidisciplinary approach facilitated the joint exploration of numerous outstanding questions and the present thesis was part of CMEDE's larger effort towards developing an integrated computational material design (ICMD) framework for Mg design.

The roots of this framework can be traced back to Olson [73], albeit it was then called integrated computational material engineering (ICME). The underlying concept is straightforward. While design paradigms and tools exist at higher levels, such as for the design of individual parts, assemblies, and final products, similar options are lacking at lower scales. Typically, material selection is made without explicit consideration of downstream design choices, constraining the design process. The goal of ICME is to provide design tools at the continuum, meso, and microscales, enabling the creation and design of materials with specific criteria tailored to final applications.

Although advances in materials are continually being made, they are not focused on specific design tasks but rather follow a general material design approach. This is due to the conventional bottom-up methodology employed in material design. This deductive approach involves characterizing material properties based on microstructure, composition, and processing. However, it is a slow, relatively expensive, and sometimes ineffective process. The material design procedure typically encompasses defining requirements, selecting a suitable material, and undertaking critical ma-

material processing steps involving mechanical and thermal methods (see inner circle in Figure 1.4). Researchers optimize processing aspects, such as mechanical processing routes, heat treatment, and hardening techniques, based on scientific intuition, modeling efforts, and prior experiences with other materials. The resulting microstructure is then evaluated, as it significantly influences the final material properties. Factors such as grain size, twins, precipitate size and distribution, voids, and inclusions need to be taken into account to fully comprehend the material behavior. In the case of alloys, the type and composition may also impact the processing steps, necessitating a modified approach. Overall, the material design process is complex and iterative, requiring a comprehensive understanding of the material's properties and behavior.

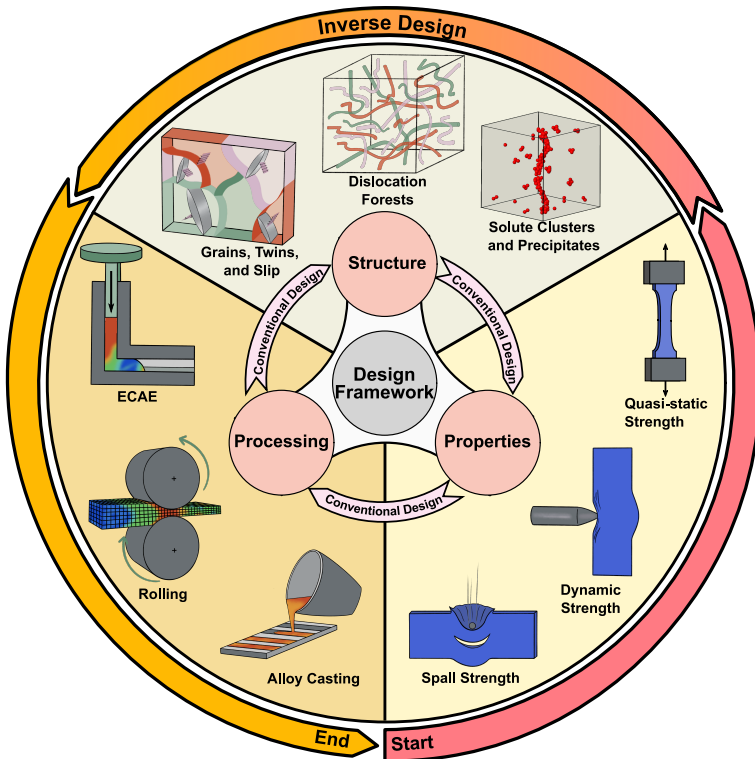


FIGURE 1.4: Depiction of the conventional and inverse design of Mg alloys, courtesy of Suhas E.P.

On the other hand, the ICME (or ICMD) approach represents a top-down methodology that involves the inductive design of materials [73]. Unlike the deductive pathway, where material properties and behavior are observed in hindsight, the ICMD approach aims to utilize highly performing computational models to identify the optimal structures, processing pathways, and event types required to achieve specific desired properties in the final product. However, this inversion of the traditional design process poses significant challenges.

The successful implementation of ICME relies on a comprehensive understanding of the intricate interplay among thermal, chemical, and mechanical factors across all length scales. These effects must be accurately and efficiently modeled to guide the processing and design of materials. Therefore, the computational aspect plays a crucial role in ICME. Predictive models need to capture the behavior, interplay, and effects of different material compositions and processing routes based on underlying mechanisms. Achieving accuracy in these models is particularly important when considering the small scales at which ICME operates [74].

It is important to note that ICME differs from conventional multiscale modeling approaches in that the primary goal is the efficient exploration of the design space, rather than solely focusing on accuracy or understanding the material itself. However, accuracy remains a crucial aspect, especially at the small scales where ICME is applied.

Furthermore, the feasibility of the model inversion process is of utmost importance. It involves both physical and computational constraints. On one hand, the combinations of composition, processing, and microstructure must align with the real behavior of materials. On the other hand, the inversion process needs to be feasible within an acceptable time frame, considering the available computational resources. The successful implementation of this inversion process presents a formidable challenge. Two potential approaches can be considered: an iterative numerical approach or a data-driven approach. In both cases, the objective is to expedite the development and discovery of novel materials, surpassing the pace of traditional experimentation.

For a successful implementation of an inverse design approach, an iterative route is followed. This necessitates highly efficient and adaptable models that accurately represent key mechanisms and perform computations with precision within limited time frames. The challenge extends across multiple scales, each requiring appropriate modeling techniques. While a seamless bottom-up scaling approach would be ideal, it often

exceeds computational resources. Moreover, scale-bridging processes introduce potential errors and uncertainties that cannot be quantified, affecting the accuracy of predictions [74]. Therefore, a combination of models, suited to their respective scales, is advantageous. However, many of these models are developed for specific purposes, posing constraints. Empirical continuum models, for example, are tailored for specific applications and have limited validity for deviations in the microstructure. In a material design framework, continuum-scale models must adequately account for influential factors such as deformation physics, texture, microstructure, and temperature, which significantly impact material behavior. Incorporating lower-scale effects is challenging, and the accuracy of models without a foundation in underlying physics is questionable. Reduced models offer a better trade-off between approximation quality and computational cost, but their accuracy may be compromised due to simplifications. Crystal plasticity (CP) models, while providing insights into physical behavior and texture development, often rely on simplifying assumptions about the interaction of different deformation modes. The treatment of lower-scale phenomena such as slip-precipitate interaction is typically simplified. Despite the availability of more accurate models for investigating specific material behaviors, their integration into an inverse design framework becomes questionable due to computational demands.

High-quality data for material design is often scarce and available in non-standardized formats, posing challenges in the creation of comprehensive databases. While more researchers are publishing their data, it remains a limited resource, especially experimental data, which is often limited to a few investigations per study. Therefore, obtaining a complete dataset often requires combining data from multiple studies. The absence of extensive databases has been recognized as a limiting factor for the development of data-driven methods [74].

The question arises whether the ICME approach is bound to fail due to insurmountable computational challenges, lack of data, and the perpetual trade-off between accuracy and efficiency.

The answer is, luckily, no, as solutions emerge from the field of machine learning and data-driven modeling. Although comprehensive databases for directly inferring material properties from processing routes and microstructures are currently limited, data-driven methods have proven highly useful in overcoming computational bottlenecks encountered in conventional modeling techniques.

Two main strategies are followed. The first strategy involves accelerating the computation of high-fidelity models by incorporating neural networks into the models themselves, addressing issues related to small temporal resolutions or computationally intensive simulations. For example, Ibragimova et al. [13] employed this strategy to accelerate CP modeling of an FCC material. However, the performance of these models relies on the quality and breadth of the training data and cannot extrapolate beyond it. The second strategy involves surrogate modeling, where machine learning models fully learn the characteristics of a physical model, providing a more efficient yet accurate representation of the physical constitutive model. This approach has been demonstrated by Bonatti, Berisha, and Mohr [75], Bonatti and Mohr [76], and Yuan et al. [77] for surrogate modeling and by Mozaffar et al. [78] and Bhattacharya et al. [79] for learning the homogenized behavior of materials. Remarkably, significant progress has been made, enabling the modeling of complex physical material behavior with high accuracy using various approaches such as Bayesian models, recurrent neural nets (RNNs) [80], and artificial neural nets (ANN) [13]. Surrogate models have exhibited exceptional performance in certain domains, such as predicting the texture evolution of polycrystalline materials [81] or designing the stiffness of spinodoid metamaterials [82]. Although these examples demonstrate the feasibility of the inversion process, they still lack the elements necessary for a prime example of ICMD, such as complex materials and microstructural and lower-level information. Some neural network architectures still face drawbacks including lengthy and challenging training processes, large data requirements, and resolution dependence, limiting their applicability for bridging timescales in an ICME context [83].

Therefore, as a second topic of high interest, the investigation of data-driven methods capabilities to aid in achieving an ICMD framework was identified.

1.4 SCOPE OF THE PRESENT THESIS

This thesis and the research conducted herein were part of the Mg research team in collaboration with scientists from CMEDE across the United States. The design of Mg alloys in a multiscale setting presents numerous exciting research possibilities. Addressing them all is, sadly, beyond the scope of this thesis, interested readers are referred to CMEDE's website and publications for an overview of their achievements.

Our work concentrates on two critical aspects. First, the thermomechanical behavior of Mg, which significantly influences the texture evolution, recrystallization, and ductility of the material, still lacks comprehensive understanding. Temperature has a profound impact on processing and interacts with smaller-scale phenomena like precipitation and solute segregation, which are crucial for addressing challenges in Mg alloys. While a detailed numerical investigation of recrystallization in Mg lies beyond the scope of this thesis, existing research on the topic [49, 68, 69, 84] has been limited by the absence of rigorously developed thermomechanically coupled models. Strain-induced precipitation, another thermal process that can significantly harden the material, also requires further attention in Mg [1, 42]. The presence of solute elements and precipitation adds to the problem's complexity and may introduce ambiguity, hence we here focus on pure Mg and discuss important aspects pertaining to solutes and alloys on occasion. Additionally, the precise role of various micromechanical mechanisms in enhancing or reducing the ductility of Mg and its alloys remains unclear. Hence, the primary focus of this thesis is to develop an efficient and accurate temperature-aware model for pure Mg, aiming to gain more insights into these thermomechanical aspects of plasticity.

The second part of the thesis centers on enhancing the efficiency of modeling techniques, with a specific focus on their seamless integration into multiscale models, particularly the ICMD (Integrated Computational Materials Design) framework. To accomplish this objective, we address various computational bottlenecks present in physical models, including stability constraints, challenges in bridging different scales, limitations in parallelization, and the need for accurate parameter calibration. Our aim is to develop an efficient data-driven model that exhibits high computational efficiency, easy parallelization, stability, and robustness. Due to the unavailability of extensive datasets suitable for our purposes, we create the necessary training data using our novel thermomechanical model, introduced in chapter 3. This data is subsequently utilized to train our model. This approach empowers us to explore larger parameter spaces and tackle more complex systems, ultimately leading to an improved understanding and predictive capability of material behavior. This application also requires utter efficiency of our primary developed model. By achieving greater computational efficiency and overcoming modeling challenges, our research aims to advance the incorporation of data-driven techniques into multiscale modeling paradigms, facilitating more accurate and insightful predictions in materials science.

The subsequent sections of this thesis are organized as follows. In chapter 2, we offer a comprehensive overview of the mechanics in Mg and traditional modeling methodologies. This chapter serves to justify the selection of our physical model and elucidates fundamental concepts relevant to our research. In chapter 3, we introduce the physical model and perform a rigorous assessment of its quality and accuracy. Moving forward, chapter 4 is dedicated to the introduction and evaluation of the data-driven model. Here, we delve into the details of the data-driven approach and thoroughly evaluate its performance and capabilities. Lastly, chapter 5 brings the thesis to a conclusion, summarizing the research conducted and assessing the progress and advancements achieved throughout this work. This concluding chapter provides a comprehensive analysis of the contributions made and outlines potential avenues for future research in this domain.

BACKGROUND

CHAPTER OVERVIEW

Our pursuit of developing high-efficiency and accurate models demands a profound understanding of both the physical and numerical aspects crucial for these models' development. In this chapter, we present a comprehensive overview of these essential aspects, alongside the state-of-the-art data-driven methodologies pertinent to our research. The structure of this chapter is organized as follows. We commence by delving into the multiscale nature of material design and modeling, elucidating the intricate interactions and dependencies that arise at different scales (Section 2.1). Subsequently, we explore the mechanical and physical processes in detail, starting from the crystallographic structure of Mg and extending to the intricate role of defects and their connection to plastic deformation (Section 2.2). To accomplish this, we draw insights from numerous cutting-edge experimental and numerical investigations, aiming to gain a comprehensive grasp of the underlying mechanisms. In Section 2.3, we embark on a review of existing modeling techniques, considering various scales and weighing the merits and drawbacks of different approaches. Moreover, we critically evaluate the viability of scale-bridging techniques, notably homogenization, seeking the most suitable methodology for achieving our overarching objectives. Finally, we delve into the realm of data-driven methods in Section 2.4, where we survey the available tools and techniques for accelerating multiscale modeling of Mg, particularly with a focus on their application within the ICMD framework. Having established a solid foundation of knowledge from these various aspects, we then formulate our modeling approach and identify the tools and methods to be employed in our subsequent applications. This strategic formulation sets the stage for the implementation and realization of our research objectives.

2.1 MULTISCALE DESCRIPTION OF MATERIALS

Let us now dive into the complex and exciting world of Mg. The behavior of many engineering materials, and thus Mg, is influenced by a multitude

of factors operating at different length- and time scales. Elastic and plastic mechanical properties, chemical or thermal properties, all trace their origins back to the lower scales of the material but are effectively characterized by macroscopic or effective properties. In this chapter, we delve into the diverse range of multi-scale effects, spanning from the continuum scale at the upper end down to the atomic length scale at the lower end of the spectrum. It becomes evident that many of the macroscopic properties exhibited by materials can be traced back to their underlying lower-scale phenomena. Therefore, it is prudent to consider (at least some of) these effects when modeling materials, as they play a pivotal role in determining the material's overall behavior.

We commence by gaining a comprehensive understanding of the different length scales involved in material modeling and the specific setting and scales, applicable to our model. At the highest level, we encounter the continuum scale, which represents the observable length scale spanning from a few millimeters (in small mechanical parts, encountered in watches or medical devices) to multiple kilometers (in cases such as geological applications). This scale typically exhibits a certain level of homogeneity, making it a homogenized representation of the material. Even at this scale, however, interesting phenomena, especially directional material behavior, can occur.

Upon observing materials under a microscope, however, the seemingly homogeneous structure unravels, revealing an array of lower-level structures with diverse shapes, sizes, orientations, and properties. These structures are referred to as grains in metals, fibers in woods or polymers, or cells in tissues. They exist on a length scale known as the mesoscale. The mesoscale ranges from a few to several hundred micrometers, depending on the material (see Figure 2.1). For the purposes of this thesis, our focus primarily lies on metals, and as a result, we will exclusively discuss grains and related concepts, although some of these notions possess broader applicability.

At the mesoscale, materials exhibit a complex structure composed of multiple grains. This plays a crucial role in the mesoscopic description. Multiple grains collectively form polycrystals, a concept that is extensively discussed in this thesis.

Polycrystals are structures made from numerous single crystals, at least some dozen to hundreds of micrometers in size, but can be much larger, technically, depending on the grain size and the macroscopic sample size. They consist of numerous single grains (crystals) that typically vary in

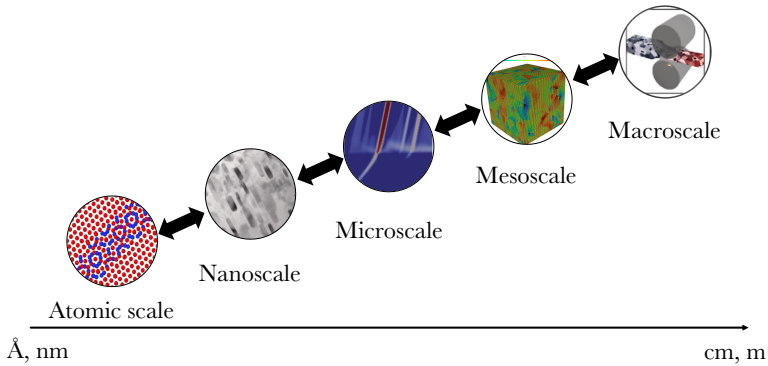


FIGURE 2.1: Relevant length scales for Mg material-by-design frameworks, from the atomic to the continuum scale. On the macroscale, a hot-rolling simulation is schematically depicted, courtesy of Suhas E.P. At the mesoscale we show a representative volume element of multiple grains simulated with our self-developed full-field methods. The microscale shows the propagation of twin needles across a grain boundary, adapted from [4] with permission from Elsevier, whilst the nanoscale shows a micrograph of precipitates in alloy A9, courtesy of Suhas E.P. Finally, the depiction at the atomic scale is that of solute atoms embedded in a matrix, courtesy of P. Yi.

size from approximately 1 to 100 micrometers, although nano-crystalline materials also hold significance, particularly in Mg [48].

Polycrystals are typically specified via two primary aspects: the grain size and the underlying texture. The texture refers to the distribution of crystallographic orientations within polycrystals. When a majority of grains align in one or multiple distinct directions, we say that the polycrystal exhibits a strong texture. In contrast, when grains are oriented more randomly, the texture is diffuse.

Understanding grain orientations may initially seem like a daunting task, but it can be easily described by the crystallographic directions of each unit cell. In the hcp system under investigation, the main directions are represented by the $\langle c \rangle$ direction, which corresponds to the height of the unit cell, and the three *linearly dependent* $\langle a \rangle$ directions lying in the basal plane (see Figure 2.2(a)). The orientation of grains is typically described via a rotation matrix, using the Bunge convention that involves three Euler angles. However, alternative representations such as quaternions may be used, depending on the specific field and application.

Texture representation, on the other hand, often employs a pole figure, a concept that maps a 3D orientation onto a 2D space using a stereographic projection (see Figure 2.2(b)). A stereographic representation maps the intersection of a chosen direction (a representative crystal axis) with the equator plane of the unit-sphere, whereby the crystal axis conventionally originates at the south pole of the sphere. The crystal axis (in our example this is the c -axis) is rotated via the rotation matrix obtained from the Euler angles. Each grain inside a polycrystal is thus mapped to a 2D surface, where the texture is quantified using an orientation density function (ODF). Its value at a given point describes the probability of finding grains that intersect the equatorial plane at this place. This provides a clear graphical and mathematical representation of the strength of the texture.

Finally, the other main descriptor of polycrystals is the grain size which has several implications on the material behavior due to hardening mechanisms associated with the grain size and size effects, as discussed in Section 2.2.6.

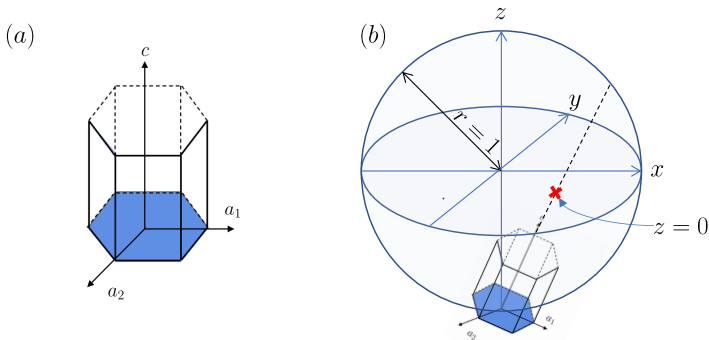


FIGURE 2.2: Main crystal axes in the hcp system are shown in (a), with the basal plane represented in blue. Only two independent a -directions are shown, a_3 can be constructed by a linear combination of a_1 and a_2 . A schematic representation of a stereographic projection is shown in (b).

Upon further magnification of the material, we reach the microscale and the view changes again, namely to single grains. Each grain represents a periodic arrangement of atoms on a lattice, with a given lattice structure. In metals, the most common lattice structures include face-centered cubic (fcc), body-centered cubic (bcc), hexagonal closest packed (hcp), and some

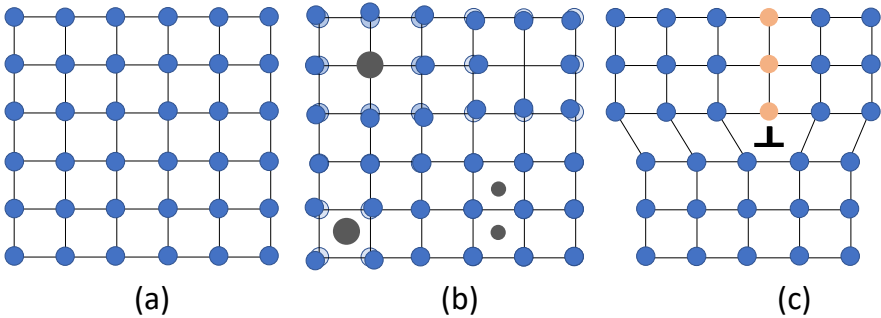


FIGURE 2.3: Lattice defects in metals. (a) represents a perfect lattice, (b) shows point defects such as large and small interstitial atoms, a lattice vacancy and a substitutional atom. (c) shows a line defect known as edge dislocation.

mono- and triclinic lattices. However, it is important to note that the atomic arrangement within grains is rarely perfect. Advanced microscopy techniques such as transmission electron microscopy (TEM) allow us to observe various defects within the grains, including precipitates, and dislocations. Precipitates are relatively large aggregations of an alloy phase that form their own lattice structures, and they exist on the microscale. Dislocations on the other hand are faults in the stacking order of the material and occur naturally upon solidification, as well as during loading, in pure or alloyed material. They play a crucial role in plastic deformation and are discussed in more detail in Section 2.2. Further, defects, such as inclusions, solutes, and vacancies, exist on this scale.

These defects are typically classified into different dimensions: 0-D point defects, 1-D line defects, and 2-D surface lattice defects. Point defects include vacancies (missing lattice atoms), small and large interstitial atoms (atoms of different types located between lattice sites), and small and large substitutional atoms (atoms of different types replacing lattice atoms). Figure 2.3(b) and (c) illustrate examples of point and line defects within an otherwise perfect lattice.

On an even finer level, individual atoms are resolved. The atoms are arranged in a grid, held in place by the interatomic interaction forces, derived from the energy potential. The latter governs the strength of the lattice as well as all of the physical properties associated with the material. During elastic deformation, the atoms are stretched away from their equilibrium

positions r^* a stretched position r^{elast} , thus increasing the energy of the material. If released, the atoms would return to their equilibrium positions.

2.1.1 Lower-Scale Effects on Plasticity

In contrast to elastic deformation, plastic deformation in materials involves the irreversible displacement of atoms or entire atomic planes to neighboring equilibrium positions, leading to lasting deformation and an increase in energy within the material. The presence of defects within the material significantly affects the energy landscape, thereby influencing the ease or hindrance of plastic deformation. In the case of point defects, such as an interstitial atom, the lattice atoms in the vicinity of the defect experience compression, resulting in a higher energy state that impedes atom movement. Conversely, in the presence of a vacancy, the lattice atoms are spaced further apart, facilitating the movement of atoms into the vacant position and leading to a lower energy state. Figure 2.3 illustrates a schematic representation of these point defects.

Similarly, line defects such as inserted dislocations increase the energy in the surrounding lattice but also reduce the energy barrier for plastic deformation. However, it is more challenging to visually showcase their impact on the energy landscape. Additionally, the presence of multiple dislocations affects one another and increases the resistance to plastic flow. A detailed discussion of these aspects, particularly related to hardening, is provided in Section 2.2.6.

At the atomic scale, additional factors come into play, such as the thermal motion of atoms and the interaction forces between lattice atoms. For example, an increase in temperature enhances the mobility of atoms and facilitating plastic flow. Consequently, the constitutive behavior observed in materials encompasses a wide range of scales, spanning from a few Angstroms at the lower end to meters at the continuum level.

In an ideal scenario, a model would seamlessly integrate the effects of all scales to provide a macroscopic representation of the material. However, dealing with such a broad range of scales poses numerous challenges for modeling, and unfortunately, achieving this is practically infeasible. The computation of all interactions between atoms, even in a relatively small cube of 1 cm^3 , would surpass the capacities of most supercomputers due to the immense complexity of the algorithms and the extended time scales associated with the smallest resolutions. Consequently, attempting to model systems as complex as airplanes or cars with such an approach would

be impractical. Instead, researchers often make simplifying assumptions to derive descriptions of the material at higher length scales, allowing for computationally feasible representations. This represents an important factor for consideration in the choice of modeling methodology in the present thesis.

2.2 MECHANICAL PROCESSES DURING PLASTIC DEFORMATION IN MG

Before delving into the modeling approach, it is essential to provide a comprehensive understanding of the material behavior of Mg, including its deformation modes, micromechanics, and associated mechanisms. While this chapter offers a broad overview, more detailed discussions on specific topics will be presented in subsequent chapters or can be found in extensive reviews by Eswarappa Prameela et al. [1], Nie, Shin, and Zeng [2], Kecskes et al. [58], and Huang and Logé [85].

Mg-based materials exhibit several distinctive phenomena. They display pronounced plastic anisotropy, meaning that the material exhibits directional plastic behavior. In Mg, this results in certain directions exhibiting a somewhat brittle response with little ductility, while others show weaker, more ductile behavior [86–88]. This phenomenon is observable at the level of a single crystal as well as at the mesoscopic and macroscopic levels [2, 8, 18, 19, 21, 86, 89, 90]. Additionally, tension-compression asymmetry is observed in single crystals of pure Mg [91], as well as in Mg alloys. Further, this behavior extends to polycrystals, as shown in Figure 2.4 (a). This is especially the case when the texture is pronounced [92, 93], and in a much weaker manner, the phenomenon occurs in as-cast alloys, exhibiting more diffuse textures [94]. Consequently, the pronounced anisotropy and tension-compression asymmetry occur for polycrystals forming strong textures such as pure Mg and AZ series [2, 5, 8, 9, 95]. This is particularly the case for Mg alloys subjected to cold and hot rolling, and extrusion [2, 5, 96], see e.g. results for rolled Mg alloy AZ31 in 2.4(a). The propensity of Mg to form strong textures, as well as the anisotropic material response, stem from underlying deformation mechanisms and must be accounted for in our model.

Further, Mg single and polycrystals exhibit a phase transformation under certain loading conditions, called twinning. Twinning is a process of local reorientation of the atomic lattice and induces a significant change in the material properties for compression along the rolling direction (RD) and transverse direction (TD) of the underlying samples. The behavior is shown

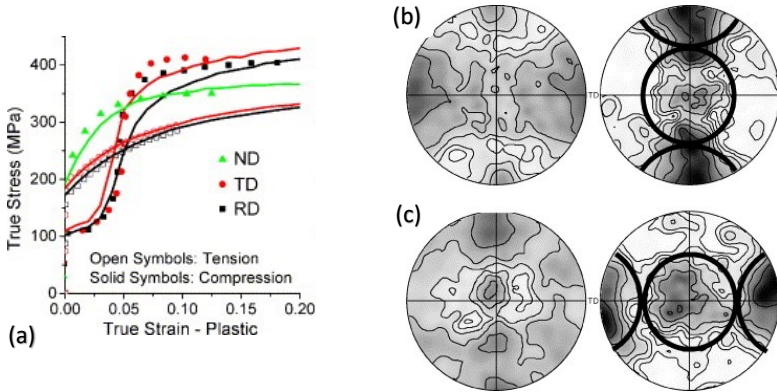


FIGURE 2.4: (a) Stress-strain curves of AZ₃₁B rolled sheet data loaded under compression and tension along the three main directions. (b) and (c) show the resulting texture after compression in the rolling direction and the transverse direction, respectively. Adapted from [5] with permission from Elsevier.

clearly in Figure 2.4(a), for the TD and RD cases under compression. At around 4.5 – 5% true plastic strain the hardening rate of the TD and RD samples rapidly increases, linked with the reorientation in the crystals due to twinning – a phenomenon that we discuss in more detail later in this Section. This behavior renders modeling the material more challenging, as the mechanism has to be efficiently integrated into the constitutive description. Further, the change of orientation of the lattice has to be accounted for, which depends on the loading direction, as shown in Figure 2.4(b,c), where the polycrystals were loaded along the rolling and transverse directions, respectively and yield a different final texture.

In the remainder of this Section, we provide an overview of the essential underlying mechanical processes in Mg that lead to these phenomena. We begin by introducing the crystallographic structure of Mg that leads to many of the observed behaviors in Mg, followed by a description of the mechanics of plastic deformation in Mg and polycrystalline behavior, slip and twinning. Next, we explore the characterization of single-crystalline behavior at ambient temperatures, followed by the thermal behavior of Mg and the polycrystalline characteristics. Finally, we introduce a number of relevant hardening mechanisms.

2.2.1 Crystallography and Stacking Faults in Mg

The hcp structure in Mg is at the core of the numerous peculiarities of the material. It has a closest-packed plane in (0001) and close-packed directions of $\{11\bar{2}0\}$ ¹ and normally follows an A, B, A, B, \dots, A, B stacking sequence with hexagonal unit cells as shown in Figure 2.5. The atoms of the A layers are shown in blue, whereas the ones belonging to the B layers are shown in yellow. In addition, the main close packed planes and directions are shown in 2.5 (a), with the normals and directions being shown in Miller indices. Further, the main directions, a and c of the unit cell are shown. Due to its hexagonal structure, Mg shows symmetries around the c -axis, leading to three *linearly dependent* a directions in the basal plane. We only show two here, as there are only two *independent* ones, a notion that becomes important later in our discussion of plastic deformation modes in Mg. In Figure 2.5 (b), the most common twin planes are shown.

During plastic deformation, perfect and imperfect dislocations occur. Perfect dislocations have Burgers vectors in the basal plane along $\langle a \rangle$, the plane perpendicular to it along $\langle c \rangle$, or as a sum of the two $\langle c + a \rangle$, whereas imperfect dislocations occur on the basal plane with either a Shockley partial-type Burgers vector, a Burgers vector perpendicular to the basal plane, or a combination of the two [2]. These dislocations, among other systems, lead to the formation and propagation of stacking faults. The stacking faults are bounded by partial dislocations at each end, and the stacking fault energy (SFE) is given by

$$W_{SFE} = \frac{Gb^2}{4\pi d'} \quad (2.1)$$

where G is the shear modulus, b is the Burgers vector of the partial dislocations and d' is the distance between the two partial dislocations. In the following we discuss the different types of stacking faults that exist in Mg, before giving a more in-depth overview of the types of plastic mechanisms leading to Mg's peculiar plastic behavior.

There are numerous types of stacking faults in Mg, including the four primary ones – the intrinsic faults I₁ and I₂, the extrinsic fault E, and the twin-like fault T₂ [97]. The I₁ fault is produced by removing a basal plane and shearing the remaining planes. It changes the stacking order of close-packed planes and can be formed through dissociation of a perfect dislocation or vacancy condensation, resulting in two sessile Frank partial

¹ denoted in Miller indices

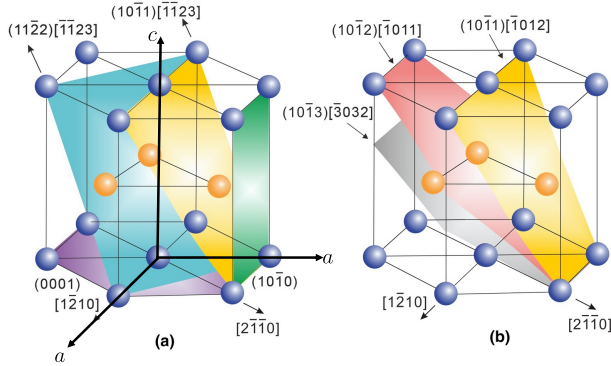


FIGURE 2.5: Hexagonal closest-packed unit cell with corresponding closest packed planes allowing for dislocation movement. The planes best suited for dislocation movement are shown in (a), while the planes best suited for twin-like stacking faults are shown in (b). Adapted from Nie, Shin, and Zeng [2], reproduced with permission from SNCSC.

dislocations at each end [2]. Further, solute atoms may accumulate in I1 faults, but there are few experimental studies verifying this [2]. Most rely on computational models with one solute atom. For commonly used elements in Mg alloys, Al, Mn, Zr, Y, Nd, Ce, La, and Ca, solute segregation in I1 faults lowers the SFE, suggesting that their presence may cause more I1 stacking faults. The effect in ternary or higher-order alloys has not been studied. The validity of these data has not been verified by experiments. While some solutes seem to not affect the slip in I1, others are thought to increase or decrease the SFE [2]. A representation of the stacking faults is shown in Figure 2.6.

The I2 fault is formed by shearing the hexagonal lattice by $1/3\{10\bar{1}0\}$ or by dissociating a perfect $\langle a \rangle$ dislocation with a Shockley partial dislocation on the basal plane. I2 faults are generated by the precipitation of a plate-shaped particle or the formation of steps of single-layer height on twin boundaries. Further, the energy of the stacking fault is affected by the presence of solutes in solid solutions of some binary Mg alloys [2]. However, there is a lack of data for ternary and higher-order Mg solid solutions, and caution is needed when characterizing stacking faults using conventional TEM. The SFE of I2 faults is about twice that of I1 faults in pure Mg [70].

The extrinsic fault E is formed by inserting a C plane into the hexagonal stacking sequence, or the dissociation of a dislocation. It is bounded by Frank partial dislocations. The stacking order of the close-packed planes

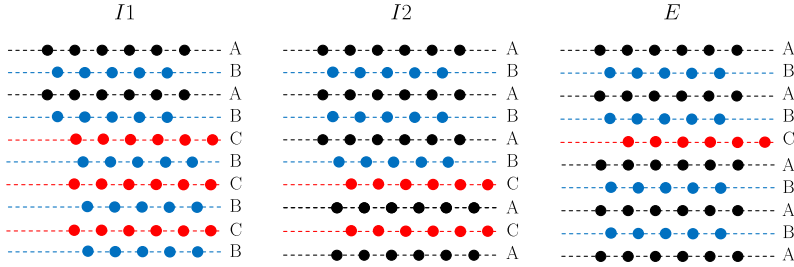


FIGURE 2.6: I₁, I₂ and E stacking faults in hcp crystal lattice.

outside this segment is different from that associated with an I₂ fault. The SFE of this fault is roughly three times that of the I₁ fault in pure Mg [70].

The T₂ fault can arise from an I₂ fault or solute segregation [98]. It results from displacing atomic columns by a partial dislocation ($1/3 \{01\bar{1}0\}$) in an A or B plane, altering the stacking sequence. This creates a twin-like arrangement of close-packed planes with respect to the fault plane. The energy of the T₂ fault in pure Mg is $41\text{--}43 \text{ mJ m}^{-2}$, which is higher than the I₁ and I₂ faults but lower than the E fault.

Finally, stacking faults out of the basal plane have also been reported along the prismatic I $\{10\bar{1}0\}$, prismatic II $\{11\bar{2}0\}$, pyramidal I $\{10\bar{1}1\}$ and pyramidal II $\{11\bar{2}2\}$ planes [99–101], despite a lack of experimental validation [2]. Stacking faults on pyramidal planes (SFpyI and SFpyII) have been observed in molecular dynamics simulations, and their values for pure Mg are 164 and 168 mJ m^{-2} , respectively. These values decrease with increasing solute concentration, such as Y [2] and Al [102], but the impact of many other solutes is yet unknown. One approach to improving the ductility of Mg alloys thus lies in solute-assisted dislocation climbing via cross-slip, especially with rare-earth solutes. The presence of pyramidal stacking faults in microstructures can be readily detected by modern TEM or STEM techniques, however, it is yet to be fully determined whether the reduction of energy barriers to the pyramidal cross-slip is the primary cause of improved ductility in some Mg alloys.

For crystals to accommodate plastic deformation, in general, 5 independent deformation mechanisms must be present. This is called the Taylor (or Von Mises) flow criterion after Taylor and Floyd [103] and Von Mises [104]. The stacking faults and their associated energy in a material, however, deeply affect this criterion. The SFE is a key determinant for the types of deformation activity of the material. High SFE materials tend to deform by

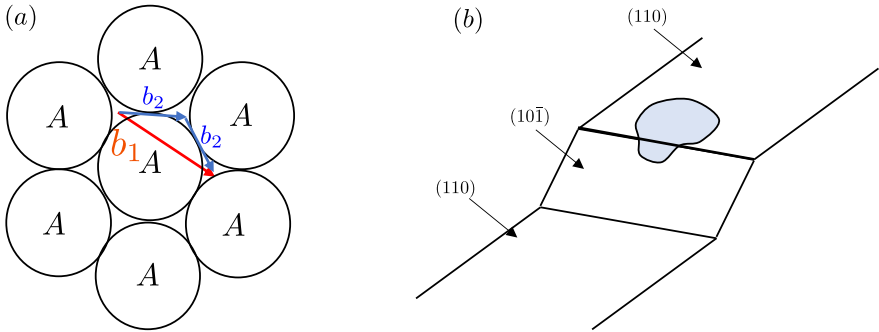


FIGURE 2.7: Dissociation of a perfect dislocation into two partial dislocations in (a) and propagation of a screw dislocation via cross-slip onto another plane exemplified for an fcc crystal in (b).

edge dislocations and screw dislocations that may cross-slip. This reduces the number of necessary independent deformation modes to 4 in high SFE materials, typically enhancing ductility [105, 106]. Contrarily, in low SFE materials, cross-slip is inhibited and dislocations tend to dissociate, this process is schematically shown in Figure 2.7 (a). Thus, low SFE materials form T2 stacking faults that are bounded by partial dislocations. Since they cannot cross-slip, the number of deformation modes required remains at least 5. Mg has low and high energy stacking faults, meaning it falls into a realm in between the extremes. This has deep-reaching implications for its plastic deformation mechanisms.

2.2.2 Slip and Twin Systems in Mg

Let us now dive deeper into plastic deformation mechanisms in Mg. During plastic deformation, irreversible displacement is accumulated in the form of dislocations on slip systems, as well as the reorientation inherent to twinning that leads to shear on twin systems. Each of those systems consists of a slip (or twin) direction, as well as a normal, describing the plane on which deformation occurs. We show the main slip and twin systems exhibited in Mg in Figure 2.5.

Edge dislocations are the consequence of the movement of a half-plane along a given slip direction on a slip plane by a given amount $|b|$, corresponding to the length of Burger's vector, whereas screw dislocations move perpendicular to the Burger's vector of the dislocation. The length of

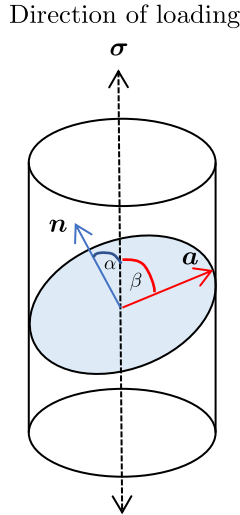


FIGURE 2.8: Schematic depiction of the Schmid law.

Burger's vectors for different slip systems varies. For basal and prismatic slip, the length is 3.2 \AA , whereas for pyramidal systems it is 6.1 \AA . For twins, typically a distinct amount of shear is associated with the accumulation of deformation, depending on the type of twin system.

This movement incurs different energy barriers. Propagation of a dislocation along a system occurs when these energy barriers are overcome. In a microscopic description of plastic deformation, usually, stress measures are used to describe the barriers associated with plastic deformation. The minimum stress required along the slip direction for a given Burgers vector of the dislocation to initiate slip is called the critical resolved shear stress (CRSS), τ_{CRSS} , and is directly linked to the energy of the stacking faults created in the process.

For a given applied Cauchy stress, σ , the resolved shear stress (RSS), τ_{RSS} , on a slip plane and direction is determined by the angles α and β , which represent the angle between the stress axis and the slip (or twin) direction, and the plane normal, respectively. A graphical representation is given in Figure 2.8. It is often assumed that all slip and twin systems follow the Schmid law for activation. For slip to occur, the RSS must be equal to or greater than the CRSS of the system.

τ_{RSS} on a slip plane and direction, is given as

$$\tau_{\text{RSS}} = \sigma \cos(\alpha) \cos(\beta), \quad (2.2)$$

where the expression $\cos(\alpha) \cos(\beta)$ is called the Schmid factor, and the law (2.2) is called the Schmid law, whereas σ is the stress applied to the material. Although this is still debated for the case of certain twin systems, for the remainder of this thesis we assume that the Schmid law holds for the evolution of all plastic deformation modes.

2.2.2.1 Slip

Let us begin our discussion with slip activity. The hcp crystal structure allows for a large number of readily activated slip modes that allow for basal plane deformation, indicated by the $\langle a \rangle$ direction. Of these, basal slip is the prime deformation mode, due to its low CRSS value, and accounts for a large portion of the overall slip activity, which has been confirmed experimentally [3, 8, 9, 19] as well as numerically [5, 107, 108]. It leads to line dislocation movement in the basal plane and is associated with stacking fault I1. It does, however, only provide the grains with two individual slip systems, an insufficient amount to allow them to deform freely while accounting for the deformation of neighboring grains (in polycrystals) and to fulfill the Taylor (or von Mises) flow criterion [103, 104]. Therefore, non-basal slip on either the prismatic or pyramidal systems is necessary to accommodate these types of deformation, where possible. These deformation modes, however, exhibit much higher CRSS values, as shown in Figure 2.9. Their activity is also discussed in Kelley and Hosford [8], Chapuis and Driver [9], and Yoshinaga and Horiuchi [17].

In contrast, only a limited number of deformation modes exist to accommodate deformation in the direction of the c -axis. Those modes comprise the Pyramidal I & II $\langle c + a \rangle$ slip, as well as the tensile $\{10\bar{1}2\}$ and the compressive $\{10\bar{1}1\}$ twin systems, whose discussion we postpone for now. It is widely believed that slip deformation along this direction is mainly attributed to the pyramidal II systems [3, 8, 9, 18, 19, 25, 108, 109], despite some recent studies by Kweon and Raja [54] and Xie et al. [110] suggesting the pyramidal I $\langle c + a \rangle$ system, plays a crucial role in slip behavior. This latter variant is, however, difficult to trace experimentally and therefore often assumed to play a minor role.

Pyramidal II slip, despite its relatively large CRSS value, is comparatively often observed, due to its occurrence along one of the ideal dislocation directions in the system [2, 17, 25]. Further, pyramidal II dislocations have

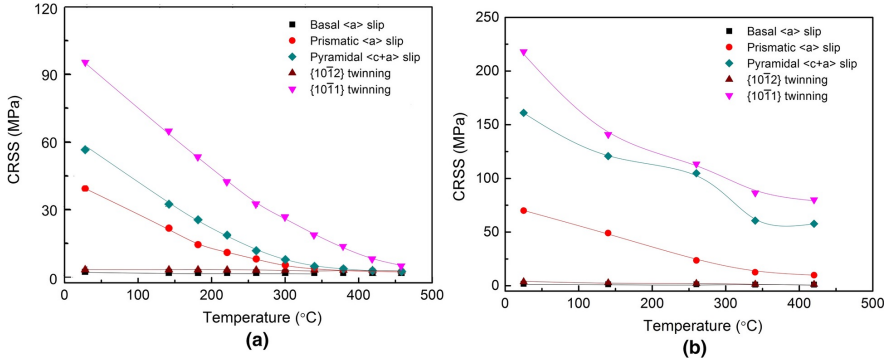


FIGURE 2.9: Evolution of the CRSS values of distinct slip systems with temperature are shown for pure Mg in (a) and after the addition of 1 wt% of Al solute in (b). Reprinted from [2] with permission from SNCSC.

the potential to exhibit cross-slip, a phenomenon that reduces the required number of deformation modes. However, recent studies have shown that the $\langle c + a \rangle$ edge dislocations involved in pyramidal II slip tend to dissociate into immobile structures [7, 21, 53, 111]. They are typically observed in conjunction with $\langle c \rangle$ and $\langle a \rangle$ dislocations [7, 112], leading to significant cross-hardening. Moreover, the $\langle c + a \rangle$ edge dislocations were found to be inherently unstable, leading to limited mobility. Consequently, the immobilization of these dislocations results in a rapidly hardening stress-strain response, leading to brittle failure in Mg crystals [8].

Experimental results reported by Kelley and Hosford [8] and Wonsiewicz and Backofen [19] show the extent of the anisotropy for Mg single and polycrystals. We discuss these results in more detail in Section 2.2.3. The Taylor flow requirement is slightly relaxed in polycrystalline media, where it was found that only four slip modes are necessary, since internal stresses at grain boundaries may cause local allocation of deformation in localized twins [7, 113]. This explains the weakened anisotropic response in polycrystalline Mg. For single crystals, however, no such option exists. Hence, despite the much larger CRSS values, the non-basal slip systems are commonly observed at room temperature, especially on microscopic scales [8, 17, 25, 114].

In alloys, the presence of solute atoms has been shown to facilitate cross-slip and the presence of pyramidal slip in the system, thereby increasing the ductility [2, 63, 115, 116]. Hence, alloying can serve as a remedy against brittle failure. For instance, in AZ₃₁ alloy, the $\langle c + a \rangle$ dislocations do not

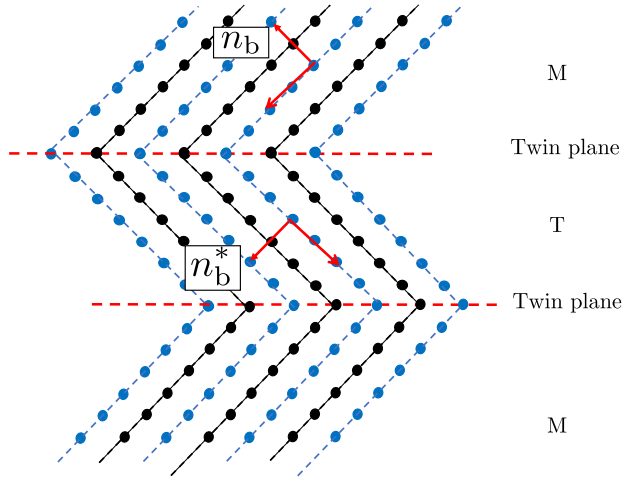


FIGURE 2.10: Schematic depiction of a twin in an hcp material following A, B, \dots, A stacking sequence. The twin planes (mirror planes) are indicated in red. The M and T labels denote the matrix and twin phase, respectively. We show the reorientation of a basal slip system with normal n_b to its new configuration with n_b^* during a twinning event.

dissociate [117]. Alternatively, elevated temperatures facilitate dislocation climbing, leading to increased ductility [118], which is often utilized during processing and is one of the focus points of the present thesis. We discuss this topic later in this chapter. At room temperature, however, the material resorts to another deformation mode, twinning.

2.2.2.2 Twins

Twinning is a process under which the material reorients parts of its lattice along a given twin plane, such as to form a reoriented phase inside the grain. The mirroring of the twin leads to a rotation in the underlying slip systems, leading to a reoriented slip system, exemplified for a basal system in Figure 2.10. This phenomenon typically occurs when it is energetically more favorable to undergo this reorientation process rather than undergo slip. This process leads to major changes in the microstructure and plays a crucial role in defining a material's constitutive behavior.

Twins are not unique to Mg but are observed in many materials. A comprehensive study was carried out by Yoo [7], comparing twinning in

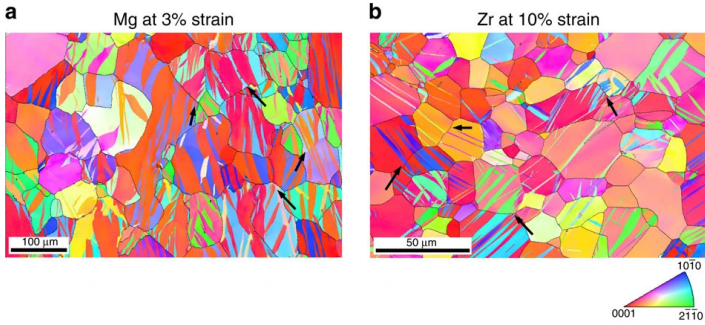


FIGURE 2.11: Electron back scattered diffraction (EBSD) scans of (a) Mg strained to 3% in-plane compression at room temperature (standard stereographic triangle showing compression direction) and (b) Zr strained to 10% in-plane compression at 76K temperature (standard stereographic triangle showing plate normal direction) at a strain rate of 10^3 s. Several adjoining twin pairs can be seen; a few are marked by black arrows [6]. Reprinted under open access creative commons license from Arul Kumar et al. [6].

Mg, Be, Zr, and Ti, among others. They compare the ductility and the plastic behavior of these materials and relate the results to the presence of twinning in the material. It was found that the presence of few twins correlated with brittle behavior in the material [7], and that the ductility of Ti and its alloys is due in part to the presence of a large number of profuse, fine twins of multiple sorts.

Twins can form under many circumstances such as homogenous nucleation, in the vicinity of lattice defects, at pre-existing nuclei, and along twin boundaries. The homogenous nucleation of twins inside grains, however, is relatively rare. As a result, twins usually occur at grain boundaries [113], precipitates, or twin boundaries, where stress concentrations tend to occur. This is clearly shown in Figure 2.11, where the transmission of twins and origination of new twins at grain boundaries is clearly shown.

The exact nucleation and growth process of twins is still the topic of investigations [71, 119], but in general, one assumes that twins follow a similar Schmid law for propagation once they are nucleated. The nucleated twins propagate quickly throughout the material, forming needle-like structures as they reach the opposite sides of grains. In this process, the twin tip propagates much faster than the lateral sides of the twins. With continued straining, new twins may appear in neighboring grains at positions where

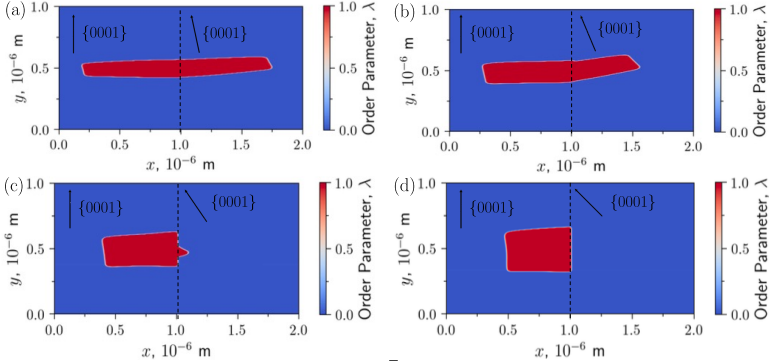


FIGURE 2.12: Illustrative example of the transmission of a twin in a Mg bicrystal PFM simulation with varying grain misorientation angles. (a) 11.25° , (b) 22.5° , (c) 33.75° , and (d) 45°

primary twins have encountered a grain boundary, a process known as twin transmission. This phenomenon is most effective when neighboring grains have small misorientation angles, as the incoming and outgoing twins provide the best accommodation for stress concentration at the boundary. We show results from a phase-field simulation showcasing the transmission of twins across a grain boundary in a bicrystal in 2.12. The transmission of the twin phase across the boundary depends on the misorientation angle between the two grains, showing that a grain boundary alone is not sufficient to nucleate twins, the orientation of the system further has to be appropriate.

Twinning in Mg

As with slip, numerous twin systems exist. In Mg and Mg alloys, there are several potential twin systems, with the most commonly observed ones being the primary twins, the $\{10\bar{1}2\}$ tensile and $\{10\bar{1}1\}$ compressive systems, as well as the secondary or double twins, $\{10\bar{1}1\}$ - $\{10\bar{1}2\}$ and $\{10\bar{1}3\}$ - $\{10\bar{1}2\}$. Other twin systems, such as the $\{10\bar{1}4\}$, $\{10\bar{1}5\}$, $\{30\bar{3}4\}$, $\{11\bar{2}1\}$, and $\{11\bar{2}4\}$ systems, are rarely observed [2].

Whether twin systems are tensile or compressive depends largely on the c/a -ratio of the material [7]. Compressive, means that the twinning leads to a contraction along the c -axis, while tensile indicates an elongation. Below a certain c/a -ratio, the system is a tensile twin (TT) system, and above, it is a compressive twin (CT) system. We show this in Figure 2.13 at the example

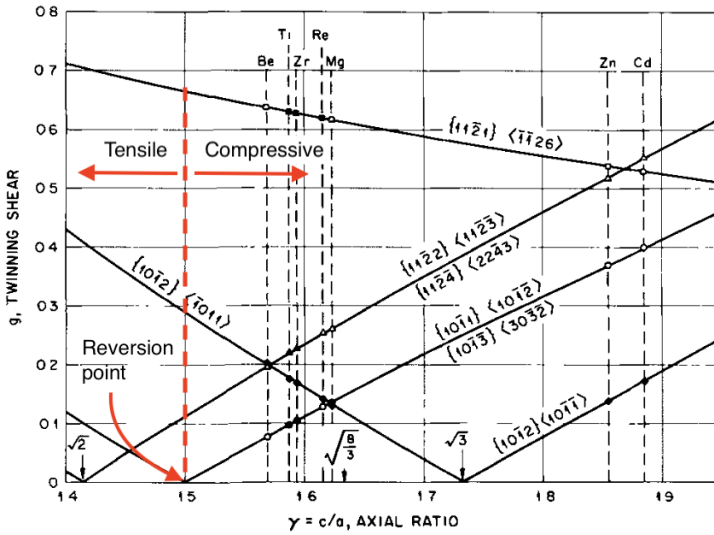


FIGURE 2.13: Twinning shear and nature of a twin system in hcp materials in dependence of the c/a -ratio. Adapted from Yoo [7] with permission from SNSC.

of the $\{1 - \bar{1}1\}$ CT system. Left of a reversion point (i.e. at lower c/a ratios) the system is tensile, meaning it elongates the c -axis upon activation. On the right of that point, however, it becomes compressive, i.e. it shortens the c -axis. Note that this is a *given* property of the system, a tensile system may never lead to a shortening of the c -axis and vice versa. In Mg, the ratio is 1.624, leading to the given types of twin systems that we discuss in this thesis. Further, each twin system leads to a predefined amount of shear in the reoriented area, depending on the twin system and the c/a -ratio. More information is given in Yoo [7]. In addition to the polar nature of twins, the CRSS value associated with the TT and the CT systems differ by orders of magnitude, see Figure 2.9 meaning that TTs may form at low stresses, whereas CTs require large stresses for activation. These factors all together lead to disparate behavior among the twin systems in Mg.

In general, both, the TT and CT system have 6 equivalent orientations (i.e. same CRSS and energy associated with the system), sufficient to accommodate almost any arbitrary deformation. However, the systems behaviour cannot accommodate the same amounts of overall deformation. This is attributed to two main effects, a rapid hardening associated with CT systems

as well as a slower propagation of CTs compared to TTs by almost one order of magnitude [108, 120, 121].

Despite these facts, CTs are shown to occur when physically *necessary* [8, 19]. However, the CTs can only accommodate relatively little deformation themselves, as they tend to harden extensively [108]. Basal slip tends to rapidly occur inside these twins, but due to the low twin volume on the CT system, the combinations of basal slip and twinning is not a sustainable mode for accommodating large amounts of plastic deformation. Instead, it leads to rapid accumulation of dislocations inside the twinned area and fracture [8].

Since only TT systems can accommodate large amounts of deformation, the requirement of profuse twinning for improved ductility, mapped out by [7] is only met under tensile loading of the crystals along the c -direction. In contrast, the capability of the crystals to accommodate compression in this direction is severely limited - either the CT systems or the pyramidal II slip systems are required, and both are hard to activate and harden rapidly and extensively.

A number of studies indicate that the two systems may, in fact, be in competition [8, 15, 19, 25, 56, 122, 123], however, the investigations remain somewhat inconclusive. In the following, we provide a more detailed view on the material behavior and the potential competition of CT and pyramidal slip that may be key to the low ductility of Mg.

2.2.3 Mechanical Response and Microstructure in Mg Single-Crystals

Numerous experimental methods are employed to characterize the properties of materials, such as micropillar compression, tension and compression loading of bulk single-crystalline magnesium, and nano-indentation [8, 18, 25, 124]. At room temperature, the variety of the behavior in the slip systems leads to the aforementioned strong plastic anisotropy. This was first investigated thoroughly by Kelley and Hosford [8]. In their experimental series, they performed channel-die experiments of $\geq 99.8\%$ purity Mg single crystals to isolate the behavior under slip- and twin-governed plastic deformation. Figure 2.14 shows the results of Mg single crystals experiencing plane-strain compression for the room-temperature experiments in pure Mg, reported by Kelley and Hosford [8]. 7 cases, A through G were chosen with the aim to isolate the activation of given slip and twin systems. Six of the cases were chosen with the aim to suppress the ubiquitous basal slip, expecting pyramidal II $\langle c + a \rangle$ to occur in cases A and B, prismatic slip

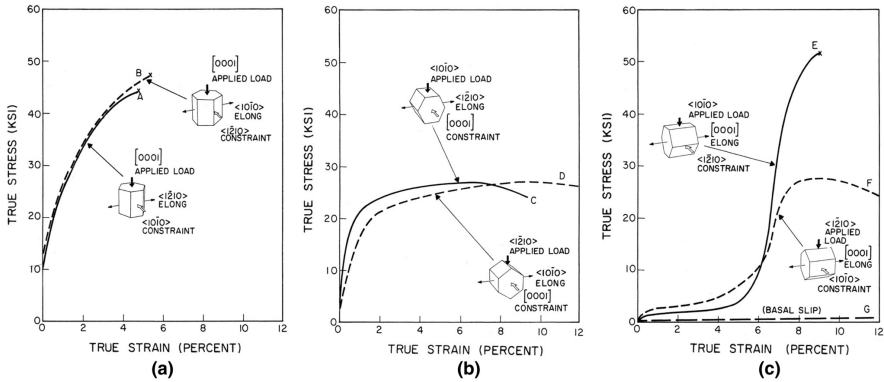


FIGURE 2.14: True stress-true strain response under plane-strain compression of Mg single crystals at room temperature. Adapted from [2, 8], reproduced with permission from SNCSC.

in cases C and D, and tensile twins to dominate cases E and F. Finally, case G was chosen with the expectation for basal slip to occur predominantly.

Cases A and B, on the left, show the response typically associated with the immobilization of the $\langle c+a \rangle$ slip at low strains but high stress levels. Surprisingly, in the experiments by Kelley and Hosford [8], no traces of pyramidal slip were reported. Instead, slight misalignment from the c -axis could already lead to basal slip activation. Fracture occurred early on at about 4% deformation, with traces of CTs present in the material [8]. On the other hand, cases C and D exhibit ductile behavior at lower stress levels. While these crystals are ideally oriented for prismatic and pyramidal $\langle a \rangle$ slip, they did not occur. Rather, a combination of basal slip and profuse twin was reported [8, 19], findings that were later confirmed experimentally and numerically by Selvarajou et al. [124].

With the c -axis freely extensible under plane-strain compression, the crystals show a strongly twin-dominated behavior. Cases E and F showcase the two cases from Kelley and Hosford [8]'s studies. The initial strain-hardening rate of the single crystals is weak, showing the ease of activation of the TT systems. The crystals deform mostly via the activation of the tensile systems up to about 6% strain, at which point the twins in the crystals begin to saturate. The saturation coincides with an overall stiffening of the plastic response. This is related to a reorientation of the slip systems in the rotated lattice. In case E, a rotation of about 86° occurs [8], which leaves the newly oriented systems in a similar configuration to cases A and B. The

resulting rapid increase in stress levels and the similar strain-hardening behavior confirms that. It was observed by Kelley and Hosford [8] that fracture occurred along the $\{10\bar{1}1\}$ and the $\{11\bar{2}4\}$ planes, associated with CTs and pyramidal slip, similar to the ones in case B. Crystals in case F exhibit a different type of orientation than crystals in case E, this is mostly due to the changes in the active slip systems. While the reorientation in case E was about 86° , the one in case F was around 31° . This reorientation led to the activation of some basal slip, explaining the larger ductility.

The last case is case G, where the orientation of the c -axis is such that it is 45° from the compression direction. This orientation is ideal for basal slip activity. These crystals are characterized by ductile behavior and low stress levels. It was later reported in Nie, Shin, and Zeng [2] and Molodov et al. [125, 126] that these crystals can undergo up to 40 to 60% of true strain before showing significant levels of strain hardening.

These experiments constitute some of the most complete experimental studies on the characterization of pure Mg single crystals at room temperature and have since played an important role, in shaping our understanding of the material behavior. They are to this day often used as benchmarks for the calibration of Mg crystal plasticity models, such as by [52, 107, 108, 122], by lack of better data.

Hence, confusion arises due to contradictory findings reported by Lilleodden [25] in their investigation of microcompression on Mg single crystals. Their more recent research examined the material and uncovered no indications of preexisting twin nuclei or other nucleation sites prior to micropillar compression – in their absence, no activity in the CT or TT systems during and after compression was reported. Instead, the study suggests that the deformation of the single crystals can be reasonably attributed solely to pyramidal II slip, since, as the authors contended, the pyramidal II slip systems are the only ones exhibiting non-zero Schmid factors. Although Kelley and Hosford [8] acknowledged a similar phenomenon, they swiftly dismissed it, postulating that minor crystal misalignments could facilitate basal slip. In contrast, Lilleodden [25] argue that the disparity between the observations could arise from the potential presence of twins or nucleation sites in the bulk Mg crystals examined by Kelley and Hosford [8] and Wonsiewicz and Backofen [19]. Moreover, they acknowledge the potential influence of a size effect related to twins, a notion that is now corroborated. However, it is noted that twinning ceases to play a significant role in sub-micron and nanocrystalline materials, whereas Lilleodden [25] conducted experiments on crystallites ranging from 2 – 10 μm in size.

We hypothesize that the CTs are a symptom of necessity in Mg at low temperatures, due to the strong hardening of the pyramidal II slip and if possible, the activation of pyramidal slip is favored. Further, we assume that increased mobility of the pyramidal slip system is the reason for the improved ductility in Mg at elevated temperatures and that CTs should gradually vanish with increased temperature. We explore the experimental findings in this regard to strengthen our hypothesis before building a temperature-aware model incorporating these ideas in chapter 3.

2.2.4 *Mechanical Response at Elevated Temperatures*

The influence of temperature on the mechanical properties of Mg has been the subject of investigation in multiple studies [9, 16, 18, 19, 21]. Collectively, these studies have revealed that the deformation mechanisms observed at elevated temperatures differ from those observed at room temperature. Elevated temperatures enhance the mobility of lattice atoms within the hcp structure. This heightened mobility reduces the energy barrier for plastic motion, thereby promoting slip. This effect is particularly pronounced along non-basal planes, where substantial slip activity is hindered by high room temperature CRSS values. This behavior is illustrated in Figure 2.9 (a). While basal slip and the TT systems exhibit nearly temperature-independent characteristics, non-basal slip systems experience a significant reduction in CRSS values. This outcome results in a greater variety of available slip systems, encompassing various slip types.

Experiments on single crystals under compression along various directions were conducted by Chapuis and Driver [9], Yoshinaga and Horiuchi [16], and Wonsiewicz and Backofen [19]. A gradual transition was observed in the region from 25°C to 300°C, with plastic flow occurring at lower stress levels and higher plastic deformation being accommodated before fracture, even for the stiffest orientations. Around 180°C, the ductility of the material begins to significantly improve, allowing for the accommodation of large degrees of deformation [2, 5, 56]. Initially, it was speculated that twinning at lower temperatures leads to rapid hardening and fracture of crystals, while the onset of dynamic recrystallization at elevated temperatures is responsible for softening and increased ductility [50]. However, the role of dynamic recrystallization in rapid softening remains unclear and requires further investigation.

Chapuis and Driver [9] offer relatively recent studies of Mg single crystals subject to plane strain loading at elevated temperatures. They characterized

the CRSS values based on the stress-strain response of the single crystals. The characterization of the CRSS values for slip and twin systems was taken at 1% plastic strain, as shown in Figure 2.15. It is evident that the temperature has a significant effect on the stress levels and the overall stress-strain behavior of Mg.

Figure 2.15 (a) shows the response of the crystals oriented in a similar fashion as those of cases A and B from Kelley and Hosford [8] and Wonsiewicz and Backofen [19]. The crystals show a more ductile response and a rapid decay of the ultimate stress levels with increasing temperatures. Further, at 150°C a relaxation of the stresses is observed around 1.5 – 2% strain. This is attributed to the formation of compressive $\{10\bar{1}1\}$ and $\{10\bar{1}3\}$ twins, however EBSD maps of the crystals show that the volume fractions of these twins are small. Further, there is significant deviation from the ideal orientation in this experiment, as the crystals ideal orientation in Euler angles would be (0,0,0) but the authors report (45,1,17). As previously shown by Kelley and Hosford [8], even small misalignment leads to the activation of basal slip, explaining the ductility at 150°C, opposed to the results reported by Wonsiewicz and Backofen [19]. With increasing temperatures, the authors report fewer and fewer occurrences of twinning and report the deformation via pyramidal slip. In addition, they report the presence of recrystallized zones throughout.

Figures 2.15 (b) and (c) show the response of single crystals under a -axis compression, similar to cases E and F, and C and D, respectively. The same trends as previously were observed, where increasing temperature leads to a (relatively) rapid reduction of the overall stress levels. Case (b) showcases the results for crystals ideally oriented for TT systems. At room temperature, the corresponding EBSD map shows profuse twinning at 4% strain, as seen in Figure 2.16 (a). Roughly 50-60% of the crystals are reoriented at this stage which is shortly before the stress-strain response begins to drastically change, c.f. Figure 2.15 (b). Figure 2.16 (c) shows the EBSD map for a crystal deformed at 350°C after 9.6% strain. It is evident that twinning is present at this temperature, however the stresses are severely reduced compared to the room-temperature case. This indicates that the material undergoes the same reorientation at elevated temperatures as it does at low temperatures, however, the reoriented region exhibits a far more compliant response to deformation.

Finally, figure 2.15(d) shows the response of a crystal ideally situated for basal slip, similar to case G from Kelley and Hosford [8]. The results show inconclusive relationship between the stress-strain behavior of the

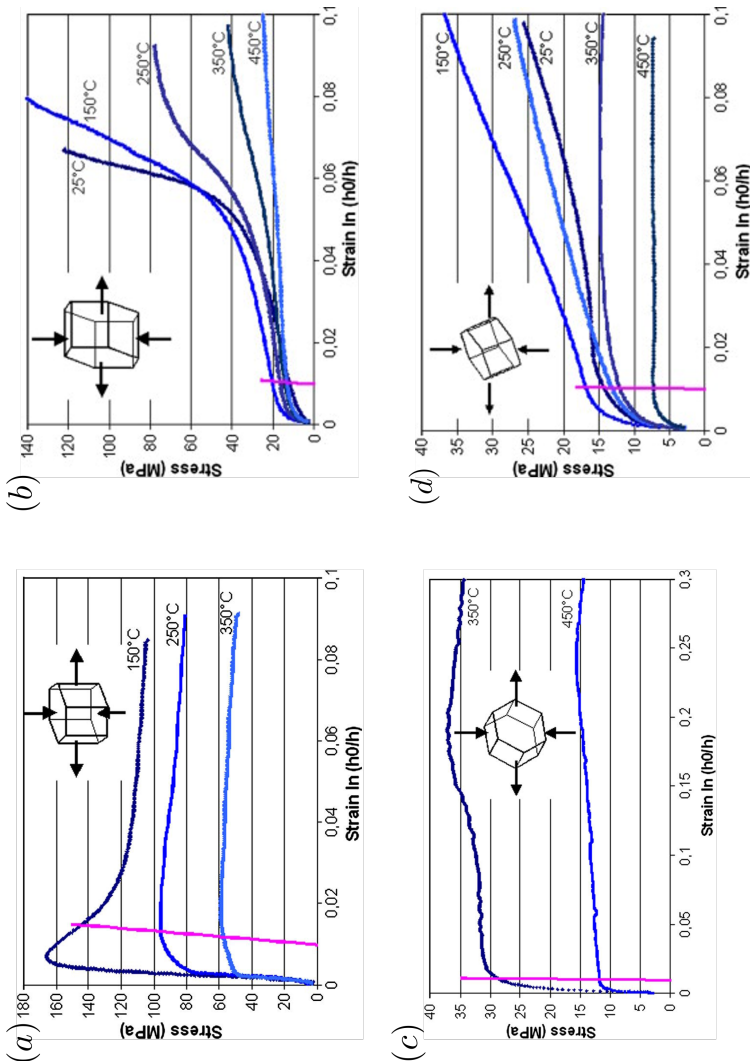


FIGURE 2.15: Response of Mg single crystals under plane strain compression in (a), c -axis compression, (b), a -axis compression with *unconstrained* c -direction, (c) in a -axis compression with *constrained* c -direction, and (d) at an 45° angle to the c -axis such as to promote basal slip. Reprinted from Chapuis and Driver [9] with permission from Elsevier.

crystals and the temperature, with stress levels at 150°C exceeding those at room temperatures. Likely, the orientations of the crystalline samples were different. This showcases how sensitive the material is to alteration in the crystal's orientation, as described in Nie, Shin, and Zeng [2].

Although this study confirms many ideas and findings from previous works, it unfortunately has a number of uncertainties and inconsistencies in the reported behavior, likely due to the non-ideal orientation of the crystals. Hence, they must be used with caution and in conjunction with other studies, such as the ones performed by Ono, Nowak, and Miura [3], Akhtar and Teghtsoonian [18], Wonsiewicz and Backofen [19], Al-Samman et al. [50], and Molodov et al. [125].

The latter investigated the large-strain temperature-dependent material response of single crystals compressed 45° along the *c*-axis and confirmed the temperature-independence of the basal systems up to 40% stress. Both Wonsiewicz and Backofen [19] and Al-Samman et al. [50] observed increased dynamic recrystallization in the grains, which could contribute to softening at elevated temperatures.

Overall, experimental evidence underscores the substantial ductility of Mg at intermediate and higher temperatures, implying that the flow criterion must be satisfied. Studies by Jain and Agnew [5] and Barnett [56] demonstrated that CT mechanisms alone cannot sufficiently account for significant deformation along the *c*-direction, even at elevated temperatures. Interestingly, the frequency of CT diminishes with increasing temperatures across a range of alloys and pure Mg, as reported by Jain and Agnew [5], Chapuis and Driver [9], and Wonsiewicz and Backofen [19]. Given our earlier discussion, which highlighted twinning as an alternative mode of deformation arising due to the absence of more preferable modes, it becomes apparent that slip systems must play a more prominent role.

We see an explanation for the improved ductility is based on the increased mobility of $\langle c + a \rangle$ dislocations, as proposed by Yoshinaga and Horiuchi [17] and confirmed by Chapuis and Driver [9], which strengthens our hypothesis. Subsequent analysis confirmed the presence of pyramidal II slip across temperatures ranging from 20°C to 600°C [21]. Evidence was found that above approximately 200°C, the number density of immobilized long dislocations was reduced significantly, further enhancing our hypothesis [21].

A numerical investigation of this phenomenon is now in order, however this necessitates a well-calibrated model. Numerous challenges persist in characterizing and comprehending thermal effects in Mg, even from an

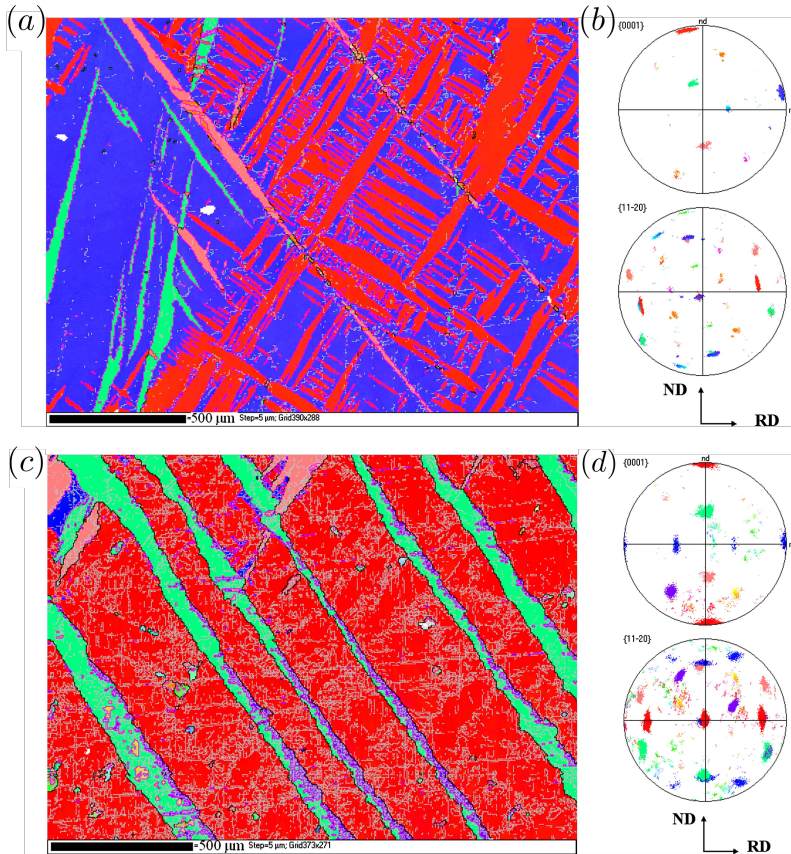


FIGURE 2.16: EBSD map and corresponding pole figure of single crystal after unconstrained a -axis compression at room temperature (a,b), $\epsilon = 0.04$, and at 350°C (c,d), $\epsilon = 0.096$. The parent grain is shown in blue, the twins in red. Note the presence of small recrystallized zones in (c) at the twin boundaries. Reproduced from Chapuis and Driver [9] with permission from Elsevier.

experimental standpoint. These discrepancies outlined above encompass variations in ultimate stresses and the overall transition into a smoother plastic flow regime. This fact underscores the difficulties inherent in experimental examinations of the material and, consequently, in accurately characterizing its behavior. The findings of Chapuis and Driver [9] and Wonsiewicz and Backofen [19] constitute a comprehensive collection of studies pertaining to the temperature-dependent material response in Mg single crystals, and these findings are frequently employed for the calibration of material models.

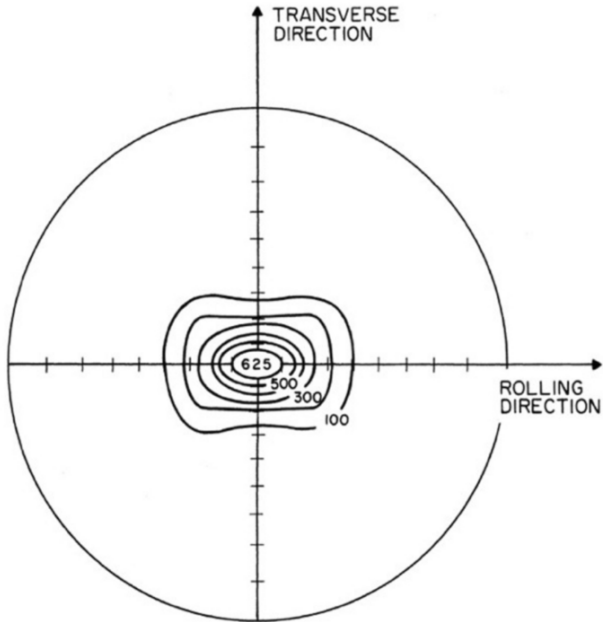
2.2.5 *Mechanical Characterization of Polycrystals*

Before delving into the realm of Modeling and its own complexities, it is worth obtaining a more in-depth understanding of the behavior of polycrystalline materials. In this setting, numerous additional factors such as the texture and grain size influence the material's response. The same studies that offered unprecedented insight into the single crystal behavior of Mg are also a knowledgeable resource to further our understanding of polycrystalline behavior [8, 19].

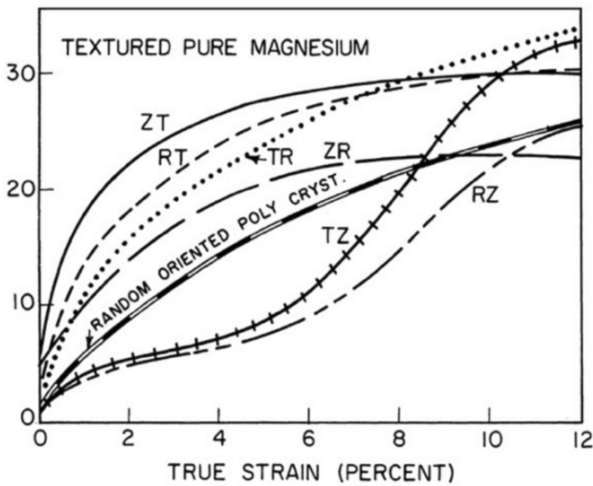
Kelley and Hosford [8] were among the first to evaluate the properties of pure Mg polycrystals. The same series of experiments, as described previously for single crystals, was performed on samples of pure Mg extracted from rolled Mg sheets.

The texture of the sheet material is depicted in Figure 2.17 (a). Here, a basal pole figure is chosen. A strong propensity of the grains to orient along the normal direction of rolling is observed, which is typical behavior for Mg [2, 66]. The texture formation is owed to the strong prevalence of twinning and basal slip during the rolling process.

The samples were cut from the rolled sheet along different orientations and loaded under plane strain compression at quasi-static strain rates along the normal, rolling, and transverse directions (ND, RD, and TD, respectively), with varying combinations of ND, RD, and TD constrained, to evaluate the polycrystalline response of the material. The exact nomenclature is explained in Kelley and Hosford [8]. The authors observed that polycrystalline Mg generally behaves similarly to single crystals, with a somewhat weakened response. Cases RZ and TZ exhibit twin-dominated behavior, leading to a double-S shape of the stress-strain curve due to twinning. It was observed that twinning did not lead to the same sharp change in behavior as in the single-crystal case, which is attributed to the fact that



(a)



(b)

FIGURE 2.17: The texture of polycrystalline rolled Mg sheet, reported by [8], is shown in (a). The corresponding experimental stress-strain curves of the polycrystals under plane strain compression are shown in (b). The nomenclature chosen by Kelley and Hosford [8] is described in chapter 3 and in Kelley and Hosford [8].

a number of grains are oriented away from the ideal position, leading to a mixed, weakened response. The same observations hold true for all other cases, such as ZT and ZR whose texture leads to similar orientations as cases A and C, respectively. Similar experiments were conducted later by Wonsiewicz and Backofen [19] for polycrystals at elevated temperatures. Together, these experiments form the basis for a number of material models, as they both were conducted under almost identical conditions, making them ideal candidates for model calibration and validation.

Further experimental studies for pure Mg polycrystals were conducted by e.g. Ono, Nowak, and Miura [3] who investigated the grain-size effect of polycrystalline Mg at varying temperatures. They observed a temperature dependence of the grain-size hardening factor, although it is unclear, whether this is due to temperature dependence of the process itself or of the plasticity of the slip and twin systems.

Far more experimental and numerical data is available for polycrystalline material, especially for alloys. These contributions cover a number of varying topics, ranging from the investigation of recrystallization, the characterization of sheet material, and texture evolution. The overall characterization of these effects lies outside the scope of the thesis, hence at this point, we refer the interested reader to further literature [5, 49, 65, 68, 86, 89, 127–129].

2.2.6 *Hardening Mechanisms in Mg and its Alloys*

For a complete understanding of the material behavior, however, a number of aspects are still missing. Most notably, there exist a number of hardening effects that may or may not need to be accounted for. The overall material response of a material is composed of a number of mechanisms. We provide an overview of the relevant mechanisms in Mg. For a constitutive model, work hardening needs to be accounted for and for an extension to alloys, a number of other hardening mechanisms could become important. Hence, let us introduce the main hardening effects here.

2.2.6.1 *Work Hardening*

The first and most important hardening mechanism for this thesis is strain (or work) hardening. Work hardening occurs due to dislocation pile-up, where the presence of dislocations leads to a back-stress, increasing the stress required on a slip system to further the dislocation movement, [103]. In its most general form, the hardening mechanism is a function of the

dislocation density and material constants and affects the CRSS, as defined previously, via the relation

$$\tau_{\text{CRSS}} = \tau_0 + G\alpha b\rho^{1/2}, \quad (2.3)$$

with dislocation density ρ , Burger's vector b , shear modulus G , and a material specific correction term, α .

From this formulation, it follows that the stress required to further move dislocations along a given system increases with the square root of the density of dislocations. This formulation is a relatively simple one and more accurate formulations exist that take into account the presence of dislocations on various slip systems and the types of dislocations, such as in the model presented by Liu et al. [4]. It is important to note that plastic deformation moves existing dislocations along a slip direction, but further, dislocations are generated in the process in dislocation sources.

There are a number of dislocation generation mechanisms. The main nucleation mechanisms of interest here are homogeneous nucleation and the nucleation at Frank-Read (FR) sources.

For one, homogeneous nucleation of dislocations occurs when atomic planes rupture, creating two opposite-facing half-plane dislocations in the material. Further deformation leads to these dislocations moving in separate directions.

In addition to that, dislocations may emerge from FR sources. An FR source is a dislocation that is pinned at two points, either by precipitates, other dislocations, or solutes. Due to continued loading, the dislocation bulges and begins to loop around itself, thus effectively creating a new dislocation loop that in turn gets pinned, thus increasing the dislocation density massively, see Figure 2.18. It has long been argued that this mechanism is the main contributor to dislocation nucleation, however, a relatively recent study by Murr [130] challenges this understanding and argues that ledges at grain boundaries are the main mechanism. This has, however, not been verified.

In contrast to the nucleation of dislocations, there are also annihilation processes via recovery mechanisms and when dislocations of opposing directions combine to a full plane (the inversion of the homogeneous nucleation process).

2.2.6.2 Grain Size Hardening

In addition to strain hardening, grain-size hardening plays an important role in the contribution to the yield strength. It is a hardening mechanism that

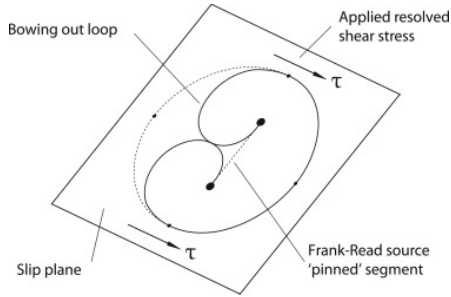


FIGURE 2.18: FR dislocation source. (a): bulging of pinned dislocation, (b): looping of the dislocation around itself, (c): forming of a new dislocation loop. Reprinted from Gurrutxaga-Lerma et al. [10] via Open Commons License.

mostly resides on the polycrystalline level, in contrast to work hardening that occurs for single crystalline descriptions. It is characterized via the Hall-Petch effect [131, 132] and postulates a hardening of the following form

$$\sigma_y = \sigma_0 + \frac{k_0}{\sqrt{d_g}}. \quad (2.4)$$

Thus, the yield strength of the material, σ_y , increases by adding a size-hardening term k_0 , divided by the square root of the grain size d_g . This hardening term is added to the base strength at large grain sizes, σ_0 . The yield strength is typically measured at the onset of plasticity at 0.2% plastic deformation [3] before strain hardening plays a significant role in hardening.

An extensive study was performed by Ono, Nowak, and Miura [3] for the grain size dependence in rolled Mg samples at various temperatures. It was reported that the grain-size hardening effect receded with increasing temperatures. Few studies reporting grain-size effects in pure Mg exist, and even fewer characterizing the impact of temperature. Sadly, this study has some extensive drawbacks. First, no texture is reported in the study. While the stress-strain plots suggest that the tension must have occurred in the TD or RD direction of the rolled specimen, it is unclear. Second, the effects of recrystallization were disregarded. While it is true that this may not have a strong impact on the yield stress, since recrystallization is expected to occur only during plastic deformation, some of the reported yield values were taken at 2% plastic deformation, at which point recrystallization in Mg would already begin, leading to softening [49, 50]. Finally, Mg is a highly anisotropic material exhibiting a tension-compression asymmetry.

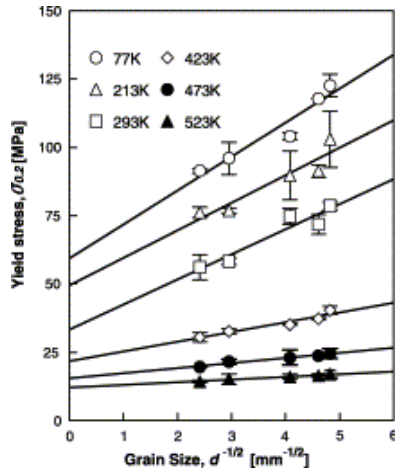


FIGURE 2.19: Hall-Petch hardening in rolled Mg polycrystals tested under tensile load. The direction of loading is unknown. Reprinted from [3], with permission from Elsevier.

This could have severe effects on the Hall-Petch hardening curves under various loading conditions, which was not investigated in this study.

A later study by Caceres, Mann, and Griffiths [133] sheds more light on the directional dependence in Mg and Mg-Zn alloys. Their findings suggest differences in Hall-Petch hardening depending on whether the samples are loaded in tension or in compression. However, they used cast samples instead of rolled samples, thus disregarding the potential effects due to texture. More recent studies and an ongoing effort, such as by Wei et al. [134], show that there are still open questions pertaining to the grain size hardening of Mg and Mg alloys. It is in itself a phenomenon still not well understood and requires further research.

2.2.6.3 Solute Hardening

There are multiple aspects to solute and precipitation hardening as can be seen in e.g. [1]. First and foremost, there are the hardening effects from solute atoms in the lattice on the various slip systems. Solute atoms represent small obstacles to dislocations, inhibiting dislocation movement and thus increasing the CRSS of the respective system. The strengthening effect of

solute in Mg was investigated in a number of scientists' work, involving experimental [18, 135] and *ab-initio* studies [136, 137].

The general approach to solute hardening is given as [138]

$$\Delta\tau_{\text{CRSS}} = Gbe^{3/2}\sqrt{c}, \quad (2.5)$$

where G is the shear modulus of the material, b is the burger's vector of the dislocation, e is the lattice distortion term and c is the solute concentration.

This assumption does not hold for all types of dislocations, and different types of dislocations (edge vs screw) are affected unequally by the presence of solutes, where screw dislocations experience much less hardening.

A comprehensive study on the impact of the presence of solutes in Mg was only performed for basal slip by Tehranchi, Yin, and Curtin [136], who identified the solute strengthening in a range of temperatures, showing thermal effects of the solute hardening in multiple regimes.

2.2.6.4 Precipitation Hardening

Precipitation hardening is a hardening effect associated with the presence of second-phase particles inside grains and along grain boundaries. These second-phase particles pose larger obstacles to dislocations than individual solutes and typically cause more strengthening.

The strengthening mechanism of precipitates is the so-called Orowan strengthening and takes the form

$$\Delta\tau_{\text{CRSS}} = \frac{Gb}{2\pi\lambda\sqrt{(1-\nu)}} \ln \frac{d_p}{r_0}, \quad (2.6)$$

where G represents the shear modulus of the material, b stands for the Burger's vector, λ is the effective inter-obstacle spacing on the slip plane, d_p is the mean planar diameter of the obstacles and r_0 represents the core radius of dislocations. Depending on the precipitate shape and orientation as well as on the slip system being considered, the specific values for d_p and λ as well as the Burgers vector of the dislocation vary. The effects of different precipitate shapes and sizes on basal [90] and non-basal slip [139] were rigorously derived and evaluated for a given number density and precipitate volume fractions between 1% and 5%. The results show that prismatic plate precipitates achieve the highest degrees of hardening due to their potential to reduce the inter-particle spacing the most [90]. Only at low volume fractions, the $\{0001\}$ rod-shaped precipitates are more efficient

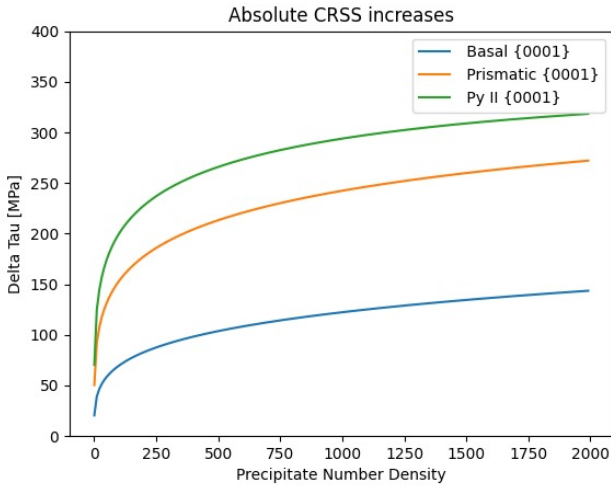


FIGURE 2.20: The theoretical precipitate hardening effect of unshearable, evenly distributed Mg-Al precipitates at 7% volume fraction is shown.

strengtheners. For all precipitate types investigated the precipitate hardening increases with increasing form factors for the basal and prismatic plates and remains almost constant for the rods. For a given volume fraction, the number density of precipitates also plays a significant role, with a higher number density of relatively small precipitates leading to much higher hardening than few, larger, precipitates, see e.g. for basal plate precipitates in Mg-Al alloys the correlation between the number density and the change in CRSS computed for the main slip systems in Figure 2.20

The theoretical hardening, however, is much larger than the effectively observed response. This phenomenon was investigated by Cepeda-Jiménez, Castillo-Rodríguez, and Pérez-Prado [39], who found that the origin of the lower precipitation hardening in Mg alloys lies in the ease with which dislocations in the basal plane can shear the $Mg_{17}Al_{12}$ plate precipitates.

2.3 MODELING APPROACHES FOR MG

While experimental studies guide our understanding of materials, under some circumstances, they reach limitations such as challenges in obtaining in-situ data or different studies reporting contradictory findings. In these

instances, it can often be useful to use models as a tool to test hypotheses and gain insights beyond the experimental limitations.

A variety of models are at our disposal to investigate the differing aspects of Mg, from the atomistic scale to the continuum level. The focus of this thesis lies on the intermediate scales ranging from the micro- to the mesoscale and beyond and will be discussed in detail. For the sake of completeness, however, a short overview of findings from the lower scale modeling is given here.

2.3.1 *Sub-Micro Scale Modeling of Mg*

For investigations on the lowest scales, atomistic or molecular dynamics (MD) simulations and density functional theory (DFT) are employed. These methods have proven invaluable in obtaining insights that are otherwise challenging to get. Yi [63] for instance used MD simulations to investigate the role of prismatic $\langle a \rangle$ dislocation climb near solute clusters in the softening of the material response at room temperature. A single dislocation line is tracked in a simulation box with solute atoms and vacancies present and it was observed that the dislocation climbs to overcome solute obstacles. This appears to be directly correlated with the softening of the pyramidal I glide and thus reduces the anisotropy of the materials even at room temperature. In another instance, Hu et al. [71] investigated the formation and growth of twin embryos via means of MD simulations, gaining insights into the correlation of the twin tip velocity and the applied shear as well as confirming results experimentally. The origin of some of Mg's key characteristics relating to the poor ductility of $\langle c + a \rangle$ pyramidal slip was investigated by [53] via MD and DFT-validated interatomic potentials.

These methods offer unprecedented insights into sub-microscopic processes, however, suffer significantly from scaling issues. Large-scale simulations with this level of resolution are simply impossible, due to the sheer computational cost. Hence, for this thesis, we focus on models on the micro- and macroscales and their integration into higher scales, via multi-scale modeling and a process called homogenization, described in Section 2.3.4. These models offer a good trade-off between physical accuracy and computational speed (as well as scalability), making them good candidates for both, investigating physical phenomena and efficient modeling of the materials that are at the core of the ICMD framework.

2.3.2 Micro- and Mesoscale Modeling Techniques for Mg

When modeling the behavior of Mg on a larger scale, it is essential to employ models capable of capturing its complex mechanics, governed by slip and twin systems. Several approaches with varying levels of accuracy and computational expense exist, such as discrete dislocation dynamics (DDD) and crystal plasticity (CP). DDD may be the most natural approach to modeling plasticity, as the motion of individual dislocations is tracked and computed, which makes it a high-fidelity approach. It allows us to show and investigate local effects of slip and twin systems and their corresponding dislocations in the material, showcasing potential size effects and local interactions, see e.g. Figure 2.21. It typically is constrained to observations of a few 1-10 grains due to the computational expense associated with it and suffers from limitations in approximating twinning.

Fan et al. [11] for instance performed DDD simulations of single and polycrystals of pure Mg investigating the interplay of twin boundaries and slip dislocations. Their results show that tensile twin boundaries pose significant hardening obstacles to slip and contribute significantly to overall material hardening. While these are valuable and high-fidelity findings, the sheer computational cost of this method renders it prohibitive for our sought-after applications.

On the other hand, twins can be interpreted as a phase-transformation process and as such, twins are often modeled as a phase-transformation mechanism via phase-field models (PFM). One example is the PFM utilized by Clayton and Knap [140] to describe twin propagation in an elastic medium. It was later extended to model complex media and materials and found application in Mg from Liu et al. [141] and Ocegueda and Bhattacharya [142].

To explore the solutions derived from these PFMs, we consider the simple case of twin systems embedded in an elastic medium within a large-strain setting, similar to the study conducted by Clayton and Knap [140]. Suppose an otherwise elastic material, with a number of twin systems, β , each described by a twin normal n_β and a direction a_β is given on a domain $\Omega \in \mathbb{R}^d$, $d = 2, 3$. At each point of the domain \mathbf{X} , the material may be in either the matrix or the twin phase.

The overall deformation at large strains is described by the deformation gradient \mathbf{F} , which may be decomposed into elastic and plastic contributions, following the approach of Kalidindi [143]

$$\mathbf{F} = \mathbf{F}^e \mathbf{F}^p, \quad (2.7)$$

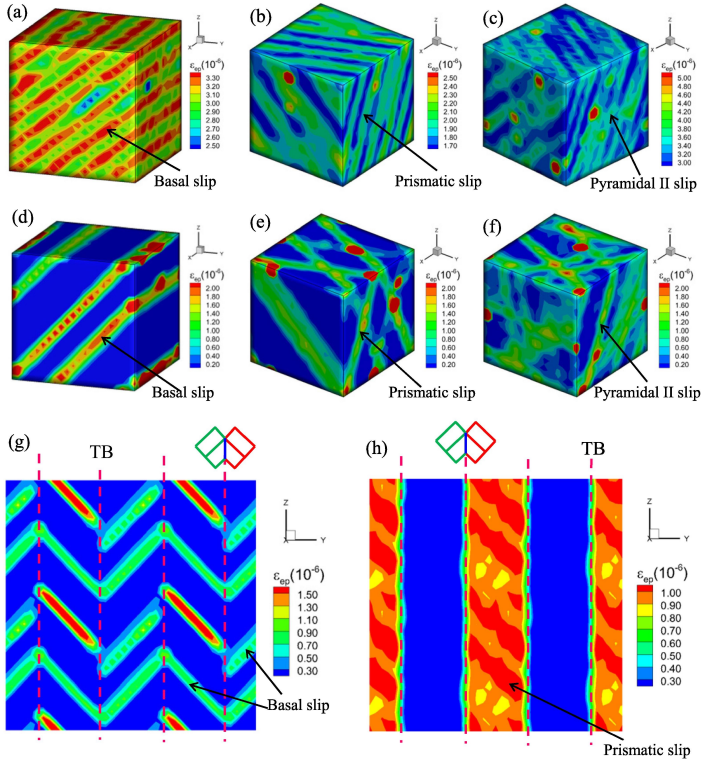


FIGURE 2.21: DDD simulations of pure Mg single crystals and polycrystals, performed in 3D ParaDiS code. Adapted from Fan et al. [11], with permission from Elsevier.

where the superscripts e and p represent the elastic and plastic parts, respectively. One possible approach to further decompose the plastic part is given as $\mathbf{F}^p = \mathbf{F}^s \mathbf{F}^{\text{tw}}$, [144], further decomposing into slip and twin components. This approach and the exact type and order of the decomposition, however, are still disputed.

In the absence of slip, the only plastic component in \mathbf{F}^p stems from the twin components, leading to

$$\mathbf{F}^p = \mathbf{F}^{\text{tw}}. \quad (2.8)$$

Since twin formation involves a discrete amount of plastic simple shear deformation, characterized by its twin normal and direction [145], each twin system, leads to the simple shear deformation [140],

$$\mathbf{F}^{\text{tw}}(\mathbf{X}) = \mathbf{I} + \gamma_{\text{tw}} \beta a_\beta \otimes n_\beta. \quad (2.9)$$

In this instance, γ_{tw} represents the discrete twinning shear associated with each system based on the c/a ratio of the material – in our example, we assume all systems are equivalent and have the same inherent twinning shear. A more general formulation follows from the rate-form of the updates, described in detail in chapter 3. For the TT systems in Mg, with $c/a = 1.624$, the resulting twinning shear is 0.129.

In PFMs, each phase is described via a phase-field (or order) parameter λ . In the case of multiple phases, a vector of phase-field parameters is employed, that represents the volume fraction of the material in a given phase. At any given time, each point of the system must be in either one of the states – the twinned or the matrix phase. A phase may also never be negative since volumes cannot be negative. Further, all volume fractions must sum up to one. Hence at all times, and at each point, it must hold

$$\lambda_\beta(\mathbf{X}) = \begin{cases} 0 & \text{if } \mathbf{X} \in \text{matrix} , \\ (0,1) & \text{if } \mathbf{X} \in \text{boundary} , \\ 1 & \text{if } \mathbf{X} \in \text{twin} , \in [0,1], \end{cases} \quad (2.10)$$

and at every point, $\sum_\beta \lambda_\beta(\mathbf{X}) = 1$. The total deformation from twins depends on the portion of the material that is in the twinned phase, leading to

$$\mathbf{F}^{\text{tw}} = \mathbf{I} + \gamma_{\text{tw}} h(\lambda_\beta) \sum_\beta a_\beta \otimes n_\beta, \quad (2.11)$$

where we use λ_β as a descriptor for the overall volume fraction of the material in phase β (i.e. twinned along system β). Further, we use h as an interpolation function that depends on the phase-field parameter $\lambda(x)$ and satisfies the conditions $h(0) = 0$ and $h(1) = 1$. Choices for h vary, e.g. in Clayton and Knap [140] vs. Liu et al. [141]. This function must satisfy some conditions, such as differentiability and continuity. A simple choice is $h(\lambda) = \lambda$.

Now, the overall Helmholtz free energy density is represented as

$$W(F^e, \lambda) = W^e(F^e, \lambda) + W^{\text{tw}}(\lambda) + W^{\text{int}}(\nabla \lambda), \quad (2.12)$$

with contributions from the elastic and twin components. Typically, for $W^{\text{tw}}(\lambda)$ a multi-well potential is chosen. With one single twin system, this potential takes on the form

$$W^{\text{tw}}(\lambda) = A\lambda^2(\lambda - 1)^2, \quad (2.13)$$

with an energy barrier A to overcome for the phase transition, see Figure 2.22. In the presence of multiple twin systems, the double-well potential

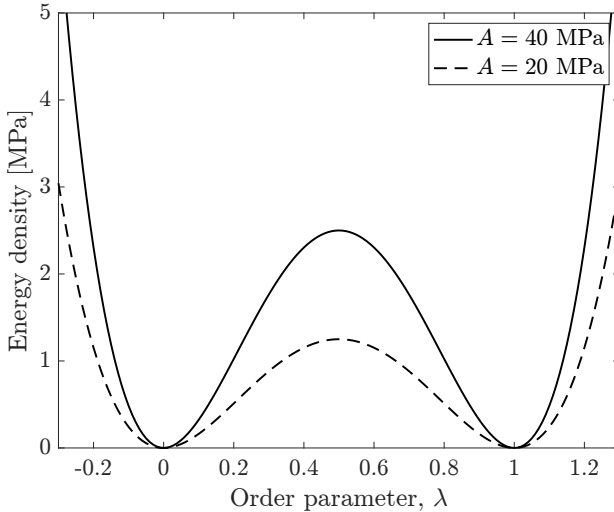


FIGURE 2.22: Double-well potential typically used in phase-field modeling with single twin variant.

turns into a multi-well potential depending on the order parameters of each individual twin system.

$$W^{\text{tw}}(\boldsymbol{\lambda}) = A \left[\sum_{\beta} \lambda_{\beta}^2 - 2 \sum_{\beta} \lambda_{\beta}^3 + \left(\sum_{\beta} \lambda_{\beta} \right)^2 \right] \quad (2.14)$$

In addition, an interfacial energy is introduced to represent the energy associated with twin boundaries and follows from the Cahn-Hilliard formalism [146]. It typically takes the form

$$W^{\text{int}}(\nabla \boldsymbol{\lambda}) = \boldsymbol{\eta} : (\nabla(\boldsymbol{\lambda}) \otimes \nabla(\boldsymbol{\lambda})), \quad (2.15)$$

with a second-order tensor $\boldsymbol{\eta}$. In the simple case of isotropic interfacial energy, $\boldsymbol{\eta} = \eta \mathbf{I}$.

The solution to the spatial distribution of the order parameter is obtained by minimizing the energy with respect to the order parameters, while solving the governing equations on the body, for details, see e.g. Clayton and Knap [140]. Although computationally expensive, this approach allows for a good approximation of the twin microstructure within the crystals, seen e.g. in Figure 2.12. While these models offer high accuracy and spatial resolution, computational complexities arise when incorporating slip and multiple twin systems due to the coupling of these mechanisms and challenges in solving non-convex optimization problems [147]. Furthermore, in these coupled descriptions, scale separation issues can occur between slip and twin, as the latter can occur at the nanoscale, resulting in nano-twins that are only a few atomic layers wide. Achieving this level of resolution on a mesoscopic scale with phase-field models is challenging. Additionally, phase-field models tend to overestimate interfacial energies, requiring much larger driving forces than those observed experimentally. This poses both physical and computational drawbacks, where accuracy needs to be compromised [141, 142], or investigations are limited to lower scales.

2.3.2.1 Twins as Pseudo-Slip Systems

CP models, on the other hand, offer a different approach to describe plastic deformation by accounting for individual slip and twin systems, however on a much higher level than DDD and without the complexity of PFMs. CP originated by searching for an efficient manner of representing slip, while twin contributions were only included in the formulations later. In classical CP, slip systems are described by the accumulated plastic deformation on

each respective system [148–151]. Early work by Kalidindi [143] and Agnew, Yoo, and Tome [46] and Staroselsky and Anand [47] considered twins in Mg as pseudo-slip systems. However, in hcp materials like Mg, twin-induced reorientation and the coexistence of twinned and untwinned states play significant roles. These aspects were considered in later approaches by Staroselsky and Anand [47], Zhang and Joshi [108], and Proust, Tomé, and Kaschner [152], where reorientation was incorporated using a flow rule based on the work by Kalidindi [143], capturing the effects of lattice reorientation within grains.

Several models have addressed the issues of convexity and the coexistence of twinned and untwinned states, accounting for lattice reorientation [107, 108, 144, 153, 154]. In one approach, Homayonifar and Mosler [144] replaced nonconvex energies with a convex envelope [147]. However, these approaches suffer from high computational costs, limiting their application to small samples. Another approach, as proposed by Zhang and Joshi [108], introduced lattice reorientation via pseudo-slip systems for twins using an integration-point-based procedure.

Chang and Kochmann [107] integrated the strengths of Zhang and Joshi's [108] lattice reorientation approach with the variational nature of Homayonifar and Mosler [144] and Ortiz and Stainier [154]. These variational models offer several advantages, including the direct evolution of internal variables through the minimization of a single potential, avoiding the need for solving multiple coupled energy minimizers such as in phase-field models. The implicit formulations introduced by Chang and Kochmann [107] provide computational benefits by allowing larger time steps and more efficient numerical implementation. The model considers a reduced number of slip and twin systems, demonstrating that pyramidal II $\langle c + a \rangle$ slip, prismatic and basal slip, and CT systems are sufficient to capture the material behavior. The model was calibrated using a bottom-up approach based on single-crystal experiments and applied to various scenarios such as rolling and tensile studies, as well as comparisons with reduced models [155]. However, incorporating multiple slip and twin systems within the implicit scheme presents stability challenges [59].

On the contrary, Zhang and Joshi [108] adopted a more comprehensive approach by considering multiple slip and twin systems, including basal, prismatic, pyramidal I $\langle a \rangle$, and pyramidal II $\langle c + a \rangle$ slip, as well as the most commonly observed tensile and CT variants in Mg. This inclusion of multiple mechanisms leads to a competition between different slip and twin modes, which presents challenges in identifying model constants, as

noted by the authors. The calibration process becomes particularly challenging and iterative, requiring repeated simulations and reassessment of the constants. Despite these difficulties, once calibrated, the model provides unprecedented insights into the competition among different deformation mechanisms and enables various studies.

Both of these models take a bottom-up approach, starting with the evaluation of single-crystal behavior and using it as a reference for calibration. In contrast, models for Mg alloys, such as [5, 68, 152, 156], take a top-down approach where single crystal data is not available. In these top-down approaches, physical parameters are typically inferred from the response of polycrystalline materials. Figueiredo et al. [157] even developed a comprehensive framework for the inverse calibration of model parameters in AZ31 alloy. However, top-down models suffer from certain drawbacks related to the uncertainties in calibration. The polycrystal response strongly depends on texture, which plays a crucial role in Mg but can exhibit significant variation across different samples. Additionally, the homogenization technique employed to represent polycrystals significantly influences model parameters. For example, the finite element method (FEM) used in [157] approximates polycrystal behavior reasonably well but incurs higher computational costs.

2.3.3 *Modeling at Elevated Temperatures*

Relatively few models for Mg have investigated the temperature dependence of Mg and its alloys, and when conducted, they predominantly employed top-down approaches [5, 156, 158], resulting in inconclusive findings due to the aforementioned reasons. However, only two bottom-up models have been used previously, yielding significantly different outcomes [15, 159]. Both Liu, Roy, and Silberschmidt [159] and Wang, Liu, and Soh [15] based their models on Zhang and Joshi [108]'s formulation of the crystal plasticity (CP) model and incorporated a larger number of slip systems compared to Chang and Kochmann [107]. The models differ in their treatment of the temperature dependence of the compression twin (CT) and pyramidal II slip systems. While Liu, Roy, and Silberschmidt [159] reported greater CT activity at room temperature and minimal activity at elevated temperatures, Wang, Liu, and Soh [15] presented contrasting results. They observed some CT activity at room temperature, consistent with [108], but at intermediate temperatures, a significant amount of pyramidal II slip was observed before the CT systems dominated at higher

temperatures. However, CT systems are known to exhibit slow evolution and limited deformation capability, and these results contradict certain experimental observations and explanations, highlighting the persistent challenges and confusion surrounding the mechanical properties of Mg at elevated temperatures.

2.3.4 *Homogenization Methods*

With a suitable description of the microscale chosen (e.g. via CP models), the next steps consist of finding an appropriate representation of the polycrystals via homogenization. Homogenization, in our application, consists in representing the underlying heterogeneous material via an effective, macroscopic response, that is the average of the underlying inhomogeneous, microstructural behavior at each point. For homogenization to be feasible, a separation of scales must apply, i.e. the characteristic length scale of the homogenized scale must be orders of magnitude larger than the lower scale. In general, many approaches are conceivable to attain this, such as simple averaging or defining representatives, but some assumptions must be made and boundary conditions imposed.

We generally differentiate the number of possible approaches into mean-field and full-field methods. On one hand, mean-field methods (also sometimes called self-consistent methods) study high-dimensional stochastic systems (such as polycrystals with larger numbers of grains) by studying a simplified model characterizing the stochastic averages of the system. This could be as simple as repeatedly solving the single crystal problem and taking the average of n simulations as a representative response of polycrystals. They are based on relatively simple and natural assumptions on how to model polycrystals, but not without validity! Full-field methods, on the other hand, aim to directly model the underlying system and return an averaged material response. This is typically attained by creating a representative volume element (RVE) that represents the underlying microstructure and whose average deformation is equivalent to the deformation experienced by the higher scale. Since only an average is imposed, individual grains may exhibit vastly varying behavior, so long as the imposed average is maintained. As such, they offer much higher accuracy than mean-field techniques, however, they come at a higher computational cost.

In the following, we provide a short overview of relevant homogenization techniques beginning with the mean-field methods.

2.3.4.1 *Mean-Field Methods*

Mean-field methods are commonly employed in mechanics to simplify complex problems by making certain assumptions. One approach is to assume that all grains in a polycrystalline material are of equal size and do not interact with each other. This simplification is known as the upper-bound model or Taylor model, introduced by Taylor [103]. In this model, grains are treated as springs in parallel, with each grain experiencing the same deformation and the properties of the spring (grain) being the only differentiating factor in the individual stress-strain responses of the grains. Due to its assumption of iso-strain, the Taylor model provides an upper bound to the material response. On the other end of the spectrum, the iso-stress model, proposed by Sachs [160], assumes equal stresses in each grain, as would be the case if the springs were connected in series. Both the upper-bound and iso-stress models have been extensively used to study the plastic behavior of materials [47, 143, 161–163].

Another commonly used mean-field representation of polycrystals is the self-consistent approach, which originated from the work of Kroner [164]. The self-consistent model assumes that each grain can be represented as an ellipsoidal inclusion within an elastic, homogeneous matrix. Building upon the solution for an elliptical inclusion in an elastic medium developed by Eshelby [165], researchers have further developed the self-consistent model to account for small-strain consistent polycrystals [166, 167]. The model has also been extended to include viscoplastic flow [168] and applied to hexagonal close-packed (hcp) materials [169, 170]. The VPSC model has since been extensively utilized in modeling Mg [156, 158, 171, 172] and has frequently been employed in top-down calibration approaches. These models have successfully captured texture evolution and complex thermo-mechanical phenomena such as dynamic recrystallization [68, 158]. The Taylor model has also been used repeatedly, e.g. by [107], who demonstrated that relaxing the Taylor model based on loading conditions can yield comparable results to FEM approximations in textured Mg polycrystals, and by Styczynski et al. [66], who approximated the rolling texture of Mg alloy AZ31.

These computationally efficient mean-field models provide an averaged representation of the microstructure of polycrystalline materials. This inherent averaging or homogenization process makes them computationally efficient. At the same time, these assumptions induce errors and lead to drawbacks, inherent to the model description. However, a significant drawback of these approaches lies in their simplified representation of microstructural features. The VPSC model, for instance, does not track

individual grains but instead considers average grain packages, compromising accuracy. Furthermore, the VPSC model can be computationally expensive, particularly for large-scale simulations and it shows poor scaling with parallelization [173]. Further, parameter calibration typically poses a challenge, due to the wide range of potential parameters and the numerous combinations that can yield similar stress-strain behavior, resulting in non-uniqueness and varying outcomes.

2.3.4.2 Full-Field Methods

Alternatively, one can conceive an approach to representing the polycrystal that takes into account much more detail, such as the size of the grains, relative positions, and boundary conditions such as continuity in displacement across the grains. The resulting description is much more complicated and requires far more components than the simplified This typically happens via homogenization. For this thesis, the difference between homogenization methods is quite relevant and shall be further elaborated here.

The full-field representation of materials offers a description with local information of the microstructure, thus yielding a spatially resolved description of stress, strain, or texture *field* on the lower scale. The most common representatives are spectral methods (named after the use of the spectral Fourier transform) and the FEM. Both of these methods solve the mechanical boundary value problem (BVP) on the entire volume of the representative volume element (RVE) with respective Dirichlet and Neumann boundary conditions for displacements and tractions

$$\nabla \cdot \mathbf{P}(\mathbf{X}) - \rho(\mathbf{X})\mathbf{a}(\mathbf{X}) = \mathbf{F}_{\text{body}}(\mathbf{X}) \quad : \text{in } \Omega, \quad (2.16)$$

$$\mathbf{u}(\mathbf{X}) = \hat{\mathbf{u}}(\mathbf{X}) \quad : \text{on } \partial\Omega_{\text{D}}, \quad (2.17)$$

$$\mathbf{P}(\mathbf{X})\mathbf{N}(\mathbf{X}) = \hat{\mathbf{t}}(\mathbf{X}) \quad : \text{on } \partial\Omega_{\text{N}}. \quad (2.18)$$

Here, $\mathbf{P}(\mathbf{X})$ is the first Piola stress, $\mathbf{F}_{\text{body}}(\mathbf{X})$ represents the body forces, $\rho(\mathbf{X})$ the density of the material, which can vary locally, $\mathbf{a}(\mathbf{X})$ stands for the acceleration on the body. $\hat{\mathbf{u}}(\mathbf{X})$ is the displacement on the Dirichlet boundary, $\hat{\mathbf{t}}(\mathbf{X})$ stands for the traction, and $\mathbf{N}(\mathbf{X})$ for the normal at each point of the Neumann boundary.

Body forces are typically omitted in purely mechanical problems on the RVE level, and with the exception of dynamic problems (impact, vibrations, etc.), one may also omit inertia effects, such that (2.16) simplifies to

$$P_{ij,j} = 0 \quad : \text{ in } \Omega, \quad (2.19)$$

$$u_i = \hat{u}_i \quad : \text{ on } \partial\Omega_D, \quad (2.20)$$

$$P_{ij}N_j = \hat{t}_i \quad : \text{ on } \partial\Omega_N. \quad (2.21)$$

The difference between the FEM and spectral methods lies in the way the problem is solved. The above notation is the strong form of the BVP. We first show how the FEM solves the mechanical BVP, before diving into the spectral method at a later point.

The Finite Element Method

Let us discuss how we can find a solution to the problem (2.16) with the FEM. The form (2.16) is called the strong form of the problem. In the strong form, the requirements for any acceptable solution u are given as $u \in C^2(\Omega) \cap C^0(\bar{\Omega})$, where Ω represents the domain of the body we seek the solution for. This means the solution u needs to be twice continuously differentiable and continuous. These are strong requirements for a solution field, rendering the direct numerical solution challenging.

Hence, it is often more advantageous to find the solution in an alternative way [174]. An alternative solution may be found by casting the problem into a variational form, describing the total potential energy via a functional,

$$I[\varphi] = \int_{\Omega} W(\mathbf{F})dV - \int_{\Omega} \rho_0 \mathbf{B} \cdot \boldsymbol{\varphi}dV - \int_{\partial\Omega_N} \hat{\mathbf{T}} \cdot \boldsymbol{\varphi}dS, \quad (2.22)$$

where we aim to find solutions to the deformation mapping, φ ,

$$\varphi \in \mathcal{U} = \{\varphi \in \mathcal{H}^1(\Omega) : \varphi = \hat{\varphi} \text{ on } \partial\Omega_D\} \quad \text{such that } \varphi = \arg \min \mathcal{I}[\varphi]. \quad (2.23)$$

By assuming that the undeformed and deformed configurations of our systems coincide, we may rewrite $\varphi = \mathbf{x} = \mathbf{X} + \mathbf{u}$ and hence reformulate the variation in terms of the displacement field $\mathbf{u} \in \mathcal{U}$ [174]. Any admissible deformation \mathbf{u} must therefore be the minimizer of this functional, hence we seek solutions u that fulfill the boundary conditions on $\partial\Omega_D$ and minimize the functional, i.e., [174]

$$\mathbf{u} = \arg \min \mathcal{I}[\mathbf{u}] : \mathbf{u} = \hat{\mathbf{u}} \text{ on } \partial\Omega_D. \quad (2.24)$$

The solution follows by taking the first variation of \mathcal{I}

$$\delta\mathcal{I}[\mathbf{u}] = \int_{\Omega} \underbrace{\frac{\partial W(\mathbf{F})}{\partial F_{ij}}}_{P_{ij}} \delta u_{i,j} dV - \left[\int_{\Omega} \rho b_i u_i dV + \int_{\partial\Omega_N} \hat{t}_i \delta u_i dS \right] = 0, \quad (2.25)$$

where we made use of the relationship $P_{ij} = \partial W / \partial F_{ij}$, and the fact that $\mathbf{F} = \mathbf{I} + \nabla \mathbf{u}$ to take the first variation [174], which has to be equal to zero for a stationary point. We may reformulate this equation into

$$\delta\mathcal{I}[\mathbf{u}] = \mathcal{G}(\mathbf{u}, \delta\mathbf{u}) = \mathcal{A}(\mathbf{u}, \delta\mathbf{u}) - \mathcal{L}(\delta\mathbf{u}) \forall \delta\mathbf{u} \in \mathcal{U}_0(\Omega). \quad (2.26)$$

Further, by interpreting $\delta\mathbf{u}$ as virtual displacements \mathbf{v} , we recover the principle of virtual work, such that

$$\mathcal{G} = \int_{\Omega} v_{i,j} \underbrace{\frac{\partial W(\mathbf{F})}{\partial F_{ij}}}_{P_{ij}} \delta u_{i,j} dV - v_{i,j} \left[\int_{\Omega} \rho b_i u_i dV + \int_{\partial\Omega_N} \hat{t}_i \delta u_i dS \right] = 0, \quad (2.27)$$

and attain the weak form

$$\mathcal{G}(\mathbf{u}, \mathbf{v}) = A(\mathbf{u}, \mathbf{v}) - L(\mathbf{v}) = 0, \quad (2.28)$$

with

$$A(\mathbf{u}, \mathbf{v}) = \int_{\Omega} P_{ik}(\nabla \mathbf{u}) v_{i,j} dV, \quad (2.29)$$

and

$$L(\mathbf{v}) = \int_{\Omega} \rho b_i v_i dV + \int_{\partial\Omega} \hat{t}_i v_i dS. \quad (2.30)$$

Here, A represents a generally non-linear operator for the relationship between \mathbf{P} and W (the internal forces due to deformation), and L represents the sum of all external forces (body forces plus traction forces on the boundary). Further, from the principle of virtual work, we know that $\mathcal{G}(\mathbf{u}, \mathbf{v}) = 0$ must always be satisfied for all permissible displacements \mathbf{u} and the virtual displacements \mathbf{v} . This allows us to rephrase (2.28) into

$$\underbrace{A(\mathbf{u}, \mathbf{v})}_{\mathbf{F}_{\text{int}}(\mathbf{u})} = \underbrace{L(\mathbf{u}, \mathbf{v})}_{\mathbf{F}_{\text{ext}}}. \quad (2.31)$$

Finally, the weak form needs to be solved on domain Ω with displacements \mathbf{u} that need only satisfy

$$\mathbf{u} \in U = \{ \mathbf{u} \in H^1(\Omega) : \hat{u} \text{ on } \partial\Omega_D \}, \quad (2.32)$$

much weaker requirements than in the strong form.

As a numerical approach, the FEM aims to find an approximate solution, as it cannot directly determine the exact solution. Instead, it seeks an approximate solution within a finite-dimensional subspace $U^h \subset U$, where U is the solution space and U^h contains approximate solutions u^h . This subspace is numerically approximated, often employing the Bubnov-Galerkin approximation, leading to an approximation of the displacement as:

$$u^h(x) = \sum_{a=1}^n u^a N^a(x), \quad (2.33)$$

where $N^a(x)$ represents the so-called *shape functions*. The choice of shape functions, for example, linear or polynomial, influences their capability to interpolate the solution over the domain. These shape functions interpolate the displacement along the element and must adhere to certain requirements, such as:

- $N_i = 1$ at position $x = x_i$ for node i ,
- $N_i = 0$ at position $x = x_j$ for node $j \neq i$,
- $\sum_i N_i(x) = 1$ for all positions x .

The discretized and approximated displacements at each element are incorporated into the weak form (2.28). By inserting the Ansatz (2.33) for \mathbf{u} and \mathbf{v} into the weak form (2.28) one obtains

$$\mathcal{G}(\sum_a \mathbf{u}^a N^a(x), \sum_b \mathbf{v}^b N^b(x)) = A(\sum_a \mathbf{u}^a N^a(x), \sum_b \mathbf{v}^b N^b(x)) - L(\sum_b \mathbf{v}^b N^b(x)) = \mathbf{0}. \quad (2.34)$$

This leads to the discrete weak form

$$\sum_{a=1}^n v_i^a \left[\int_{\Omega} P_{ij}(\nabla \mathbf{u}^h) N_{,j}^a dV - \int_{\Omega} \rho p_i N^a dV - \int_{\partial\Omega} \hat{t}_i n^a dS \right] = 0, \quad (2.35)$$

for all admissible virtual displacements \mathbf{v}^a [174]. This results in a nonlinear system of equations to be solved.

$$\mathbf{F}_{\text{int}}(\mathbf{u}^a) - \mathbf{F}_{\text{ext}} = \mathbf{0}, \quad (2.36)$$

with

$$F_{\text{int},i}^a \int$$

This system of equations can be solved numerically for the global force equilibrium.

While various approaches exist for solving problems using global shape functions defined over the entire domain, these methods bring about challenges when dealing with Dirichlet boundary conditions (BCs). When applying BCs to a 1D bar with prescribed displacements at both ends (e.g., $u(0) = 0$ and $u(L) = \Delta L$), all unknown coefficients are constrained. This constraint becomes even more burdensome and impractical in higher dimensions when using global shape functions. Moreover, utilizing global shape functions leads to densely populated stiffness matrices, which can negatively impact numerical efficiency and computational performance [174]. In FEM, shape functions are locally defined on each element. This local definition enables the straightforward application of Dirichlet boundary conditions on the nodes, ensuring continuity across elements. Within each element, the nodal displacements u_{i_e} for each degree of freedom n are enforced via element boundary conditions, and the displacements inside the element are approximated using these shape functions. The accuracy of the solution is influenced by the choice of shape functions and elements, with specific selections leading to numerical advantages and disadvantages. For further insights, refer to Kochmann [174].

To achieve this, all displacements and forces are assembled into global vectors $\mathbf{U} \in \mathbb{R}^{d \cdot n}$ and $\mathbf{F}_G \in \mathbb{R}^{d \cdot n}$, where n represents the number of elements, and d denotes the total degrees of freedom. This assembly process gives rise to immense (sparse) matrices and necessitates significant computation times. The nonlinear system of equations is typically solved using a numerical solver, with the Newton-Raphson solver being one of the most common choices.

As the discretization of the body becomes finer, the approximation improves, and the solution approaches the analytical solution more closely. However, finer discretization also leads to an increased number of elements and degrees of freedom, resulting in substantial computational overhead. Furthermore, the FEM is susceptible to significant errors due to poor element choices and numerical issues like shear locking and hourglassing.

Spectral Methods

In contrast, spectral methods typically solve for the displacement field directly, meaning they solve the strong form of BVP (2.19) for all positions $\mathbf{x} \in \Omega$ simultaneously. This idea was introduced by Moulinec and Suquet [175], as a relief from the large computational cost associated with FEM.

It bypasses the need for meshing and makes direct use of microstructural images.

We follow the discussion for the mechanical BVP as discussed in Vidyasagar, Tan, and Kochmann [176]. $\mathbf{P}(\mathbf{X})$ results from a (typically non-linear) relationship between the local deformation measure (\mathbf{F}) and the material properties. We can rewrite

$$\mathbf{P}(\mathbf{X}) = \mathcal{C}^0 \mathbf{F}(\mathbf{X}) - \boldsymbol{\tau}(\mathbf{X}), \quad (2.38)$$

with a (strongly) elliptic fourth-order stiffness tensor \mathcal{C}^0 (typically chosen as the RVE-average of $\mathcal{C}(\mathbf{X})$, the latter being the local stiffness at each position) and a perturbation stress $\boldsymbol{\tau}(\mathbf{X})$. Further, by exploiting the relation

$$\mathbf{F} = \text{Grad}(\phi(\mathbf{X})), \quad (2.39)$$

where ϕ represents the mapping of the deformation from the material to the current configuration. By combining (2.38), (2.39), and (2.19), one obtains

$$\nabla \cdot \left[\mathcal{C}^0 \nabla(\phi(\mathbf{X})) - \boldsymbol{\tau}(\mathbf{X}) \right] = \mathbf{0}, \quad (2.40)$$

which in index notation gives

$$\left[\mathcal{C}_{ijkl}^0 \phi_{k,L}(\mathbf{X}) - \tau_{ij}(\mathbf{X}) \right]_{,L} = 0. \quad (2.41)$$

Assuming $\mathcal{C}^0 = \text{const.}$, the latter is a linear equation in ϕ which can be easily solved in Fourier space, due to the linear nature of derivatives in Fourier space. Let us first introduce the (discrete) Fourier transformation as

$$\phi(\mathbf{X}) = \sum_{\mathbf{K} \in N_f} \hat{\phi}(\mathbf{K}) \exp(ih\mathbf{K} \cdot \mathbf{X}), \quad (2.42)$$

with wave vectors \mathbf{K} , for a discrete number of frequencies N_f , and variable $h = 2\pi/L_{\text{RVE}}$, where L_{RVE} is the length of a side of the RVE.

Transforming (2.41) into Fourier space yields

$$-h^2 \mathcal{C}_{ijkl}^0 \hat{\phi}_k(\mathbf{K}) K_J K_L = -ih \tau_{ij}(\mathbf{K}) K_J. \quad (2.43)$$

By introducing the acoustic tensor as

$$\mathcal{A}_{ik}(\mathbf{K}) = \mathcal{C}_{ijkl}^0 K_J K_L, \quad (2.44)$$

we may solve directly for the deformation mapping in Fourier space as

$$\hat{\phi}_k(\mathbf{K}) = \frac{i}{h} \mathcal{A}_{ik}^{-1}(\mathbf{K}) \hat{\tau}_{ij}(\mathbf{K}) K_J. \quad (2.45)$$

Note that this solution relies on the inversion of the acoustic tensor, which is not possible for $\mathbf{K} = 0$. Further, note that we may write

$$\hat{F}_{kL}(\mathbf{K}) = ih\hat{\phi}_k(\mathbf{K})K_L. \quad (2.46)$$

Hence we may find updates to the deformation gradient \mathbf{F} as

$$\hat{F}_{kL} = \begin{cases} \langle \mathbf{F} \rangle & \text{if } \mathbf{K} = 0 \\ \frac{i}{h} \mathcal{A}_{ik}^{-1}(\mathbf{K}) \hat{\tau}_{iJ}(\mathbf{K}) K_J K_L, & \text{else.} \end{cases} \quad (2.47)$$

Here, $\langle \mathbf{F} \rangle = \hat{\mathbf{F}}(0)$. Also, note that this algorithm is part of an iterative scheme since τ depends on \mathbf{F} via the deformation. Hence, solutions to this problem are found in an iterative manner.

The strength of full-field methods lies mainly in identifying local deformations due to the underlying microstructure. This can be seen in a number of studies performed successfully with FFT-based solvers. For instance, Vidyasagar, Tutcuoglu, and Kochmann [12] used spectral methods to capture deformation patterning in Mg single and bicrystals during a variety of loading paths (see Figure 2.23), and Tutcuoglu et al. [59] predicted local grain reorientation during recrystallization in Mg with these methods.

Typically, spectral methods are more efficient and faster than FEM solutions. This is largely due to the ease with which the DFFT (discrete fast Fourier transform) can be parallelized in a multi-core environment, as well as the fact that they are a little more light-weight, owing to the fact that there is no need to assemble global matrices in contrast to the FEM. Spectral methods do, however, also come with some serious drawbacks. First of all, the spectral nature of the updates means that only periodic boundary conditions can easily be imposed. Second, due to the constraint in (2.45), the average deformation must always be known in order to solve the BVP, which makes the solution of complex deformation paths more challenging. Especially with anisotropic materials, the deformation can lead to directional deformation, and imposing a general deformation can be problematic. Further, an important drawback is the presence of Gibbs ringing artifacts near sharp interfaces, such as inclusions or jumps in stiffness. The treatment of these issues is non-trivial and a promising method based on finite-difference approximations of the derivatives in Fourier space was discussed by Vidyasagar, Tan, and Kochmann [176].

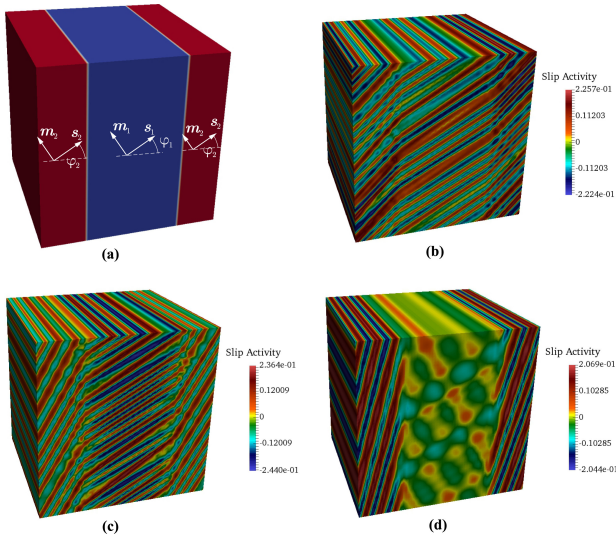


FIGURE 2.23: We show the laminated pattern formation in bicrystals under shear. (a) depicts the geometric arrangement of the two grains within the bicrystal RVE along with the definition of angles in the blue and red grains, respectively. Results for varying angles are shown in (b) through (d). Reprinted from Vidyasagar, Tutcuoglu, and Kochmann [12] with permission from Elsevier.

2.3.4.3 Multiscale Modeling

In many cases, the bridging between scales is not limited to two but to a number of scales, e.g. from the micro to the meso scale, and again, from the meso to the macro scale. Each of those steps of homogenizing the lower scale and including it as an effective material response on the next larger scale induces computational overhead. For a material-by-design approach, as sought after in the ICMD framework of MEDE, efficiency is therefore key.

Most models at the macroscale use the FEM to represent the macroscopic body under consideration, such as a sample of material during impact or during a rolling process. This is in part, because of the ease, with which the boundary conditions can be imposed in commercial FEM software, such as Abaqus. Commercial software is typically well parallelized and computationally efficient.

More options arise on the lower scales, on how to bridge the gap between the meso and the microscale. One option is, of course, to use the FEM again, in computing the effective response of an RVE. This approach leads to the FE^2 method, illustrated in Figure 2.24. The addition of a second layer of FE problems at the lower scale, however, poses an almost insurmountable computational effort that drastically reduces the feasibility of a truly multiscale study. This approach has been used in the past, though, see e.g. Fritzen and Hodapp [177]. On the other hand, spectral methods could also be used at this lower level, but the computational cost remains elevated.

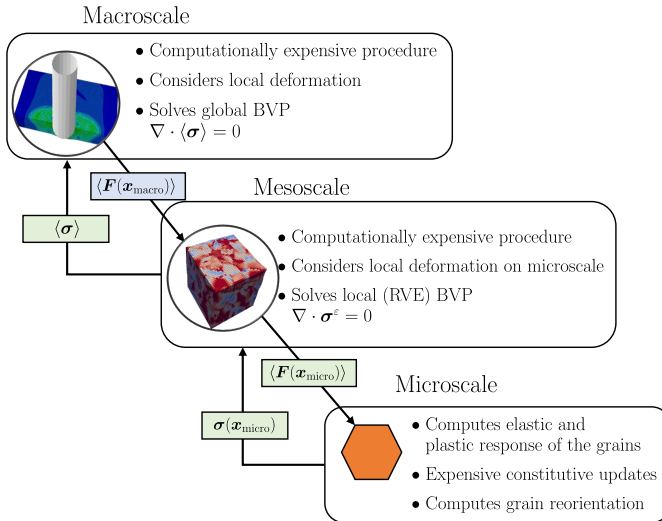


FIGURE 2.24: Schematic depiction of the FE^2 method.

The better options in terms of computational efficiency stem from using mean-field approximations at lower levels, such as the Taylor, Sachs, or VPSC method, see Figure 2.25 for an illustration for a FExTaylor approach. While the VPSC method offers good results, it is poorly parallelizable and therefore often lacks computational speed [173]. Instead, Taylor models have been used repeatedly in the past, such as by Tutcuoglu et al. [59, 84]. Despite the good parallelization possibilities and lightweight methodology, simulation times can still exceed weeks and months, as shown e.g. in Tutcuoglu et al. [84].

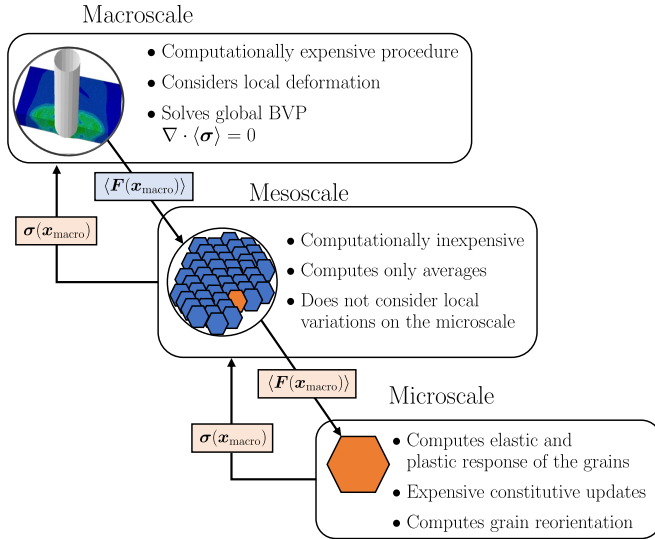


FIGURE 2.25: Schematic depiction of the FExTaylor method.

2.3.5 Preliminary Conclusions

A number of physical modeling techniques were introduced and discussed. Each scale warrants the formulation and implementation of distinct modeling techniques, each suited to capture the intrinsic processes that occur on either scale. CP models offer a good trade-off between accuracy and computational cost, integrate key aspects of plasticity seamlessly and efficiently, and provide a good choice for a representation of the microscale.

Further, there are a number of possible techniques to bridge the gap between micro and macro scale via homogenization. Bridging from the micro to the macro scale requires a number of layers of homogenization to include lower-scale effects in macro-scale simulations and with each layer of homogenization, the computational cost increases, to the point of being unfeasible with regard to an ICMD approach. This warrants the investigation of other techniques to reduce the computation time of multiscale simulations. Approaches could lie in either accelerating the computation of the underlying material models or accelerating the scale bridging. Another approach, still, lies in leveraging data-driven methods as surrogate models, using them for their unparalleled computational speed. In this thesis, we explore this latter approach, illustrated in Figure 2.26.

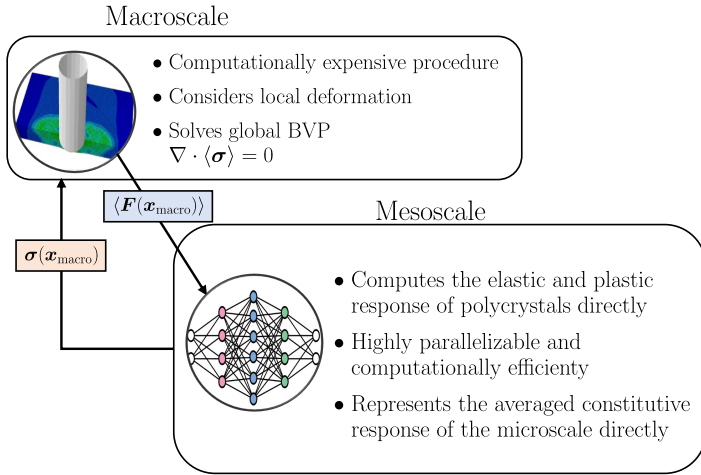


FIGURE 2.26: Schematic depiction of the FExSurrogate model approach.

It consists in replacing the mesoscopic computation entirely via a trained neural network. In the next chapter, we discuss the requirements such a neural network must fulfill.

2.4 DATA-DRIVEN METHODS

Our approach to accelerating the multiscale modeling lies in accelerating the computation speed of the lower-scale material models by creating a surrogate for the homogenized behavior of the material at the mesoscale. This is achieved, first, by creating a vast amount of data from a highly efficient mesoscale model, followed by introducing a data-driven method capable of representing the mesoscopic behavior of the material. In the following Section, we explore the background of data-driven material modeling and provide a state-of-the-art overview, followed by an explanation of the approach we chose. The detailed implementation of the surrogate model is provided in chapter 4.

2.4.1 *Introduction to Data-Driven Methods*

Machine learning (ML) has a history of achievements across various domains. It is commonly divided into three sub-classes: supervised, unsupervised, and semi-supervised learning algorithms. The distinguishing factor lies in the availability of labeled data. The data is then used to compute a loss criterion for evaluating algorithm performance. Supervised and semi-supervised learning utilize labeled data for model training and are well-suited for tasks such as classification and text recognition. Its applications are ubiquitous in our daily lives, encompassing a wide range of tasks. For instance, supervised ML techniques are employed in computer vision applications such as facial recognition systems that grant access to our smartphones [178] and in spam filtering. Furthermore, it is increasingly utilized in consumer sentiment analysis [179] and even predicting consumer behavior, exemplified by platforms like Netflix and Amazon recommending personalized movies and products based on the purchasing patterns of similar users. The realm of advertising has also witnessed a surge in targeted campaigns tailored to individual preferences. Additionally, ML algorithms enable our phones to learn our language patterns, improving their text completion capabilities. Another application goes even further and recognizes a person's mental health status based on changes in their writing style [180].

In contrast, unsupervised learning operates on unlabeled data, primarily utilized for discovering patterns and performing clustering analysis on unlabelled data. For instance, unsupervised learning was used to iden-

tify patterns and connections in quantum data sets [181] or for improved classification of bird songs [182].

While many methods and algorithms have been developed and some have been employed for decades, the field of ML is still evolving. It is one of the most proliferous fields of science and sprouts uncountable numbers of new contributions. Therefore, it makes no sense to attempt to provide an overview of the entirety of the field.

Many methods applied in ML have previously been used for decades, and hence the exact line between ML and e.g. descriptive statistics remains blurry. With these methods entering the field of mechanics, however, more architectures and methods are being fitted and specialized for the tasks at hand. In the following, we provide a short history and overview of the most important concepts and veer towards those with relevance to applications in mechanics.

The simplest form of ML constitutes the artificial neural network (ANN). ANNs trace their roots back to a simple idea, the perceptron, introduced by psychologist Hebb [183]. Hebb created perceptrons as a simplified concept of human brain neurons and can be seen as a one-layer neural network that was initially used as a linear classifier [184, 185]. ANNs have since gained popularity and thanks to the added computational power and the availability of data, their applications and performance have increased. A schematic representation of a perceptron is shown in Figure 2.27, with inputs x , bias b , and weights w . The output it generates is denoted y , and mathematically it is described as

$$y = \sum_{i=1}^N x_i w_i + b_i. \quad (2.48)$$

Even a simple problem such as the linear classification problem performed by [183, 184], required a rule to learn the value of the weights and bias terms. This was initially done via Hebbian learning [183], a method that was further improved by Oja [186] and Sanger [187]. Today, ANNs and subsequent architectures use back-propagating gradient-descent for error minimization as the main method to learn the model parameters [185]. To this end, the output is compared in a sensible way to the input, via an error function to be minimized.

ANNs in their single-layer form, however, are still severely limited. Modern applications typically use feed-forward neural networks (FFNNs), stacked layers of ANNs, in which each new layer computes an output based on the previous layer's output [185, 188, 189]. The name feed-forward

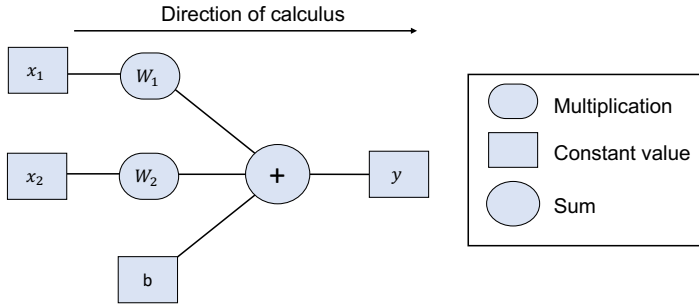


FIGURE 2.27: Schematic representation of a perceptron

stems from the one-way direction in which the input signal traverses the net.

When large numbers of layers are stacked, the nomenclature typically changes and we speak of deep neural networks (DNN) [185] or deep learning (DL) methods. Again, the exact line between FFNNs and DNN is blurry. DNN architectures allow for a larger number of tunable parameters to better approximate complex functions, however, this also brings a few drawbacks. First of all, the added processing power required for DNN networks is considerable and requires more expensive and performing computers. Second, a purely numerical issue occurs: the vanishing and exploding gradient problem occurs due to the depth of the NNs. In essence, the problems are related to the gradients updating the weights on early layers in the networks vanishing or exploding, due to the repeated multiplication with small or large numbers. This problem becomes even more prevalent for another type of network, the recurrent neural networks (RNNs), [190].

For now, let us introduce two specific types of DNN architectures. The first type is the convolutional neural networks (CNNs) that are ubiquitous in image recognition and classification applications [185, 191–193]. In CNNs, one or multiple convolutional layers scan the input for patterns, before forwarding information down the processing chain. The second type of important DNN architectures is the gated neural network architectures, consisting of the long short-term memory (LSTM) [194] and gated recurrent unit (GRU) [195] architectures. LSTM cells and GRUs (an architecture derived from the LSTM) contain a hidden state vector that allows for information from the earlier layers to trickle down the deep architecture, thus improving model performance [185]. A similar idea, to feed-forward

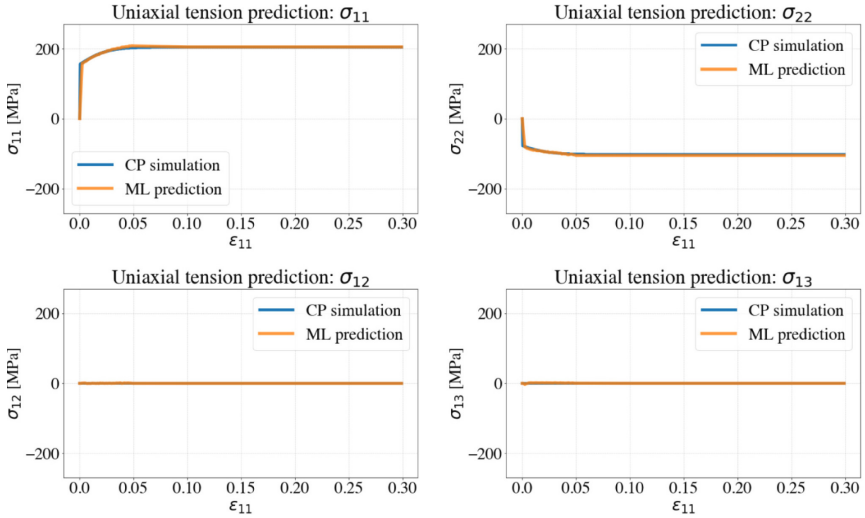


FIGURE 2.28: Stress-strain response of the ANN-enhanced CP model presented by Ibragimova et al. [13]. Graphic adapted from Ibragimova et al. [13], with permission from Elsevier.

information to further-down layers, is found in a special type of CNN, the U-net [196].

DL methods have gained significant traction in the field of computational mechanics, as evidenced by numerous applications and studies (for a comprehensive review, refer to Kollmannsberger et al. [197]). These methods are frequently employed to approximate solutions to specific partial differential equations (PDEs) or to enhance the computational efficiency of existing methods Li et al. [23], Oishi and Yagawa [198], Haghghat et al. [199], and Guo, Li, and Iorio [200].

One common approach in DNN-based computational mechanics involves learning fixed-dimensional mappings for PDE solutions, as demonstrated by Guo, Li, and Iorio [200]. While effective, these methods heavily rely on the underlying mesh structure and require recalibration and modification when applied to new problem domains or resolutions.

Alternatively, there are techniques that directly approximate the solution function using neural networks, as explored by Lu, Jin, and Karniadakis [201] and Bar and Sochen [202]. In this approach, the neural network learns to represent a specific instance of the PDE, making it mesh-independent.

However, the computational cost associated with these methods remains a concern [23].

A promising avenue in DNN-based computational mechanics is the utilization of neural operator architectures. These mesh-free, infinite-dimensional approximation operators, as proposed by Bhattacharya et al. [203], offer the ability to transfer solutions across different meshes, eliminating the need for recalibration for each new application. However, these architectures have historically suffered from significant computational costs due to the evaluation of integral operators.

To address this limitation, a novel type of neural operator architecture called Fourier Neural Operator (FNO) was introduced by Li et al. [23]. This groundbreaking approach enables the efficient solution of various PDEs, including Darcy flow, Navier-Stokes equations, and Burger's equations, with unprecedented speed and accuracy. While its applications to mechanical problems are still in progress, the FNO architecture shows great promise.

An important observation should be made at this point. Feed-forward networks, in general, are commonly employed to enhance existing physical solution methods, to circumvent costly numerical computations [13, 198], or to learn solutions to specific PDEs [23, 201]. Some ANNs are used to directly predict certain material properties or behavior, or measures of interest, for instance in anisotropic hyperelasticity [204]. In the field of plasticity, Shen et al. [205] used an ANN to predict the yield surface of porous materials with Von Mises plasticity. However, little research has been conducted to leverage feed-forward deep learning architectures for learning and modeling the constitutive response of plastic/inelastic materials, specifically for plastic material behavior. This limitation arises from a significant drawback of feed-forward neural networks (FFNNs), namely their lack of "memory" or the ability to retain information from previous outputs. Plasticity, however, is an inherently memory-dependent process, as previous deformation or strain history impacts the constitutive response.

2.4.2 Recurrent Neural Networks Applied to the Dependence in Plasticity

To overcome this limitation, another type of architecture, the recurrent neural network (RNN), comes into play. RNNs are capable of storing and remembering past outputs, allowing them to generate new outputs and capture temporal dependencies by "unrolling" the networks through time. Figure 2.29 provides a simple and illustrative example of this concept, where the output from a previous time step serves as input for the next

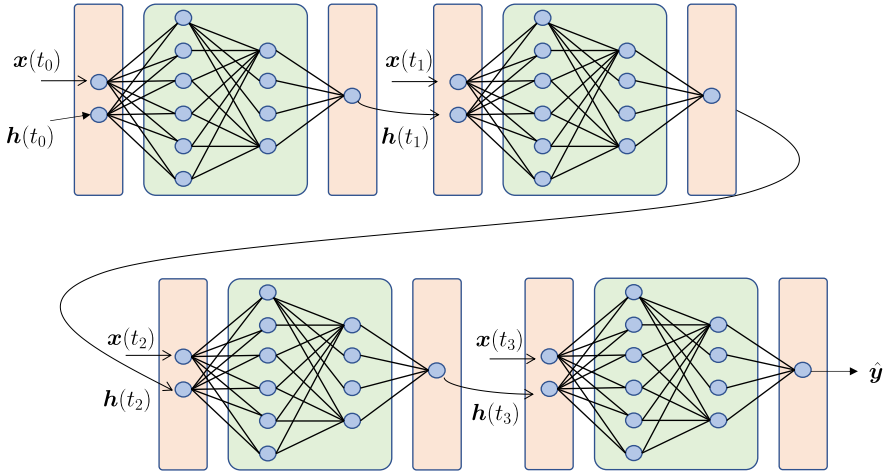


FIGURE 2.29: Schematic visualization of a simple RNN with two inputs and one of which being propagated through time.

time step. This memory effect enables the prediction at the new time step to incorporate information from previous outputs, a key requirement for their viability as surrogates for (crystal) plasticity material models. Wang and Sun [206], for instance, used RNNs to model the poroplasticity of geological materials.

In the following, we first introduce what RNNs are and discuss different issues arising from the new architecture. We will introduce the long short-term memory LSTM [194] and GRU cells, concepts borrowed from language processing, that were developed to mitigate these issues and give some examples of the successful application of RNNs as surrogate models for plastic materials. We then introduce a specific kind of architecture derived from these two cell types, the minima state cell (MSC) [76] that was developed specifically for the modeling of plastic material responses, and discuss its existing advantages and drawbacks. Finally, we conclude this Section by introducing the foundational work used for the CP surrogate model employed in this thesis, the Markovian description introduced by Bhattacharya et al. [79].

2.4.2.1 Specific Recurrent Network Architectures

Consider the unrolled RNN depicted in Figure 2.29. Assume we wanted to investigate a time- and path-dependent problem, such as plasticity. To this

end, we would track the evolution of the output over time, and use it to make the next prediction. In an RNN, the same network is invoked at each time step. This means that the weights and biases must be learned such as to best approximate the response at each timestep t_i . The conventional back-propagation technique reaches a limitation. The problem is remedied with a new type of back-propagation capable of "flowing back in time" to past weights and inputs [190], in a process called back-propagation through time (BPTT). This process is described in detail in Hochreiter [190] and we offer only a short overview here.

Let us begin by taking the derivative of the error-function w.r.t. all weights θ ,

$$\begin{aligned}\frac{\partial J}{\partial \theta} &= \sum_{t=1} \frac{\partial J_t}{\partial \theta} \\ &= \sum_{t=1} \frac{\partial J_t}{\partial \hat{y}_t} \frac{\partial \hat{y}_t}{\partial \theta}.\end{aligned}\tag{2.49}$$

Here, \hat{y}_t depends on the hidden state h_t , which in turn depends on the weights θ of all previous instances of the RNN in time. Hence, we obtain the following form for the derivative:

$$\begin{aligned}\frac{\partial J}{\partial \theta} &= \sum_{t=1} \frac{\partial J_t}{\partial \theta} \\ &= \sum_{t=1} \frac{\partial J_t}{\partial \hat{y}_t} \frac{\partial \hat{y}_t}{\partial h_t} \frac{\partial h_t}{\partial \theta}.\end{aligned}\tag{2.50}$$

In fact, the present hidden state also depends on the previous hidden states of previous unrolled networks. Hence, by applying the chain rule, one obtains

$$\begin{aligned}\frac{\partial J}{\partial \theta} &= \sum_{t=1} \frac{\partial J_t}{\partial \theta} \\ &= \sum_{t=1} \frac{\partial J_t}{\partial \hat{y}_t} \frac{\partial \hat{y}_t}{\partial h_t} \prod_{k=1}^{t-1} \frac{\partial h_{tk}}{\partial h_{t(k-1)}} \frac{\partial h_{t1}}{\partial \theta}.\end{aligned}\tag{2.51}$$

In essence, the "unrolling" of RNNs through time leads to deep network architectures. The deeper the network, the more multiplications with derivatives of the hidden state occur. The hidden state itself, however, also entails an activation function, whose derivatives lie in $[0, 1)$ for most traditional choices, meaning the chain rule of differentiation used in backpropagation leads to the multiplication of small numbers with themselves. This

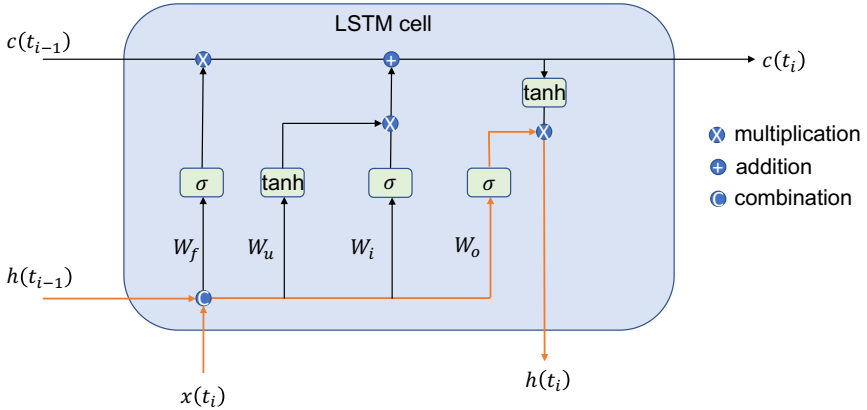


FIGURE 2.30: Graphical representation of an LSTM cell. The LSTM cell has two memory vectors, the hidden vector $\mathbf{h}(t)$ and the cell state $\mathbf{c}(t)$, carrying information through time. These vectors are updated based on "gates", the forget gate, update gate, input gate, and output gates. The output of the cell is the new hidden state $\mathbf{h}(t_i)$.

occurs as often as the network is unrolled, rendering the numbers almost infinitesimal, as is seen in the term $\prod_k \frac{\partial \mathbf{h}_{tk}}{\partial \mathbf{h}_{t_{k-1}}}$ of (2.51) that represents a repeated multiplication of values, typically smaller than 1. This leads to infinitesimally small updates on the network weights, thus having barely any effect on the network performance, meaning these kinds of networks become challenging to train. It can be remedied by increasing or decreasing the learning rates, however, this also entails new issues. Alternatively, one could use activation functions whose gradients can be larger than 1. In this case, repeated multiplication has the potential to lead to the opposite phenomenon, where the gradients grow uncontrollably [207]. This latter problem is known as the exploding gradient problem and both of these issues together have led to novel architectures for RNNs.

One such architecture stems from Hochreiter and Schmidhuber [194], who recognized the issues associated with the exploding and vanishing gradient phenomena. As RNNs are, in essence, deep neural nets, it is no surprise that the LSTM cells are commonly found in RNN architectures [194]. They differ substantially from classical RNNs in that they contain LSTM cells at each layer, depicted in Figure 2.30

The LSTM cell produces two outputs, the cell state $\mathbf{c}(t_i)$ and the hidden state, which is at the same time the output, $\mathbf{h}(t_i)$, at the new time. At each

time, the old cell state and hidden state are updated via a number of gates. First, the old hidden state and the new input at time t_i are combined into a new combined input vector,

$$\mathbf{x}(t_i) = \mathbf{x}(t_i) + \mathbf{h}(t_{i-1}). \quad (2.52)$$

Based on this input, the cell first decides how much information to forget. This is done via the forget gate. The forget gate consists of a linear layer with trainable weights W_f and a sigmoid activation function, $\sigma = \frac{1}{1+e^{-x}}$. They produce a forget vector, \mathbf{f} , whose values lie in $[0, 1]$, of the following form

$$\mathbf{f} = \sigma(\mathbf{W}_f \mathbf{x}(t_i) + \mathbf{b}_f). \quad (2.53)$$

Here, W_f represents the trainable weights of the forget gate, $\mathbf{x}(t_i)$ represents the input at a time t_i , and \mathbf{b} the bias terms of the gate. This operation is equivalent to rating the information from not important at the lower end to important at the upper end. The vector is then point-wise multiplied with the old cell state $c(t_{i-1})$, effectively removing the unimportant information and storing only what is deemed important,

$$\mathbf{c}(t_i) = \mathbf{f} \odot \mathbf{c}(t_{i-1}), \quad (2.54)$$

where \odot stands for point-wise multiplication. The fact that W_c are trainable weights allows the cell to learn which values are important and which are noise.

Next, the input gate is activated. The input gate works in the same way as the forget gate, except that here, it is decided which information is required to be kept. Thus, the input i is given as

$$\mathbf{i} = \sigma(\mathbf{W}_i \mathbf{x}(t_i) + \mathbf{b}_i), \quad (2.55)$$

, with input-gate weights W_i and biases \mathbf{b}_i , and the update to the cell vector, \mathbf{u} , is given as

$$\mathbf{u} = \tanh(\mathbf{W}_u \mathbf{x}(t_i) + \mathbf{b}_u), \quad (2.56)$$

again with trainable weights and biases W_u and \mathbf{b}_u . The update gate decides what information from the input vector is retained. The update values always lie between -1 and 1, thus preventing exploding values. They are again point-wise multiplied to filter out the irrelevant information and then added to the cell state resulting in an updated cell state

$$\mathbf{c}(t_i) = \mathbf{c}(t_i) + \mathbf{u} \odot \mathbf{i}. \quad (2.57)$$

At this point, the cell carries all the previous and updated information in the new cell state $c(t_i)$ and it is time to make a new prediction. The output gate provides information about what information from the current input should be carried on. It computes an output vector \mathbf{o} as

$$\mathbf{o} = \sigma(\mathbf{W}_o \mathbf{x}(t_i) + \mathbf{b}_o). \quad (2.58)$$

This information is multiplied with the information passed down from memory (new cell state), which is again passed through a sigmoid activation function to determine which entries the new hidden state should carry on. Finally, the new hidden state $h(t_i)$ is computed as

$$\mathbf{h}(t_i) = \mathbf{o} \odot \tanh(c(t_i)), \quad (2.59)$$

and is used to make predictions and to be passed into the next unrolled cell.

This architecture largely prevents the issues with the vanishing and exploding gradients. The proof is quite tedious and thus omitted in this thesis, but the interested reader is referred to DiPietro and Hager [208] for a more in-depth discussion and explanation.

Their main drawbacks stem from a large number of trainable parameters. This renders the LSTMs quite heavy and lengthy to train. Further, they require large amounts of data, which is typically a pitfall in computational mechanics applications.

Alternatively, another type of cell was introduced as a simpler alternative to LSTMs, the GRU, depicted in Figure 2.31. GRUs have a similar architecture as the LSTM cells, as they are derived from the same concept, however, they only have two gates and have removed the cell state, only storing information in the hidden state vector. This reduces the number of parameters and increases the efficiency with which GRU networks can be trained.

We will not discuss the GRU in detail here, but Chung et al. [195] and DiPietro and Hager [208] offer comparisons with LSTMs and assess the viability of GRUs. In general, GRUs and LSTMs tend to perform relatively similarly, but LSTMs are more heavy-weight, thus often requiring longer training and more data. In practice, engineers will often try out both architectures and see which one works best for their application.

Both GRUs and LSTMs have been used in the field of data-driven computational mechanics quite extensively. Especially for CP surrogate modeling, texture evolution, and plasticity in general, these RNN architectures make a lot of sense and show promise. The hidden and cell states are a natural

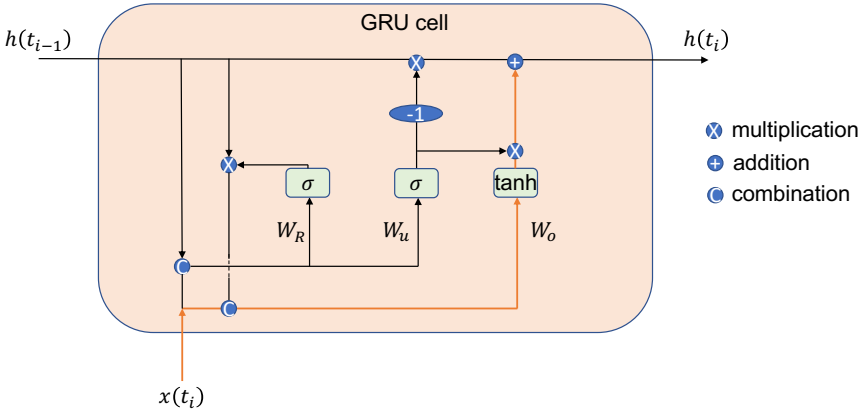


FIGURE 2.31: Sketch of a fully gated GRU cell with a reset and an update gate and a hidden state h .

way to include the history-dependence of plasticity and are analogous to internal variables, often used in CP models, to describe the state of the material. Another application of the texture evolution is shown in Pandey and Pokharel [81]’s work, which uses LSTMs to learn the evolution of Euler angles on an RVE of pure Cu crystals. The LSTM surrogate led to a significant reduction in computation speed compared to the CP-FFT model used as a ground truth. Frankel, Tachida, and Jones [209], used an adapted version of the LSTM, the Convolutional STM, to learn the stress-strain response of polycrystals with multiple realizations of the microstructure. The study attained mixed results, achieving good results for the average stress measures and somewhat higher errors for the overall stress field, nevertheless demonstrating the power of data-driven methods for these applications. Another example showcasing the potential of data-driven methods in computing the plastic response of material stems from Mozaffar et al. [78]. They used a GRU-based architecture to learn the homogenized response of a composite 2D RVE, containing a plastic matrix and stiff inclusions. To this end, the RVE is loaded with a variety of randomized load paths. This ensures that the overall response of the material is captured in the randomness of the deformation and that the NN extracts the key aspects of the constitutive behavior. For training, the NN receives the strain data as input and learns the corresponding stress and energy outputs. This allows the NN to be used on other, arbitrary paths in the future that may not have figured in the initial training data. The GRU-based architecture

captures the behavior of the material accurately and is capable of predicting the yield surface when shown the same loading paths as the RVE.

2.4.2.2 *Drawbacks of Existing Architectures*

Despite the positive preliminary results of these methods, a number of substantial drawbacks exist that should be addressed. The first drawback for GRUs and LSTMs lies in the lack of interpretability. GRU and LSTM states (or hidden vectors) are typically large and carry no intrinsic meaning. Especially with regards to CP modeling, this is a drawback to be addressed. Hidden states can be interpreted analogously to internal variables in CP modeling, and hence an interpretable state vector is desirable. Further, both, LSTMs and GRUs, suffer from relatively high training times due to the large number of parameters associated with each of their gates. For large networks and hidden state vectors, the training time of these methods is typically long [76, 80].

One approach that has tackled the issue of a non-interpretable state vector stems from [76]. Their idea of creating a custom architecture based on LSTM gates led to the minimal state cell (MSC), an architecture capable of identifying the number of state variables required for relatively simple plastic material models, as well as creating a direct link between those state variables and the stress state at any time. The MSC was successfully applied to learn a large number of materials' constitutive responses, such as Von Mises plasticity, crushable foams, and other materials, whose main descriptor was the total accumulated plastic strain ϵ_p . These physical models, however, remain fairly simple.

As an additional drawback, the gate functions used in LSTMs, GRUs and MSCs are time-agnostic. This means that they are not aware of temporal resolution in training, which makes the extension to applications outside of the training resolution quasi-impossible. When used as surrogate models, this is an especially taxing drawback, since simulations can effectively only be performed at the training resolution, limiting the utility of the models. To overcome this limitation Bonatti and Mohr [83] introduced modulations to the gate functions such as to be self-consistent.

Thus far, the MSCs were shown to be successful in capturing the material behavior of simple plasticity models, see e.g. the models employed in [76] as well as "identifying" the state variables included. Their applications to more complex material models such as in CP do not yield the same astonishing results. In Bonatti, Berisha, and Mohr [75], linearized MSCs (developed in Bonatti and Mohr [83]) are applied to learn the homogenized

constitutive behavior of an fcc material. They found that the MSCs require a large number of internal state variables to perform sufficiently well and show that for more complex problems, the MSCs are still somewhat limited. No interpretation of the state variables was possible.

2.4.2.3 The Markovian Recurrent Neural Operator

On the contrary, Liu et al. [14] and Bhattacharya et al. [79] have developed a custom RNN operator based on a physically motivated approach that shows promise in providing both, a means to identifying the number of required state variables, as well as a resolution-independent ML surrogate. We only give a minimal overview here, since the architecture is explained in detail in chapter 4.

Their approach consists of learning a (hidden) state vector ξ , without any *a-priori* knowledge of the material model, followed by a map from the state vector to the stress state of the material. This is achieved in a two-stage process, by two functions \mathcal{F} and \mathcal{G} [79], where

$$\dot{\xi}(t) = \mathcal{G}(\mathbf{F}(t), \xi(t)), \quad (2.60)$$

and

$$\sigma(t) = \mathcal{F}(\mathbf{F}(t), \dot{\mathbf{F}}(t), \xi(t)), \quad (2.61)$$

where \mathbf{F} represents the overall deformation gradient, and σ the Cauchy-stress. The state vector at each time t is given as

$$\xi(t) = \xi(t - \Delta t) + \Delta t \dot{\xi}(t), \quad (2.62)$$

and $\xi(0) = \mathbf{0}$.

The Forward-Euler integration in time has allowed the authors to find a time-resolution independent description in the surrogate models of a Kelvin-Voigt material, [79], as opposed to the LSTM and GRU gate functions that are not capable of handling different resolutions.

An application showcasing the potential of the architecture is found in Liu et al. [14]. They learned the constitutive response of viscoelastic and elastic-viscoplastic materials in two and three dimensions and investigated the resolution independence and the capability of the architecture to identify the minimal state variables. They identified that for the viscoelastic composite material in two dimensions, three state variables were minimally required without strain hardening present and four state variables were required with strain hardening. Contrarily, for the elasto-viscoplastic material with strain hardening, only two state variables are required, see e.g. Figure 2.32.

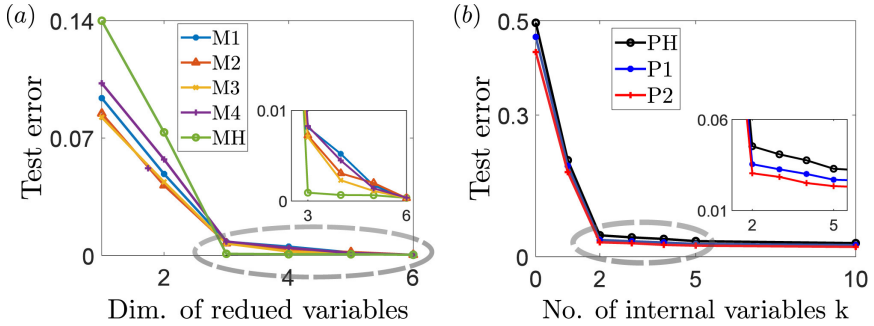


FIGURE 2.32: Test error of the trained model for elasto-viscoplastic material model in (a), and for the viscoelastic model in (b). Reprinted and adapted from Liu et al. [14] with permission from Elsevier.

Further, the study shows that resolution independence follows naturally from the description if the architecture is representative of the physics of the underlying material. The authors investigated this by comparing the capabilities of a viscoelastic and an elasto-viscoplastic RNO to learn the homogenized behavior of an elasto-viscoplastic material with exponential hardening. The viscoelastic RNO contained an explicit dependence on the rate of change of the deformation gradient, whereas the elasto-viscoplastic one does not. As shown in Figure 2.33, both architectures perform relatively well at the training resolution. For increasing refinement (higher resolution), however, only the RNO with the appropriate architecture retains a low error measure.

2.5 OUTLINE OF THIS THESIS

We have presented an overview of the physical and data-driven modeling techniques for Mg in this chapter. Let us first provide a short recapitulation of the key points of this chapter and define the research question and niche for this thesis.

As previously shown, Mg is an interesting candidate for a number of applications in the automotive and aerospace industries. In its pure form, its properties are far too poor for actual application in industry, but even specially designed alloys still require improved material properties, such as improved ductility for processing and improved stiffness and hardness of the material. Many of the processes associated with improving these aspects

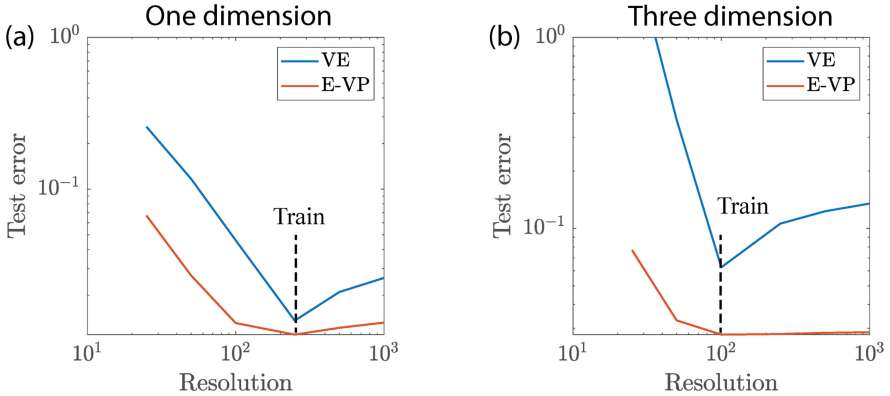


FIGURE 2.33: Comparison of the test error of an RNO trained with training data at a resolution of 200 time-steps against test data at various resolutions, for both the elasto-viscoplastic RNO labeled “E-VP” and the alternate viscoelastic RNO labeled “VE”. (a) One-dimensional elasto-viscoplastic composite (b). Reprinted from Liu et al. [14] with permission from Elsevier.

of the material are temperature dependent, such as precipitate formation that leads to precipitate hardening or recrystallization that leads to grain refinement, increasing the ductility of the material and leading to grain-size hardening. Many of these effects are still not understood properly and need further investigation.

Further, this thesis was written as part of the effort of a larger consortium that follows an ICMD approach to material design, a process that requires an enormous computational effort on multiple scales. The key to any successful ICMD approach is the efficient modeling of material behavior via physically meaningful and efficient predictive models. These models have to account for a plethora of mechanical effects on a large number of different scales (in space and time) and each scale warrants its own modeling techniques (Atomistics, MD, DFT, CP, Continuum models), with varying degrees of physicality and associated computational cost. We discussed existing CP models containing both slip and twin descriptions, allowing for rapid and easy modeling of these mechanisms in Mg. From these findings, we deduce the following two contributions to be addressed in this thesis.

First, it is apparent that the thermal effects on the plastic behavior of Mg are not yet fully understood. Hence, the first primary objective of this thesis is to further investigate the thermally-driven competition between

the CT and pyramidal II systems while developing a robust and highly efficient temperature-aware material model for Mg using a bottom-up approach. Our aim is to achieve a high level of physical accuracy by leveraging efficiency-improving strategies such as representing twins through effective volume fractions as proposed by Chang and Kochmann [107] and employing the relaxed Taylor model. We will also restrict the use of slip systems to those that are relevant within the scope of our investigation, aiming to reduce calibration ambiguity and gain insights into the mechanics of CT and pyramidal II competition. To address stability issues encountered by Chang and Kochmann [107], explicit updates are employed to investigate the constraints on material parameters. Furthermore, our model formulation will be based on the variational approach proposed by Ortiz and Stainier [154], allowing the derivation of slip and twin behavior through an optimization framework.

Second, in view of the sought-after applications of our model in an ICMD framework, the development of a suitable data-driven surrogate is required. While some of the works conducted previously have already showcased the capabilities and potential of ML applications in accelerating modeling and reducing computational costs, as well as their prowess to predict material behavior when used as surrogate models, a number of open challenges remain that offer opportunities for research. The material models whose behaviors were learned are still relatively simple, such as the von Mises or the J2 models. The MSC architecture used by Bonatti and Mohr [76] was efficient at learning these material representations, however, as shown in Bonatti, Berisha, and Mohr [75], it performs worse on actual CP data. Further, the CP model used in Bonatti, Berisha, and Mohr [75] is that of an fcc material with isotropic hardening, and does not account for effects such as twinning, necessary for simulating Mg. Further, while some work has been done on learning the effect of temperature [210], its effect are not commonly included. Hence, the second contribution of this thesis is based on the development and implementation of a suitable NN architecture with the goal of developing a surrogate model for the physical model. This research question is in itself an interesting challenge, as we wish to overcome several limitations of existing ML approaches in mechanics, such as the resolution dependence and the lack of interpretability. The complexity of the material behavior in Mg poses a challenging task and an interesting case study for the capability of NN algorithms. As part of this second contribution, we apply and compare multiple NN approaches such as GRUs and LSTMs, as well as Liu et al. [14] and Bhattacharya et

al. [79]’s recurrent neural operator to textured Mg polycrystals in a bid to learn the constitutive behavior without any *a-priori* knowledge of the underlying physics and evaluate the performance, interpretability, and resolution-dependence of the surrogate. We then implement the surrogate in Abaqus/Explicit to perform truly multiscale simulations of textured Mg polycrystal samples on the macroscale.

EFFICIENT TEMPERATURE-DEPENDENT CRYSTAL PLASTICITY MODEL FOR PURE MG

This chapter has been adapted from **Hollenweger** and Kochmann [52]. "An efficient temperature-dependent crystal plasticity framework for pure magnesium with emphasis on the competition between slip and twinning". *International Journal of Plasticity* 159 (2022)

CHAPTER OVERVIEW

The first contribution of this thesis focuses on the development of an efficient, temperature-aware, predictive model for Mg on the micro and mesoscale. In this Chapter we give a renewed, short introduction to the important topics covered hereinafter. We then provide a detailed description of the kinematics and the constitutive relations, before describing the temperature-dependent mechanisms in Mg in detail. The competition between the CT and pyramidal II systems at varying temperatures warrants the implementation of two distinct versions of the model. We then calibrate and explain the identification of model parameters for both models based on test cases and provide single and polycrystalline results to showcase the capabilities of the presented constitutive model and the competition of the pyramidal II and CT systems.

3.1 INTRODUCTION

In practical applications, the utilization of Mg and Mg alloys has been limited due to several fundamental drawbacks. These materials exhibit relatively low corrosion resistance and are challenging to harden using conventional thermal methods [1]. Additionally, their poor forming capabilities stem from plastic anisotropy, a phenomenon attributed to the hexagonal close-packed (hcp) atomic crystal structure. The plastic behavior of hcp materials involves the collective activation of various slip and twin mechanisms. Specifically, basal, prismatic, and pyramidal slip systems, as well as tensile and compressive twin systems (TT and CT, respectively), are commonly observed deformation modes, as schematically depicted in Figure

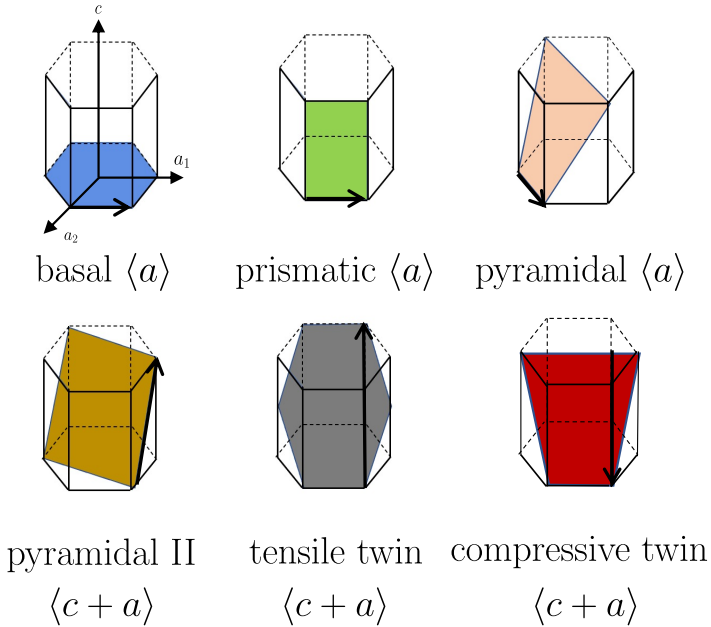


FIGURE 3.1: Main deformation modes occurring in Mg

3.1. For brevity, we will refer to the second-order pyramidal $\langle c + a \rangle$ system as pyramidal II throughout this work. The limited number of activatable deformation modes in the hcp structure restricts its ability to accommodate plastic deformation at room temperature [45–47]. Consequently, plastic deformation localizes in twins, leading to premature failure at room temperature [2, 8, 19]. These limitations, along with others (see e.g., Nie, Shin, and Zeng [2], Kecskes et al. [58], or Eswarappa Prameela et al. [1]), have hindered the widespread industrial use of Mg alloys.

Various approaches have been employed to enhance the ductility and workability of Mg. Notably, Zeng et al. [48] demonstrated that even pure Mg can exhibit exceptional malleability and ductility through severe grain refinement. One common strategy to improve the formability of Mg involves working at elevated temperatures, which capitalizes on the increased lattice mobility accompanying temperature rise. This allows for a greater number of available deformation modes compared to room temperature conditions, resulting in more homogeneous plastic deformation [2, 9, 26, 45, 56, 86, 118, 123]. The improved isotropic and ductile behavior enhances workability and formability during processing. Consequently, Mg alloys

are often subjected to hot processing techniques to overcome the aforementioned limitations [211–215]. However, a comprehensive understanding of the thermo-mechanically coupled microstructure evolution and the lack of a reliable predictive model remain significant challenges. In this chapter, we present our own temperature-aware predictive model, validate it using experimental data from multiple sources, and employ the model in polycrystal simulations to assess its viability and investigate the influence of temperature on the microstructure.

3.1.1 *Experimental Investigations*

The plastic behavior of Mg and Mg alloys has been the subject of experimental studies for decades [7–9, 16, 18, 19, 45, 86, 120]. It was observed that single-crystals and textured polycrystals show strong plastic anisotropy.

Single- and polycrystal experiments revealed that basal slip and TTs dominate at room temperature [2, 8, 18, 19, 108], while the contributions of the various non-basal systems increase with increasing temperature [3, 9, 16, 21, 123, 151, 216–218]. Due to the reduced activation stresses on these systems, at elevated temperature, pyramidal and prismatic slip accommodate a larger portion of the plastic deformation. This leads to a smaller relative contribution of basal slip and twin systems to accommodate the overall deformation [2, 56, 58]. Hence, a strong temperature dependence of the non-basal slip systems was inferred, whereas, surprisingly, it was found that basal slip as well as TTs show little to no change in behavior with increasing temperature and are often assumed to be virtually temperature independent [2, 9].

Although most studies confirm the above general trends, there exists contradictory experimental evidence and interpretation of the microstructure of Mg, both at room temperature and at elevated temperature. One such controversy lies in the presence of pyramidal II slip at room temperature. Ono, Nowak, and Miura [3], Koike et al. [127], and Muránsky et al. [219] reported significant contributions of pyramidal slip starting at ambient temperature. Further, Lilleodden [25] reported that only pyramidal II slip was active during their micro-compression studies, whereas Kelley and Hosford [8] and Wonsiewicz and Backofen [19] found no evidence of this deformation mode. Another controversially discussed aspect is the role of the CT systems with increasing temperature. CTs have been observed in both single- and polycrystal studies at room temperature [19, 56, 123] and are considered one of the main reasons for the early failure of Mg alloys

Al-Samman, Li, and Chowdhury [51], Zhou and Sui [220], and Chakkedath et al. [221]. Their temperature dependence, however, has remained an open question. Wonsiewicz and Backofen [19] observed an increasing amount of CTs in their single-crystal experiments at higher temperatures, whereas [56, 58, 123, 221] noted a reduced propensity for twinning and especially for CT with increasing temperature. To accommodate deformation along the c -axis of the crystal, the material must exhibit some deformation mode(s) with a c -component in the Burgers vector. Due to the polar nature of twinning, the $\{10\bar{1}2\}$ TT system can only do so under c -axis extension, and the $\{10\bar{1}1\}$ CT systems only under compression. The nature of a twin system (tensile or compressive) is due to the c/a ratio of the material Yoo [7]. Pyramidal II systems, by contrast, can account for both types of deformation. Interestingly, this results in a competition between these aforementioned deformation modes. Understanding the nature of the controversial findings and the competition between the pyramidal II and the CT systems will, among others, be the subject of this investigation. Recently, the question was raised whether pyramidal I $\langle c + a \rangle$ or pyramidal II slip was the predominant mode: Kweon and Raja [54], Zecevic, Beyerlein, and Knezevic [222], and Xie et al. [110] suggested that pyramidal I $\langle c + a \rangle$ slip may be the dominant mode. Since, however, little is known about the temperature-dependent behavior of pyramidal I $\langle c + a \rangle$ slip, investigating this additional controversy lies outside the scope of this work.

3.1.2 Numerical Studies

Thanks to the advent of inexpensive and accessible computational power, a steadily growing number of numerical techniques have been employed to improve our understanding of plasticity in hcp metals. Modelling occurs on a variety of length (and time) scales, from the atomic to the continuum level, each providing different insight and suffering from different limitations. Molecular Dynamics (MD) simulations have provided insight at the scale of lattice defects, including the formation of dislocations, twins, and voids as well as solute clustering in alloys [62, 71, 223, 224]. At larger scales, phenomenological models trade efficiency for accuracy and mechanistic rigor to allow for simulations of large, especially polycrystalline, systems. This includes primarily phase field and crystal plasticity models as well as combinations thereof [4, 47, 108, 140, 159], which live at continuum scales. A noteworthy advance in the efficient representation of deformation twinning on larger scales is due to Tomé, Lebensohn, and Kocks [225], who

introduced the predominant twin reorientation model, capturing the texture change in zirconium due to twinning events and contributing significantly to the texture modelling of hcp materials.

In this study, we focus on continuum-level mesoscale modelling, which admits simulating large ensembles of grains, while being efficient and incorporating the underlying deformation modes to investigate the microstructure evolution. When adopting the nomenclature of Liu, Roy, and Silberschmidt [159], phenomenological mesoscale approaches can be categorized as *top-down* [156, 158, 226, 227] and *bottom-up* [54, 107, 108, 159] based on the model calibration. Top-down approaches use experimental polycrystal data to calibrate the model parameters, whereas bottom-up approaches calibrate a single-crystal plasticity (SCP) model with available experimental data and use that SCP description locally in a polycrystalline simulation framework. In comparison, this latter approach shows superior accuracy and is applicable to general polycrystalline textures. As a bottom-up example, the variational SCP framework of Chang and Kochmann [107] for pure Mg used a reduced set of active deformation mechanisms for an efficient representation of the Mg microstructure. When embedded in finite element (FE) [155] or Fast Fourier Transform (FFT) [12] homogenization schemes, this model was shown to efficiently predict the stress-strain behavior and texture evolution of polycrystals.

Both bottom-up and top-down approaches have proven successful in capturing essential features of Mg's plastic behavior. Ardeljan et al. [156] captured the temperature and strain rate dependence of Mg alloy AZ31 in a multiscale "FE×Taylor" top-down framework. Further, Jain and Agnew [5] successfully investigated the temperature effects on twinning in Mg alloy AZ31B by means of a top-down viscoplastic self-consistent model, and Walde and Riedel [68] successfully modeled recrystallization in AZ31 with a similar approach. More recently, Tam et al. [158] accurately modeled the temperature-dependent response of AZ31 polycrystals as well as the texture evolution and the dynamic recrystallization, while Sahoo et al. [228] investigated the texture evolution in an all-twin-variant crystal plasticity model for hcp materials, capturing the twin effects and intersecting twin variants. Despite these successes, top-down approaches typically suffer from significant drawbacks, including a strong dependence on the choice of the calibration data and of the homogenization method [156], the inability to apply at the single-crystal level, and a lack of microstructural insight [122].

Despite the wealth of models for hcp materials, only a small number of temperature-dependent models for Mg exist. On the one hand, the bottom-up approach of Zhang and Joshi [108] for the room-temperature description of Mg single- and polycrystals was adopted by Liu, Roy, and Silberschmidt [159] and extended to the temperature range from 298 K to 523 K, observing a transition in deformation modes with increasing temperature. The latter was primarily associated with a decrease of basal slip at elevated temperature at the expense of pyramidal $\langle a \rangle$ slip as well as a transition from CT to pyramidal II slip with increasing temperature. On the other hand, Wang, Liu, and Soh [15] used a Johnson-Cook-type hardening law for single-crystals and included temperature dependence, while considering CTs as quasi-inactive at room temperature, while showing a transition away from pyramidal slip to CT above 423 K. The reported microstructures of both approaches were substantially different and to some degree contradictory. Furthermore, the assumptions made by Wang, Liu, and Soh [15] on the behavior of CTs were not supported by the observations of Barnett [56] and Barnett et al. [123]. Both Wang, Liu, and Soh [15] and Liu, Roy, and Silberschmidt [159] included the entire range of possible deformation (slip and twin) modes. This choice is problematic from a calibration point of view, as, e.g., pyramidal $\langle a \rangle$ slip and prismatic slip, as well as pyramidal II slip and CTs are in direct competition, which may corrupt or at least exacerbate the calibration, even on the basis of single-crystal experiments, as noted by Zhang and Joshi [108].

3.2 KINEMATICS

Let s_α and m_α denote the slip directions and normals of the N_p slip systems $\alpha \in [1, N_p]$, whereas a_β and n_β are the twinning directions and normals of the N_{tw} twin systems $\beta \in [1, N_{tw}]$. The total deformation gradient is assumed to follow a multiplicative decomposition into elastic and inelastic contributions [143, 148], so

$$\mathbf{F} = \mathbf{F}_e \mathbf{F}_{in}, \quad (3.1)$$

where \mathbf{F}_e represents the elastic part, and \mathbf{F}_{in} stems from the combined slip and twin activity of the respective systems. Note that the above choice of the decomposition is non-unique and other approaches exist, in which the deformation gradient is decomposed further into components for slip and twinning [144], resulting in the interactions of twin and slip activity at the kinematic level. In our case, the interaction between slip and twinning is embedded in the constitutive relations, as discussed in Section 3.3.

The total velocity gradient follows as

$$\begin{aligned} l &= \dot{\mathbf{F}}\mathbf{F}^{-1} \\ &= \underbrace{\dot{\mathbf{F}}_e\mathbf{F}_e^{-1}}_{\mathbf{l}_e} + \mathbf{F}_e \underbrace{\dot{\mathbf{F}}_{\text{in}}\mathbf{F}_{\text{in}}^{-1}}_{\tilde{\mathbf{l}}_{\text{in}}} \mathbf{F}_e^{-1}, \end{aligned} \quad (3.2)$$

with elastic and inelastic contributions \mathbf{l}_e and $\tilde{\mathbf{l}}_{\text{in}}$, respectively. The latter is further decomposed into slip and twin components:

$$\tilde{\mathbf{l}}_{\text{in}} = \tilde{\mathbf{l}}_{\text{p}} + \tilde{\mathbf{l}}_{\text{tw}}, \quad (3.3)$$

where $\tilde{\mathbf{l}}_{\text{tw}}$ results from the combined effect of the changing N_{tw} twin volume fractions λ_β . With γ_β^{tw} denoting the twinning shear strain (a material constant known from the crystallography [108]) associated with system β , this implies

$$\tilde{\mathbf{l}}_{\text{tw}} = \sum_{\beta=1}^{N_{\text{tw}}} \dot{\lambda}_\beta \gamma_\beta^{\text{tw}} \mathbf{a}_\beta \otimes \mathbf{n}_\beta. \quad (3.4)$$

$\tilde{\mathbf{l}}_{\text{p}}$ stems from the activities of the slip systems in the twinned and untwinned regions of the crystal, so that

$$\tilde{\mathbf{l}}_{\text{p}} = \sum_{\alpha=1}^{n_s} \dot{\gamma}_\alpha \underbrace{\left[\left(1 - \sum_{\beta=1}^{N_{\text{tw}}} \lambda_\beta \right) \mathbf{s}_\alpha \otimes \mathbf{m}_\alpha + \sum_{\beta=1}^{N_{\text{tw}}} \lambda_\beta \mathbf{s}'_\alpha \otimes \mathbf{m}'_\alpha \right]}_{=\mathbf{p}_\alpha}. \quad (3.5)$$

Here, the slip rates $\dot{\gamma}_\alpha$ are assumed to capture slip in both untwinned and fully twinned regions, the latter being defined for twin system β by

$$\mathbf{s}'_\alpha = \mathbf{Q}_\beta \mathbf{s}_\alpha; \quad \mathbf{m}'_\alpha = \mathbf{Q}_\beta \mathbf{m}_\alpha. \quad (3.6)$$

with the householder mapping

$$\mathbf{Q}_\beta = \mathbf{I} - 2\mathbf{n}_\beta \otimes \mathbf{n}_\beta, \quad (3.7)$$

which describes the reorientation of the lattice due to the twinning of the crystal around the plane normal of system β [120].

3.3 CONSTITUTIVE RELATION

Following Chang and Kochmann [107], we introduce the Helmholtz free energy density, here dependent on temperature T , as

$$W(\mathbf{F}, \mathbf{F}_{\text{in}}, \boldsymbol{\epsilon}, \boldsymbol{\lambda}, T) = W_e(\mathbf{F}_e, T) + W_p(\boldsymbol{\epsilon}, \boldsymbol{\lambda}, T) + W_{\text{tw}}(\boldsymbol{\lambda}, T), \quad (3.8)$$

consisting of a (hyper-)elastic energy density W_e and the stored plastic energies (i.e., energy irreversibly stored in the microstructure) due to slip and twinning, W_p and W_{tw} , respectively. The latter two depend on the twin volume fractions $\lambda = \{\lambda_1, \dots, \lambda_{N_{tw}}\}$ and the accumulated plastic strains $\epsilon = \{\epsilon_1, \dots, \epsilon_{N_p}\}$, which evolve according to $\dot{\epsilon}_\alpha = |\dot{\gamma}_\alpha|$, $\dot{\gamma}_\alpha$ being the slip rate on system α .

The twin and slip contributions to the energy density account for self- and latent hardening. We base our description of the twin hardening on Tutcuoglu et al. [59] and Chang and Kochmann [107], while incorporating the CT effect similar to Zhang and Joshi [108], assuming they follow the same Schmid-type behavior as TTs ¹. The hardening of TTs and CTs is assumed to follow a linear law, which leads to

$$W_{tw} = \underbrace{\sum_{\beta=1}^{n_t} \frac{k_\beta(T)}{2} \lambda_\beta^2}_{\text{self-hardening}} + \underbrace{\frac{1}{2} \lambda \cdot \mathcal{K}(T) \lambda}_{\text{cross-hardening}}, \quad (3.9)$$

whereas plastic hardening due to slip is based on

$$W_p = \left\{ \begin{array}{l} \underbrace{\sum_{\alpha=1}^{n_s} \sigma_\alpha^\infty(T) \left[\epsilon_\alpha + \frac{\sigma_\alpha^\infty(T)}{h_\alpha^0(T)} \exp\left(-\frac{h_{0,\alpha}(T)\epsilon_\alpha}{\sigma_\alpha^\infty(T)}\right) \right]}_{\text{self-hardening}} \\ + \underbrace{\frac{1}{2} \epsilon \cdot \mathcal{H}(T) \epsilon}_{\text{cross-hardening}}, \quad \text{if } \lambda < \lambda_{\text{crit}}, \\ \underbrace{\sum_{\alpha=1}^{n_s} \sigma_\alpha^\infty(T) \left[\epsilon_\alpha + \frac{\sigma_\alpha^\infty(T)}{h_\alpha^0(T)} \exp\left(-\frac{h_{0,\alpha}(T)\epsilon_\alpha}{\sigma_\alpha^\infty(T)}\right) \right]}_{\text{self-hardening}} \\ + \underbrace{\frac{1}{2} \epsilon \cdot \mathcal{H}(T) \epsilon}_{\text{cross-hardening}} + \underbrace{\sum_{\alpha=1}^{N_s} c_\alpha(T) \epsilon_\alpha}_{\text{twin-slip interaction}}, \quad \text{if } \lambda \geq \lambda_{\text{crit}}. \end{array} \right. \quad (3.10)$$

\mathcal{K} is a positive semi-definite matrix, having twin cross-hardening terms $k_{\beta\beta'}$ in its off-diagonal components and a zero diagonal to represent twin-

¹ It was noted as early as by Kelley and Hosford [8] that CTs may in fact *not* follow this pattern. In modelling, however, when included, CTs are generally assumed to follow approximately a Schmid law with a medium to high critical resolved shear stress (CRSS) value and strong hardening [15, 108, 159]. For the sake of simplicity we here follow this assumption – investigating the physics behind CTs goes beyond the scope of this contribution and requires lower-scale models of experimental insight.

twin cross-hardening. Specifically, the values of $k_{\beta\beta'}$ are chosen such as to admit only one active (compressive or tensile) twin variant at a time [107]. Analogously, $\mathcal{H}(T)$ is a positive semi-definite matrix, capturing slip-slip cross-hardening through terms $h_{\alpha\alpha'}$ on its off-diagonals and a zero diagonal.

Twin hardening effects on the slip systems are included via a saturation hardening law. Upon reaching a critical twin volume fraction, the twin is considered saturated and set to be fully reoriented. This leads to strain hardening [58] (due to twin boundary and geometric hardening, while the Basinski effect leads to the transformation of glissile into sessile dislocations [229, 230]). As we do not resolve twins spatially nor account for the formation of twin lamellae (such as, e.g., in the composite grain model of Proust, Tomé, and Kaschner [152]), these effects are condensed into a single hardening parameter c_α , applied upon twin saturation. Jain and Agnew [5] noted that not all systems are affected equally by the presence of twins, which is why their model introduced a stronger latent hardening factor for basal slip. Similar observations were made by Yu et al. [231], who investigated experimentally the hardening effect of twinning on basal and prismatic slip in AZ31, noticing an increased effect of twin hardening on basal systems as compared to prismatic systems. Here, this phenomenon is accounted for by different choices for the parameters c_α in (3.10).

Assuming that both slip and twinning follows a Schmid-type law, the resolved shear stress (RSS) of slip system α is

$$\tau_\alpha^p = \boldsymbol{\Sigma} \cdot \mathbf{p}_\alpha, \quad (3.11)$$

with \mathbf{p}_α from (3.5). Equivalently, the RSS for twin system β becomes

$$\tau_\beta^{\text{tw}} = \boldsymbol{\Sigma} \cdot \gamma_\beta^{\text{tw}} \mathbf{a}_\beta \otimes \mathbf{n}_\beta, \quad (3.12)$$

with the Mandel stress tensor $\boldsymbol{\Sigma}$, defined as

$$\boldsymbol{\Sigma} = \mathbf{F}_e^T \mathbf{P} \mathbf{F}_{\text{in}}^T \quad \text{with} \quad \mathbf{P} = \frac{\partial W}{\partial \mathbf{F}}. \quad (3.13)$$

The evolution laws for the plastic slips in this variational setting follow as

$$\dot{\gamma}_\alpha = \dot{\gamma}_{0,\alpha} \left| \frac{|\tau_\alpha^p| - \frac{\partial W_p}{\partial \epsilon_\alpha}}{\tau_{0,\alpha}(T)} \right|^{1/m_p} \text{sign}(\tau_\alpha^p), \quad (3.14)$$

with reference slip rates $\dot{\gamma}_{0,\alpha}$, a temperature-dependent CRSS $\tau_{0,\alpha}$ for each slip system, and hardening exponent m_p . Analogously, the twin volume fractions evolve according to

$$\dot{\lambda}_\beta = \dot{\lambda}_{0,\beta} \left| \frac{|\tau_\beta^{\text{tw}}| - \frac{\partial W_{\text{tw}}}{\partial \lambda_\beta}}{\tau_{0,\beta}} \right|^{1/m_{\text{tw}}} \quad (3.15)$$

with a reference rate $\dot{\lambda}_{0,\beta}$, hardening exponent m_{tw} , and temperature-independent CRSS $\tau_{0,\beta}$.

The constitutive model is completed by a choice of the elastic energy density. Chang and Kochmann [107] showed that – owing to its low level – elastic anisotropy has a negligible effect on the texture evolution and stress-strain relation of Mg. For simplicity, we thus choose a compressible Neo-Hookean strain energy density

$$W_e(\mathbf{F}_e, T) = \frac{\mu(T)}{2} (\text{tr } \bar{\mathbf{C}}_e - 3) + \frac{\kappa(T)}{2} (J - 1)^2 \quad (3.16)$$

with

$$\bar{\mathbf{C}}_e = \bar{\mathbf{F}}_e^T \bar{\mathbf{F}}_e, \quad \bar{\mathbf{F}}_e = \frac{\mathbf{F}_e}{J^{1/3}}, \quad J = \det \mathbf{F}_e = \det \mathbf{F} \quad (3.17)$$

and temperature-dependent shear and bulk moduli μ and κ , respectively.

3.4 TEMPERATURE DEPENDENCE

The temperature dependence of slip and twinning was studied, among others, by Chapuis and Driver [9] and Wonsiewicz and Backofen [19], who concluded that basal slip and tensile twins are largely temperature insensitive, whereas non-basal slip and compressive twins (CT) show a moderate to strong temperature dependence – as also argued by Nie, Shin, and Zeng [2], Wang, Liu, and Soh [15], and Liu, Roy, and Silberschmidt [159].

We note that some studies observed reduced twin activity with increasing temperature [5, 9, 19, 58], which can be explained by the fact that other deformation modes can more readily accommodate the deformation due to the increased lattice mobility, leading to a reduction in twinning. Further, the accrued slip may have an inhibitory effect on twinning. Jain and Agnew [5] assumed an *inverse* temperature dependence of the CRSS of TT systems in their study of AZ31, leading to hardening and a reduction of twin activity with increasing temperature. Although that assumption does yield

the expected result of a decrease in twin activity at elevated temperature, it is questionable, whether the phenomenon they observed is due to an actual increase in the CRSS value or due to other effects, such as the increased propensity for precipitates in the alloy, which are known to promote twin hardening [72]. As the present formulation of the model cannot account for complex mechanistic effects, we follow Chapuis and Driver [9] and Wonsiewicz and Backofen [19] and assume that the TT (and basal slip) systems are temperature-independent, so that temperature dependence is incorporated only in the non-basal slip systems, and in CTs, as in Wang, Liu, and Soh [15] and Liu, Roy, and Silberschmidt [159].

Similar to Wang, Liu, and Soh [15], Liu, Roy, and Silberschmidt [159], and Beyerlein and Tomé [232], we assume an Arrhenius-type law for the temperature dependence of the CRSS values, so the temperature dependence of the non-basal slip systems is assumed to decay exponentially with temperature, i.e.,

$$\tau_{0,\alpha}(\bar{T}) = \begin{cases} \tau_{0,\alpha}(T_{\text{ref}}) & \text{for basal systems,} \\ \tau_{0,\alpha}(T_{\text{ref}}) \exp(-\omega_{\alpha}\bar{T}) & \text{else,} \end{cases} \quad (3.18)$$

with distinct parameters $\omega_{\alpha} > 0$ for the prismatic and pyramidal systems, and the dimensionless temperature

$$\bar{T}(T) = \frac{T - T_{\text{ref}}}{T_{\text{melt}} - T_{\text{ref}}}. \quad (3.19)$$

The melting temperature of Mg is $T_{\text{melt}} = 650^{\circ}\text{C}$, while we take as a reference the ambient temperature $T_{\text{ref}} = 25^{\circ}\text{C}$.

The exponential ansatz is also used to describe the temperature sensitivity of the Voce hardening parameters:

$$\begin{aligned} h_{\alpha}^0(\bar{T}) &= \begin{cases} h_{\alpha}^0(T_{\text{ref}}) & \text{for basal systems,} \\ h_{\alpha}^0(T_{\text{ref}}) \exp(-\eta_{\alpha}\bar{T}) & \text{else,} \end{cases} \\ h_{\alpha\alpha'}(\bar{T}) &= \begin{cases} h_{\alpha\alpha'}(T_{\text{ref}}) & \text{for basal systems,} \\ h_{\alpha\alpha'}(T_{\text{ref}}) \exp(-\chi_{\alpha}\bar{T}) & \text{else,} \end{cases} \\ \sigma_{\alpha}^{\infty}(\bar{T}) &= \begin{cases} \sigma_{\alpha}^{\infty}(T_{\text{ref}}) & \text{for basal systems,} \\ \sigma_{\alpha}^{\infty}(T_{\text{ref}}) \exp(-\nu_{\alpha}\bar{T}) & \text{else.} \end{cases} \end{aligned} \quad (3.20)$$

Analogously, the hardening laws for TTs are assumed to be temperature insensitive:

$$k_{\beta}^0(\bar{T}) = \begin{cases} k_{\beta}(T_{\text{ref}}) & \text{for TT systems} \\ k_{\beta}(T_{\text{ref}}) \exp(-\zeta_{\beta}\bar{T}) & \text{for CT systems.} \end{cases} \quad (3.21)$$

The entries of \mathcal{K} are temperature-*independent*. The twin-twin cross hardening matrix ensures no more than one twin system is active at the material point. This assumption does not collapse for elevated temperatures.

Finally, the elastic constants are chosen as $\mu(T) = 17 \exp(-3\bar{T})$ GPa and $\kappa(T) = 16 \exp(-3\bar{T})$ GPa, by extending the (room-temperature) Neo-Hookean formulation from Vidyasagar, Tutcuoglu, and Kochmann [12].

3.5 PARAMETER IDENTIFICATION AND MODEL VALIDATION

Polycrystalline materials serve as a valuable source of experimental data, particularly for alloys where growing single crystals is challenging or impractical. In the case of Mg and Mg alloys, the available data primarily pertains to wrought sheet materials or extruded billets [55, 57, 58, 87, 233–236]. During processing, polycrystalline Mg exhibits a strong texture that is influenced by grain reorientation and recrystallization [57, 236]. Cold and asymmetric hot rolling lead to the development of a prominent basal texture, while extruded material acquires a distinct texture resulting from a combination of reorientation and recrystallization [2, 49, 51, 58, 86, 96]. Basal slip, which can be activated by small Schmid factors (even as low as 0.4° misalignment from the normal direction according to Kelley et al. [8]), is a prevalent deformation mode in polycrystalline materials. As a result, the directional behavior of single crystals is imparted to the polycrystals, albeit with some attenuation due to the presence of basal slip [5, 8, 96, 157, 234].

From a modeling standpoint, these observations have significant implications. Since texture cannot be precisely controlled and is influenced by factors such as strain rate, processing temperature, and pre-existing grain sizes, it becomes challenging to extract or define physical parameters directly from polycrystalline data. This variability in texture is one possible explanation for the range of reported values for individual critical resolved shear stresses (CRSS) in the literature, as well as the diversity of models employed [5, 156, 157, 234]. Inferring single-crystalline parameters from polycrystals presents significant drawbacks, as highlighted by Herrera-Solaz

et al. [89]. The numerous influencing factors, such as grain size, texture, presence of precipitates and solutes, among others, result in a large number of parameters to be determined, making the task of finding an optimum solution neither easy nor guaranteed.

Therefore, our (bottom-up) strategy is to first calibrate the *room-temperature single-crystal* model, followed by calibrating the *temperature-related* parameters, for both of which the Taylor model provides *poly-crystal* predictions for validation. We begin by calibrating the room-temperature single-crystal model, using the data reported by Kelley and Hosford [8], who performed a series of room-temperature channel-die experiments. They used seven distinct orientations of their single-crystal samples with respect to the applied loading, denoted by cases A through G, which were designed to isolate the behavior of individual slip and twin systems in Mg at room temperature. Table 3.1 provides an overview of the applied deformation and constraints as well as the deformation mechanism(s) calibrated by each case.

TABLE 3.1: The seven cases in the channel-die experiments of Kelley and Hosford [8]. Single-crystals were subjected to plane-strain compression, being compressed in the *Compression* direction with a rigid constraint imposed in the *Constraint* direction, while being unconstrained in the third (orthogonal) direction. Each case is designed to promote the activity of the denoted system (*Deform. Mode(s)*), including pyramidal (Py), prismatic (Pris) and basal slip as well as tension twins (TT) and compressive twins (CT).

Case	A	B	C	D	E	F	G
Compression	{0001}	{0001}	{10 $\bar{1}$ 0}	{1 $\bar{2}$ 10}	{10 $\bar{1}$ 0}	{1 $\bar{2}$ 10}	{0001} @ 45°
Constraint	{10 $\bar{1}$ 0}	{1 $\bar{2}$ 10}	{0001}	{0001}	{1 $\bar{2}$ 10}	{10 $\bar{1}$ 0}	{10 $\bar{1}$ 0}
Deform. Mode(s)	Py & CT	Py & CT	Pris & CT	Pris & CT	TT	TT	Basal

Simulations for calibration were performed under quasistatic conditions at a strain rate of $\dot{\epsilon} = 10^{-4}\text{s}^{-1}$. The channel-die setup—with compression being applied in the x_3 -direction and the sample surfaces perpendicular to the x_1 -direction left free and constrained in the x_2 -direction, is approximated by imposing the deformation gradient

$$\mathbf{F} = \begin{pmatrix} F_{11} & F_{12} & F_{13} \\ 0 & 1 & 0 \\ 0 & 0 & e^{\dot{\epsilon}t} \end{pmatrix}. \quad (3.22)$$

The unknown entries F_{1i} (accounting for the free boundaries of the channel) are found by solving for the traction-free boundary conditions $P_{1i} = 0$ [147].

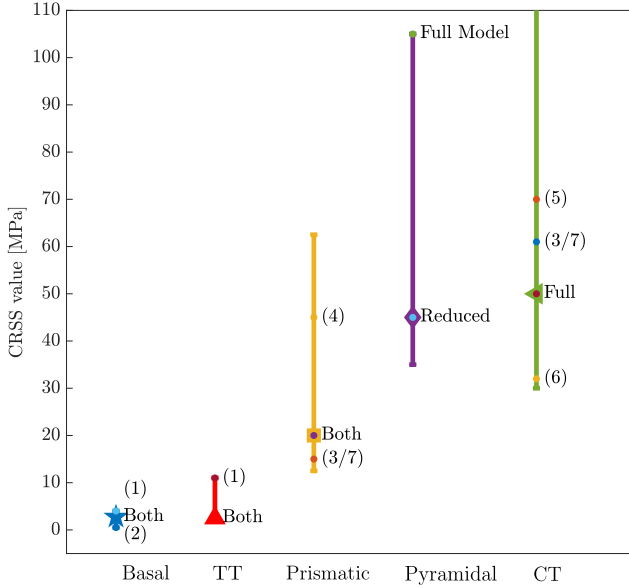


FIGURE 3.2: Range of the experimentally reported CRSS values for the slip and twin systems. The shown ranges were obtained from Wang, Liu, and Soh [15] and expanded with experimental data from Chapuis and Driver [9](1), Kelley and Hosford [8](2), Yoshinaga and Horiuchi [16, 17](3,7), Akhtar and Teghtsoonian [18](4), Wonsiewicz and Backofen [19](5), and Kitahara et al. [20](6). The pyramidal II CRSS of the reduced model coincides with the experimental values of Obara, Yoshinga, and Morozumi [21]

Parameter calibration starts with the room-temperature CRSS values, which were chosen to lie in the range reported experimentally (see Fig. 3.2), with the parameters reported by Chang and Kochmann [107] used as initial guess. The room-temperature CRSS values were, once chosen, held constant for the remainder of the calibration process.

The calibration for each case in Table 3.2 (assuming that only the indicated deformation modes are active) follows the same protocol. With the Voce hardening laws, the initial onset of plastic flow is governed by the CRSS values of the active systems. The peak stress depends mostly on the saturation stress σ_{α}^{∞} , while the shape of the plastic stress-strain curve depends primarily on the self-hardening factor h_{α}^0 . The large-strain behavior additionally depends on the cross-hardening factors $h_{\alpha\alpha'}$ and h_{α}^0 . Calibra-

tion of the model was accomplished by critically comparing the results of the simulated single-crystal behavior to the experimental stress-strain data of Kelley and Hosford [8], calibrating the relevant model parameters one at a time to capture the onset of plastic flow, hardening, and large-strain behavior in a similar spirit to Zhang and Joshi [108].

This procedure works best when there is no ambiguity in the deformation modes during plastic deformation. Hence, Case G, involving only basal slip, proves easiest to calibrate, so optimal material parameters were readily obtained. Analogously, case E is ideally suited to calibrate the TT systems. Since twins follow a slightly different hardening law than the slip systems, hardening parameter k_0 was calibrated with the initial response of the single-crystal experiments from Kelley and Hosford [8] to fit the slope of the twin hardening region up to 6% strain. The bifurcation point, indicating the saturation of the twin system and the subsequent reorientation of the lattice, corresponds to the results obtained by Zhang and Joshi [108] for a critical volume fraction of 0.9.

Calibration of the pyramidal II and prismatic systems was less trivial, as both systems in principle occur simultaneously in cases A and C (along with CT). As a simplifying assumption, we assume that simulations of case A are dominated by pyramidal II slip and CT activity, and case C by the prismatic systems and CTs (as indicated in Table 3.2). This led to an iterative calibration route of those systems. Cases B and D, which feature the same deformation modes but to different extent, were used to check and validate the calibrated model parameters.

While in the reduced model (without CT) the seven cases were well suited to isolate each deformation mode, the ambiguity linked to the presence of the CT systems in the full model led to challenges (similar challenges were noted by Zhang and Joshi [108]). As a remedy, we assume, based on data from Kelley and Hosford [8], Yoshinaga and Horiuchi [16], Wonsiewicz and Backofen [19], and Kitahara et al. [20], that CTs exhibit a lower CRSS than the pyramidal II systems at lower temperatures. In fact, in the full model this assumption was necessary to obtain CT contributions in the first place. The self-hardening factor k_{CT}^0 of the CT systems was calibrated such as to capture the initial slope of case A, see Fig. 3.8. The excessive self-hardening is in agreement with experimental observations and simulation results [19, 108]. Upon saturation (not due to reaching the critical volume fraction, but instead due to extensive self-hardening) additional deformation is accommodated by pyramidal II slip.

Once calibrated at room temperature, the single-crystal model was made temperature-dependent, as described in Section 3.4, again beginning with the CRSS values, for which an exponential ansatz was chosen for the pyramidal II and prismatic $\langle a \rangle$ slip as well as the CT systems (see Section 3.4). Unfortunately, the experimentally reported CRSS values are inconclusive. For instance, the CRSS values for the prismatic systems reported by Yoshinaga and Horiuchi [16] and Akhtar and Teghtsoonian [18] differ substantially. The exponential decay parameters were thus obtained by critically comparing the predicted CRSS values with the range of experimental results reported by Nie, Shin, and Zeng [2], Chapuis and Driver [9], Yoshinaga and Horiuchi [16], Akhtar and Teghtsoonian [18], and Obara, Yoshinga, and Morozumi [21]. Due to the wide range of experimental data, we note that the calibrated CRSS values may not represent physical material constant. We observe, however, good agreement with the experimentally reported values for the temperature range up to 300°C, see Fig. 3.3.

Calibration of the hardening parameters at elevated temperature was performed via optimization, using the Nelder-Mead optimization routine from the SciPy library [237]. For each case, an initial guess was chosen manually. As in the room-temperature case, the calibration of these systems is not straight-forward, and cases A and B need to be considered jointly. Therefore, in the numerical optimization, the objective was to minimize the mean square error (MSE) of the accumulated stress-strain error of both cases (A and C) at temperatures of 116°C, 200°C, 271°C for case A, and 110°C, 180°C, and 270°C for case C. This allowed us to identify the temperature parameters η_α , ξ_α , and ν_α for each deformation mode. Note that no global optimum was found, and the temperature-dependence depends on the initial guess. The optimization procedure was repeated 20 times, and the best set of parameters (in terms of the lowest stress-strain MSE) was chosen.

The calibration of the temperature parameters proved to be complex, since the room temperature data for cases A, B, C, and D from Kelley and Hosford [8] and Wonsiewicz and Backofen [19] differ significantly (see Fig. 3.4). While both authors reported similar peak stresses and general behavior, the path to failure varied. Data from Kelley and Hosford [8] shows strong initial hardening in the elastic region with a flow stress of around 100 MPa, followed by a slow transition into a peak-stress around 300 MPa at 4% strain. The behavior reported by Wonsiewicz and Backofen [19] exhibits a different initial hardening behavior: the material seems to exhibit an early onset of plastic flow at considerably lower stresses of around 40 MPa, followed by slower and less pronounced hardening, which abruptly plateaus at around

TABLE 3.2: Model parameters for the slip systems at room temperature, calibrated based on the experimental data of Kelley and Hosford [8]. All values are for the reduced model, unless those marked by †, which are for the full model including the CT systems. Values marked by an asterisk (*) were calibrated based on data from Kelley and Hosford [8], Chapuis and Driver [9], Akhtar and Teghtsoonian [18], Lilleodden [25], and Ando et al. [26] The temperature dependence of the CRSS values was calibrated such as to lie in the range of experimentally reported data, see Fig. 3.3.

Parameter	Symbol	Unit	Basal	Prismatic	Pyramidal II	Reference/Calibration
CRSS	τ_0	MPa	2.0	20	40 (100 [†])	calibration*
Self hardening factor	h_0	MPa	750	6000	13000	calibration
Cross hardening factor	h_{ij}	MPa	10	10	12	calibration
Saturation stress	σ^∞	MPa	0.8	72	115 (60 [†])	calibration
Twin-slip cross-hardening factor	c_α	MPa	20	10	5	calibration
Reference slip rate	$\dot{\gamma}_0$	s^{-1}	10 ⁻³	10 ⁻³	10 ⁻³	Zhang and Joshi [108]
Slip exponent	m_p	-	0.5	0.5	0.5	Chang and Kochmann [107]
CRSS temperature factor	ω	-	-	3.0	2.95 (5.5 [†])	calibration*
Self-hardening temperature factor	η	-	-	5.2	4.5 (2.2 [†])	optimization
Cross-hardening temperature factor	ν	-	-	1.3	2.5	optimization
Saturation stress temperature factor	ξ	-	-	2.5	4.05 (2.5 [†])	optimization

TABLE 3.3: Model parameters for the twin systems in full and reduced models, calibrated based on the data of Kelley and Hosford [8] and Wonsiewicz and Backofen [19]

Parameter	Symbol	Unit	TT	CT	Reference/Calibration
CRSS	τ_0	MPa	3.5	50	calibration
Self hardening factor	k_0	MPa	25	3000	calibration
Twin shear	$\dot{\gamma}_0$	-	0.129	0.138	Chang and Kochmann [107] and Zhang and Joshi [108]
Cross hardening factor	h_{ij}	MPa	100	100	Chang and Kochmann [107]
Critical volume fraction	v_{crit}	-	0.9	0.9	Zhang and Joshi [108]
Twin rate	$\dot{\gamma}_0$	-	10 ⁻³	10 ⁻⁴	Zhang and Joshi [108]
Twin exponent	m_{tw}	-	1	1	Chang and Kochmann [107]
CRSS temperature factor	ω	-	-	3.5	calibration
Self-hardening temperature factor	ξ	-	-	4.0	calibration

5.5% strain before fracture occurs at 6% strain. We show a comparison for case A in Fig. 3.4, but the same trends persist for cases B, C, and D. While the differences in experiments rendered the calibration task more challenging, the fact that the peak stresses appear to be unaffected by the difference in experimental setups, the model was calibrated to the available single-crystal data despite the apparent differences. This calibration required manual tuning, as the optimizer generally tends to over-predict the stress at elevated temperature and under-predict at lower temperatures.

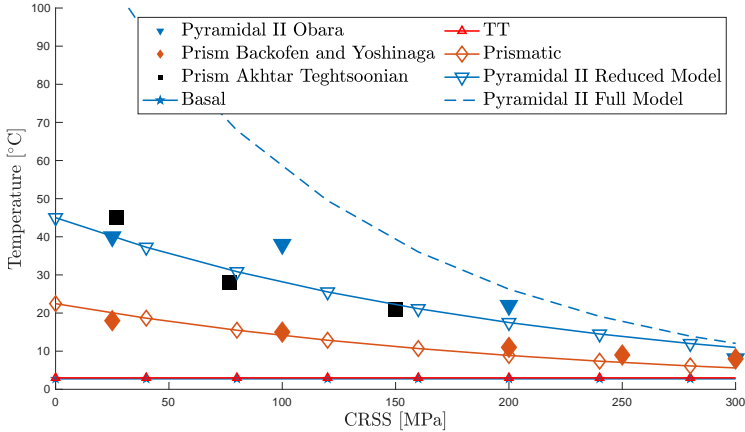


FIGURE 3.3: Experimentally measured CRSS values for the slip and TT systems in Mg in comparison with this model over the studied range of temperatures. The filled markers show experimentally reported data from Yoshinaga and Horiuchi [17], Akhtar and Teghtsoonian [18], Wonsiewicz and Backofen [19], and Obara, Yoshinga, and Morozumi [21]. The solid lines with markers represent the data for the reduced model, the dashed lines for the full model. The TT and basal CRSS values were constant for both models.

3.6 SINGLE CRYSTAL SIMULATIONS

The single-crystal response of Mg is highly sensitive to the crystal orientation with respect to the applied loading, and it depends on temperature. Unfortunately, the literature is controversial when it comes to the non-basal slip vs. twin activity. Compression along the c -axis requires the activation of deformation modes such as pyramidal II slip or CTs [16, 21, 216]. According to Ono, Nowak, and Miura [3], $\langle c + a \rangle$ pyramidal slip is a prominent deformation mode for through-thickness compression along the c -axis. In a similar spirit, Obara, Yoshinga, and Morozumi [21], Koike et al. [127], and Muránsky et al. [219] reported pyramidal II slip activity at room temperature. These findings stand in contradiction to the observations of Kelley and Hosford [8] and Wonsiewicz and Backofen [19], who observe mostly $\{10\bar{1}1\}$ CTs and $\{10\bar{1}2\}$ TTs alongside large amounts of basal slip at room temperature and, in part, at elevated temperature, where especially the presence of TTs appears counter-intuitive due to the polar nature of the

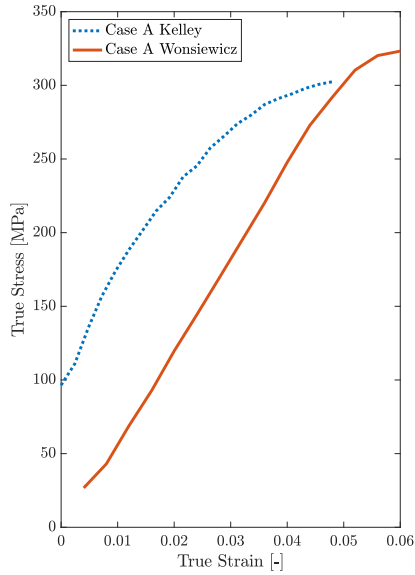


FIGURE 3.4: Stress-strain data for the channel-die experiments of Kelley and Hosford [8] (dotted line) and Wonsiewicz and Backofen [19] (solid line).

twin systems. With increasing temperature, Wonsiewicz and Backofen [19] further observed increasing amounts of twinning and double twinning in Mg single-crystals, when compressed along the c -axis. This, in turn, is in contradiction to the more recent investigations by Barnett [56], who found CT activity to be inversely proportional to temperature. Above a transition temperature, CTs were found to be less dominant, while non-basal slip systems account for the increasing amount of deformation [123]. Similar findings were reported by Khosravani et al. [238] for alloy AZ31B, where this transition temperature was found to be as low as 350K. Wonsiewicz and Backofen [19] reported evidence of CTs even at room temperature for cases C and D, in which the crystal is not ideally oriented for CTs to show activity. With the goal of shedding light into these controversial reports (while also validating the model's suitability), we proceed to model the response of Mg single-crystals, using the two versions of our model (reduced and full, where only the latter accounts for CT) along with a detailed comparison

and discussion—and we do so both at room temperature and at elevated temperature.

3.6.1 Room-Temperature Single-Crystal Response

In the following we simulate the room-temperature mechanical response of Mg single crystals and compare our results with experimental benchmarks. We begin by showing the results of the reduced representation, followed by those of the full model, including CTs. Finally, we compare both implementations and assess their results critically.

3.6.1.1 Reduced Representation of the Microstructure (without CT)

Fig. 3.5 shows the stress-strain behavior of Mg single-crystals for cases A through G, predicted by the reduced model with the material parameters in Table 3.2. The predicted response captures the salient features and compares well with the experimental data in all cases. To highlight the microstructure evolution, we also report the predicted activity of the various deformation modes. To this end and to compare the activities, we introduce as a qualitative measure the *relative activity of each deformation mode* as

$$\mathcal{Y}_{\text{bas./prism./pyr.}} = \frac{\Gamma_{\text{bas./prism./pyr.}}}{\sum_{\alpha=1}^{N_s} |\gamma_{\alpha}|}, \quad (3.23)$$

where $\Gamma_{\text{bas./prism./pyr.}} = \sum_{\alpha} |\gamma_{\alpha}|$ represents the sum of either all basal, all prismatic, or all pyramidal slip activity. We define an analogous *relative TT activity*

$$\mathcal{Y}_{\text{TT}} = \sum_{\beta=1}^{N_t} \lambda_{\beta}, \quad (3.24)$$

which is a qualitative measure of the overall TT activity ($\mathcal{Y}_{\text{TT}} = 0$ implying no TT activity). Let us comment on the individual load cases and their predicted microstructural characteristics.

***c*-axis compression:**

Mg crystals under plane-strain compression along the *c*-axis of the crystal are distinguished by strong strain hardening, characteristically followed by rapid fracture at roughly 4% to 6% strain [8, 19]. The resulting limited formability is related to the localization of deformation due to an insufficient number of deformation modes, resulting in the formation of shear bands and ultimately failure [2, 8, 19, 45]. Both cases A and B are similar in nature,

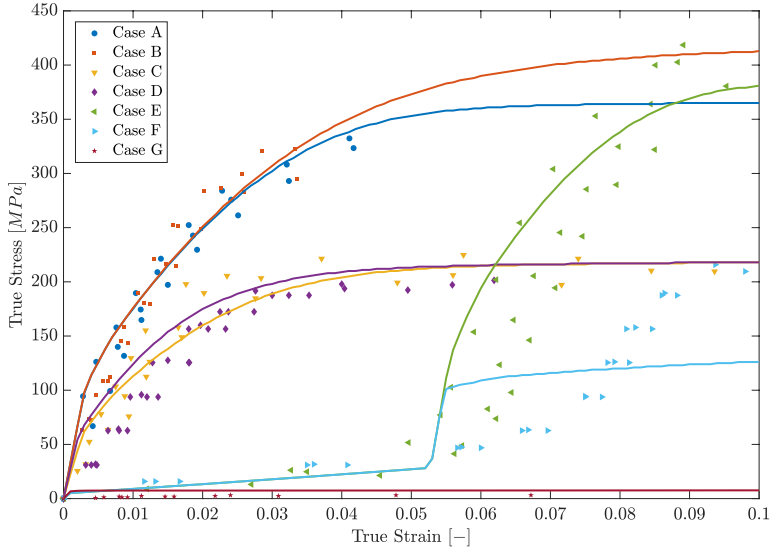


FIGURE 3.5: Stress-strain responses of cases A through G. Dots represent experimental data by Kelley and Hosford [8], solid lines are results simulated with the reduced model.

B showing a slightly higher peak stress [8, 19]. The reduced model captures this phenomenon accurately.

The relative activities in Fig. 3.6 for cases A and B show a predominant activation of pyramidal systems, which agrees with the results by Wang, Liu, and Soh [15] and Zhang and Joshi [108]. In the absence of CTs, pyramidal slip is the only option to accommodate compressive c -axis deformation. Experimentally, the presence of pyramidal slip at room temperature was shown by Ono, Nowak, and Miura [3], Obara, Yoshinga, and Morozumi [21], Lilleodden [25], and Muránsky et al. [219]. Since the pyramidal II systems have a Burgers vector with both, c - and a -components, and a constraint is applied, some of the deformation along the a -axis induced by the activity of the pyramidal systems requires compensation. This induces a smaller degree of prismatic slip. The change in orientation in case B leads to an increased activity in the prismatic systems. Similar effects were reported in previous numerical studies [107, 108, 159]. The larger peak strain in case B comes from the effect of the constraint which effectively hardens the pyramidal systems [108] as well as the increased slip activity on the

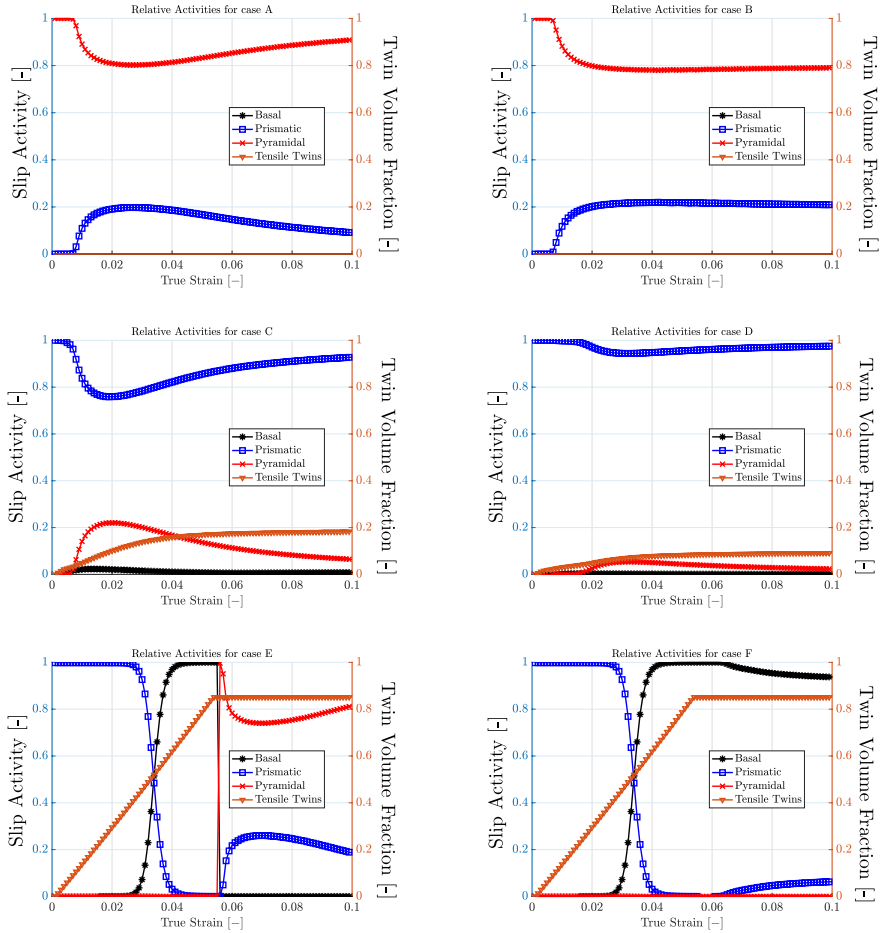


FIGURE 3.6: Relative twin and slip activities for cases A, B, C, D, E, and F. Case G shows only basal activity, as expected, and is hence omitted here.

prismatic systems, which lead to a hardening effect.

***a*-axis compression with constrained *c*-axis:**

Mg single-crystals under *a*-axis compression typically exhibit strong initial strain hardening, followed by a gradual strain softening and no explicit peak stress. This case is also characterised by an exceptionally high ductility, as it can accommodate large strains before fracture [8, 19]. This behavior is accurately described by the present formulation. In both cases C and D, the constraint is applied in the $\{0001\}$ direction, and the prismatic systems are expected to be the predominant sources of plastic slip. In addition, the non-zero resolved stresses on the TT systems along with their low CRSS lead to a significant amount of TTs despite the hard constraint. The deformation along the *c*-axis, which results from the TTs, is offset by elastic deformation in the channel wall as well as by the activity of CTs in an experimental setting, allowing up to 20% twin volume fraction[19]. In our simulations, however, the channel is rigid and CTs are not accounted for in the reduced model, yet TTs are also observed. This is possible as the strain along the constrained *c*-axis due to TTs is offset by activating the pyramidal systems. Case C exhibits a larger TT contribution, which plateaus at about 3% strain. In agreement, the pyramidal II contributions tend to vanish beyond this level of strain, as little *c*-axis deformation is induced (see Fig. 3.6). Conversely, case D exhibits less TT activity, in agreement with the pyramidal activity also being reduced.

***a*-axis compression with unconstrained *c*-axis:**

Cases E and F are dominated by TTs, characterized by low strain hardening up to 6% strain. TT in Mg is easy to activate, and twins grow until they reach saturation, thus showing little strain hardening during the initial deformation phase (see Fig. 3.5). Upon saturation, the crystal reorients around the twin plane of the active twin system, which leads to a drastic change in the stress-strain response, as demonstrated by cases E and F.

Twinning is an asymmetric deformation mode², which is captured by the reduced model, as shown in Fig. 3.7.

² The characterisation as a “compressive” vs. “tension” twin depends on the *c/a* ratio of the material [7]. For materials with a $c/a < \sqrt{3}$ (which includes Mg) the $\{10\bar{1}2\}$ twinning mode is a tension twin, i.e., it elongates the *c*-axis. It hence activates under *c*-axis tension, while showing no activity under *c*-axis compression.

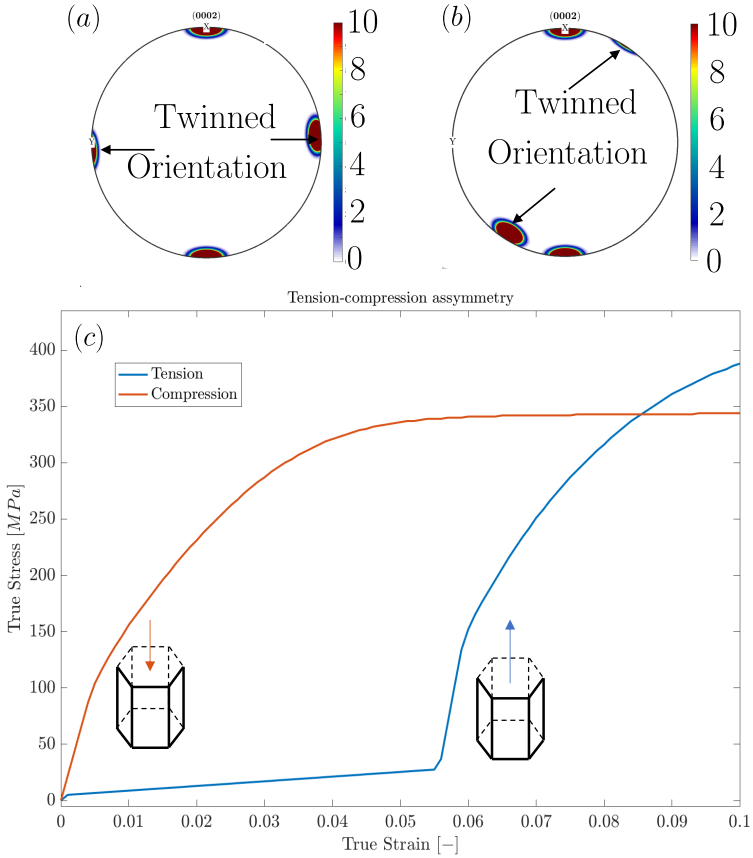


FIGURE 3.7: Tension-compression asymmetry and the reorientation of the crystal: due to the imposed initial orientation of the crystal, the x -direction is unconstrained, and the loading direction corresponds to the y -direction in the pole figures (a.b). Case E leads to a reorientation by 86° (a), whereas case F leads to a reorientation by 30.3° (b) [15, 19]. (c) shows the tension-compression asymmetry of the TT system, which is active under c -axis extension but inactive under c -axis compression.

For case E, the unobstructed c -axis allows the TT to grow, contributing a $\langle c + a \rangle$ component to the total deformation. Initially, this leads to the activation of prismatic systems to offset the $\langle a \rangle$ contributions against the constraint. After about 2% strain the crystal has sufficiently reorientated due to slip, so that basal slip becomes active and almost instantaneously governs the deformation. The twin system saturates at about 6%, which leads to an instantaneous change in the stress-strain behavior. In case E of the simulations, the twins reorient the material by 86.3° , which is close to the orientation initially shown in cases A and B [8]. In this configuration, the shear stress on the basal systems is minute, in contrast to the pyramidal systems, which are now again favorably aligned. Note also that the total amount of slip is small during the first 6% of deformation, since the pyramidal slip almost instantaneously accounts for the majority of all slip upon reorientation. The reoriented crystal is close to cases A and B, but the response is stiffer, which was also noted by Kelley and Hosford [8] and which is attributed to prior twin-hardening of the material.

The situation is different for case F, where the twins reorient the material such that the basal plane forms a 31° angle with the loading direction (Fig. 3.7), thus enabling basal slip to emerge easily [8]. As noted by Wang, Liu, and Soh [15], the orientation of case F leaves the basal systems ideally oriented and explaining the different behavior of the twinned crystal. Further, in case F four TT systems are ideally oriented for activation, as noted by Kelley and Hosford [8]. As seen in Fig. 3.7, we capture the reorientation of both cases E and F accurately in our simulations. The discrepancy in the predicted stress for case F is due to other aspects. The predominant twin model used here (only the twin system with the largest CRSS is active) cannot capture multiple twin systems. This leads to premature saturation of a single system and the subsequent lack of twin-slip hardening yields a lower stress at larger strains.

Orientations promoting basal slip:

Under plane-strain compression with the c -axis forming a 45° angle to the compression direction (case G), basal slip is favored. Samples in this case exhibit considerably higher plastic strains and noticeable hardening is observed only at large strains, as is evident from the data of Nie, Shin, and Zeng [2] and Kelley and Hosford [8]. The low hardening rates and early onset of plasticity reflect the discrepancy in CRSS and hardening behavior between the basal systems and all others, as basal slip is solely active up to 10% strain in this case. At higher strains, deformation is also accommodated

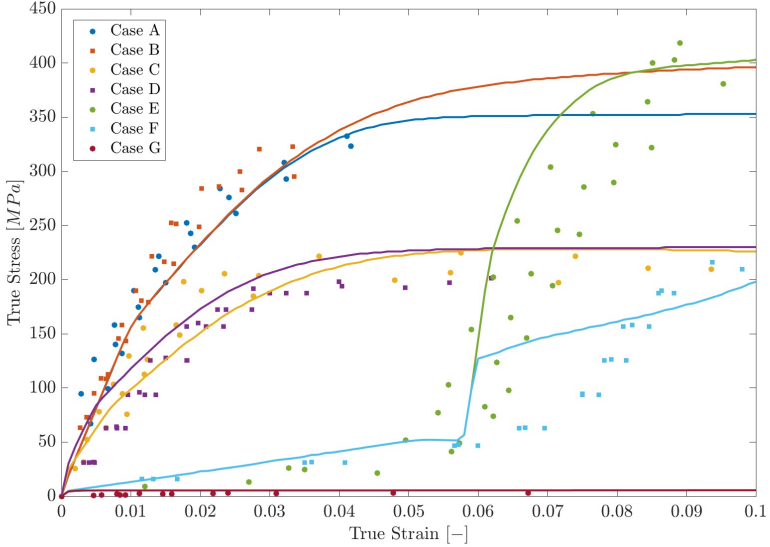


FIGURE 3.8: Stress-strain responses of cases A through G, as obtained from the full model including CT. Dots represent experimental data of Kelley and Hosford [8], lines are simulated results.

via twin band formation. After about 50%-60% strain, the crystal hardens extensively, as the twinned volume fraction increases [2].

3.6.1.2 Full Representation (including CT)

The full model including CT (calibrated through cases A and C, as explained in Section 3.5) leads to the stress-strain responses shown in Fig. 3.8 for all seven cases. Again, good agreement with experiments is achieved, and the key aspects of the stress-strain behavior are captured. CTs lead to a slightly stiffer initial response for cases A and B as well as under reorientation due to twinning. This is related to the high hardening and slow kinematics of the twin propagation generally associated with CT [15, 19, 108] as well as with the change in CRSS and initial hardening parameters of the pyramidal systems, as obtained from the calibration of the full model (see Table 3.2). Predictions for cases E, F, and G are close to those of the reduced model, so that we will focus on the cases A and C to discuss the influence of CTs.

***c*-axis compression:**

CTs offer a second deformation mode next to the pyramidal II systems to accommodate deformation along the *c*-axis under compression, while also affecting the crystal reorientation. Fig. 3.9 shows the activity of the deformation modes, highlighting the competition between the CT and pyramidal II systems. Initially, basal slip occurs alongside CT formation in agreement with experimental observations [19]. The reorientation due to CT is, however, minimal, seen over the entirety of the crystal, and the volume fraction remains below 10% for the duration of the simulation. CTs are known to propagate more slowly than their tensile counterparts [108] and to harden more extensively. Due to the slow propagation of CT lamellae in the crystal (described in our model by the reduced reference growth rate) the crystal must activate pyramidal slip once the CT systems have hardened substantially (which occurs at about 3% strain, when the CT system has hardened so much that any further increase in the twin volume fraction is unfavourable). The deformation is henceforth accommodated by a combination of pyramidal and prismatic slip, in a similar fashion to case A in the reduced configuration.

***a*-axis compression with constrained *c*-axis:**

Wonsiewicz and Backofen [19] reported a significant amount of $\{10\bar{1}2\}$ twin formation with some $\{10\bar{1}1\}$ CTs, which “could only have happened to relieve the *c*-axis expansion generated by the $\{10\bar{1}2\}$ twinning”. The CT banding is hence activated as a mechanism to reduce the stress induced by the TT formation. The full model captures this behavior, as shown in the relative activities in Fig. 3.9. Initially, a combination of basal slip, CT, and TT is activated, followed by a sharp increase in prismatic slip activity. Up to approximately 3% strain, CT balance the *c*-axis extension induced by TT. Upon hardening at strains larger than 3%, the CTs saturate and small amounts of pyramidal slip activity accommodate further *c*-axis deformation. TTs slowly saturate around 6% strain, which also leads to a reduction in pyramidal activity. *a*-axis deformation is accommodated by a combination of mostly prismatic and a smaller portion of basal slip.

***a*-axis compression with unconstrained *c*-axis:**

Simulations of crystals with an unconstrained *c*-axis, again, show the typical twin-dominated deformation behavior, as seen with the *reduced* model. The initial deformation is accommodated mostly by the TT system alongside basal and small amounts of prismatic slip for compatibility reasons. At

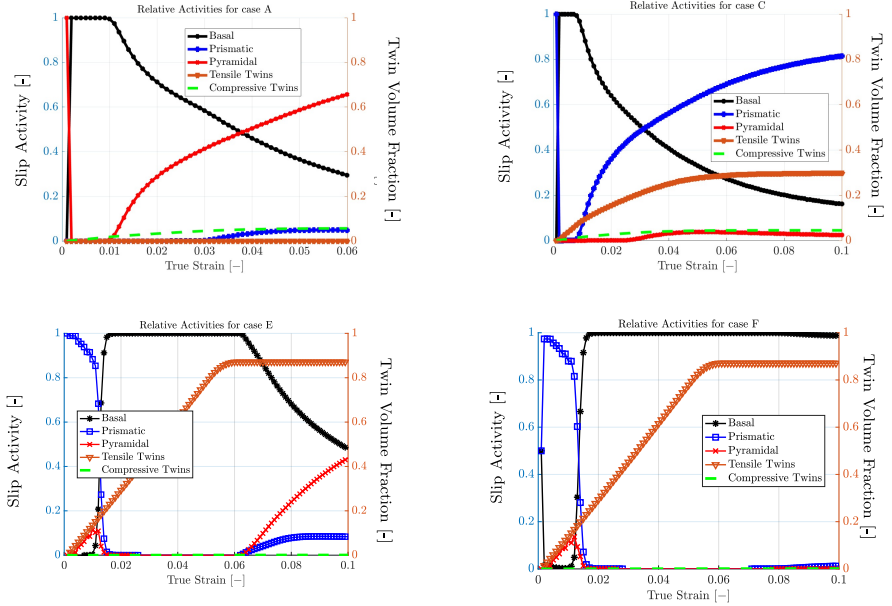


FIGURE 3.9: Relative activities of the deformation modes, as obtained from the full model including CT. Results are for a single-crystal under plane-strain compression, mimicking cases A, C, E, and F of the experiments by Kelley and Hosford [8]

close to 6% strain, the twins saturate and the crystal is fully reoriented [8], bringing it close to the orientation of cases A and B. Upon reorientation in case E, pyramidal II slip is slowly activated in the reoriented region. Due to the larger CRSS of the pyramidal slip, the activity of this deformation mode increases more slowly than for the *reduced* model. Case F shows generally a similar behavior: the first 6% strain are governed by the TT system. Upon reorientation, however, due to the different orientation of the twinned region, the basal plane is favorably oriented for slip [8]. Hence, basal activity is the key contributor to deformation in the reoriented crystal, which is captured accurately in both implementations of the model. The observed microstructures are generally in good agreement with the observations of Kelley and Hosford [8] observations. One exception is the fact that Kelley and Hosford [8] reported $\{10\bar{1}1\}$ activity right before fracture for case E, which is not captured here as we do not account for double-twinning.

3.6.1.3 *Summary*

In summary, both full and reduced models capture the stress-strain behavior of Mg qualitatively and quantitatively well in comparison to experimental data, which also extends to the microstructural mechanisms. The key difference lies in how deformation along the c -axis in compression is accommodated—either involving the CT systems or non-basal slip systems. Results indicate that both versions (with properly calibrated plastic material parameters, which differ in the full and reduced models) capture the salient stress-strain response. The full model, which includes the CT systems, shows the competition between the CT and the pyramidal systems, previously reported in experiments, and offers an insight into their relative activities at room temperature.

3.6.2 *Temperature Dependence of Monocrystalline Mg*

Let us proceed to test the two models for their temperature-dependent predictions. While the basal and twin systems were chosen to be temperature-independent, prismatic and pyramidal slip undergo a strong increase in activity at elevated temperature Nie, Shin, and Zeng [2], Ono, Nowak, and Miura [3], and Chapuis and Driver [9]. This has a marked influence on the activity of deformation modes with increasing temperature, as we will demonstrate in our comparison of results, again beginning with the reduced model before advancing to the full one.

3.6.2.1 *Temperature Dependence in the Reduced Model*

As cases A and C prominently activate the temperature-dependent deformation modes, we evaluate these two cases for their temperature-dependent response. Experimental single-crystal data is available from Wonsiewicz and Backofen [19] at temperatures of 116, 200, and 271°C for case A, and at 110, 180, and 270°C for case C. Fig. 3.10 shows good agreement between the model predictions and the experimental data under c -axis compression at four selected temperatures (results at 25°C (room temperature, RT) are identical to those in Fig. 3.5). Strain hardening and peak stresses significantly reduce with increasing temperature, as expected. Differences at low strains primarily stem from the fact that, as discussed before, the experimental data of Kelley and Hosford [8] and Wonsiewicz and Backofen [19] differ (hardening rates in Wonsiewicz and Backofen [19] are consistently smaller than those of Kelley and Hosford [8], while the peak stresses match

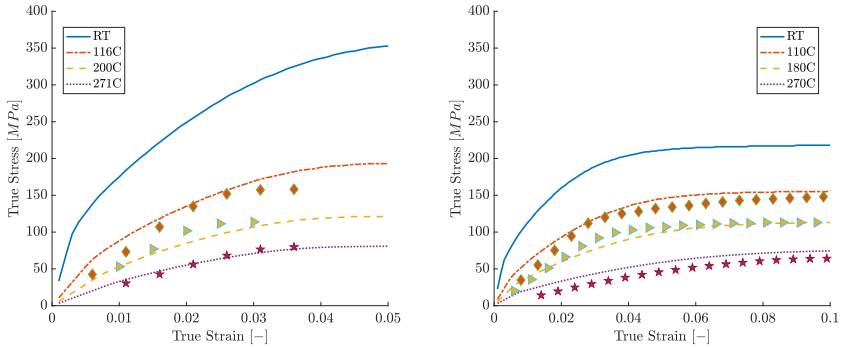


FIGURE 3.10: Temperature-dependent stress-strain response of Mg single-crystals, corresponding to cases A (left) and C (right). Solid lines are predictions by the *reduced* model, whereas the scatter plot represents the experimental data obtained by Wonsiewicz and Backofen [19]

closely). Since we calibrated the single-crystal RT response with the data of Kelley and Hosford [8], the observed differences especially in the low-strain regime may be expected. In fact, such strong temperature-induced softening in the experimental data in the low-strain regime seems unusual. Other data from Ono, Nowak, and Miura [3] and Chapuis and Driver [9] do not show such behavior; however, Ono, Nowak, and Miura [3] provide only polycrystal data, while Chapuis and Driver [9] does not provide sufficient data at elevated temperature. Further, note that above 170°C the material is prone to show crack formation as noted by Wonsiewicz and Backofen [19]. As we do not capture failure in this model, an overestimation of the stresses at large strains is the result. Dynamic recrystallization (DRX) may also play a role (Wonsiewicz and Backofen [19] reported that twinned regions often show recrystallized areas, even at room temperature; Sitdikov and Kaibyshev [239] noted low-temperature twin DRX as a mechanism in Mg, alongside the early onset continuous and discontinuous DRX depending on the temperature). While such effects are not accounted for in the chosen SCP model, the overall temperature-dependent stress-strain behavior at all shown temperatures is captured adequately. This includes the typical reduction in yield stress and work hardening with increasing temperature.

Kang et al. [118] reported that pyramidal slip may be tightly related to dynamic recovery mechanisms in Mg. As the dislocations move across dislocation lines by double-cross slip, they lead to dislocation annihilation. This

increases the ductility of the material and reduces work-hardening. While the present SCP model does not capture recovery, the chosen temperature-dependent formulation reproduces the reduced work hardening with increasing temperature due to the strong decrease of the self- and crosshardening parameters.

In case C, the crystals are oriented with their c -axis perpendicular to the loading direction and hence show higher ductility. The model accurately predicts the stress-strain response of this case throughout the temperature range (see Fig. 3.10). Again, experimental data show discrepancies, yet predictions deviate less from experiments than in case A. The low hardening rates reported in experiments (and seen in Fig. 3.10) are captured by the strongly reduced self-hardening factors. Overall, the reduced model reflects the experimentally observed single-crystal response of Mg properly.

3.6.2.2 Temperature Dependence in the Full Model

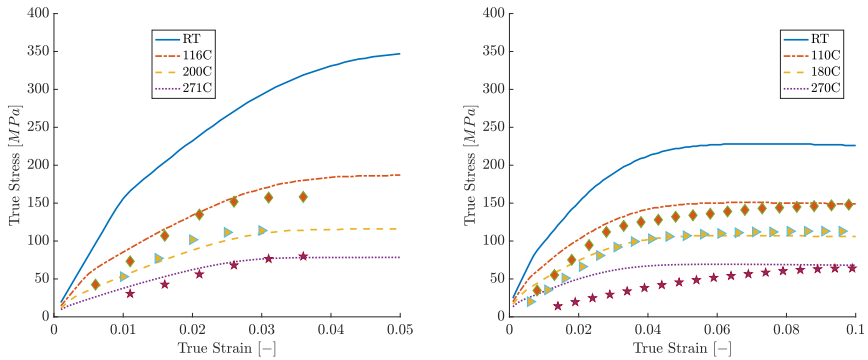


FIGURE 3.11: Temperature-dependent stress-strain response of Mg single-crystals, corresponding to cases A (left) and C (right). Solid lines are predictions by the *full* model, whereas the scatter plot represents the experimental data of Wonsiewicz and Backofen [19].

It is often assumed that CTs show a strong temperature dependence and are either more active [15] or less active [56] at elevated temperatures. The reduced activation barrier for pyramidal slip at elevated temperatures leads to the preferred activation of this slip mode over CT. Barnett [56], Barnett et al. [123], and Liu, Roy, and Silberschmidt [159] reported temperature dependence in the activity of twinning, notably the existence of a transition temperature for Mg and Mg alloys (around 450-475K in pure Mg, which

is affected by alloying elements), above which CT activity is reduced at the expense of other deformation modes, contradictory to the observations made by Wonsiewicz and Backofen [19], who observed an increase in CT activity under *c*-axis compression at all tested temperatures. The stress-strain curves for cases A and C are shown in Fig. 3.11. Surprisingly, the single-crystal curves obtained by Wonsiewicz and Backofen [19] show relatively strong softening in the initial region, which is in disagreement with temperature data from Chapuis and Driver [9] and polycrystal data from Ono, Nowak, and Miura [3].

With the full model, good agreement with experiments is obtained for the individual cases, except for case C at the highest temperature, where the initial hardening rates are overpredicted significantly. This may be attributed to the early onset of recrystallization in experiments (Wonsiewicz and Backofen [19] noted the presence of recrystallization, especially in twin bands), which is not captured by the model.

To highlight the predicted microstructure evolution, Fig. 3.12 shows the slip activities for case A at 271°C. For both models, the contribution of pyramidal slip increases with increasing temperature, indicating that the pyramidal systems tend to dominate the competition with CTs. The model agrees with the experimental observations of Barnett [56] and Khosravani et al. [238], who observed increased pyramidal activity. The reduced hardening also allows for higher levels of deformation to be accommodated by this deformation mode alone (compared to at room temperature). Nevertheless, CTs remain present in the full model (they may vanish at higher temperatures, but this is outside our scope).

In both models, prismatic slip dominates the deformation during case C at elevated temperature with only minor differences. In the reduced model, we attribute the predicted presence of pyramidal slip to the constrained *c*-direction, while TTs also contribute to the deformation at elevated temperature—in agreement with experimental observations by Wonsiewicz and Backofen [19]. However, TT is reduced to lower volume fractions than at room temperature. The full model shows a similar transition in deformation modes, with more slip activity on the prismatic systems and TT. Unlike at room temperature though, the pyramidal systems seem to be activated to offset the TT-induced elongation of the *c*-axis.

In conclusion, the full model captures the competition between the CT and pyramidal systems accurately across the examined range of temperatures, and a good correlation with the experimentally reported microstructural deformation modes is observed. In all cases, the CT volume fraction

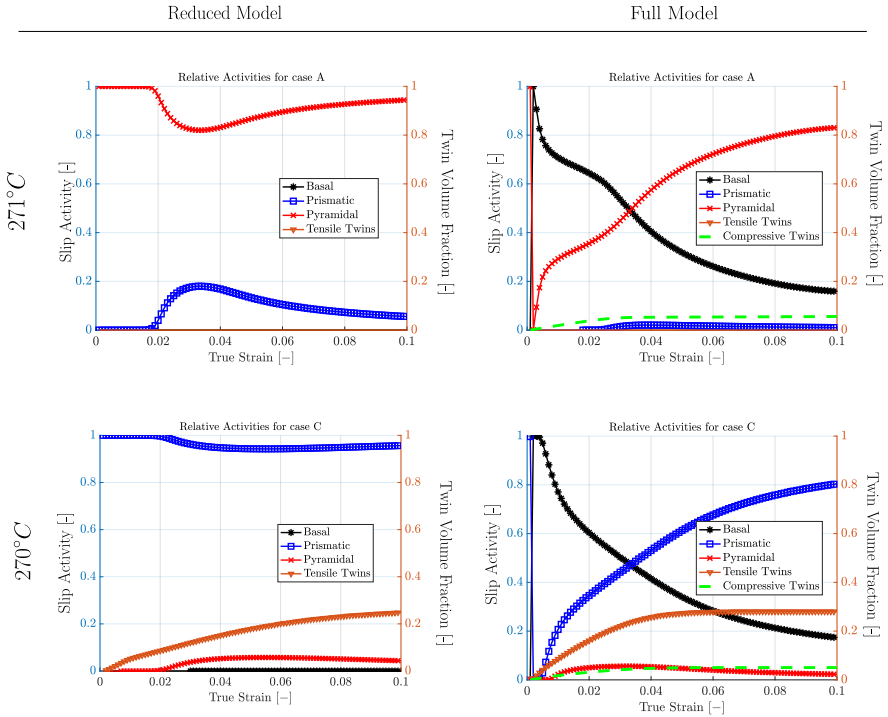


FIGURE 3.12: Relative activities of the slip and twin systems in Mg single-crystals for cases A at 271°C and C at 270°C . Results on the left were obtained from the reduced model, and results on the right from the full model.

remains small despite the included temperature dependence of their CRSS values and hardening parameters in the model. This hints at the fact that the CT systems may in fact not be temperature-dependent (the inclusion of temperature dependence in the model has no impact on the predicted deformation modes), but that their apparent temperature dependence in experiments is implicitly a result of the temperature-dependent pyramidal systems.

3.7 POLYCRYSTAL SIMULATIONS

Having calibrated the (full and reduced) models based on their single-crystal behavior, we now predict the temperature-dependent polycrystalline response at elevated temperature as a further means of validation in comparison with experiments Wonsiewicz and Backofen [19].

3.7.1 Taylor Model for Polycrystal Simulations

A simple mean-field, Taylor-type homogenization scheme is adopted to represent polycrystals in a highly efficient and parallelizable fashion. We note that, while efficiency is one of this method's key strengths, the Taylor model does not have an intrinsic length scale and does not account for detailed spatial variations on the grain level. Those could be captured by a (significantly more expensive) spatially-resolved model [12, 107]. The present model aims to efficiently provide an estimate for the effective, macroscale response of a large ensemble of grains on the microscale. We thus consider an ensemble of N grains on the microscale, each given a volume fraction $f_i \in [0, 1]$.

Furthermore, each grain is endowed with an initial crystallographic orientation, described by a 3D rotation tensor $\mathbf{R}_i \in \text{SO}(3)$, which defines the slip and twin systems within grain i in the global coordinate system as, respectively,

$$\mathbf{s}_{i,\alpha} = \mathbf{R}_i \mathbf{s}_\alpha, \quad \mathbf{m}_{i,\alpha} = \mathbf{R}_i \mathbf{m}_\alpha, \quad (3.25)$$

and

$$\mathbf{n}_{i,\beta} = \mathbf{R}_i \mathbf{n}_\beta, \quad \mathbf{a}_{i,\beta} = \mathbf{R}_i \mathbf{a}_\beta. \quad (3.26)$$

With each grain having internal variables $\boldsymbol{\eta} = [\boldsymbol{\epsilon}, \boldsymbol{\lambda}]$, we denote the set of all internal variables in the polycrystal by $\mathcal{G} = \{\boldsymbol{\eta}_1, f_1, \dots, \boldsymbol{\eta}_N, f_N\}$, and the set of all grain orientations is $\mathcal{R} = \{\mathbf{R}_1, \dots, \mathbf{R}_N\}$.

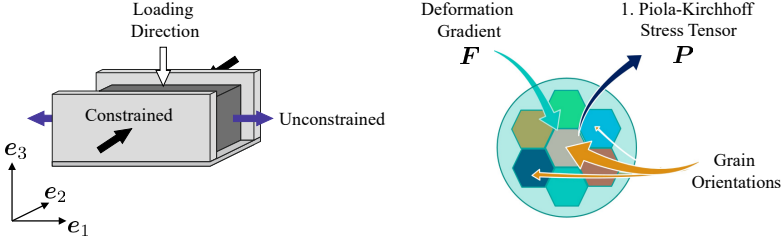


FIGURE 3.13: Schematic view of the Taylor model used for the extraction of the polycrystal response during channel-die loading with the indicated loading, constraint, and unconstrained free directions.

Following the Taylor assumption, each grain is subject to the same applied deformation gradient \mathbf{F} (hence expecting an upper bound on the effective, homogenized polycrystal response), see Fig. 3.13 for a visualization. We furthermore assume a uniform, constant temperature T across the polycrystal (thus neglecting the heat generated by plastic mechanisms under quasistatic loading). With the individual grain behavior given by the single-crystal model of Sections 3.2, 3.3 and 3.4, the response of the polycrystal is obtained from the volume fraction-weighted grain average, so the effective energy density reads

$$W_{\text{Taylor}}(\mathbf{F}, \mathcal{R}, \mathcal{G}) = \sum_{i=1}^N f_i W(\mathbf{R}_i \mathbf{F}, \boldsymbol{\epsilon}_i, \boldsymbol{\lambda}_i), \quad (3.27)$$

and the effective first Piola-Kirchhoff stress tensor follows as

$$\mathbf{P} = \frac{\partial W_{\text{Taylor}}}{\partial \mathbf{F}}. \quad (3.28)$$

3.7.1.1 Convergence of the Taylor Model

We first verify that the chosen Taylor model converges with increasing number of grains. We perform a set of 20 simulations with 24 to 200 grains, whose average stress-strain responses are shown in Fig. 3.14 (in comparison with experimental results from Kelley and Hosford [8]). The corresponding texture for the polycrystal simulations is shown in Fig. 3.15.

Initially, the grains show a purely elastic response, hence the close agreement of all curves at strains $\epsilon < 0.03$. For 24 and 50 grains, we observe a large spread in the stress-strain response, as individual grains can have a

significant impact on the average response. For 200 grains both convergence and a good approximation of the experimentally measured response are observed. We therefore deem a total of 200 grains sufficient and perform all following polycrystalline simulations with 200 grains, unless otherwise indicated.

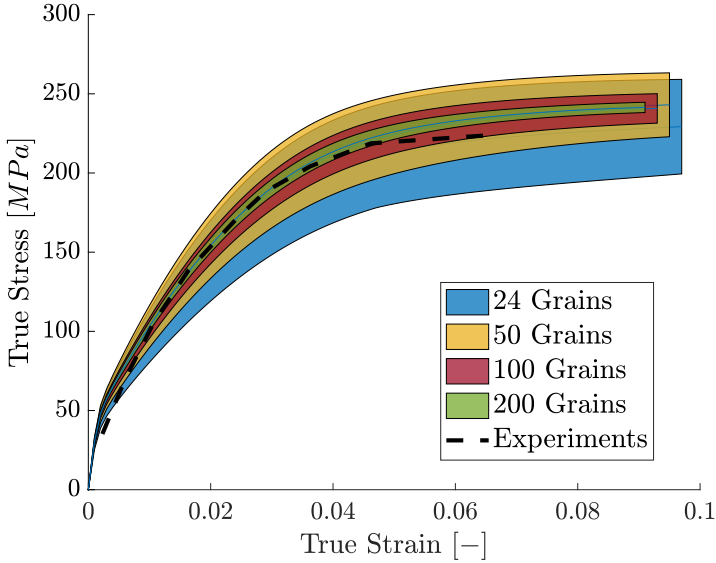


FIGURE 3.14: True stress-true strain response of textured polycrystals of pure Mg from experiments (dashed line) and from simulations with 24, 50, 100, and 200 grains simulated with the reduced model. Experimental data are from Kelley and Hosford [8].

3.8 MODEL VALIDATION

3.8.1 Textured Polycrystals at Room Temperature

Next, we perform channel-die simulations of textured polycrystals at room temperature. At room temperature, we simulate the cases labeled ZT, RT, and ZR among the experiments of Kelley and Hosford [8]. All grains are assumed to have identical volume fractions and initial orientations chosen to qualitatively match the pole figures reported by Kelley and Hosford [8],

as shown in Fig. 3.15. Fig. 3.15 confirms that the reduced model captures the stress-strain response of the textured polycrystals quantitatively well, with small deviations attributed to variations in the texture, experimental uncertainties, and the Taylor model's tendency to over-predict stresses.

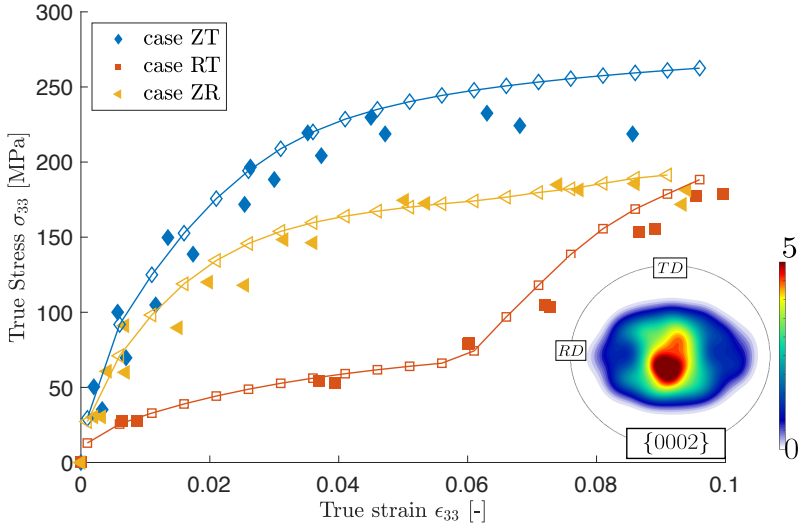


FIGURE 3.15: True stress vs. true strain response of textured polycrystals of pure Mg from experiments (markers) and from simulations with the reduced model (solid lines) at room temperature. The experimental data was obtained by Kelley and Hosford [8]. The *representative* texture utilized for the simulations is shown on the left and was chosen such as to approximate the texture reported by Kelley and Hosford [8].

In case ZT, most grains have their c -axes oriented along the loading direction while being constrained in the transverse direction. The stress-strain response resembles strongly that of single-crystal cases A and B (Fig. 3.5), yet with lower peak stresses. This is due to the non-ideal orientation of the crystals compared to cases A and B so that basal slip is favored in many grains [8]—especially in the Taylor model, grains with lower peak stresses reduce the average response.

Case RT represents compression along the rolling direction with a constrained transverse direction so that the c -axis of the majority of grains is allowed to extend. This configuration promotes significant amounts of twinning, whose reorientation of grains leads to a stiffened response at approximately 6%, analogous to single-crystal cases E and F. The transition in the homogenized polycrystal case is less sharp than for single crystals, as may be expected. Finally, case ZR imposes compression in the rolling direction with a constrained normal direction, i.e., the c -axis extension of

the majority of the grains is constrained. The resulting stress-strain curve is close to single-crystal cases C and D. (The same observations were made by Kelley and Hosford [8].) We conclude that the Taylor model captures the room-temperature response of textured polycrystals under different loading directions qualitatively and quantitatively well.

3.8.2 *Temperature-Dependent Response of Textured Polycrystals*

A comparison of simulation results with experimental polycrystal data at both room and elevated temperature is summarized in Fig. 3.16, using the experimental data of Wonsiewicz and Backofen [19]. These authors reported a texture that appears to be similar to Kelley and Hosford [8] but less pronounced. As no precise texture information was provided, we chose—based on the descriptions in Wonsiewicz and Backofen [19]—the one shown in Fig. 3.16. Wonsiewicz and Backofen [19] described the texture in their experiments as follows: “Under metallographic examination with polarized light, the material was found to be textured, somewhat diffusely but with $\{0001\}$ poles clustered around the sheet normal and spreading outwards by as much as 50° ”. We obtain the texture in Fig. 3.16 by assuming a normal distribution of the $\{0001\}$ poles around the normal direction with a standard deviation of 25° . Compression is applied along the normal direction (ND). The predicted stress-strain response of both (full and reduced) models agrees well with experiments.

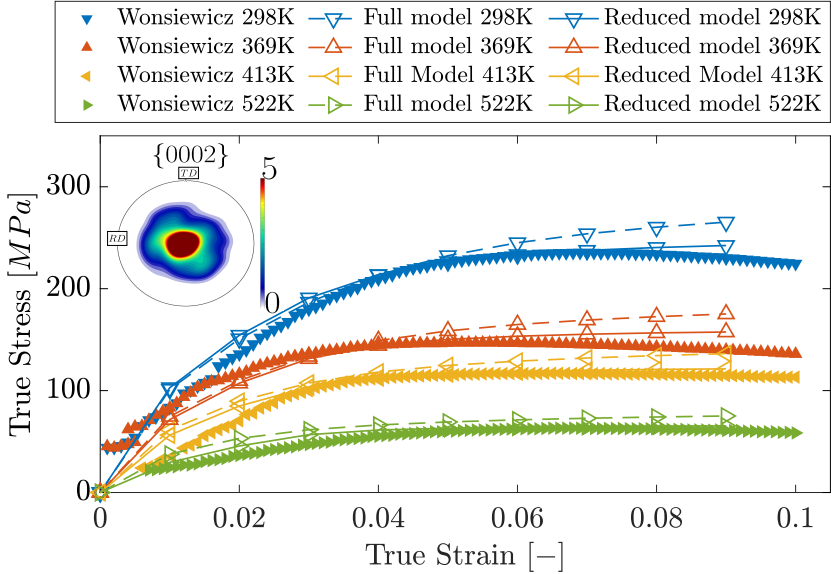


FIGURE 3.16: True stress-true strain response as obtained from polycrystal simulations, using the full and reduced models. Markers correspond to experimental data from Wonsiewicz and Backofen [19], solid lines show the response predicted by the reduced model, and dotted lines by the full model. The shown texture (used in simulations) was obtained by assuming a normal distribution with expectation value at the basal pole and outliers as far as 50° from the normal direction.

Most grains in this case are aligned with the ND (and hence similarly as in single-crystal cases A and B). The polycrystal exhibits relatively strong initial hardening in the plastic regime around 1%-3% strain, before the stress gradually plateaus. In comparison to the single-crystals, the the stress reaches its peak more gradually and the peak stresses are reduced, which stems from the influence of all other grains oriented away from the ND and contributing to the polycrystal response. At 25°C and 96°C , crystals in experiments were observed to show crack formation [19] at 7%-10%, which explains the reduction of stresses at that level of strain as compared to simulations (which do not model material failure).

Both models capture the incipient behavior up to 5% strain accurately, including the temperature-induced softening. At larger strains, experimental polycrystals showed cracks and strain localization [8, 19]. Further, effects such as grain boundary sliding may lead to softening. The Taylor model,

agnostic to those effects, consequently over-estimates stresses in the large-strain regime. It is, however, noteworthy that the full model generally predicts a higher stress level than the reduced model. We attribute this to the presence of CTs, which in turn harden the TT systems (one of the weakest deformation modes). The accuracy improves with elevated temperature, providing further evidence for this assumption. As the pyramidal systems become more prevalent, the hardening linked to CT has a smaller impact.

3.9 TEXTURE EVOLUTION IN MG

As a representative example, let us first study the texture evolution of a rolled sample of pure Mg under uniaxial compression along the rolling direction (RD). The initial texture of the polycrystal is chosen to mimic a typical rolled sheet of Mg, see Fig. 3.17, which shows a strong pole in the normal direction (ND).

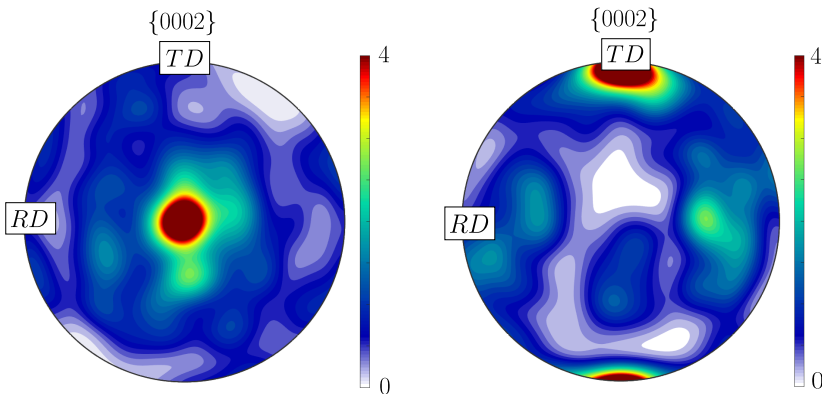


FIGURE 3.17: Texture of the undeformed (left) and deformed (right) polycrystal of pure Mg, simulated by the reduced model for the case of compression up to 30% true strain at 25°C. Initially a strong pole in the normal direction exists (left). After deformation, most grains are reoriented due to twinning, leading to a new, weaker texture with the pole in the transversal direction (TD) (right)

Assuming volume-preserving deformation due to small elastic strains and plastic incompressibility, we apply the deformation gradient

$$\mathbf{F} = \begin{bmatrix} (\dot{\epsilon}t)^{1/2} & 0 & 0 \\ 0 & (\dot{\epsilon}t)^{1/2} & 0 \\ 0 & 0 & \dot{\epsilon}t \end{bmatrix}$$

with strain rate $\dot{\epsilon} > 0$ and t denoting time, to the polycrystal model up to a true strain of 20%. At room temperature, samples are expected to show cracks at larger strains, hence setting a limit to the applied deformation. The simulated texture before and after deformation is compared in Fig. 3.17. The initially strong basal pole in the ND transforms into a weaker pole in the transverse direction (TD), capturing the essential feature of texture reorientation due to twinning and slip and qualitatively in agreement with observations made for AZ31B [5].

As a further example, we investigate the texture evolution during cold and hot asymmetric rolling. Rolling is assumed to be a superposition of compression and simple shear [147], so it can be simulated by applying the deformation gradient

$$\mathbf{F} = \begin{bmatrix} e^{\dot{\epsilon}t} & 0 & \alpha \cdot \dot{\epsilon}t \\ 0 & 1 & 0 \\ 0 & 0 & e^{-\dot{\epsilon}t} \end{bmatrix}$$

with a constant $\alpha = 3$.

We observe the formation of a split basal pole, which is slightly tilted towards the RD. The tilt is typical for the processing during asymmetric rolling, investigated here, and was reported similarly in experiments with commercially pure Mg by Beausir et al. [240]. As noted by Styczynski et al. [66], the texture evolution obtained from including basal, prismatic and pyramidal II slip as well as TTs in the Taylor model leads to the formation of a fibrous texture; similar results were obtained by Agnew, Yoo, and Tome [46] and Chang and Kochmann [107] in their rolling simulations. Here, we investigate the impact of CTs on the texture development of a polycrystal with 1000 grains and an initially randomized texture, comparing the cold-rolled textures with and without CTs. For both full and reduced models, the formation of a fibrous texture is observed (see Fig. 3.18). Most grains adopt an orientation close to the basal pole but split either way of the TD (the vertical axis). Similar trends were observed during numerical studies Agnew, Yoo, and Tome [46], Styczynski et al. [66], and Chang and

Kochmann [107] and in a less pronounced manner for certain Mg alloys in experiments Huang and Logé [85]. This indicates that the pyramidal systems are highly active [46, 66, 107]. Additionally, Styczynski et al. [66] discussed the influence of various deformation modes and reached the conclusion that the $\langle c + a \rangle$ -pyramidal systems play a major role in the splitting of the poles. They noted that a splitting of the basal pole in $\pm 15^\circ$ around the TD is commonly observed in AZ31, while Agnew, Yoo, and Tome [46] reported such a trend during processing of pure Mg. The same behavior has been observed for Mg-3Li alloys in the experiments of Agnew, Yoo, and Tome [46], further emphasizing the impact of precipitates and alloying elements on the texture evolution.

In their viscoplastic model, Agnew, Yoo, and Tome [46] found a similar behavior as Styczynski et al. [66] for the evolution of Mg sheets during rolling, yet they were able to mitigate it by increasing the CRSS of the pyramidal systems to effect an increased activity of basal and prismatic $\langle a \rangle$ dislocations.

As observed in the previous sections, CTs saturate due to self-hardening at relatively low strains. Therefore, during simulated rolling with an applied thickness reduction of up to 60%, the influence of the CT remains small. We therefore cannot observe a direct impact of the CT systems. Due to the early crack formation at low thickness reductions below 30% [241], cold-rolling of Mg is typically performed in multiple passes. Hence, for a better representation, the deformation during rolling must be applied incrementally, while accounting for thermal treatment in between passes, as is customary in industrial rolling processes. The present model cannot account for those factors. Further, in the case of a Taylor model, which is—adopting the wording of Styczynski et al. [66]—a “compatibility first” model, the texture evolution is severely impacted by the constraint of uniform deformation across all grains. A better agreement with experimental textures may hence be found by relaxing this constraint through another homogenization approach.

3.10 CHAPTER SUMMARY

The presented full and reduced models (with and without CTs) have obvious differences and limitations, which we briefly discuss here.

As the main difference, the single-crystal results highlighted the competition between the pyramidal II and the CT systems. Under c -axis compression, the reduced model can accommodate the deformation only via

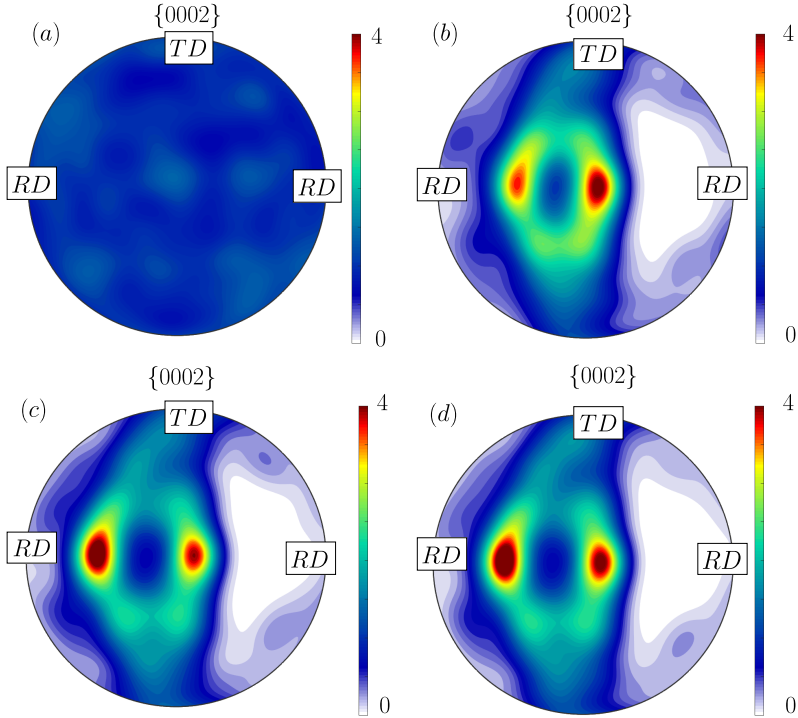


FIGURE 3.18: We show the textures of a polycrystal with 1000 grains. In (a), we depict the initial random grain orientations, whereas in (b) we show the cold-rolled texture, simulated by the reduced model. In (c) we show the hot-rolled texture predicted by the full model including CT, and in (d), the hot-rolled texture as predicted by the reduced model. The simulations were performed up to a total of 60% strain at a strain rate of $\dot{\epsilon}_{\text{true}} = 10^{-4} \text{s}^{-1}$ at a temperature of 25°C for the cold case and 270°C for the hot case

the activation of pyramidal slip, whereas the full model accommodated the early stages of plastic deformation via a combination of basal slip and CTs. Even though the effective stress-strain curves were similar, the underlying microstructural deformation modes differed substantially. In the full model, CTs were observed to saturate at relatively low strains, which is attributed to the slow kinetics of this system [108] as well as the strong self-hardening. With the saturation of CTs at low volume fractions, we infer that no viable

deformation modes are available, and while traces of pyramidal II slip may occur, the strong self- and cross hardening of this deformation mode as well as the pinning of $\langle c + a \rangle$ dislocations observed by Kang et al. [118] is what leads to significant basal slip suddenly occurring in the reoriented CT bands alongside $\{10\bar{1}2\}$ double-twinning, as observed in experiments by Wonsiewicz and Backofen [19]. The model captures such a behavior in essence. However, due to the lack of a failure criterion and the absence of double-twinning in the model, not all of the intricate microstructure evolution was captured. At elevated temperature, for both single- and polycrystals, the behavior changes [19, 123]. The apparent temperature dependence of CTs and even of TTs (Jain and Agnew [5] inferred that less twins overall are present in the material at higher temperature) can be explained by increased activity on the non-basal slip systems [123]. These observations suggest that CTs are a sub-optimal deformation mode, occurring in the absence of pyramidal II slip out of necessity to accommodate the flow criterion. In reverse, these findings also indicate that the activation of non-basal slip is what leads to the apparent temperature dependence of the CT systems and, further, could be the key to increasing the ductility of Mg.

Calibration of both models remains somewhat challenging, even at the single-crystal level, since the influence of each model parameter cannot be isolated and various deformation modes show similar stress-strain characteristics. The full model with its competition of c -axis modes proved to be more difficult to calibrate. Better agreement with experiments seems possible with an improved twin model, where the saturation of CT lies near the point of fracture. In addition, the presented full model likely understates the importance of CT mode by activating only a single twin system at a time. Nevertheless, the present assumption leads to a very good approximation for the TT systems and is hence unlikely to have a significant adverse impact. The inclusion of CTs in the model yields an overall hardening effect, as seen in Fig. 3.16. This is due to the twin-twin hardening of CTs on the TT mode—one of the easier-to-active deformation mechanisms to accommodate plastic deformation. Despite the challenges linked to including the CT systems, they play an important role on the microstructure evolution and require to be present for an accurate depiction of the material behavior.

We note that for both models a high self- and cross hardening is necessary for the pyramidal systems to capture the strong strain hardening. This observation can in part explain the nature of the ambiguity in experimental reports. Pyramidal II slip is clearly the best-suited deformation mechanism

to accommodate c -axis deformation, and hence it is not surprising that it should occur to some degree even at low temperature, as suggested by experimental results [3, 28]. The strong self-hardening, as well as the immobilization of $\langle c + a \rangle$ -dislocations noted by Kang et al. [118], however explain the scarcity of pyramidal II slip in some experimental observations. Further evidence for this hypothesis is found in observations by Lilleodden [25] who observes no CT formation during experiments and argues that CTs observed by Kelley and Hosford [8] and Wonsiewicz and Backofen [19] stem from preexisting nuclei and nucleation sites. Increasing the temperature leads to a higher activity of the pyramidal systems and thus to strain softening and an increase in ductility Chakkedath et al. [221]. Seeing that pyramidal slip provides a large number of possible deformation modes [118, 242] and considering the observations of Obara, Yoshinga, and Morozumi [21], Barnett [56], and Barnett et al. [123], pyramidal slip must be the dominant deformation mode at elevated temperature.

Model limitations lie in the simplified representation of the twins, which has implications on the accuracy of the twin predictions, as well as considering only the $\{10\bar{1}1\}$ CT variant. Further, the isostrain assumption for the Taylor polycrystal model is a strong approximation, which overpredicts local strains. While good agreement in the stress-strain data was observed, the texture evolution during rolling was not fully as expected in Mg (yet, this also depends on the chosen initial texture chosen for simulations). Further, the model does not capture (dynamic) recrystallization (DRX), whose nature in Mg is still not fully understood; see, e.g., Kecskes et al. [58], Sitdikov and Kaibyshev [239], and Kaibyshev [243] and references therein. Sitdikov and Kaibyshev [239] and Kaibyshev [243] argued that Mg exhibits multiple forms of DRX, beginning with twin DRX at lower temperature, followed by a mixture of continuous and discontinuous DRX at higher temperature. For the present models, these factors cannot be accounted for, and, as already noted by Wonsiewicz and Backofen [19], we have little understanding of their impact on the crystal behavior. There is, however, no doubt that at temperatures above 250°C recrystallization plays an important role, setting a natural upper limit to the present model and calling for models including DRX [59, 68, 84].

RECURRENT NEURAL OPERATOR DESCRIBING THERMOPLASTIC BEHAVIOR IN MG

This chapter has been adapted from **Hollenweger**, Kochmann, and Liu [244]. "Physics-Informed Crystal Plasticity RNN for Temperature-Dependent Anisotropic Plasticity in a HCP Material". *In preparation* (2023)

CHAPTER OVERVIEW

In the previous chapter of this Thesis, we introduced a temperature-aware CP model describing the plastic deformation and microstructure formation in Mg. We have shown its capabilities and its drawbacks and identified it as a suitable method for a vast range of applications. It offers a range of insights such as the type of deformation (slip, twin), texture evolution, and the stress-strain relationship. If included in a full-field method, it may also provide the user with local information about the stresses, deformation modes, and microstructure. It still suffers from a detrimental drawback, however, in terms of applicability in an ICMD setting. Despite the emphasis we put on efficiency, the computation of the plastic updates remains costly and a major bottleneck for ICMD integration.

In this chapter, we emphasize utilizing data-driven methods as a means to accelerate the computation in a multiscale setting. The chapter is structured as follows. First, we provide a short introduction to the problem and a reminder of the state of the art in section 4.1. We then introduce the proposed architecture in section 4.2. Next, we introduce the applied materials and methods, the data generation methodology and the training strategy in section 4.3, followed by the training performance of the surrogate in section 4.4. In section 4.5, we compare our architecture to existing models and discuss key features such as self-consistency before incorporating the surrogate into the commercial FEM software Abaqus/Explicit to showcase its versatility and utility in real-world applications. Finally, we provide a chapter conclusion and outlook for future work.

4.1 INTRODUCTION

Plasticity is commonly observed in engineering materials and plays a critical role in designing structures that are more durable, safer, and make efficient use of the materials. This is especially the case for metals, where plastic deformation is a crucial aspect of manufacturing and deformation processes as well as in component design. However, plasticity is a complex mechanism that is both path and history-dependent, making it challenging to model and understand, as we described in chapter 3. Plastic deformation and behavior during processing is especially important in a material-by-design approach, as it has severe implications on the properties of the finished parts. Hence, it is crucial to understand and represent the interrelationships appropriately. This is only possible with reasonably accurate and efficient models.

CP models, such as the one developed in chapter 3, have been extensively used to study and model plasticity in metals [4, 5, 12, 107, 108, 144]. These models have been used in applications such as CP-FEM, CP-FFT, and in combination with phase-field modeling, or mean-field techniques such as the VPSC model, the Taylor or the Sachs model as means to model material behavior and to investigate material properties and the microstructure evolution.

However, computing fully resolved CP-FEM or CP-FFT simulations in a computational material-by-design setting is prohibitively slow. The major drawback of most physically rooted simulations is their high computational cost, which becomes even more significant in multi-scale settings. Even the more efficient mean-field techniques, such as the Sachs or Taylor model still require too much computational effort to rapidly iterate through the solution space of process parameters and resulting material behaviors.

To address this issue, empirical mechanical models or physical reduced-order models were developed and are often employed [155]. These types of models, however, exhibit another drawback, in that they offer varying degrees of accuracy, depending on the degree of simplification. As a result, users face a trade-off between accuracy and computational efficiency (see e.g. Chang et al. [155]). Moreover, these models fare especially badly for materials exhibiting complex behavior such as anisotropy or twinning.

More recently, however, there has been a movement towards exploring the potential of data-driven methods (neural networks, mostly) in overcoming this trade-off [13, 76, 78]. We see tremendous potential in these methodologies and in the following provide a brief overview of this topic.

4.1.1 *State of the Art*

Generally, there are two main approaches to overcome the above-mentioned issue; directly representing the material's constitutive behavior via a neural network or accelerating certain aspects of the computation while keeping the physical structure of the model. Here and in the following, we call the latter approach an indirect approach. In this work, we focus on the micro- and mesoscale representation, where CP models find their application, as they provide a good compromise between accuracy and speed for modeling the microscale, however, the discussion can be extended to larger and smaller scales.

We begin our discussion with the indirect approach. Here, neural networks are used to learn a relationship between certain physical parameters. For instance, Ibragimova et al. [13] used fully connected neural networks (FCNNs) in an fcc material model for Al to accelerate the computation of costly constitutive updates, such as the evolution of slip and twin activity or the hardening laws in the CP model. The approach uses an artificial neural network to map the CRSS values of the slip systems, τ , the hardening factors h , the texture a , and the initial strain rate D to the updated texture, the stress, and variables associated with the CP model, g , and γ

$$\mathcal{F}_{\text{ANN}} : \{\tau, h, D_{ij}^n, a_{ij}^n\} \mapsto \{g, \sigma_{ij}^{n+1}, a_{ij}^{n+1}, \gamma\}. \quad (4.1)$$

These computations often exhibit stability-related constraints in CP models, therefore using a neural network to learn the relations is extremely valuable to circumvent these limitations and to allow for faster computation. At the same time, neural networks are especially efficient to compute, as they consist of highly parallelizable computations, in contrast to mostly serial computations in physical modeling. The training of their model, however, required almost 1.5 million samples for training, a vast amount of data that needs to be generated in an efficient manner. This requirement alone poses a challenging task and threatens the viability of such an approach. Another successful example of the indirect approach was provided by Sun et al. [245], who used FCNNs to predict the microstructure evolution in an fcc constitutive model that was trained on CP simulation results.

In contrast to the indirect approach lies the direct approach to learning the constitutive response of the models. This removes the need for a physical model and the computation of physically meaningful equations in the first place by learning a representation of the constitutive behavior via a neural network directly. The result is, mathematically speaking, a map,

that maps measures from one space (the input space) into another space (the results space). For instance, Al-Haik, Hussaini, and Garmestani [65] used a 3-layer FCNN to predict creep-stress in composites by accounting for temperature, strain, and time as input values. This approach maps the strain, the temperature, and the time in the input space to the creep stress in the output space,

$$\mathcal{M} : \{\epsilon \in \mathbb{R}^{d \times d}, T \in \mathbb{R}, t \in \mathbb{R}\} \mapsto \sigma_{\text{creep}} \in \mathbb{R}^{d \times d}, \quad (4.2)$$

with dimension d . Zhang and Mohr [246] later managed to represent Von Mises plastic behavior with a similar neural network based solely on the strain.

Despite these initial successes, modeling plasticity with FCNNs has severe limitations. Plasticity is inherently a history-dependent process, notably reliant on past deformation history. These architectures still require prior knowledge about the nature of the plastic process or input of the plastic flow and hardening, notably they require the plastic strain. This measure is not normally readily available but computed "on the fly" during the deformation process. For instance, Zhang and Mohr [246] pass the plastic strain as an input and compute it externally, since it is not a measure that their architecture can inherently learn. While this may be feasible in a J2 model, it is a costly matter for more complex material models. Another drawback lies in the resolution and rate dependence of these methods, as observed by Zhang and Mohr [246]. Additionally, this approach typically fails for more sophisticated plasticity models.

Hence, in order to directly learn the constitutive behavior of plastic materials, recurrent neural networks (RNNs) are more frequently utilized. They learn to predict a series of states (stresses, plastic strains, etc.) of the material in a recurrent manner; the new state is predicted from the current and/or previous states. As such, these architectures are inspired by other fields, notably natural language processing, that deal with serial inputs and outputs.

Long short-term memory (LSTM) cells, introduced by Hochreiter and Schmidhuber [194], or gated recurrent units (GRU) introduced by Chung et al. [195] are commonly employed to model plastic behavior [78, 80, 210, 247, 248]. For example, Yu et al. [80] showed the capability of LSTM and GRU models to predict plastic behavior for J2-plasticity without the need for the plastic strain as an input. Instead, the architecture carries the information in its own "hidden" state. In another study, Mozaffar et al. [78] used GRUs to model the three-dimensional path-dependent stress in elastoplastic

materials, and Gorji et al. [247] showed that a GRU-based model could capture the constitutive response of a homogeneous anisotropic hardening (HAH) 2D material. Further, Abueidda et al. [210] showed the capability of these architectures to capture complex, thermoplastic material behavior. They also noted, however, that these architectures are slow in training, rather inefficient for the task at hand. Therefore, they introduced a temporal convolutional network architecture to circumvent the issues and increase the efficiency and even the quality of the prediction. Finally, Ghavamian and Simone [248] demonstrated that RNNs with LSTM cells could learn the viscoplastic behavior of a relatively simple Perzyna viscoplasticity model and thus accelerate FE² computations by bypassing the need for the evaluation of the plastic constitutive model. In a bid to increase the generality of their surrogate model to multiple strain rates, the authors interpolated between results that were trained at different strain rates. They re-trained the NN on varying strain rates and managed to show decent agreement with the ground truth. Nevertheless, the temporal and spatial resolution dependence still poses a challenge for many applications.

In general, however, these architectures are no natural choice to capture physical processes in plasticity, as they were developed for natural language processing tasks. These problems typically contain serial input, such as text or a voice recording, however, these series are typically non-Markovian. Markovian refers to a process that fulfills the Markov property, meaning that the probability of future states of the process, given the present state and all past states, depends only upon the present state, and not any past states in addition to that. In simpler terms, in a Markovian process, the next state of the process only ever depends on the current state of the process, if that state describes the problem perfectly. In conventional plasticity models, one often assumes that all of the information describing the constitutive behavior is encoded in a set of internal variables *at each given time*. The entire history of the deformation is stored in these internal (or state) variables. This is in stark contrast to applications in natural language processing, where the meaning of a sentence depends on the location of individual words that additionally hold different weights to the overall meaning. In architectures such as the LSTMs and GRUs, this led to the development of gate functions that are trained to store long-past information, such as to account for these necessities. In applications for plasticity, however, these additional gates and the trainable weights associated with the capability to store long-past information lead to inefficiencies and long training times.

So while it is evident that LSTMs and GRUs are extremely versatile, they struggle with capturing plastic behavior *efficiently* [76]. These models require a vast number of parameters, leading to overly complex models that further lack interpretability [75, 76]. Further, the gate functions in GRUs and LSTMs, lead to an additional issue. The gates were developed to deal with sequential input of the same frequency – word for word. Hence, these architectures only perform well in applications, where the input (e.g. the strain) is provided in uniformly spaced chunks (for instance one input per second of simulation time). This is a severe limitation for surrogate modeling. For numerous reasons, it is advantageous to have varying time increments. Consider for instance dynamic impact as a scenario, where time resolution around the time of the impact is much higher than prior and after.

Therefore, customized and specialized approaches for plasticity were introduced. A prominent approach was shown in Bonatti and Mohr [76], which is known as the minimal state-cell (MSC) architecture. The MSC architecture directly maps the (plastic) deformation to the (deviatoric) stress and learns the evolution of state variables "on the go" via GRU-inspired update gates. Furthermore, the MSC approach enables the identification of a set of minimal state variables, from where it draws its name. This feature is a significant step up from the non-interpretable states in LSTMs and GRUs. It was exemplified by Bonatti and Mohr [76] in a recent study, where they utilized a large amount of data obtained from single-element simulations to predict the deviatoric stress response of various materials, encompassing different hardening types and effects such as the Mullins and Bauschinger effects from (relatively simple) underlying material models. The MSC identified the number of state variables required for each material, corresponding to the state variables of the phenomenological models used in training plus the five plastic strain components [76]. The approach was later used by Bonatti, Berisha, and Mohr [75] to capture the homogenized response of an fcc material, albeit with inconclusive results pertaining to the number of *required* internal state variables. In its original form, the MSC approach still depends on the training resolution. This issue was addressed by Bonatti and Mohr [83] in later work on the importance of self-consistency in surrogate models. The goal of their work lies not in providing an entirely temporal resolution independent formulation, but at least in guaranteeing consistency under refinement of the path sampling frequency along the time series. Their approach to self-consistency (i.e. validity across varying input frequencies) relies on constraining the gated transition functions. However,

there is no guarantee that the selected transition function is correct or works in a general sense for a wider range of problems [83].

4.1.1.1 *Problem Statement*

Hence, despite the potential shown by the introduced methods, their use comes with significant drawbacks and challenges. LSTMs and GRUs suffer from inefficient training behavior and high complexity as well as a lack of interpretability. MSCs and linearized MSCs are a significant improvement and allow (some) interpretation of the state variables. Further, they have begun to address the issues relating to self-consistency that pose a major shortcoming to the application of RNNs as surrogate models.

An additional obstacle is the need for a considerable amount of data to train models accurately, which can be both costly and difficult to obtain. Further, the requirement for more data increases with the complexity of the material behavior. Moreover, data-driven approaches may struggle to generalize beyond the conditions of the training data, emphasizing the importance of selecting representative datasets carefully. Overfitting the training data can lead to poor model performance when applied to new data, and the accuracy of data-driven models may depend on the quality and representation of the data used.

A commonality to all of these approaches further lies in the complexity of the modeled behavior. Most applications are limited to relatively simple material behavior and models. This is problematic for our goal of developing novel Mg-based materials. In fact, the vast majority of ML surrogate models have so far focused on either capturing the homogenized, often isotropic, response of a material or learning the behavior of phenomenological constitutive models with limited physical accuracy and complexity. Such models do not require a large state space and are often described via an equivalent plastic strain measure ϵ_p [76, 78] or simple hardening laws [248]. More recently, CP-RNN surrogates were introduced for single and polycrystals of fcc materials, such as by Bonatti, Berisha, and Mohr [75]. In their case the capability of the MSC to identify an exact number of state variables and any potential meaning collapsed, exposing the limitation of this architecture.

4.1.2 *Proposed Solution*

Hence, we identified the following opportunities for research in the field. First, we aim to seamlessly integrate self-consistency into the model for-

mulation, without the need for cumbersome modulation functions. To this end, we build upon another approach, based on the Markovian model, introduced by Bhattacharya et al. [79]. We describe our proposed architecture in section 4.2.

Second, we aim to learn more complex mechanical behavior at the micro-mesoscale and Mg lends itself as a good candidate due to the pronounced plastic anisotropy it exhibits, even on the polycrystal level. Further, the impact of twinning poses an intriguing challenge to ML applications, due to the nonlinearity it introduces to the behavior of the material. Further, as shown in chapter 3, the material exhibits a strong temperature dependence that alters its mechanical response substantially, leading to a more isotropic response. The thermomechanical interplay of Mg's deformation modes and linked plasticity still poses a challenge to scientists [5, 52, 122, 232], as discussed in chapter 3. In a recent publication, Eswarappa Prameela et al. [1] outlined a fully integrated computational framework for the design of Mg-based materials. For such an application, a good surrogate capable of representing such complex material behavior is of high interest.

4.2 BACKGROUND AND PROPOSED ARCHITECTURE

We consider a heterogeneous body occupying the region $\Omega \in \mathbb{R}^d$, in $d = 2, 3$ dimensions in the reference configuration, whose state is entirely defined by a set of internal variables, ξ . We are interested in the coupled thermomechanical analysis. Let us denote by $\mathbf{u} : \Omega \mapsto \mathbb{R}^d$ the displacement field, by $T : \Omega \mapsto \mathbb{R}$ the temperature field within the body, and by $\mathbf{F} = \mathbb{I} + \nabla \mathbf{u}$ the deformation gradient. This formulation is consistent with our formulations in chapter 3, however, we reformulate our relations here for consistency with the customary formulations in the literature of the field.

As before, the constitutive relation is expressed as a function of the (Cauchy) stress, $\boldsymbol{\sigma}$, the heat flux \mathbf{Q} . Further, we assume a kinematic relation $\mathbf{K}(\mathbf{F}, T, \boldsymbol{\xi}, \dot{\boldsymbol{\xi}})$ that describes the evolution of the internal variables. Further, we introduce an energy function $U(\mathbf{F}, T, \mathbf{Q})$ comprising the external heat, the stress power, and any contributions due to the dependence of the internal energy on quantities other than temperature. Finally, let $\rho : \Omega \mapsto \mathbb{R}$ and $c : \Omega \mapsto \mathbb{R}$ denote the density and specific heat, respectively.

Given initial conditions (ICs) $\mathbf{u}_0, v_0, T_0, Q_0$ at time $t = 0$ and boundary conditions (BCs) $\hat{\mathbf{u}}, \hat{v}, \hat{T}, \hat{Q}$, on the boundary $\partial\Omega$, the displacement \mathbf{u} ,

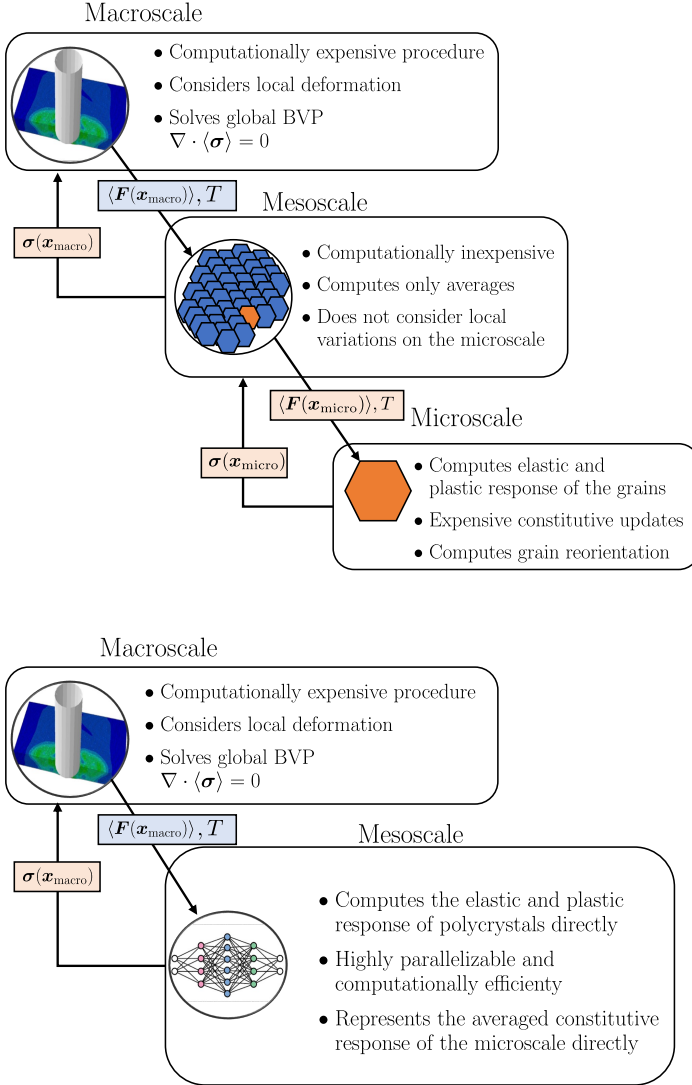


FIGURE 4.1: Graphical representation of the surrogate model in a multiscale setting. On the top, a graphical representation of a multiscale model with a FExTaylor Ansatz is shown, where the macroscopic BVP is solved via the FEM, and the mesoscopic representation is given by the Taylor mode, comprising the average of numerous grains. On the bottom, we show the same multiscale model, however, we have replaced the Taylor model with a data-driven surrogate.

temperature T , and internal variable ξ are given by the solution of the system of equations

$$\nabla \cdot \boldsymbol{\sigma}(\mathbf{x}, \boldsymbol{\xi}, T, t) = \rho \ddot{\mathbf{u}}(t) \quad \text{on } \Omega \quad (4.3)$$

$$\nabla \cdot \mathbf{Q}(\mathbf{x}, T, t) + r(T, t) = \rho c_p \dot{T} \quad \text{on } \Omega \quad (4.4)$$

$$\mathbf{K}(\mathbf{F}, \boldsymbol{\xi}, T, t) = \mathbf{0} \quad \text{on } \Omega \quad (4.5)$$

$$\mathbf{u}(\mathbf{x}, 0) = \mathbf{u}_0(\mathbf{x}), \quad \dot{\mathbf{u}}(\mathbf{x}, 0) = \mathbf{v}_0(\mathbf{x}) \quad \text{on } \Omega \quad (4.6)$$

$$\boldsymbol{\xi}(\mathbf{F}, 0) = \boldsymbol{\xi}_0(), \quad T(\mathbf{x}, 0) = T_0(\mathbf{x}) \quad \text{on } \Omega \quad (4.7)$$

$$\mathbf{u}(\mathbf{x}, t) = \hat{\mathbf{u}}(\mathbf{x}, t) \quad \text{on } \partial\Omega_{Du} \quad (4.8)$$

$$\boldsymbol{\sigma}(\mathbf{x}, t)n(\mathbf{x}) = \hat{\mathbf{s}}(\mathbf{x}, t) \quad \text{on } \partial\Omega_{Ns} \quad (4.9)$$

$$T(\mathbf{x}, t) = \hat{T}(\mathbf{x}, t) \quad \text{on } \partial\Omega_{Dt} \quad (4.10)$$

$$\mathbf{Q}(\mathbf{x}, t) = \hat{\mathbf{q}}(\mathbf{x}, t) \quad \text{on } \partial\Omega_{Nq}, \quad (4.11)$$

where we denote the Neumann and Dirichlet boundaries by N_* for the respective fields. In this extended, coupled BVP, the conservation of linear momentum (4.3) and the heat equation (4.4), respectively are described. The kinetic relation that describes the evolution of internal variables is given in (4.5).

A solution to this problem may be found in various manners, e.g. via the finite element method or the spectral method, both introduced in chapter 2. This would lead to learning a microscopic constitutive closure relation, linking the local microscopic deformation gradient $\mathbf{F}(\mathbf{x}, t)$ and the local temperature $T(\mathbf{x}, t)$ to the stress, $\boldsymbol{\sigma}(\mathbf{x}, t)$, and the heat flux, $\mathbf{Q}(\mathbf{x}, t)$, via a general map

$$\psi : \{\mathbf{F}(\mathbf{x}, t), T(\mathbf{x}, t) : t \in (0, t_{\max})\} \mapsto \{\boldsymbol{\sigma}(\mathbf{x}, t), \mathbf{Q}(\mathbf{x}, t)\}. \quad (4.12)$$

The evaluation of the mapping ψ , however, involves the repeated solution of the coupled thermomechanical RVE problem, as defined above, for each time t and macroscopic point \mathbf{X} . This process is notorious for its prohibitive expense and hence not viable for data generation. Another issue arises from a physical perspective, in the sense that it is uncertain whether a finite set of internal variables can encapsulate the dependence of stress on both deformation and thermal history at the macroscopic scale, although conventional empirical-based models, such as the Johnson-Cook model, tend to posit that ψ can be approximated with internal variables primarily dependent on the deformation history, as opposed to the thermal history. Solving this problem with a surrogate, however, would involve the costly solution of the given boundary value problem on the domain Ω

with numerous degrees of freedom and high dimensional input and output values, requiring tremendous amounts of computing power and data for training.

Hence, in this work, we omit this calculation and instead operate under the Taylor assumption from chapter 3 and assume homogeneity of the deformation on the microscale. Further, we assume that the dependency of the thermal flux, Q , on the strain and thermal history, is known a priori and that temperatures are uniformly distributed within the sample – a fair assumption given that we investigate polycrystals on a mesoscopic scale and large thermal variations are not expected at this scale. Our focus thus solely lies on the examination of the strain and thermal dependency of the *averaged* stress response.

4.2.1 Recurrent Neural Operator

As a result, we narrow our attention to a reduced map ψ^\dagger ,

$$\psi^\dagger : \mathbf{F}(t), T(t) : t \in (0, t_{\max}) \mapsto \boldsymbol{\sigma}(t), \quad (4.13)$$

independent of the position \mathbf{x} .

We address the problem with an RNO architecture such as the one proposed in Liu et al. [14] and Bhattacharya et al. [79], where we extend the original formulation to incorporate the thermal history. We assume that a relationship between the evolution of the state variables and the deformation exists that can be described by a function \mathcal{G} , and that a similar relationship exists between the state variables and the stress, denoted by a function \mathcal{F} . This is, essentially, the same assumption as previously made for the CP model in chapter 3, where we first define an evolution law for the internal variables, followed by the definition of an energy density function relating the deformation as well as the current internal variables to the stress.

Further, we exploit our description of the stress as $\boldsymbol{\sigma}$, which allows us to decompose the tensor into two parts as follows

$$\boldsymbol{\sigma}(\mathbf{F}, T) = \sigma^h(\det(\mathbf{F}), T)\mathbf{I} + \boldsymbol{\sigma}^{dev}(\mathbf{F}, T), \quad (4.14)$$

where $\sigma^h = \frac{1}{3}\text{tr}(\boldsymbol{\sigma})$ denotes the hydrostatic pressure, $\boldsymbol{\sigma}^{dev} = \boldsymbol{\sigma} - \sigma^h\mathbf{I}$ is the deviatoric stress and \mathbf{I} the identity tensor. In the following, we assume that only the deviatoric component of the stress depends on the state variables, whereas the hydrostatic pressure has no history dependence and

is simply a function of the temperature and the volumetric change, denoted by $J - \det(\mathbf{F})$. We thus obtain a description for ψ^\dagger as

$$\psi^\dagger \approx \psi_r^{dev} + \psi_r^h, \quad (4.15)$$

where we approximate both components with neural networks. The first term, ψ_r^{dev} is represented via an RNO that consists of two FCNNs $\mathcal{F}^{dev} : \mathbb{R}^{d \times d} \times \mathbb{R} \times \mathbb{R}^m \mapsto \mathbb{R}^{d \times d}$, and $\mathcal{G}^{dev} : \mathbb{R}^{d \times d} \times \mathbb{R} \times \mathbb{R}^m \mapsto \mathbb{R}^m$, such that

$$\begin{cases} \sigma^{dev}(t) = \mathcal{F}^{dev}(\mathbf{F}(t), T(t), \{\xi_\alpha^{dev}(t)\}_{\alpha=1}^m), \\ \dot{\xi}_i^{dev}(t) = \mathcal{G}_i^{dev}(\mathbf{F}(t), T(t), \{\xi_\alpha^{dev}(t)\}_{\alpha=1}^m) \quad i = 1, \dots, m, \end{cases} \quad (4.16)$$

where $\xi^h \in \mathbb{R}^l$ are internal variables that we seek to define through the training. Similarly, we construct a second network, ψ_r^h , consisting of a FCNN, $\mathcal{F}^h : \mathbb{R} \times \mathbb{R} \times \mathbb{R}^l \mapsto \mathbb{R}$ such that

$$\sigma^h(t) = \mathcal{F}^h(\det(\mathbf{F}(t)), T(t), \{\xi_\alpha^h(t)\}_{\alpha=1}^l). \quad (4.17)$$

4.2.2 Time Discretization and Operator Architecture

We note that \mathcal{G} is chosen such to predict only the *rate of change* of the state variables, i.e. it represents an evolution law, compared to e.g. in the MSC or GRU architectures, where the new state is learned directly. This formulation has an interesting advantage. It allows the RNO to be trained with data from arbitrary temporal discretization. Given a sequence of input functions $\{F^\alpha, T^\alpha; \alpha \in \{0, \dots, N\}\}$ discretized with time step Δt , we construct the RNO, ψ_r^{dev} , using a forward-Euler integration scheme:

$$\begin{cases} \sigma^\alpha = \mathcal{F}^{dev}(\mathbf{F}^\alpha, T^\alpha, \{\xi_{\alpha,j}\}_{j=1}^m), \\ \xi_{j,i}(t) = \xi_{j,i}^{n-1}(t) + \Delta t \mathcal{G}_i(\mathbf{F}^\alpha(t), T^\alpha(t), \{\xi_{\alpha,j}(t)\}_{j=1}^m), \quad \text{for } j = 1, \dots, m. \end{cases} \quad (4.18)$$

Figure 4.2 (a) provides a graphical representation of the RNO architecture. The networks \mathcal{F} and \mathcal{G} comprise four fully connected layers with Scaled Exponential Linear Units (SELU)[249] activation function.¹

To test the effectiveness of our model, in section 4.5.2, we compared it with classical neural networks based on Gated Recurrent Units (GRU) and Long

¹ Although ReLU is typically the default choice for a hidden layer's activation function, we achieved better results with SELU. We also tested the hyperbolic tangent and sigmoid functions but with limited success.

Short-Term Memory (LSTM) units which have been explored in previous studies for constitutive modeling [80]. the GRU and LSTM architectures follow a simple setup. We take four GRU (or LSTM, respectively) layers, followed by a single FCNN layer that translates the output of the gated cells to the six stress components. In doing so, we essentially follow the approaches in Yu et al. [80] and Bonatti and Mohr [76]. For completeness, we included the detailed GRU and LSTM architectures that we examined in Figure 4.2 (b) and (c) respectively.

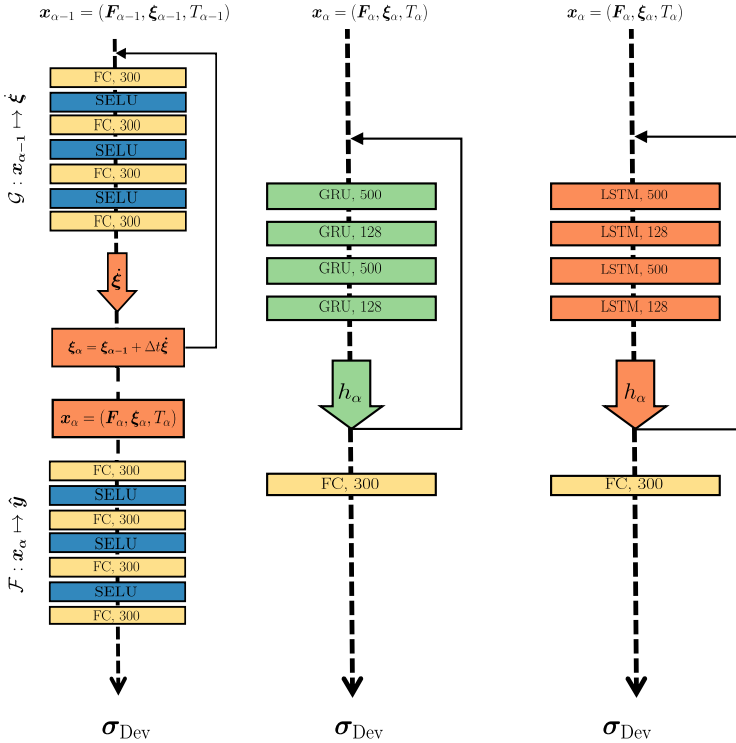


FIGURE 4.2: From left to right we show the schematic of the RNO architecture, as well as the the GRU- and the LSTM-based networks that were used for comparison.

4.2.3 Internal Variables and Markovian Description

The RNO model is an approximation [203] of the mapping ψ^\dagger that takes the deformation and temperature $\{\mathbf{F}(t), T(t)\}, 0 \leq t \leq t_{\max}$ as inputs. It contains map \mathcal{G} , charged with the identification of (internal) state variables $\xi = \{\xi^{dev}, \xi^h\} \in \mathbb{R}^{m+l}$ that encapsulate the memory/history of the thermal and deformation path at each time. Consequentially, at any time $t \in (0, t_{\max})$, the evaluation of the RNOs only require known inputs $\{\mathbf{F}(t), T(t), \xi(t)\}$, thus fulfilling the Markovian condition. In this work, we assume the existence of the internal variables but do not make any assumptions about the number of the internal variables, nor their evaluations a-priori. Instead, we train the RNO with different numbers of internal variables and seek to interpret their physical meanings from the trained networks. We discuss this in detail in section 4.5.3. This means that we require a training function for the evolution of the state variables in one way or another.

4.2.4 Loss Function

The train and test error is computed as the error over all time steps and over all samples of the testing and validating sets with the loss function given by

$$E = \frac{1}{N_s} \sum_{n_s=1}^{N_s} \sum_{\alpha=0}^N \left(\frac{(\sigma_{n_s}^{\text{truth}}(t^\alpha) - \sigma_{n_s}^{\text{approx}}(t^\alpha))^2}{(\sigma_{n_s}^{\text{truth}}(t^\alpha))^2} \right), \quad (4.19)$$

with N_s samples and N time steps of the discretization. We observe that this loss function does not provide any information regarding the internal variables ξ . Hence, in the current architecture, internal variables, and their evolution laws are learned implicitly in an unsupervised manner, based solely on the performance of the network to capture the constitutive behavior.

4.3 MATERIAL AND METHODS

Our ultimate goal is to learn and represent the thermomechanically coupled response of the mesoscopic material. However, the presented RNO has never been tested for materials exhibiting the level of anisotropy found in Mg, nor for thermal effects. Hence, we take a step-by-step approach. First, we evaluate the capability of the RNO to represent the twin-dominated response of

Mg appropriately. This is followed by an extension to a temperature-aware description containing constant temperatures, such as the ones described in chapter 3 as well as arbitrary temperature paths for a more general applicability of the method.

For each of the cases, we follow the same steps. A training dataset is generated via the CP model described in chapter 3. The dataset is divided into training (85%), and testing (15%) portions. Separate data sets are used for validation, as shown in Table 4.1. If the RNO appropriately manages to represent the constitutive response at the given stage, i.e. if the validation and testing errors are small and there is good agreement with the ground truth, we expand the problem to the next stage.

In this section, we provide a detailed overview of the data generation process. First, we introduce the nomenclature that we chose to provide unique descriptors of the datasets and trained RNOs. We then provide our data generation strategy, followed by the training strategy.

4.3.1 Data Generation

We aim to learn the Taylor-homogenized response of a polycrystalline sample on the mesoscale. To ensure the applicability of our surrogate to a wider range of anisotropic materials, we require that even the averaged response exhibits a pronounced level of anisotropy. To this end, we use the reduced model, introduced in chapter 3, and a Taylor model representing 200 grains with a strong basal texture. The resulting stress-strain curves obtained from uniaxial tension and compression along the main directions are shown in Figure 4.3 (a) and (b) and the texture in 4.3 (c). The reduced version of the model leads to a representation of the deformation with a total of 18 deformation modes (three basal slip modes, three prismatic slip modes, six pyramidal II slip modes, and six tensile twin modes), shown in Figure 4.3 (d). All samples we refer to in the following were obtained with this configuration.

4.3.1.1 Training and Test Data

The training and testing data is generated by repeatedly computing the Taylor model response to varying deformation and temperature paths (histories), such as to obtain various realizations of the mapping ψ^\dagger . Hence, we first generate a series of deformation paths (in the form of deformation gradients) and associated temperature paths in Matlab. Details for the generation of strain and temperature paths are given in sections 4.3.1.4

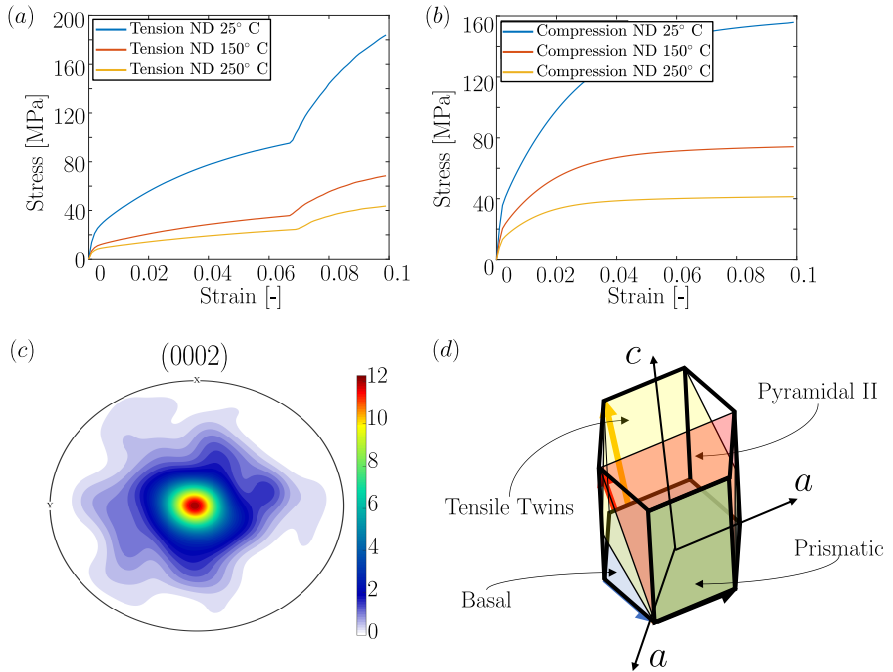


FIGURE 4.3: Depiction of the stress-strain response of the Taylor model that was chosen as the ground truth for the data generation. We show results in ND tension in (a) and in ND compression in (b). The strong basal texture we chose for our polycrystals is depicted in (c), and the deformation modes present in the reduced crystal plasticity model in (d).

through 4.3.1.7. Each deformation path consists of 10,000 increments that are further linearly interpolated to attain a total of 100,000 strain increments for the Taylor model. The time step between each increment is 10^{-3} seconds, hence the total simulation time is 100 seconds. There is no constraint on the amount of deformation within an increment, which leads to light variations in the strain rate along the strain history. The deformation gradients are subsequently applied to the Taylor model, previously introduced in chapter 3. We assume all entries are constrained and prescribed by the deformation pathways, hence there is no need to solve any boundary conditions. This assumption significantly reduces the computation time. For the grains in the Taylor model, a dominant texture in the normal direction with random rotations around the crystal's c -axis was chosen, as shown in Figure 4.3(c). This choice emphasizes the anisotropy commonly observed in Mg single and polycrystals, while mitigating the non-linearity due to twinning slightly, compared to the single crystal case.

While the initial texture significantly impacts the polycrystal's behavior [8, 19, 32, 232], exploring this added complexity falls beyond the scope of this study. Therefore, an *exactly* identical initial texture is selected for each of the polycrystalline samples. The texture is described via an initial 3D rotation tensor $\mathbf{R}_i \in \text{SO}(3)$. This rotation defines the slip and twin systems in each grain, denoted by subscript i , relative to the global coordinate system as

$$\mathbf{s}_{i,\alpha} = \mathbf{R}_i \mathbf{s}_\alpha, \quad \mathbf{m}_{i,\alpha} = \mathbf{R}_i \mathbf{m}_\alpha, \quad (4.20)$$

and

$$\mathbf{n}_{i,\beta} = \mathbf{R}_i \mathbf{n}_\beta, \quad \mathbf{a}_{i,\beta} = \mathbf{R}_i \mathbf{a}_\beta, \quad (4.21)$$

with \mathbf{s}_α , \mathbf{m}_α , and \mathbf{a}_β , \mathbf{n}_β being the slip and twin directions and normals for system α , β , respectively. \mathbf{R} remains constant for all of the simulations.

The temperature-dependent stress response of the polycrystals is subsequently computed and outputted for each strain increment. Note that the Taylor averaged stress was chosen. This leads to 100,000 stress-strain-temperature triplets for each sample. Each sample was subsequently verified (some deformation and temperature path combinations led to instability) before being added to the respective datasets. A graphical representation of the process is given in Figure 4.4.

4.3.1.2 Nomenclature

In this thesis we chose to follow an incremental approach, beginning with capturing the anisotropy of the material at room temperature and gradually

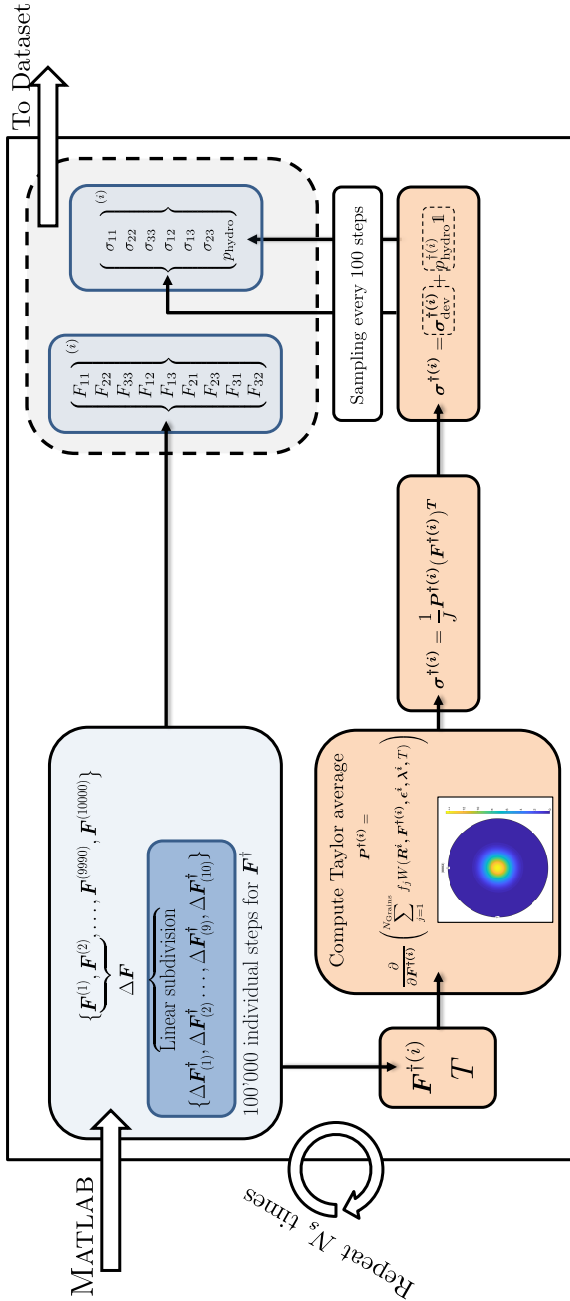


FIGURE 4.4: Schematic representation of the data generation process.

increasing the complexity of the task by first introducing constant and then varying temperatures. Therefore, throughout the remainder of the thesis, we need to handle numerous datasets for the different cases. In total we handle three types of temperature paths and three types of strain paths, resulting in nine possible combinations of data sets. An overview of our datasets and the nomenclature is given in Table 4.1. The types of temperature paths range from temperature-independent with constant, ambient, temperature to temperature varying, with (randomly) changing temperatures throughout a single deformation path. Equally, we handle deformation paths ranging in complexity from simple, linearly applied uniaxial or shear deformation to completely random (and unphysical) deformation paths. To avoid confusion, we introduce a simple nomenclature that allows for simple differentiation between the datasets and their use cases. Each dataset consists of a number of samples, N_s , as given in Table 4.1. Each sample in the set comprises a time series of stress-strain pairs that describe the deformation along a specific path at corresponding times with associated stresses.

The first dataset consists of temperature-*independent* data samples. The goal is to map the entire anisotropic stress-strain response including the effects of twinning, but without the added complexity of thermal effects. We denote it as the "TI" dataset. The second set contains temperature-*dependent* samples. We increase the complexity by providing data at different temperatures that remain constant throughout the simulations, between 25°C and 250 °C. This set is called the "TD" set. The final type of data has the highest complexity. It contains data at varying temperatures throughout the simulations. The temperatures are randomly chosen to begin with and then fluctuate throughout the simulation. These data are labeled TV.

Next, we differentiate between the applied types of deformation. The general approach utilized by Bonatti and Mohr [76] or Liu et al. [250] consists of imposing randomized deformation (though their implementations of random deformation differ). We use this as our baseline and denote the datasets with the appendix "-R". Due to the complexity of the material behavior, however, we also chose to create a separate, second type of dataset emphasizing the twin events, with predetermined loading paths, appended with "-D". Finally, we create a validation dataset labeled with "-V". A detailed explanation of the generation of these datasets follows in section 4.3.1.3.

TABLE 4.1: Nomenclature of the datasets as well as key characteristics.

dataset	N_s	Temperature	Deformation paths	ϵ_{\max}	purpose
TI-R	9965	25-25°C	random	0.1	train/test
TD-R	9894	25-250°C	random	0.1	train/test
TV-R	10034	25-250°C	random	0.1	train/test
TI-D	4997	25-25°C	component predetermined	0.1	transfer learning
TD-D	4997	25-25°C	component predetermined	0.1	transfer learning
TI-V	50	25-25°C	determined	0.1	validate
TD-V	50	25-250°C	determined	0.1	validate

4.3.1.3 Stress-Strain Paths in Data Generation

With the nomenclature defined and all possible confusion avoided, let us dive into the details of the data generation.

First, let us establish the measures of interest for our applications. We use the deformation gradient \mathbf{F} , to represent the deformation at large strains and the associated Cauchy stress $\boldsymbol{\sigma}$ at each time step as the chosen stress measure. While the first Piola Stress \mathbf{P} is the natural measure of stress associated with \mathbf{F} , our choice is based on the symmetry of $\boldsymbol{\sigma}$, which simplifies the problem's order. Alternative formulations are e.g. by using the conjugate pairs \mathbf{S} , and \mathbf{E} . The temperature in °C is represented by T .

4.3.1.4 Generation of Randomized Strain and Temperature Paths

Initially, we establish random deformation paths that serve as the basis for the model's training. These paths must satisfy specific criteria, namely, they should be continuous, smooth, and span a broad area of the possible deformation space to capture the entire range of behavior in Mg. Similar approaches and requirements were given by e.g. Bonatti, Berisha, and Mohr [75], Bonatti and Mohr [76], and Liu et al. [250], who applied the methodology before us. As such, the paths should consist of random deformations and change orientations repeatedly [250].

To sample the random input functions, we use the Ansatz outlined in Liu et al. [250]. We first divide the total time t_{\max} allotted for deformation into $N = 10^4$ intervals of equal time steps $\Delta t = t_{\max}/N$. At a given

time $t^\alpha = \alpha\Delta t$, we compute the deformation gradient $\mathbf{F}^\alpha = \mathbf{F}(t^\alpha)$ and temperature $T^\alpha = T(t^\alpha)$ as

$$F_{ij}^\alpha = \delta_{ij} + F_{ij}^{\alpha-1} + \varrho^\alpha \epsilon_{\max} \sqrt{\Delta t} \quad (4.22)$$

$$T^\alpha = T^{\alpha-1} + \kappa^\alpha \theta_{\max} \sqrt{\Delta t} \quad (4.23)$$

where $\varrho^\alpha, \kappa^\alpha \in \{-1, 1\}$ and follow a Rademacher distribution [250]. Further, $T_\alpha \in [25, 250]$ for $\alpha = 0$, and $\theta_{\max} = 225$. A total of 10,034 data were generated with $\epsilon_{\max} = 0.1$ and $\theta_{\max} = 150$. An example of a random strain and temperature path is given in Fig. 4.5. We show the time evolution of the diagonal entries in (a), where it can be seen that the paths are smooth yet may change direction throughout the simulated time. These changes in direction occur multiple times, leading to alternating types of loading. All entries start at zero and follow a random path. Conversely, in (b), we show the temperature paths. These paths are smoother than the strain paths since we observed stability issues in the CP model for rapid, large variations. In contrast to the deformation paths, the temperature can start at any value between 25 and 250 °C.

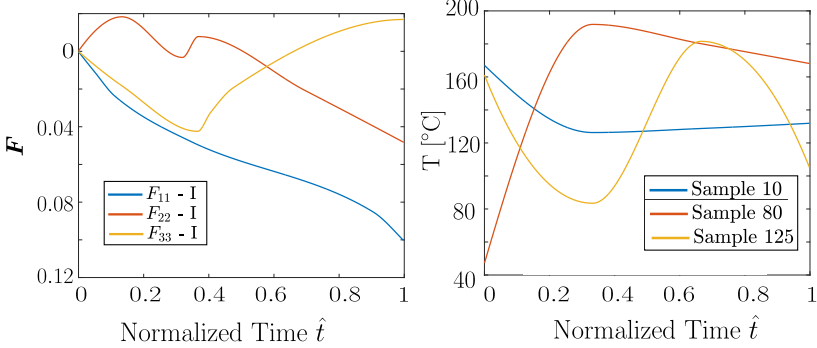


FIGURE 4.5: Example of the randomized strain and temperature paths.

4.3.1.5 Random Deformation Datasets

For all datasets labeled with "-R," the strain paths are generated following a consistent procedure. Each element of the deformation gradient follows a distribution described by (4.22). This results in volumetric deformation that is entirely random in the polycrystals. It is assumed that these deformations induce all of the material's possible constitutive behavior. However, given

the material's complexity and anisotropy, certain deformation modes, such as simple shear and twinning-controlled deformations, may be underrepresented in these datasets.

To address this issue and reduce the overall data required for training, a second type of dataset is generated, with a specific focus on these underrepresented deformation modes.

4.3.1.6 *Semi-Deterministic Deformation Paths*

This new dataset includes isochoric uni-axial loading and shear along randomized strain paths. We distinguish between nine distinct cases, covering loading in the 11-, 22-, and 33 directions, as well as shear along any of the off-diagonal directions.

Each case is assigned a number from 1 to 9 according to the following scheme: the diagonal entries F_{11} , F_{22} , and F_{33} are assigned numbers 1 through 3, while the off-diagonal entries are assigned numbers 4 through 9 in the following order: $F_{12}, F_{13}, F_{21}, F_{23}, F_{31}, F_{32}$.

For the shear cases, the corresponding entry of the deformation gradient \mathbf{F} follows smooth, yet random paths, as defined in equation (4.22). In the case of uni-axial deformation, an additional constraint is imposed on the diagonal elements to ensure that $\det(\mathbf{F}) = 1$, as shown below. Assume the load is applied on F_{11} . Then, to satisfy isochoric deformation we impose a strict constraint on \mathbf{F} ,

$$F_{(ii)} = \frac{1}{\sqrt{F_{(11)}}}, \quad i \neq 1. \quad (4.24)$$

This constraint is stricter than isochoricity but ensures that all principal directions (ND, RD, and TD, aligned with the 11-, 22-, and 33- directions) are loaded in a similar fashion. It is fair to assume for a rolled material, that the RD and TDs behave quasi-equally [86].

4.3.1.7 *Deterministic Datasets for Validation*

We proceed to generate a small set of validation data. Unlike the -D labeled datasets which rely on a stochastic approach, the -V datasets are generated using a deterministic method. Within this set, we retain the ten cases previously introduced as cases 1 through 9, and include an additional tenth case for cyclic loading along the 11- direction. This specific direction is selected due to its pronounced twin-induced plastic anisotropy, making it particularly relevant for validation purposes [52].

To ensure realism in the deformation, which is essential for validating the underlying physical model, we enforce volume preservation for each of the validation cases. In contrast to the "-D" labeled datasets, where deformation is applied in a random fashion, in the "-V" labeled datasets, a linear increase of the strain is applied for the simple shear and uniaxial tension and compression scenarios.

4.3.2 Training Methodology

Let us now dive into the training methodology used for the RNOs. We trained several neural networks to capture the constitutive behavior of magnesium under different conditions. Specifically, three types of Recurrent Neural Operators (RNOs) were trained, each targeting different aspects of the material's response.

The first RNO is temperature-independent (TI-RNO), designed to learn the constitutive behavior of magnesium at room temperature. This RNO is trained on the TI datasets, which represent the material at ambient temperature. The second case involves a temperature-dependent RNO (TD-RNO), which serves as a surrogate for the temperature-dependent CP model in chapter 3. In this case, the temperature follows a uniform distribution between $T = \mathcal{U}(25, 250)^\circ\text{C}$, and it remains constant during the simulations. A third case is presented by the TV-RNO. The TV dataset represents the material's response under varying temperature conditions, allowing the RNO to capture the temperature-dependent behavior of the material's stresses. Last, the TV-RNO is applied to the TD dataset, aiming to predict and learn the temperature-varying evolution of the stresses in the material.

4.3.2.1 Normalization and Stress Decomposition

Our method of generating the deformation gradient, F , leads to a quasi-normal distribution of the strain entries, see Figure 4.6, which is advantageous for training purposes. Due to the randomized deformation, the material experiences significant volumetric deformation, leading to large variations in the entries of the stress tensor σ . This proves to be a further advantage of the decomposition of the stress into a deviatoric and a hydrostatic part, see (4.14).

We normalize both components, σ^h and σ^{dev} , in order to represent the training data of the neural networks on the range $[-1, 1]$. We normalize all entries of the stress tensors equally, thus following the approach of Bonatti

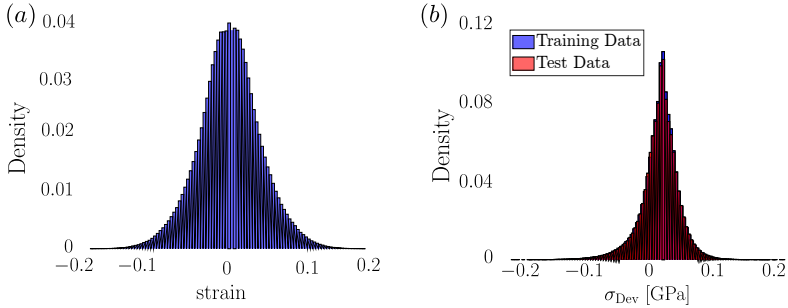


FIGURE 4.6: Distribution of the strains (a) and of the training vs. testing data sets (b).

and Mohr [76], and maintaining the relative magnitudes of the entries. σ_0 and p_0 were chosen as the maximal values occurring in the TI dataset since they represent the largest values across the training data overall.

For the RNO, the output reads

$$\mathbf{y}(t^\alpha) = \mathbf{y}^\alpha = \begin{bmatrix} \sigma_{dev,11'}^\alpha \\ \sigma_{dev,22'}^\alpha \\ \sigma_{dev,33'}^\alpha \\ \sigma_{dev,12'}^\alpha \\ \sigma_{dev,23'}^\alpha \\ \sigma_{dev,13}^\alpha \end{bmatrix} / \sigma_0, \quad (4.25)$$

whereas for the FCNN tasked with computing the hydrostatic pressure, it is $\hat{y}_{FCNN}^\alpha = \sigma^h / p_0$. The deformation gradient serves as input and remains unaltered, such as to facilitate the direct integration of the RNN in a UMAT

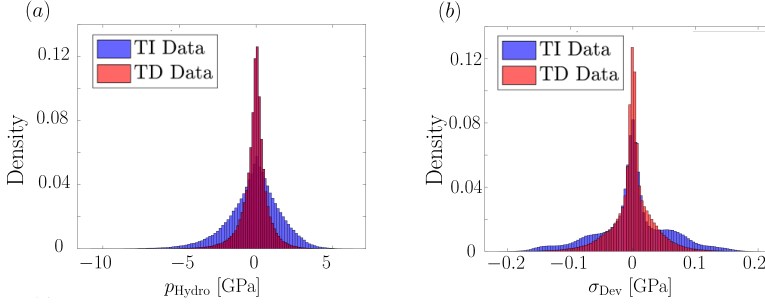


FIGURE 4.7: The distribution of the hydrostatic component (a) and of the deviatoric component (b) of the TI vs. TD datasets is shown.

and the independence of the maximal strain applied during training. In the case of the RNO it is composed as

$$\mathbf{x}^\alpha = \begin{bmatrix} F_{11}^\alpha - 1, \\ F_{22}^\alpha - 1, \\ F_{33}^\alpha - 1, \\ F_{12}^\alpha, \\ F_{23}^\alpha, \\ F_{13}^\alpha, \\ F_{21}^\alpha, \\ F_{32}^\alpha, \\ F_{31}^\alpha, \\ \Delta t, \\ \zeta_1^{\alpha-1}, \\ \dots, \\ \zeta_{n_s}^{\alpha-1} \end{bmatrix}, \quad (4.26)$$

whereas for the FCNN it is $x_{\alpha, \text{FCNN}} = (J_{\alpha'}, T_\alpha)$. We identify two normalization constants: $\sigma_0 = 0.22$ GPa for the deviatoric stress and $p_0 = 8.71$ GPa for the hydrostatic pressure, see Figure 4.7.

4.3.2.2 Hyperparameter Tuning

Finally, we aim to identify the hyperparameters for the RNO and the FCNN, such as the batch size, the learning rate, the depth and width of

the networks, as well as the size of the state vector (in the case of the RNO only). To isolate the effects of individual parameters, we conduct a series of tests. We assume as a first guess that five state variables should be sufficient to properly capture the mechanical behavior, as was shown in Liu et al. [250] for homogenized plastic behavior. We train our models on 2000 samples and use a batch size of 100, and a learning rate of 10^{-3} . For training, we down-sample the data from 100,000 data points per sample to 100, corresponding to time increments of 1s or a training resolution of 100. An initial training rate of 10^{-3} and a cosine learning rate scheduler with a reset rate of 10^{-6} were used for training all networks, as the results were satisfactory and stability was ensured. For more details, see the Pytorch website [251] or Paszke et al. [252]. Each RNO is trained for 2500 epochs.

First, we aim to identify the number of trainable parameters. To this end, we vary the width and depth of the layers in the RNO from 50 to 400 in increments of 50, as well as the number of layers from three to five in increments of one. Overall this provides us with 24 different RNO architectures and their corresponding test errors. Preliminary results showed that three layers in the RNO were by far insufficient to represent the material behavior and layers below 200 nodes were also not expressive enough. We evaluate the number of parameters for the remaining architectures via the built-in functionality in LinuxFoundation [251] and show the results in Figure 4.8. We observe that the error remains relatively high, for any of the cases. This puzzling result led us to first hypothesize that the architecture was inadequate to represent the material behavior. We settled for a network with slightly over 500,000 trainable parameters, as the test error does not improve significantly beyond that point, see Figure 4.8. This is equivalent to an RNO with four layers in \mathcal{F} and \mathcal{G} with 300 nodes per layer. In comparison, the FCNN tasked with learning the hydrostatic pressure requires four layers containing 50 nodes per layer for no further improvements in the training error. Increasing the number of training data also only had a small effect on the performance and we increased the number of training data up to 8500 samples, the maximum we allocated for training. We observed that the network is not expressive enough in its present configuration to provide a good approximation of the material behavior. Further, increasing the depth or the width of the RNO had not the significant effect on the error one would expect and hence, we deduced that the only remaining degree of freedom lay with the number of state variables.

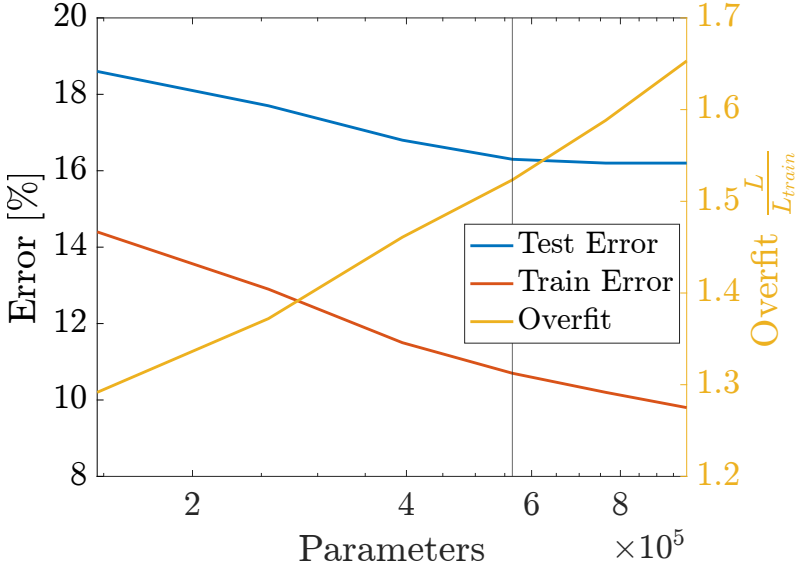


FIGURE 4.8: Training and testing error vs. the number of trainable parameters in the network.

4.3.2.3 State Variable Identification

We therefore repeat a similar experiment for the number of state variables for each type of RNO and subsequently for the three temperature cases. We vary the size of the state vector from five to 10 in steps of one and further to 50 in increments of 10, and evaluate the RNOs after 2,500 epochs of training. We show the results in Figure 4.9. For the TI case, the RNO demonstrates an exceptional convergence behavior, reaching convergence at only 15 internal variables (IVs), which is noteworthy considering that it is comparable to the number of physical internal variables needed in the material model. The error rate stabilizes at around 7.5% with insignificant improvements beyond 15 IVs.

Similarly, for the TD and TV cases, the RNOs exhibit a trend toward rapid convergence with the number of state variables. However, in these cases, the error smoothly decreases to a lower value at a higher number of state variables. This behavior is significantly different from the results reported by Bonatti and Mohr [76] and Bhattacharya et al. [79], where a clear number of internal variables can be identified based on the immediate saturation of the error. In our case, the optimal convergence is achieved

somewhere between 35 and 40 state variables. Even a finer increase of the state variables in that region did not allow for a clear identification of the state variables. For the TD case, a quasi-steady response is attained above 35 IVs at low error levels of about 5.9% with 35 state variables. The TV-trained RNO achieves an error rate of approximately 6.8% at 35 state variables, and this decreases to around 6.2% for 50 state variables. These results suggest that certain mechanisms are at play within the TD and TV cases, necessitating the use of additional state variables in the RNO. Interestingly, the two cases involving temperature as an input to the RNO converge almost simultaneously beyond 10 state variables. This indicates that the presence of temperature as an input to the RNO is a crucial factor

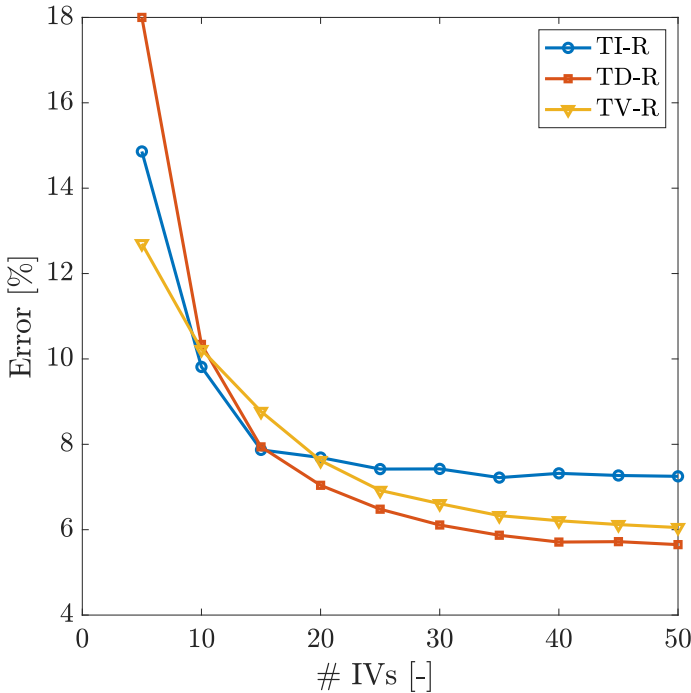


FIGURE 4.9: Convergence of the training error with the number of state variables for TI, TD, and TV cases. The TD and TV cases show the same kind of slower convergence with larger numbers of IVs (35-40) compared to the TI case, which converges much more rapidly and saturates around 15 IVs.

contributing to this phenomenon. While we accept this as a fact for now, a discussion follows later in this chapter, in section 4.5.3.

Let us briefly recapitulate the findings of this experiment so far, before discussing final training and the architecture's performance. We identified an RNO architecture with four layers and 300 nodes as the optimal solution for the architecture and a good trade-off between training performance and speed. Further, we observed that training with 8500 samples, the maximum at our disposal, led to the best results. In addition, we noticed that five state variables are insufficient to describe the state of the present material. A minimum of 15 are required for the TI case and up to 35 are required for the TD and TV cases. We also note that the learning rate of 10^{-3} and the batch size of 100 seemed adequate.

4.4 TRAINING PERFORMANCE

With these hyperparameters in mind, we now move on to a final round of training and to evaluate the performance of the RNO.

4.4.1 *Operator Training*

We begin by evaluating the performance of the RNO architecture on learning the behavior encoded in the TI-R dataset. We train an RNO with four layers in both \mathcal{F} and \mathcal{G} , with a width of 300 and a state vector size of 15. Figure 4.10 (a) displays the testing errors for 2500, 5000, and 8500 samples, as well as the training error for the last case with 8500 samples. We observe a slight over-fitting but to a non-concerning degree. We note that the errors converge to comparable values for 5000 and 8500 samples, both around 7.6%, indicating that little data is needed for our architecture to learn the behavior of the underlying material model. This stands in stark contrast with the often tens of thousands or millions of data points required in previous studies [13, 76]. For 2500 samples, the error lies above 10%, which is above our acceptance threshold. We notice that with more data used for training, the error converges faster to its ultimate value, but that it does not scale particularly well with the addition of further data. Additionally, for 2500 samples, the error curve exhibits different behavior with numerous oscillations. We believe that the parameters for the cosine-annealer or the batch size of 100 may not have been optimally suited for this small sample size. However, to ensure comparability of the results, we chose not to modify the parameters for the smaller datasets.

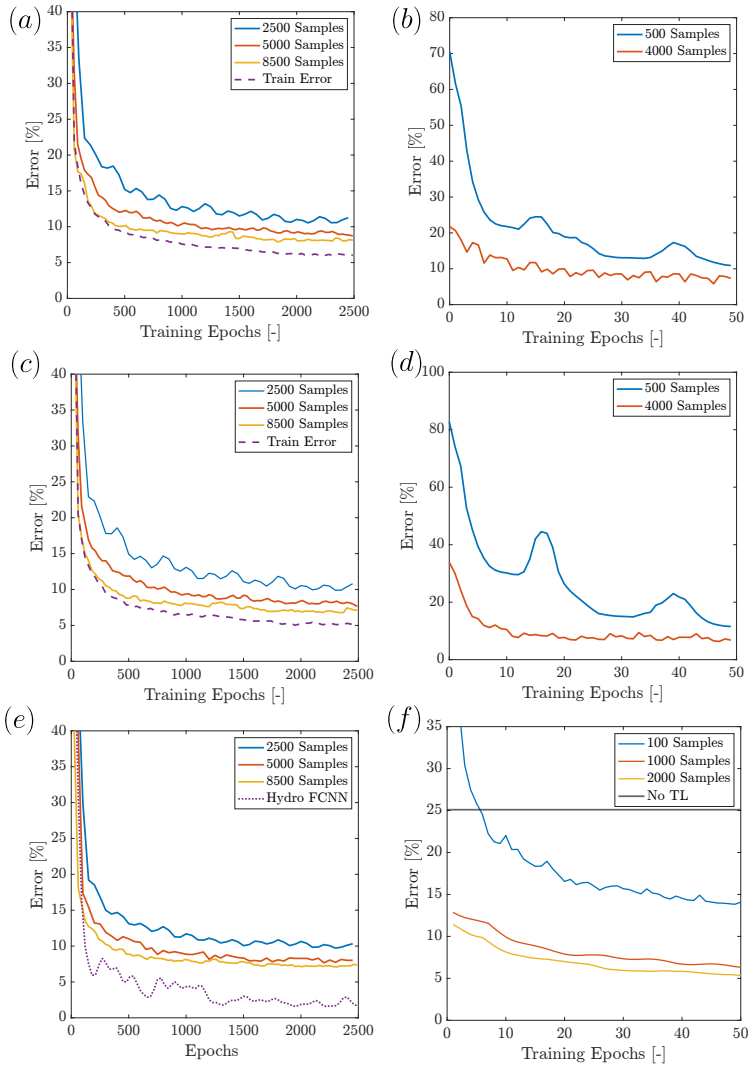


FIGURE 4.10: Test error evolution with the number of training epochs for training on the random dataset in the TI case (a), the TD case (c), and the TV case (e). Cases (b),(d), and (f) showcase the fine-tuning results of the RNOs on the -D labeled datasets.

Next, we repeat the training process for the datasets TD-R and TD-V, using temperature-dependent RNO architectures. In this case, we increase the state vector size from 15 to 35, as shown in Figure 4.9, while keeping all other parameters unchanged. The results of our training process are presented in Figure 4.10 (c) and (e) for TD-R and TD-V, respectively. Similar trends are observed as with the TI case, and a slightly lower error is attained at approximately 6.2% for both TD-R and TD-V. We attribute this improved performance to a slightly more homogeneous distribution of stresses in the presence of elevated temperatures, as seen in the distribution in Figure 4.7(b). We further showcase the results of learning the map for the hydrostatic component via the simple FCNN.

Overall, the RNO architecture demonstrates effective learning capabilities and is capable of capturing the material behavior in both temperature-invariant and temperature-dependent cases. The results indicate that the RNO achieves a reasonably low error while maintaining good convergence properties, making it a suitable choice for representing the complex material response accurately. The TI and TD cases are representative of the applications of our CP model in chapter 3, where we assumed constant temperatures during our polycrystalline simulations. Before moving on to a more generalized description with varying temperatures, we evaluate the predictive capabilities of the model. Figure 4.11 (a) and (b) display stress responses of a *testing* sample in the TI-R and TD-R sets, respectively. The solid lines mark the true response, and the dashed lines represent the RNO prediction.

We observe that the model accurately captures the deviatoric stress state for the trained samples, confirming that our achieved loss of approximately 6-7% is satisfactory. The randomized data appears to be representative of the overall mechanical behavior of the material, enabling the RNO to predict stress responses with a high level of accuracy. This indicates that our proposed architecture is capable of effectively learning the complex plastic material behavior and generalizing well to unseen data.

To further evaluate this hypothesis, we compare a directly trained RNO with a fine-tuned RNO. Fine-tuning occurred via 50 epochs of transfer learning on the TI-D and TD-D datasets. For the present evaluation, the RNOs were fine-tuned on 4000 samples. The losses are shown in Figure 4.10 (b), and (d), respectively. Fig. 4.10 (b) displays the error evolution during these 50 epochs of fine-tuning on the TI-D dataset, using 500 and 4000 samples. We observe that only a few epochs of training are needed to approximate the behavior with a small error.

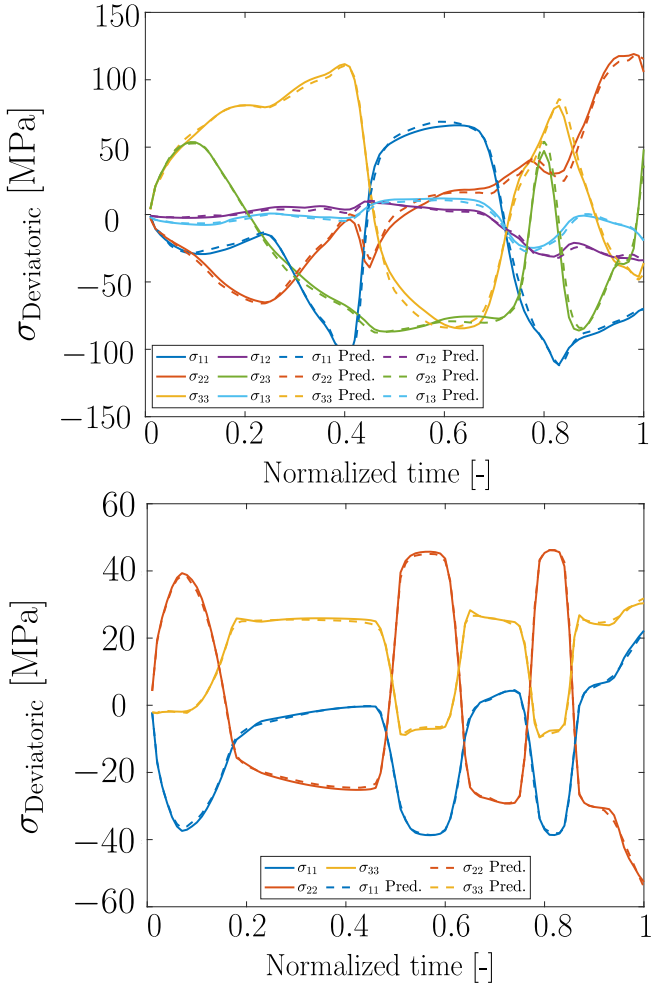


FIGURE 4.11: Stress evolution for a testing case in the TI-R (top) at 25°C and TD-R (bottom) at 241°C datasets, respectively. The ground truth is shown as solid and the predicted response from the RNO is shown in a dashed line.

Figure 4.12 depicts the true (dashed) and predicted (dotted, solid) stress-strain behavior of a simple shear case, present in the validation dataset (TI-V). The directly trained RNO predicts the stress-strain behavior relatively

well (dotted line). Intriguingly, there are nonphysical fluctuations in the prediction, specifically in the low-strain regime. Further, the prediction on the larger stress components is much better than for the lower ones. This indicates that the commonly used method of generating training data via random deformation has certain limitations for highly anisotropic materials, in that some components are better represented than others. Nevertheless, the directly trained RNOs capture the general behavior of the physics. The nonphysical fluctuations and the overall error can be significantly improved by a short period of transfer learning on a dataset containing more specific data, which we represent with the solid line. We deduct that while the physics of the material is incorporated in the training data, the smaller components of the stress tensor are underrepresented. It is likely, that a different normalization method than the one introduced in section 4.3.2.1 could alleviate these issues naturally. These findings show that the RNO architecture is versatile and rapid to adapt, allowing us to further explore the capabilities for generalizing the applications of the RNO via transfer learning.

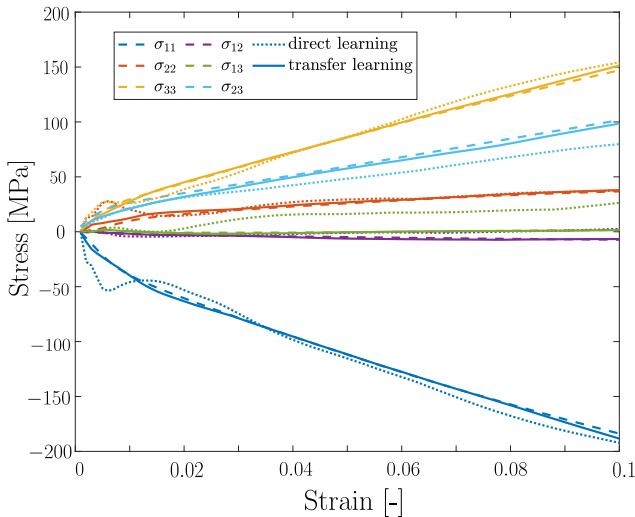


FIGURE 4.12: RNO Response pre and post-50 epochs of transfer learning on the RD-D dataset The response prior to transfer learning is shown by the dotted lines, the response afterward by the solid line. The dashed line represents the ground truth.

4.4.2 *Generalization for Various Temperature Paths via Transfer Learning*

The RNO has shown promise in learning the complex anisotropic and temperature-dependent response of the underlying material thus far. In the following, we wish to investigate whether the architecture is capable of extrapolating and representing multiple temperature paths as well. First, we evaluate whether this capability is already included in the RNO trained on the TV samples. The trained RNO is tested with the TD set and the results are included in Figure 4.13(a). We observe that the RNO trained with a random thermal history performs poorly when tested on a constant temperature path. This is not surprising, it is known that neural networks extrapolate poorly to unseen inputs.

To address this issue, we wish to evaluate whether transfer learning [253, 254] can overcome the issue. We fine-tune the trained RNO using the temperature constant dataset and perform 50 epochs of training with varying numbers of data. We show the results of the training in Figure 4.10(f). We observe that with a relatively small amount of data (1000 samples), the RNO is capable of reducing the test error from 25% to 6.5% via transfer learning. This shows the efficacy of the method as well as the versatility of the RNO. We note that while the RNO trained with a random thermal path generalizes poorly to other thermal paths, the fine-tuned RNO is capable of generalizing to temperature paths that are commonly encountered in practice. This indicates that the map from random to constant temperature paths and vice-versa is possible.

4.5 RESULTS AND DISCUSSION

4.5.1 *Validation of the RNO*

Let us now move on to the validation of the RNO's performance. For the final application, we utilize a temperature-aware RNO with four layers each for \mathcal{F} and \mathcal{G} , a layer width of 300, and 35 state variables. We initially train this RNO on 8500 samples from the TV-R dataset and then perform 1000 epochs of transfer learning on 2000 samples from the TD-D dataset. This configuration ensures that the RNO effectively represents the wide range of Mg's plastic behavior.

We use the trained RNO to predict the data inside the validation datasets, beginning with the TI case. Figure 4.14 displays the outcomes for different scenarios in the TI validation set, specifically a case of pure shear in the 13

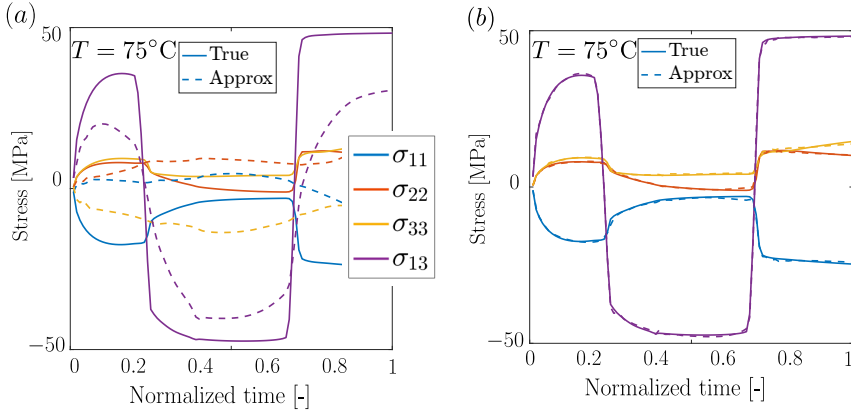


FIGURE 4.13: Performance of the TV-trained RNO before fine-tuning (a) and (b) after.

direction, and cyclic loading and unloading along the 11 direction, which is parallel to the ND of the rolled texture. The figures illustrate the time evolution of the deformation measure and the stress-strain relationship.

Figure 4.14(a) illustrates a simple shear case, where the solid line represents the ground truth predicted by the CP model, and the dotted lines depict the RNO's predictions. The RNO exhibits a close and accurate fit to the ground truth, capturing the lower stress levels associated with shear deformation precisely. In Figure 4.14(b), we present the stress-evolution over cyclic loading, showcasing the RNO's ability to accurately predict the response throughout the applied loading time. The RNO captures the different hardening rates during tension and compression, as well as the increased stress levels due to strain hardening. Remarkably, it performs well even at room temperature, despite being trained on elevated temperature cases in the TV and TD scenarios. We are pleased with the RNO's performance and proceed to evaluate its capabilities at elevated temperatures.

Figures 4.14(c) and (d) present the results for two cases of interest at three randomly sampled temperatures each. Figure 4.14(c) demonstrates uniaxial, isochoric tension along the ND – the normal direction of the sample, along which most c -axes of the crystals are aligned. The RNO accurately captures the saturation point for all three temperatures, leading to an appropriate hardening response. In the lowest temperature case, the initial hardening during twin propagation (up to approximately 6.4% strain)

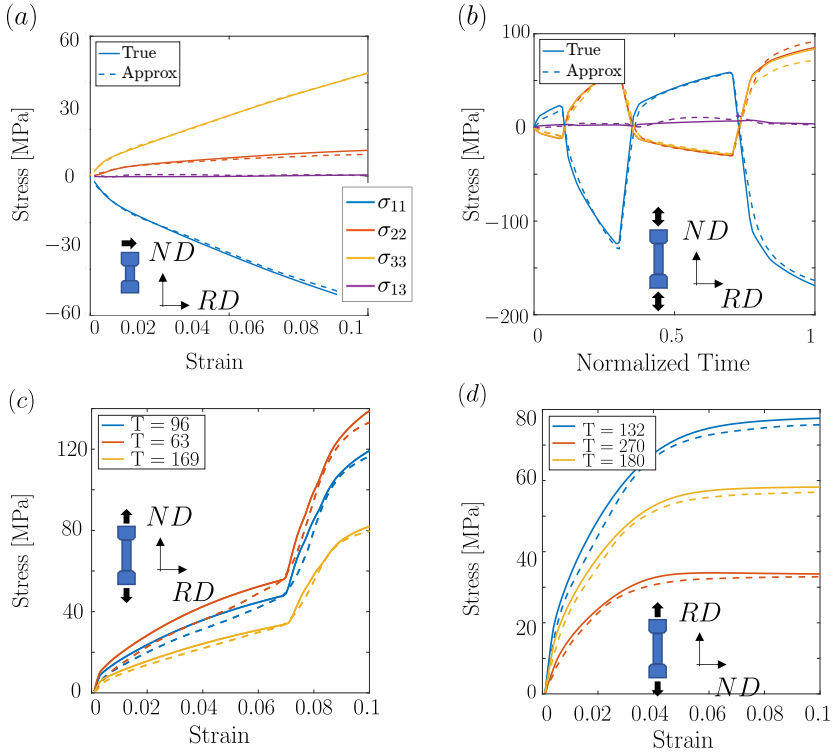


FIGURE 4.14: Predicted (dashed) and true (solid) material response for different load cases at room temperature: shear in the 13 direction in (a) and cyclic loading along the 11 direction in (b). (c) and (d) show the response for elevated temperatures instead.

is slightly underpredicted, with a maximal error of about 8 MPa, which is significant but not problematic for this deformation mode. Figure 4.14(d) depicts uniaxial tension along the RD. This mode highlights the overall softening due to thermal activity, along with changing saturation points and stress-strain curve levels. The RNO predicts the material response with great accuracy, consistently slightly underpredicting the stress level. The maximal error is approximately 2.5 MPa, indicating a good approximation.

Consequently, we explore the RNO's capability to capture strain hardening and directional anisotropy, demonstrated by cyclic loading along the ND (Figure 4.15(a)). The RNO accurately reproduces the observed behavior, showing weak strain hardening during tensile loading due to the activation

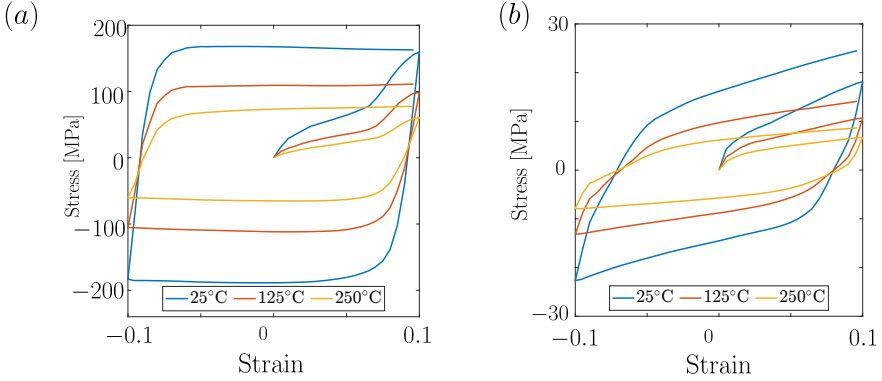


FIGURE 4.15: Bauschinger effect under uniaxisal tension/compression (a) and shear (b) at varying temperature levels captured by the RNO.

of TT systems, followed by increased strain hardening. During compressive deformation, a rapid stress increase is seen due to the presence of strong hardening associated with activated slip systems. This behavior is consistent with what would be expected from a physical material. Similarly, for cyclic shear (Figure 4.15(b)), the RNO captures the temperature-induced reduction in hardening rates. Additionally, it captures the strain hardening expected from such deformation modes. These cases highlight the RNO's capability to capture intricate effects, such as the Bauschinger effect during repeated loading and unloading. Overall, the RNO demonstrates its ability to predict complex material responses accurately across various loading conditions and temperatures.

Finally, for the sake of completeness, we show the results of the FCNN predicting the hydrostatic stress contribution in Figure 4.16. This network was trained with 300 nodes per layer and four layers, as well, for 8500 samples of the TV data set. It generalizes well for all temperature cases inside the data set and shows a low error overall, as indicated by the low error shown in Figure 4.10(e).

4.5.2 Comparison with Traditional Recurrent Architectures

We have shown the strengths of the RNO, its adaptability, and its capability to represent complex material behaviors. Many of these qualities, however, are also present in traditional architectures, explaining their widespread

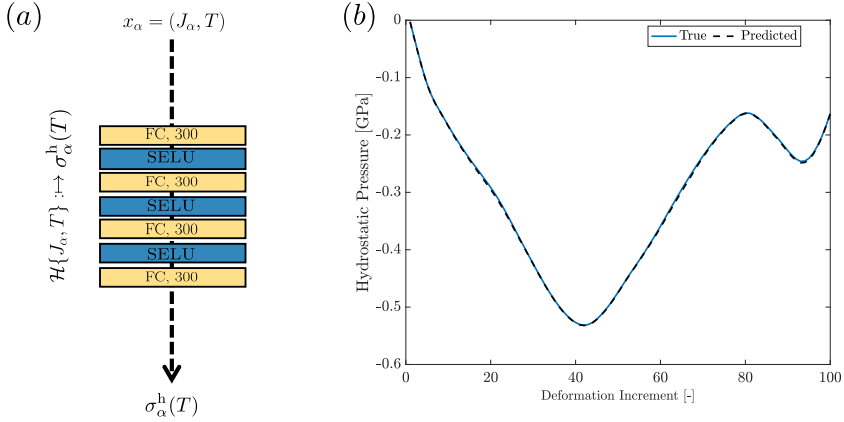


FIGURE 4.16: Architecture of the FCNN learning the equation of state, relating J and T to the hydrostatic pressure σ^h in (a) and prediction of the network for a random sample in the testing data set (b).

success. Traditionally, architectures such as GRU and LSTM-based networks have been widely used with great success to learn and predict the plastic response of materials. These architectures have demonstrated their ability to capture complex, history-dependent behavior and have achieved remarkable success in a variety of fields. Therefore, they have been applied to predict the constitutive behavior of history-dependent materials in the past. For instance, in a study by Yu et al. [80], a GRU-based and an LSTM-based architecture were successfully employed to predict the plastic stress-strain response of an elastoplastic material with J2-plasticity. We now perform a comparative study of a variety of GRU- and LSTM-based architectures and evaluate their capability to capture the constitutive behavior of our material.

We specifically focus on the simplest case, which is the temperature-independent response at room temperature, where the main challenge lies in accurately capturing the material's anisotropic plastic response using a limited number of parameters. To compare the GRU and LSTM networks directly with our proposed RNO for the temperature-invariant response, we use a small subset of 2000 samples from the TI-R dataset. We explore various GRU and LSTM architectures, as described in Table 4.2. The network (a) is directly based on Yu et al. [80], initially used for J2-plasticity, with other architectures being mostly adaptations. The adaptations are obtained by changing the hyperparameters for different architectures, such as to

investigate whether larger or different types of architectures would perform better than the suggested one. We vary the layer width in the GRU/LSTM cells, explore the addition of multiple FCNNs, and examine the impact of altering the GRU/LSTM layer width. We also investigate the effect of using a feed-forward architecture, where the final FCNN layers are aware of the input at any given time. All these investigations are carried out with the same learning rate of 0.001 (except for the LSTM network), a batch size of 100, 2000 training samples, and 7894 testing samples. The results of our investigation are presented in Table 4.2. The RNO used for this comparative study is the same architecture employed for final training and validation. It consists of two four-layer deep FCNNs with a uniform layer width of 300 and a hidden state of 35 state variables, resulting in networks of overall similar sizes [80].

We observe that among the GRU networks, the architecture proposed in Yu et al. [80] achieves the best results on the given dataset. The LSTM-based architectures, surprisingly, suffered from stability issues that led to a reduction in the learning rate for these architectures. Further, increasing the size of individual layers of the GRU did not help in improving the predictions of the networks. The comparison clearly indicates that our introduced RNO outperforms both GRU and LSTM-based architectures for this specific task. The RNO not only achieves better accuracy but also exhibits faster convergence and greater robustness, making it the preferred choice for capturing the material behavior in our study.

TABLE 4.2: GRU and LSTM architectures tested against the present RNO

network	Layers	# Train. samples	Min loss (L2)
(a)	GRU GRU GRU GRU FCN 500 128 500 128 6*	8500, lr = 0.001	unstable
(b)	GRU GRU GRU GRU FCN 500 128 500 128 6*	8500, lr = 0.0001	23.1%
(c)	GRU GRU GRU GRU FCN 500 256 500 256 6*	8500, lr = 0.001	25.8%
(d)	LSTM LSTM LSTM LSTM FCN 500 128 500 128 6*	8500, lr = 0.0005	unstable
(e)	LSTM LSTM LSTM LSTM FCN 500 128 500 128 6*	8500, lr = 0.0001	43.6%

Finally, we illustrate the testing error of the best-performing architectures, networks (a) and (g), in comparison to our proposed RNO in Figure 4.17(a). Several notable observations can be made. First, it is evident that the introduced RNO achieves significantly better performance compared to both the classical LSTM and GRU-based architectures. The GRU achieves the lowest error of 23.1%, while the LSTM only manages to reach an error of approximately 43.6% within the given training period. Although increasing the size of the LSTM improves the error, it also considerably prolongs the training time, leading us to refrain from pursuing this approach further.

Next, we observe that the RNO exhibits faster convergence towards a reasonable error. On the other hand, the GRU and LSTM seem to encounter local minima during training, as indicated by the plateaus in the testing errors. Additionally, the LSTM displays slower convergence compared to the GRU and demonstrates instances of (almost) unstable behavior, where the error increases significantly before decreasing again. Notably, around the 300 epoch mark, the LSTM error becomes exceptionally large, requiring several epochs to stabilize. This behavior persists despite the LSTM's lower learning rate in comparison to the RNO. These findings confirm the notion that GRU cells are generally more robust than LSTM cells. However, our presented RNO exhibits greater robustness for the given problem and is evidently better suited for this particular task.

During the course of our investigation, we observed that the GRU and LSTM networks necessitated much lower learning rates compared to what we were able to achieve with our RNO. Particularly, the LSTM networks were prone to exhibiting instability even at low learning rates. Consequently, the training process for these recurrent neural networks would require substantially more time compared to the current RNO. Additionally, we noted that the scalability of the GRU and LSTM networks in relation to the training set size was not adequate. Despite possessing a larger number of tunable parameters, these recurrent neural networks were unable to effectively capture the anisotropic behavior with the required precision. Subsequently, in Fig. 4.17(b), we present the stress response predicted by the GRU model at the training resolution compared to the ground truth. While the GRU model is able to capture certain aspects of the behavior, the overall error remains significant. Based on these results, we conclude that the GRU architecture introduced in [80] is not ideal for accurately capturing broader or more complex plastic behavior. Further training or larger networks may indeed improve the prediction of the GRU further, however, there is a clear discrepancy in the performance of the two architectures.

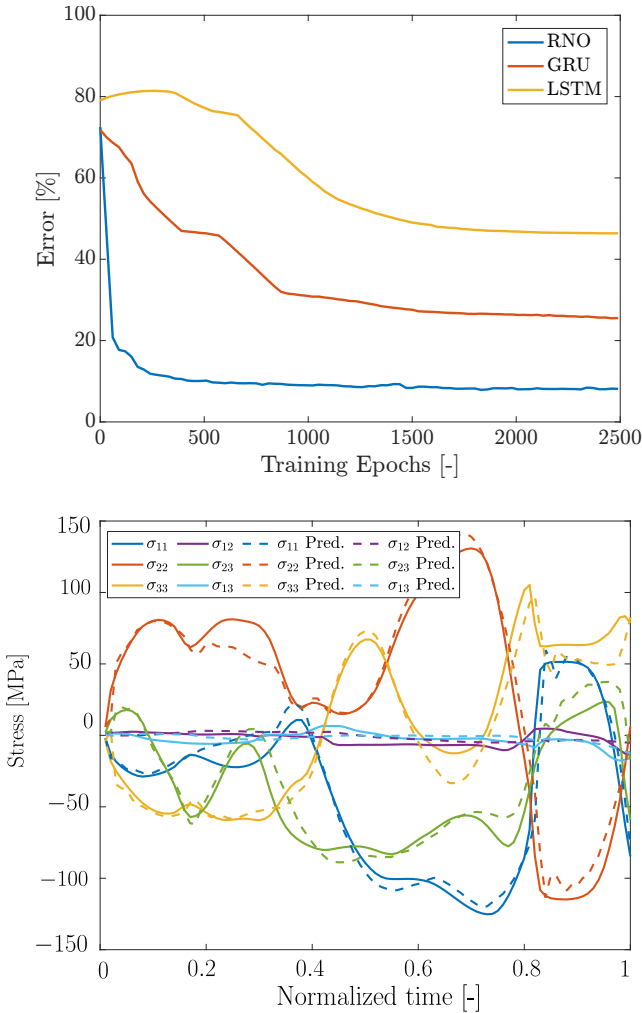


FIGURE 4.17: (a) Best performing GRU and LSTM architectures vs. TI-RNO with 300 NPL, 15 IVs. Trained on 8500 samples for the temperature invariant case at 25°C. (b) shows the prediction of the best-trained GRU model vs. the ground truth.

We have shown that the RNO has a number of advantages over its classical counterparts, such as the rapid convergence, the reduced number of parameters needed to represent the width of the behavior as well as the

relatively small number of data needed to train the model. The primary advantage of our architecture over classical RNNs, however, lies in a different aspect.

4.5.2.1 *Resolution-Dependence of Architectures*

Other architectures, including MSCs, are highly dependent on the resolution of the data, meaning that, as the data is sampled at different rates from the training resolution, the prediction error increases significantly. However, the presented RNO aims to counteract this phenomenon.

As discussed in Bhattacharya et al. [79], an effective RNO architecture should be capable of learning the true mapping from F to σ , resulting in a time-independent representation of the stress-strain relationship. If this assumption holds, then the predictions at different time resolutions should maintain a similar level of quality as the training resolution. Liu et al. [14] conducted tests to verify this hypothesis and observed that the error of the Markovian RNO remained bounded and small for resolutions higher than the training resolution, provided that the correct physics and number of internal state variables were chosen. However, there exists a lower bound for the resolution due to stability limitations imposed by the forward Euler updates, which may introduce instability for small timesteps.

We conducted a comparison between the RNO and GRU networks at different resolutions to assess their performance. Specifically, we used the trained RNO and GRU RNN models to predict the response of the test data in the TI-R and TD-R sets, respectively. The training resolution was set at 100 time steps per strain path. We then varied the sampling rate, which corresponded to different resolutions, ranging from 50 to 1000, with higher numbers indicating more steps and smaller values for the time increment Δt . Subsequently, we employed each architecture to predict the response for these various resolutions.

As anticipated, all architectures demonstrate their best performance at the training resolution. The TD RNO case exhibits approximately 7.5% testing error, while the GRU architectures on the TI case show an error of roughly 23%. At higher resolutions, the error for the RNO slowly increases to approximately 9.5%, but eventually levels off and shows no indication of further increase. At lower resolutions, the RNO initially maintains relatively small errors, but below 80, the error rapidly escalates as it approaches the stability limit, consistent with the observations made by Liu et al. [14]. Conversely, the GRU and LSTM architectures experience a rapid decay in the prediction quality as the time increment changes compared to the training

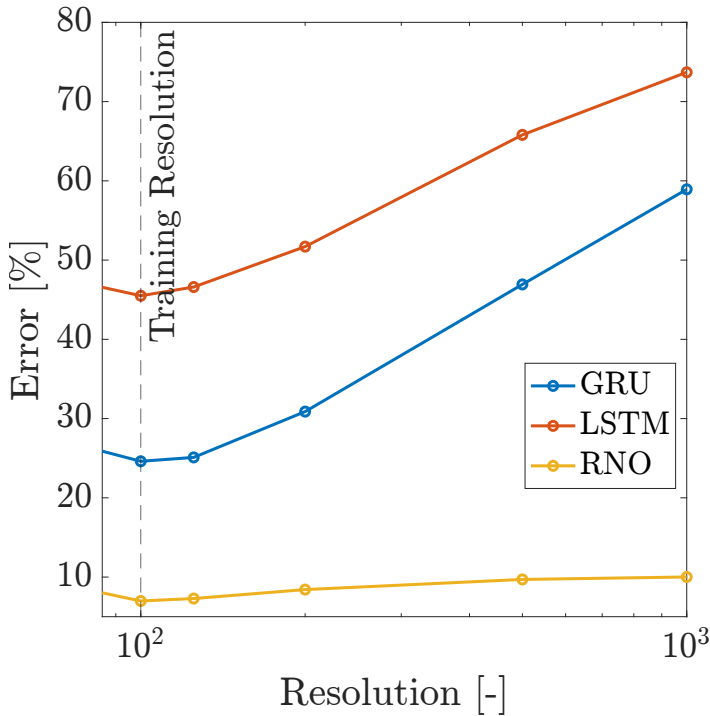


FIGURE 4.18: Resolution dependent test error of the GRU, LSTM and RNO. The GRU and LSTM networks show a strong resolution dependence with the error increasing as soon as one moves away from the training resolution. The RNO's error at finer resolutions, however, remains bounded.

resolution. This limitation becomes particularly significant when the goal is to employ the trained RNN model in a multiscale framework where the resolution may vary. The RNO demonstrates a robust performance, as long as the actual resolution does not fall below the stability limit, ensuring sensible predictions and maintaining accuracy close to the trained level. This feature of the RNO is of high importance. As we have shown, the training resolution is relatively large, leading to good training performance. The true strength of the RNO lies in its ability to almost arbitrarily refine the temporal resolution. We show the use of this property in section 4.5.4, where we perform multiscale impact simulations.

We have thus proven that the RNO naturally includes self-consistency, an important step for applications in multiscale models, as the deformation increments in FE-simulations typically occur on orders of magnitude lower time scales than the training resolution. This advantage of the RNO is crucial in the following step, the implementation in a commercial FE software. Before delving into this step, however, let us perform a final investigation on the RNO, linked to its state variables.

4.5.3 *Behavior of State Variables*

The presented architecture has demonstrated impressive capabilities in learning and predicting complex plastic material behavior with relatively small amounts of training data. Further, the predicted temperature-aware response of the material aligns well with the predictions from the CP model presented in chapter 3. Moreover, it outperforms other architectures like GRUs and LSTMs in accuracy and training time. The flexibility of the RNO further allows for the reduction of timestep as desired, making it well-suited for implementation in dynamic simulations (see section 4.5.4).

One fundamental question remains, however; How does the RNO achieve this? And moreover, is it possible to extract any meaningful insights from the state variables or the model's learning process? Previous research, such as that by Liu et al. [14] or Bonatti and Mohr [76], has managed to identify some meaning in the state variables for the averaged responses of polycrystals. For instance, [250] revealed that the internal variables have a meaningful interpretation in the 2D mean-field response of polycrystals, potentially representing the independent entries of the plastic strain tensor. A similar understanding was found in Bonatti and Mohr [76], where the architecture identified the exact number of internal variables used in the underlying model, along with the five independent components of the plastic strain tensor. We explore this path in the present work as well.

The architecture's nonlinear mapping between state variables and the final stress, unlike the linear map used in the MSC architecture used in Bonatti and Mohr [76], renders this task quite complex. Nevertheless, we can investigate the evolution of state variables for distinct loading cases. Under cyclic loading we observe that certain state variables mimic the cyclic evolution of deformation, see Figure 4.15 (a). We show the evolution of all state variables as a heat map with the time on the y -axis and the internal variable identifier on the x -axis, such as to get a visual representation of the states. We observe that certain state variables show similar behaviors

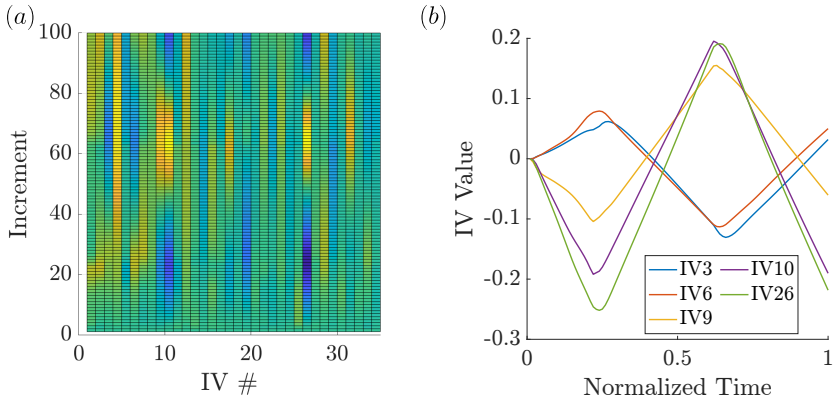


FIGURE 4.19: Evolution of a given set of internal variables depicted as a surface plot with the y -axis being the time increments and the x -axis depicting the state variable identifier (a). The color indicates intensity. In (b), we show the five state variables that were identified to follow the cyclic deformation closely.

decreasing and increasing in intensity cyclically, thus mirroring the cyclical load. From Figure 4.19 (a) we identify five internal variables that exhibit a cyclical behavior. Further exploration reveals that they precisely mirror the cyclic load, as shown in Figure 4.19 (b). This finding is intriguing in the light of Bonatti and Mohr [76] and Liu et al. [250]’s findings. They identified five state variables corresponding to the five independent entries of total plastic deformation. While direct comparisons beyond this point are not (yet) possible, we believe that there is an inherent connection between the state variables and the deformation history of the material. These results, however, remain indicative at this stage.

We further test our hypothesis by evaluating the evolution of the hidden states for known deformations of the TI-validation samples. Notably, we consider shear along the 23– and 13–directions, tension along the 11– direction (i.e., tension along the ND), and tension along the 22– (RD) direction. Each of those cases should (in theory) lead to the activation of different components in the strain tensor. We perform all of those tests on the RNO trained for the temperature-dependent data. Again, we show the results of the internal variables for each case as a heat map, see Figure 4.20.

We observe that, depending on the different deformation cases, the activity of the states changes, and there appears to be unique combinations of states for each of the deformation cases. This is sensible in the light of the

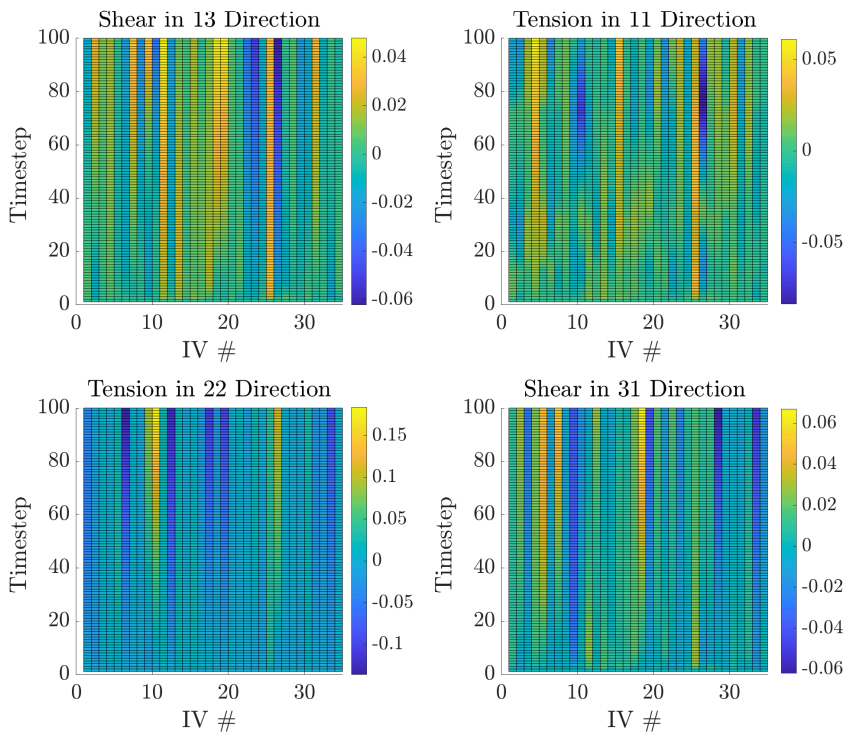


FIGURE 4.20: Heat map showing the time evolution of the activity levels of the states in the TD-RNO at 25°C for four distinct loading cases.

physics at play, for instance, in tension along the 11– vs. 22– directions, different deformation mechanisms are activated and would lead to different strains inside the material. In contrast to results by Bonatti and Mohr [76],

We further observe that each of those deformation modes leads to the activation of various deformation modes such as slip and twinning. Naturally, this begs the question of whether the state variables are related to the slip and twin systems of the material. Our findings remain, unfortunately, inconclusive at this point. First, we experimented with identifying a map between the evolution of the state variables and the evolution of the averaged slip and twin activities, such as shown previously in chapter 3. We trained a single-layer neural network to map the output of net \mathcal{G} to the averaged

slip and twin activities of the polycrystal with the goal of identifying such a linear relationship

$$\mathcal{L} : \xi \mapsto \gamma, \quad (4.27)$$

where γ represents the average slip and twin activities of all 200 grains in the polycrystal. We first investigate the prediction for a single sample of the data set and observe a good agreement with the ground truth right away, see Figure 4.21. We observe a very good fit between the prediction and the ground truth, however with some oscillatory behavior in the twin systems. Clearly, a linear relationship *can* be found between the internal variables and the slip activities for this simple case. Considering the strong correlation between the deformation and the evolution of the internal variables, this may come as no surprise. Upon increasing the number of training samples, however, the error quickly deteriorates and it becomes impossible to identify a common map between the state variables and the slip and twin activities. We hypothesize that this has to do with the numerous possible combinations of slip in the material to accommodate certain types of deformations. Further attempts were made to improve the mapping, such as by investigating only the total amounts of basal, prismatic, and pyramidal slip or by simplifying even further, to account only for $\langle a \rangle$ and $\langle c + a \rangle$ systems. However, our efforts to find a global map were, so far, unsuccessful, even by abandoning the idea of a linear map and increasing the number of layers in the network. Nevertheless, it is clear from the behavior of the state variables, such as outlined in Figures 4.19 and 4.20 that they hold a certain meaning. What this meaning could be, is left for future work to uncover.

4.5.3.1 *Temperature-Varying vs. Temperature Invariant State Variables*

Finally, an additional topic concerning the state variables warrants further investigation. As discussed in section 4.3.2.2, we observed the intriguing phenomenon of requiring additional state variables to accurately represent the temperature-dependent behavior of the material. In this section, we conduct a deeper analysis of this behavior, employing the temperature-dependent RNO. Our hypothesis is that certain internal states primarily or strongly correlate with changes in temperature, while others are more closely linked to deformation.

To test this hypothesis, we closely examine the evolution of the internal states of the fully trained RNO with temperature dependence, utilizing samples from the temperature-independent validation (TI-V) and temperature-independent deterministic (TI-D) datasets. Specifically, within

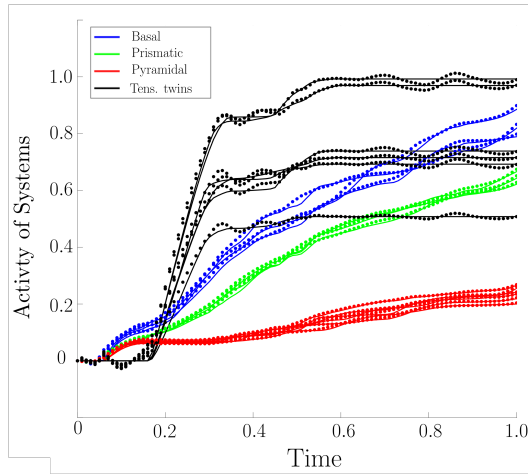


FIGURE 4.21: Prediction of the slip and twin activity for a single sample of the dataset via one linear layer. The solid lines are the results from the Taylor model, whereas the dotted lines are the predictions from the network.

the temperature-dependent validation (TD-V) dataset, we identify three commonly occurring deformation cases at different temperatures: shear in the 23-direction, shear in the 13-direction, and tension in the 11-direction.

To assess the effect of temperature, we follow the outlined procedure below:

- First, we calculate the mean activation values of individual states over time for each specific temperature.
- Second, we construct an array of values for each sample, which contains the time-averaged means of the states.
- Finally, we compute the variance of this array with respect to temperature as a measure of the temperature's impact.

This methodology allows us to identify the state variables that genuinely exhibit high variance in response to temperature changes, while others should demonstrate minimal or no change. We apply this approach to the entire set of 50 samples in the temperature-independent validation (TI-V) dataset, while keeping the temperature constant, to evaluate the effect of deformation using the same measure. The findings from these analyses are presented in Figure 4.22.

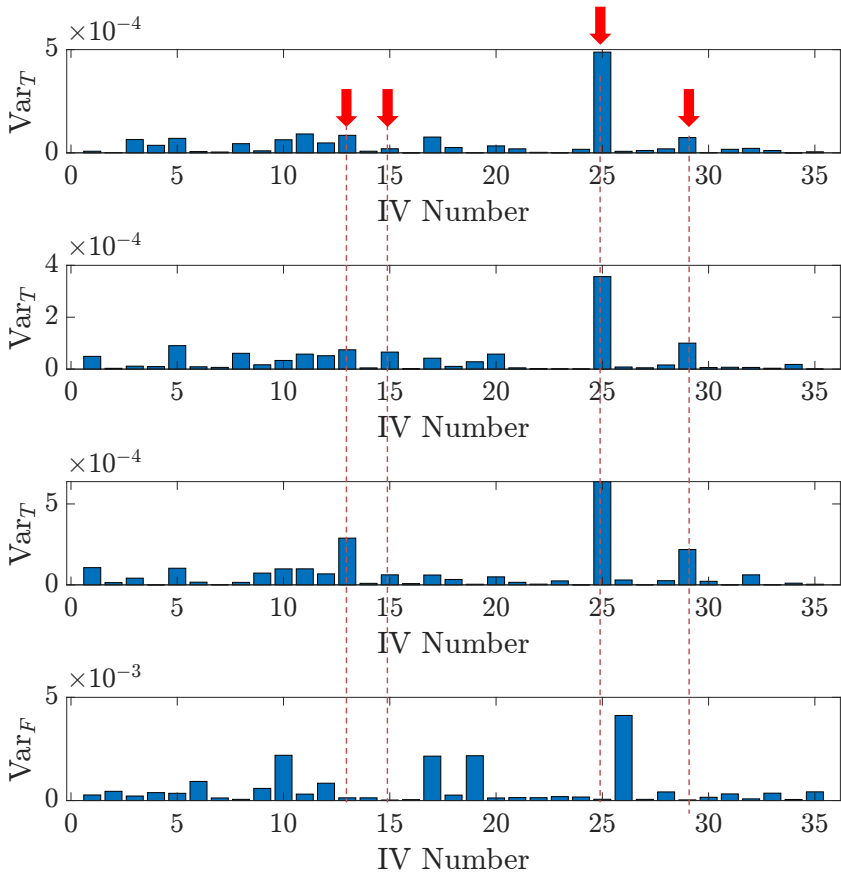


FIGURE 4.22: Variance of state variables with respect to temperature, denoted by Var_T , and mechanical deformation at room temperature, denoted by Var_F .

We observe several noteworthy phenomena from our analysis. First, the individual state variables exhibit varying levels of variance, with a few state variables showing significant activity, while most exhibit only minor variance in response to temperature or deformation. It is important to note that the absolute values of the state variables do not directly correspond to their importance in our context.

Second, in cases where temperature changes are considered, certain state variables demonstrate higher variance in activity levels compared

to others. Although the specific values of these states differ across the three realizations of the test, a discernible pattern emerges. Notably, a group of states, indicated by red arrows, displays the greatest variance with temperature, while the other states remain relatively unaffected.

Third, we find that some state variables show no significant changes with temperature but exhibit considerable variance when subjected to different loading conditions (denoted as Var_F). Conversely, a different set of state variables display significant variance in response to deformation modes but remain insensitive to temperature changes. However, it is worth noting that the majority of state variables demonstrate some degree of variance with both temperature and deformation.

These findings lead us to hypothesize that certain state variables play a prominent role in capturing temperature variations, while others are primarily associated with mechanical deformation. The implications of these findings raise intriguing questions regarding the additional memory requirements associated with temperature effects, namely that the thermal past of the material also introduces a history dependence.

We examine this intriguing phenomenon further. To this end, we compare the final stresses of polycrystals undergoing a predefined strain path, but with two kinds of temperature paths – one linearly connecting the initial and final temperatures, and one varying randomly such as used in the TV data set. We put an emphasis on both temperature paths to begin and end at the exact same temperature. Our hypothesis is that if temperature induces a history in the material, then the final stresses should differ. For our investigation, we chose a single deformation path and 100 pairs of random and linear temperature paths to predict with the RNO. Further, we repeat the same experiment a few times in the Taylor model as a control mechanism to ensure our results are not linked to the nature of the RNO.

We show the results of our study in Figure 4.23. In (a), we illustrate the maximal difference between the varying and linear temperature pathways for one of the samples. In (b), we show the distribution of the final stress differences, $\sigma_{11}(t_{\max})$, between the linear and random temperature histories. In addition, we show the temperature at which the experiment terminated. As expected, if the temperature paths are quasi-equivalent and have small differences in temperatures at any given time, the final stresses coincide. However, with increasing d_T , we observe a clear trend towards an increasing difference in the ultimate stresses. This trend persists throughout the range of the final temperatures, although it is apparent, that the differences are smaller for higher ending temperatures. We attribute

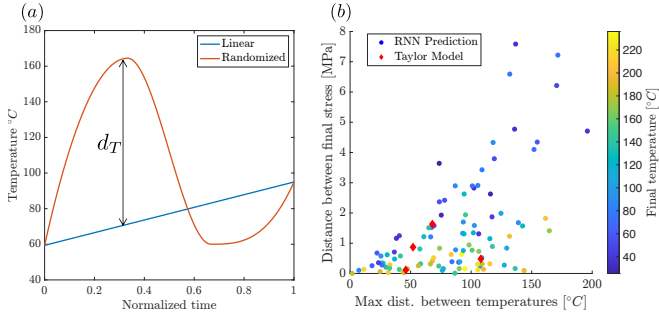


FIGURE 4.23: Depiction of the linear and varying temperature paths of a sample used for data generation in (a) – we show the maximal distance between the temperatures with d_T . (b) shows the distribution of the stress difference (in MPa) of linear v.s. varying temperature paths along the same deformation pathway. Here, 100 pairs of linear v.s. varying temperature paths are shown for the same deformation path. The dots represent the predictions from the RNO, whereas the red diamonds show the results from the Taylor model for comparison. Finally, the color indicates the temperature at the final time step.

this phenomenon to the overall lower stress levels associated with elevated temperatures. Ultimately, our findings suggest that the temperature history influences the final stresses of the material and that the additional internal variables needed for the temperature-dependent RNO are related to the corresponding phenomenon. At this point, however, the exact meaning of the additional variables is still unknown and warrants further investigation in future work.

4.5.4 Application in Multiscale Simulations

In the following section, we shift our focus to the application of the RNO as a surrogate model. The utilization of surrogate models offers a significant advantage in terms of computational efficiency for large multiscale simulations [203]. Conventional physical models, like CP, require the repeated updating of numerous physical parameters and equations at each iteration. In dynamic simulations, explicit time updates are often employed due to the small time steps involved, leading to a rapid increase in computational inefficiency and time consumption with traditional models. However, our RNO was trained efficiently on a large timestep, and its resolution indepen-

dence, as discussed in section 4.5.2.1, allows it to be seamlessly applied in dynamic simulations without any further adjustments.

To demonstrate the performance and potential applications of our architecture, we conduct a series of multiscale simulations that would have been impractical or even infeasible using other physical models within short time frames. We assess the runtime improvements achieved by employing the RNO as a surrogate model whenever possible, providing estimates of the computational time saved compared to traditional approaches. The ability to efficiently perform these simulations with the RNO surrogate underscores the value of our approach in addressing computational challenges and advancing the scope of applications in multiscale simulations.

4.5.4.1 Taylor Anvil Test

In order to demonstrate the capabilities of the RNO architecture, we conduct a Taylor anvil test. The test involves a sheet of rolled magnesium (Mg) with a specific texture, as described earlier. Cylinders are extracted from the sample with diameters of $D = 1$ mm and heights of $H = 5$ mm, oriented along the rolling direction (RD) and the normal direction (ND), respectively. This orientation ensures that the majority of Mg grains are aligned longitudinally or radially.

The simulations involve cylinders impacting a frictionless wall at time $t = 0$ with an initial velocity of $V = 200$ m/s. We conduct the simulations at three different temperatures, 25°C , 115°C , and 205°C , for both configurations of the cylinder (RD and ND). The goal is to study the material's response under these conditions and observe any temperature-dependent effects on the deformation behavior. By performing these simulations with the RNO as a surrogate model, we aim to showcase its efficiency in handling complex multiscale problems, like the Taylor anvil test, which would otherwise be computationally intensive and time-consuming using traditional physical models.

In both cases of the Taylor anvil test, an elastic wave is transmitted upon impact, followed by plastic deformation. Cross-sections of the impactor after 10^{-6} ms are shown in Figures 4.24 (a) and (b), which illustrate the impact of the change in orientation. At this time, the elastic wave has largely dissipated from the impact zone, allowing for a more accurate investigation of the plastic behavior.

In Figure 4.24 (a), the sample is oriented such that the normal direction (ND) lies in the plane of impact, resulting in compression along the transverse direction (TD). The deformation is borne by a mixture of basal

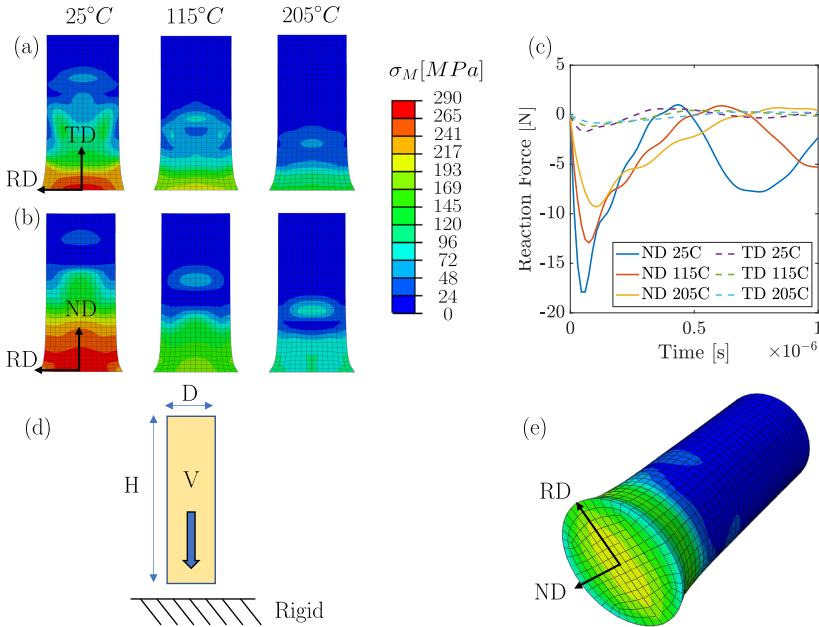


FIGURE 4.24: Von Mises equivalent stress distribution in the Taylor anvil for impact along the (a) TD and (b) ND at 25, 115, and 205°C after $e \times 10^{-7}$ seconds. The corresponding reaction forces over the duration of the simulation are shown in (c). Observe the varying stress levels for both cases. (d) shows a set of the simulation setup and (e) exemplifies the anisotropic stress distribution on the impact face at 115°C under impact along the TD (configuration (a)).

and prismatic slip, leading to a relatively weak material response. The maximum stress is concentrated at the center of the impact zone, where a combination of compression along the longitudinal direction (RD) and tension in the radial direction is experienced. Tension along the RD or TDs is relatively stiff compared to the tensile deformation along the ND of the rolled sample, leading to the observed asymmetric response. As the deformation progresses, twinning is expected to occur, leading to a drastic increase in stress along the ND. This behavior persists at elevated temperatures, as shown in Figure 4.24 (e) for the case at 115°C.

Conversely, impact along the ND leads to a different overall response, as the material is oriented such that the ND aligns with the impact direction. This results in a much stiffer material response compared to the previous

case. Overall higher stresses are observed in a larger region near the impact zone. The stress level decreases rapidly with temperature, rendering the overall response more isotropic.

Figure 4.24 (c) shows the reaction forces measured at the nodes of the impact face for all six cases. Large differences are observed between the two orientations and across the temperatures, as expected. The RNO accurately captures the temperature-dependent elastic component of the CP model, as evident from the reaction force responses, particularly in the ND impact cases. The reaction force rapidly increases, followed by the propagation and reflection of an elastic wave at the free end of the material. The wavelength of the elastic wave changes with temperature due to the variation of Young's modulus, which is captured by the hydrostatic component of the stress, as described earlier.

4.5.4.2 Plate-Impact Test

As another application of the present RNO, we conduct a numerical impact test on a plate of Mg along the rolling direction (RD) at room temperature. During such loading conditions, the temperature in the material is known to rise [22]. This temperature increase is generally attributed to two phenomena.

First, a portion of the plastic energy is dissipated into heat [22, 255]. Typically, a linear relationship is assumed, where the increase in temperature is directly correlated with the dissipated energy through a proportionality factor. In the case of Mg and AZ31B, it has been shown that this factor depends on the orientation of the material [255]. However, in the case of impact along the RD, the percentage of plastic energy dissipated into heat is fairly low, and therefore, for the time being, we neglect this contribution.

The second mechanism is associated with the quasi-isentropic elastic compression of the material [22]. This phenomenon can be described by the equation [256]

$$dT = \frac{a_{\text{TH}} \exp(-mp) T dp}{C_p \rho_0}. \quad (4.28)$$

Here, T represents the temperature, $a = 7 \times 10^{-5} \text{K}^{-1}$, $m = 0.0021 \text{GPa}^{-1}$, p is the hydrostatic pressure, and ρ_0 is the initial density of the material. The specific heat, $C_p = (900 + 0.446T) \text{Jkg}^{-1}\text{K}^{-1}$. We solve (4.28) explicitly for every timestep in Abaqus.

Figure 4.25 (a) shows the Von Mises stress distribution across the plate during impact at 10^{-8} , 8×10^{-8} and $1.6 \times 10^{-7} \text{s}$ after impact. Stress peaks

are observed near the edge of the rounded impactor which relatively rapidly dissipates in the material. In Figure 4.25 (c) we observe that the stress distribution inside the material is anisotropic due to the differences between the ND, TD and RD. Unfortunately, there is no reliable comparison data available for this test. However, we are able to compare the evolution of the temperature for the predicted stresses with experimental results from Ravindran et al. [22].

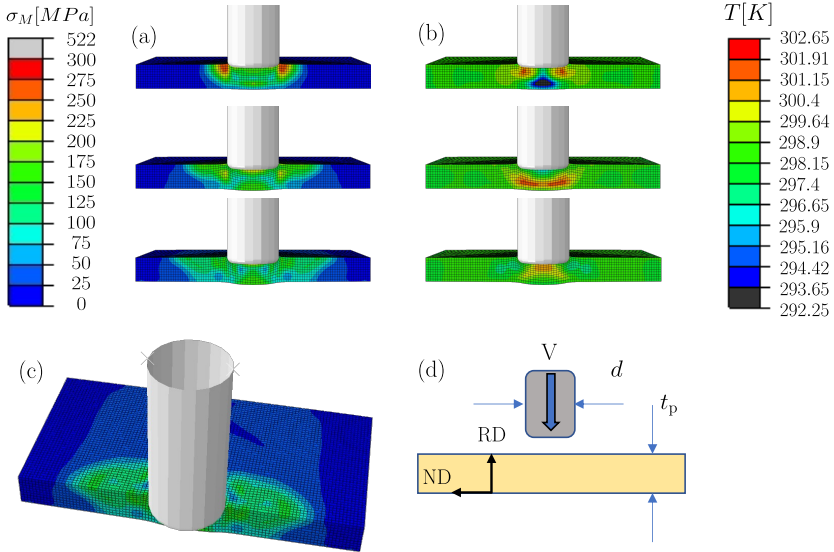


FIGURE 4.25: Depiction of the Von Mises Stress (a) and the temperature distribution (b) in the Mg plate during impact. Distribution of the stress showcasing the anisotropy in Mg (c) at 25°C during impact. The geometry of the plate impact test (d).

Figure 4.26 shows the results of the isentropic hardening in a Mg sample from Ravindran et al. [22]. They conducted pressure shear-plate experiments under high velocity impact and observed temperature rise due to shear and normal shock. The simulated temperature rise of our experiments agrees well with the experimental data, as shown in Figure 4.26. We note that our results were obtained for far smaller pressures, limited to roughly 1-2 GPa, but follow the same trend line as shown in Ravindran et al. [22]. This indicates that the presented multiscale setup provides a sensible approximation for the impact application under consideration.

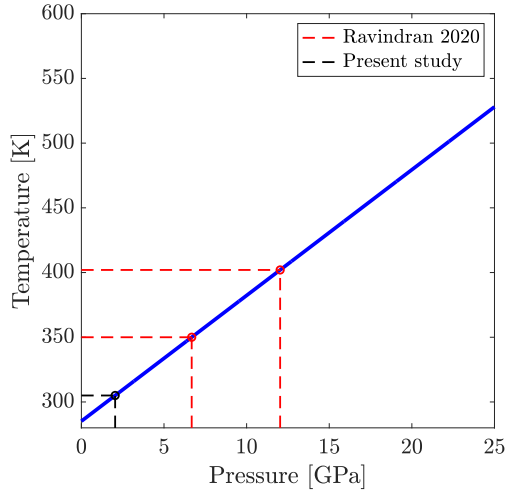


FIGURE 4.26: Isentropic heating contributions vs. the hydrostatic pressure. Comparison of the experimental study by Ravindran et al. [22] and our present model. The model prediction coincides well with the observed trends in Ravindran et al. [22].

4.5.5 Runtime Comparison

Finally, we perform a runtime comparison to showcase the speedup potential of using a surrogate model instead of the underlying CP model. Material point computations are performed with the CP-Taylor model with 200 grains on one side and the RNO on the other. Each computation is repeated five times and the average duration is reported. In each case, we perform simulations up to 10% compressive strain along the 11-direction in 100,000 steps at a strain rate of $\dot{\epsilon} = 10^{-4}$. The total simulated time is thus 100 seconds and the timestep $\Delta t = 10^{-3}$ s. Simulations for the RNO are performed on a single core of a MacBook Pro 2019 with a 2.6 GHz 6-Core Intel Core i7 processor and 16 GB of RAM, whereas the Taylor model was run on one node of ETH's cluster Euler VI on 16 cores of an AMD EPYC 7742 processors and 64 GB of RAM. Both simulations run in a virtual environment on the system. The Taylor model is a highly efficient C++ application, while the RNO is a non-parallelized PyTorch job *without* CUDA support. In the next step, we also show the improvement with parallelization in the Taylor model vs. the RNO.

TABLE 4.3: Runtimes of the physical model vs. the RNO for multiple applications

Simulation	#steps	Simulation Time [s]	Threads cores
Taylor 200 Grains	10^5	77.07	1 / 1
Taylor 200 Grains	10^5	8.520	16 / 16
Taylor 200 Grains implicit	4000	48.7	1
RNO	100	0.0583	1

Table 4.3 shows the execution times for the RNO and Taylor models in sequential and parallelized execution. Compared to the single-core sequential Taylor model, the RNO yields a 1321.9 times speedup, and compared to the parallelized 16-core Taylor model it still represents a speedup of 146 times. This is likely due to the improved stability and the much larger timesteps the RNO can accommodate. Even when the explicit solver in the CP model is replaced by an implicit solver, the RNO still leads to an 835 times faster execution. In addition, the implicit solver has its own drawbacks, especially in dynamic simulations and it faces stability issues, described in Chang and Kochmann [107]. The RNO is much more robust than the CP models we investigated, which was especially noticeable in the Abaqus simulations.

4.6 CHAPTER SUMMARY

In conclusion, we have introduced a novel Recurrent Neural Ordinary (RNO) architecture for temperature-dependent, anisotropic plasticity problems and compared its performance to state-of-the-art RNNs used in surrogate modeling. Our findings can be summarized as follows:

- The RNO exhibits easier and more accurate training compared to LSTM and GRU-based RNNs with the same amount of data. It generally represents the material behavior better and with fewer data than reported in literature [75, 76, 80], notably, the optimizer converges faster and the accuracy is higher.
- Further, the RNO naturally exhibits self consistency at resolutions finer than the training resolution. The error remains bounded and the predictions accurate, a capability lacking in LSTM and GRU architectures. This feature effectively allows the RNO to be employed for effective time steps anywhere below 1 second and in general, below the training resolution.

- Additionally, we have identified temperature-dependent phenomena that require a larger number of state variables in the RNO. Some of these state variables are solely dependent on temperature, while others are influenced by the mechanics of the material. However, the full interpretation of these state variables remains a topic for further investigation.
- The RNO performs well on validation data, accurately capturing the overall material response, including key mechanics such as phase-change-induced nonlinearity due to twinning and material anisotropy over a range of temperatures. It also effectively captures the Bauschinger effect at multiple temperatures and various loading conditions.
- Integrating the RNO into Abaqus/Explicit simulations leads to significant speedups and improved simulation stability.

Limitations of the methodology naturally persist. In the present configuration, the RNO surrogate does not offer as detailed physical insight as a CP model, however, this is likely possible to achieve in the near future for instance by including slip and twin activity as a metric to be learned or providing the RNO with further information on the deformation modes. Further, the model is currently only validated for one type of fixed texture. This limits the model for now, however, thanks to short training times and ease of application, the RNO can be easily extended to multiple textures. Finally, it is not known whether the presented RNO could be subject to vanishing or exploding gradient problems, as these issues did not arise in the study. Technically, however, it is possible that these issues could limit the wide-spread use of the RNO architecture and a solution is needed.

From our findings, new opportunities for future research also arise. Texture evolution, particularly in the context of magnesium, remains an interesting topic to explore. Additionally, utilizing the RNO as a pre-trained network for transfer learning in other materials is a promising avenue for further investigation. Furthermore, the RNO's speed and efficiency make it well-suited for inverse design problems, opening new possibilities for its application.

CONCLUSION AND OUTLOOK

5.1 CONCLUDING REMARKS

Let us finalize this thesis with some concluding remarks on the success of our work in the context of the primary research goals. The goal of this work was to identify and model thermal effects on the microstructure of the material and the corresponding response of Mg in an efficient manner in a push toward an ICMD framework. This goal was further divided into two parts.

In the first part, the need for a dependable and efficient predictive model, capable of capturing the thermal effects on the microstructure evolution in Mg and quantifying the competition between the CT and pyramidal II systems that still poses an open question in the field, was identified. To this end, a novel model was formulated, calibrated, and validated. This temperature-aware CP model for pure Mg was developed and implemented in two distinct flavors - one including the CTs and one describing the behavior solely based on the pyramidal II systems. The results were compared and critically assessed. Single and polycrystal simulations we performed as means to calibrate and validate the models. Notably, single-crystal channel-die simulations with relaxed material-point simulations were performed, capturing the reported stress-strain and slip behavior reported by Kelley and Hosford [8] and Wonsiewicz and Backofen [19] over the range of temperatures from 25°C to 250°C as well as polycrystalline behavior reported by Wonsiewicz and Backofen [19]. Further, we investigated the competition between said mechanisms in a comparative study of both models. We identified that CTs play a significant role in the early stages of deformation at RT and that their presence can explain the presence of basal slip in the early stages of c -axis compression of single crystals, as observed by Wonsiewicz and Backofen [19]. Due to the larger twinning shear, slow propagation, and high hardening levels associated with the CTs, however, they appear ill-suited to accommodate large amounts of plastic deformation. We also observed less twin activity at elevated temperatures where the balance tips in favor of the pyramidal II systems, which is in agreement with experimental studies and observations. Overall, our findings agree well with the hypothesis and offer an explanation that the main driver behind the low

ductility of Mg at lower temperatures lies with the strong hardening and pinning of the pyramidal $\langle c + a \rangle$ dislocations since CTs play too small a role in accommodating large amounts of plastic deformation. These findings capture the experimental observations and indicate that the CT system is a symptom of the aforementioned strong hardening of the pyramidal II systems. Our results indicate that the key to improved ductility in Mg alloys therefore lies in improving the mobility of pyramidal II dislocations. Finally, rolling simulations with the relaxed Taylor model as described by Chang [147] were performed, during which good qualitative agreement with the expected results was observed.

In the second part of the thesis, the aim was to further improve the efficiency of the modeling process. To this end, the temperature-dependent constitutive behavior of the material was learned via a custom architecture RNO based on learning a set of state variables such as to describe the state of the material entirely. The RNO was trained on randomized stress-strain data for three distinct use cases, including temperature-dependent and independent loading paths. The need for additional state variables was identified in the latter cases, allowing for the distinction between temperature and mechanistic state variables as two archetypes of states required to describe material behavior. In addition, it was shown that the present architecture outperforms RNNs such as LSTMs and GRUs in a comparative study in terms of accuracy, training time, and especially, the fact that the formulation of the RNO seamlessly leads to self-consistency. The RNO's predictions were validated via the stress-strain response of textured Mg polycrystals without any prior knowledge of the underlying physics, and show that the RNO captures complex anisotropic plastic behavior as well as the effect of the twinning-induced phase transformation on the stress. Finally, the RNO was used as a surrogate model and included as a VUMAT in ABAQUS/explicit to perform true multiscale simulations at unprecedented speed. During this process, we further validated the sensibility of the results by comparing them to experimental results of heat generation during isentropic deformation by Ravindran et al. [22].

The results from both parts of this thesis clearly meet the goals and represent a clear improvement in the state of the art, both in the realms of physical and data-driven modeling. We have contributed to a better understanding of the competition between the CT and pyramidal slip systems and enriched the field with an easy-to-calibrate predictive temperature-aware material model for hcp materials, based on a reduced number of slip- and twin systems. In addition, the potential of our RNO to learn and represent

complex material behavior from limited amounts of data, as well as the massive speedup and robustness they bring to multiscale simulations, was clearly showcased. This makes the method suitable for an ICME (or ICMD) approach and highlights the potential yet to be discovered in these methods.

The impact of these contributions is still to be seen in the future, however, with both approaches, we laid the groundwork for future research, both in the realm of physical modeling, as well as for opportunities related to data-driven methods in mechanics and plasticity.

Drawbacks and Solutions

Naturally, our methods also suffer from drawbacks and require further improvements. First, the CP model we introduced relies heavily on the availability of single-crystal data for calibration. This data is not available for a majority of the alloys, hence bottom-up calibration is a limiting factor. This issue can, however, be bridged with enhanced calibration methods. For one, the approach of Herrera-Solaz et al. [89] could be used to calibrate the CP model for alloys. Further, due to the efficiency of the Taylor model, even a relatively simple optimization approach could prove to be promising for calibrating the material behavior for a given texture for alloys. This would lead to unprecedented versatility for CP modeling.

Further, recrystallization evidently plays an important role in Mg even at relatively low temperatures [49, 50]. Hence, for a more complete picture, future work should aim at including recrystallization in Mg. Ground-laying work was already performed by e.g. Walde and Riedel [68] and Tam et al. [69], however, these models still rely heavily on empirical parameters and thus do not offer a proper predictive methodology. The predictive model we introduced can be used for further evaluation of dynamic recrystallization (DRX) mechanisms in Mg and its alloys. With a solid foundation in physics and an efficient computational approach, the addition of recrystallization effects should be possible without the need for the empirical parameters needed in Walde and Riedel [68] and Tam et al. [69]. Further, the Taylor model has significant advantages over the VPSC model, used in Walde and Riedel [68] and Tam et al. [69], when it comes to modeling DRX. Newly formed grains are mostly elastic and the assumptions in the VPSC could lead to misrepresentation of the energies in the material which are often used to compute grain growth and further recrystallization waves [59, 84]. Additionally, the formation of new grains increases the computational load, even in efficient mean-field models [84]. Here we see a potential for the RNO to represent single-crystal stress-strain relationships and serve as a

highly efficient surrogate for DRX simulations, cutting the computational expenses even further. This latter approach would require further work in including the single-crystal slip behavior or texture reorientation in the RNO description. The data for this process is, however, easily obtainable and no major concerns around its feasibility exist to date.

Third, a promising path lies in further enhancing the physical model with additional features, such as rate-dependence and solute- and precipitate-hardening effects and mechanisms. The addition of these effects would prove to be the first holistic approach of this type for Mg and is subject to ongoing work [257]. The addition of the solute and precipitation hardening effects is relatively straightforward. Preliminary work on these topics has already been carried out. For instance, the precipitation-hardening effects have been implemented. The calibration and validation thereof, however, still remain an open challenge. As explained in Cepeda-Jiménez, Castillo-Rodríguez, and Pérez-Prado [39], different types of slip systems have a tendency to shear the precipitates due to a high degree of compatibility of the respective slip systems. So while including the hardening effect of non-shearable precipitates is straightforward, understanding the effect of shearable particles in Mg still remains a somewhat open question. Further, the calibration of this holistic model suffers from the absence of data. We performed some work on including the grain-size refinement in Mg based on data from [3], however, too little is known about the effect of the grain size on the individual slip systems.

5.2 OUTLOOK

The next steps will include addressing these issues and enhancing the capabilities of our methods. Further, there is ongoing, soon-to-be-published work that proves to be an interesting application of the presented methods.

Ongoing Work

First, we showcase an interesting application of the model introduced in chapter 3, related to seeking solutions to some of Mg's existing drawbacks, notably the weak hardening effects observed during conventional aging. The presence of solutes and precipitates in alloys plays an important role in the path to future work, especially with respect to applications in industry. It was shown by Eswarappa Prameela et al. [1] that a high number density of small precipitates has the potential to harden Mg alloys substantially, and further, such nano-precipitates were observed experimentally in experi-

mental work by Eswarappa Prameela et al. [257]. Hence, a topic of interest lies in the optimization of processing routes for Mg alloys to promote nano-precipitation and solute cluster segregation, both of which are seen as a means to alleviate the weak thermal hardening exhibited by Mg as well as potential sites that facilitate the cross-slip of $\langle c + a \rangle$ [62, 63, 118].

To this extent, Eswarappa Prameela et al. [257] investigated the formation of precipitates in rolled Ag samples compressed under quasi-static conditions at various temperatures. In thermal aging, the precipitation sites are typically observed to be continuous precipitation inside grains and discontinuous precipitation at grain boundaries. These precipitation pathways typically lead to relatively large, shearable, and scattered precipitates, resulting in poor hardening effects [39]. In contrast *thermomechanical* aging an interesting phenomenon called deformation-induced precipitation (DIP) occurs [1, 257], leading to novel types of precipitation pathways, such as along propagating twin boundaries and in combined reaction zones, local occurrences where dynamic recrystallization and precipitation occur simultaneously. The nucleation paths are schematically shown in 5.1. It has been investigated in Al-alloys by [258], who saw promising results regarding an improved hardening response. Bignon, Shanthraj, and Robson [258] suggest that the average size of the precipitates during this process could be far inferior compared with thermal aging. This indicates an increased potential for hardening of the material. The plasticity model used in Bignon, Shanthraj, and Robson [258], however, is relatively simple in nature and accounts only for averaged measures. In our ongoing investigation, we couple efficient spectral methods with our crystal plasticity model from chapter 3 to investigate the dynamics of precipitation pathways. To this end, we combine the model with a nucleation criterion, such as the classical nucleation theory. It became evident that nucleation, as described by classical nucleation theories such as the Kampmann-Wagner nucleation (KWN) models [259, 260], is subject to various influencing factors. The process of new nucleus formation follows an exponential decay pattern, governed by an incubation time denoted as $\tau = 1/(2\beta^*Z^2)$. This phenomenon can be mathematically expressed as follows

$$i = Z\beta^*N_c \exp\left(-\frac{\Delta G^*}{k_B T}\right) \exp\left(-\frac{\tau}{t}\right). \quad (5.1)$$

Here, ΔG^* signifies the nucleation barrier, represented by the equation $\Delta G^* = \frac{f\gamma^3}{F^2}$, where f denotes a shape factor (for spherical precipitates, $f \leq 16\pi/3$ [138]). In this equation, N_c stands for the count of available

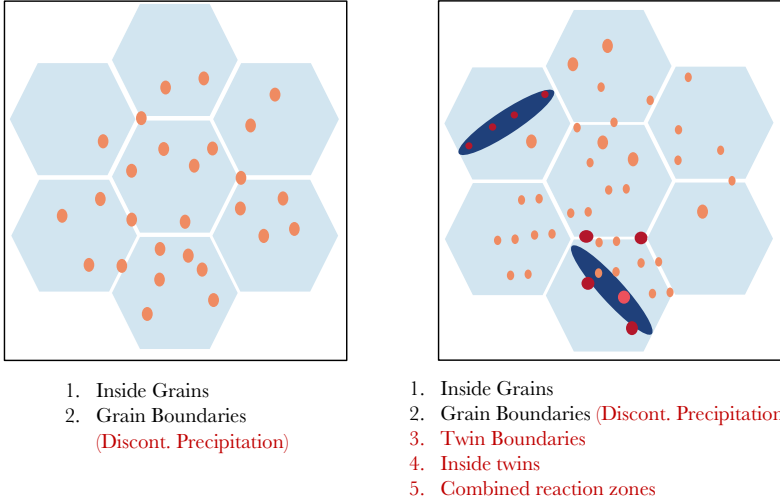


FIGURE 5.1: Deformation pathways in thermal aging (left) and during thermo-mechanical aging (right).

nucleation sites, while Z represents the *Zeldovich* factor ($= 10^{-2}$, as defined in [261]). β^* is the atomic attachment rate for the critical radius, given by [260], which relies on the lattice spacing a , diffusion coefficient $D_{m,Al}$, and mean site fractions in the matrix $u_{m,Al}$:

$$\beta^* = \frac{4\pi\rho^{*2}}{a^4} D_{m,Al} u_{m,Al} \quad (5.2)$$

The diffusion coefficient, in turn, depends on factors such as hydrostatic pressure, as demonstrated by Yi [63], as well as the count of excess vacancies [258], which can be expressed as:

$$D_{\text{eff}} = D_{\text{th}} \left(1 + \frac{c_{\text{ex}}}{c_{\text{th}}} \right). \quad (5.3)$$

Here, c_{ex} represents excess vacancies and $c_{\text{th}} = 23.8 \exp(-\frac{Q_f}{k_B T})$ [258, 262] stands for equilibrium thermal vacancies. Additionally, Bignon, Shanthraj, and Robson [258] presents an explanation for the evolution of excess vacancies using empirical constants, dislocation density, and terms accounting

for the generation and elimination of vacancies. This can be represented by the following equation:

$$\frac{dc_{\text{ex}}}{dt} = \left(\chi \frac{\sigma \Omega_0}{Q_f} + \zeta \frac{c_j \Omega_0}{4b^3} \right) \dot{\epsilon} - \left(\frac{\rho}{\kappa^2} + \frac{1}{l^2} \right) D_v c_{\text{ex}}. \quad (5.4)$$

In this equation, χ represents a phenomenological constant, indicating the proportion of mechanical work converted into vacancies. Ω_0 stands for the atomic volume of the matrix, b represents the Burgers vector, and c_j signifies the concentration of thermal jogs, calculated from the formation energy Q_j as $\exp(-\frac{Q_j}{k_B T})$. Lastly, ζ is a parameter relating the contribution of thermal jogs to the generation of excess vacancies and the dislocation density.

With a constitutive model such as introduced in chapter 3, the dislocation density must be obtained through an approximation, e.g., the Lukac-Balik model, proposed by Lukáč and Balík [263]:

$$\frac{d\rho}{d\epsilon} = K_1 + K_2 \rho^{1/2} - K_3 \rho - K_4 \sigma \rho^{3/2}, \quad (5.5)$$

Here, empirical constants K_1 through K_4 are involved in the formulation. For dislocation-based crystal plasticity models such as the one used in [141], the dislocation density could be directly obtained. Full-field RVE simulations conducted for a rolled Mg sample characterized by a uniform texture, such as shown in Figure 5.2, disclose significant variations in local measures inside the RVE, such as in the hydrostatic pressure and the stress. We show results for three temperature cases, 25°C, 100°C, and 200°C, in Figure 5.2. It remains to connect these insights with a suitable precipitation model and to compare the simulated and experimental results. In doing so, we propose a comprehensive modeling framework with the potential to facilitate the design of deformation-induced precipitation (DIP)-hardened Mg superalloys.

In theory, the essential components for creating such a fully coupled thermomechanical precipitation model are already available. Certain key elements necessary for the calibration and validation of this model, however, are still missing and require further work. The scarcity of quantifiable data surrounding precipitation in Mg renders the calibration of the multitude of empirical values a formidable challenge. Additionally, there is a significant lack of experimental validation concerning DIP particle densities and sizes in Mg alloys. Nevertheless, this model framework presents an exceptional opportunity to gain unparalleled insights into the underlying mechanisms

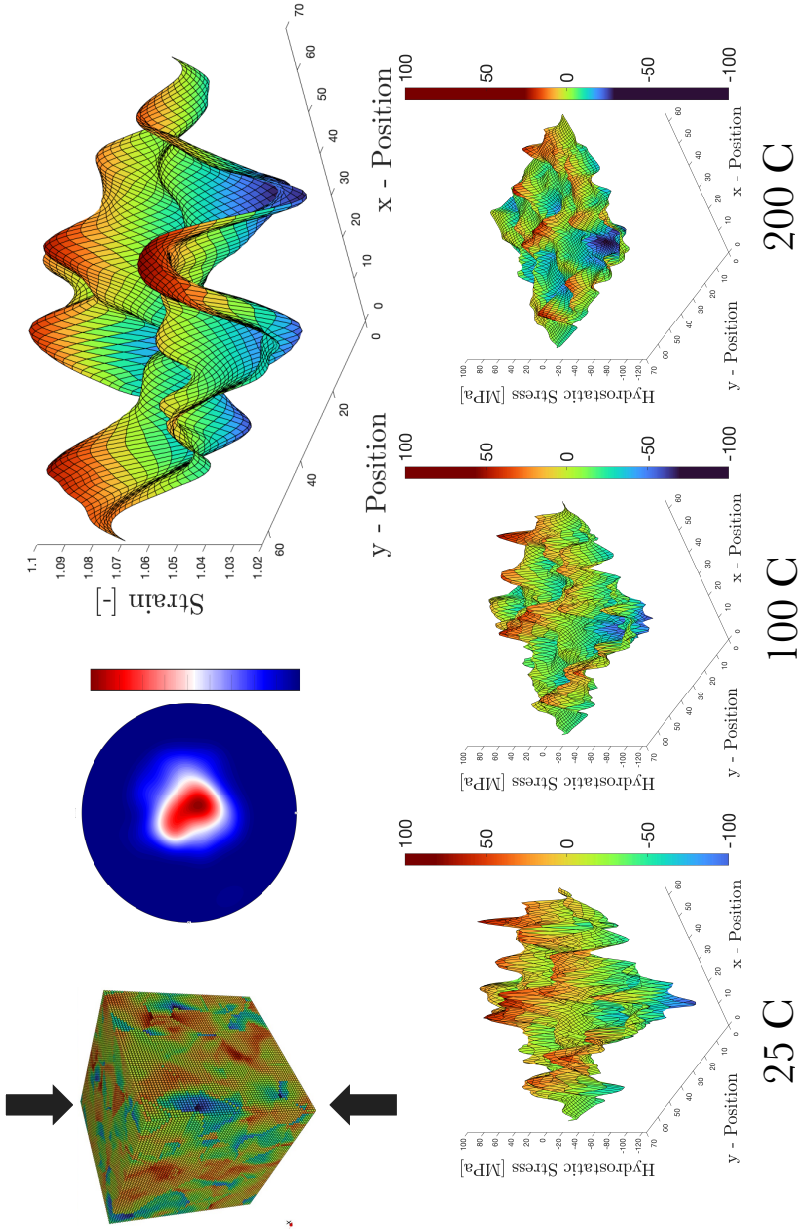


FIGURE 5.2: Heterogeneity of the stresses, hydrostatic pressure, and plastic activity across the RVE in a rolled Mg sample.

of Mg and with meticulous calibration, it holds the promise of becoming the foremost predictive model of its kind. the potential to significantly quicken the development of Mg alloys with the sought-after properties.

Opportunities Arising from Data-Driven Methods

Finally, let us also explore additional opportunities stemming from the use of data-driven methods, a field that offers uncountable room for future work.

One additional exciting potential avenue for future exploration involves the extension of surrogate modeling into the realm of full-field techniques. The RNO presented in chapter 4 learned to represent the mean-field stress-strain relationship of a highly intricate material. However, for an inversion of the design process and higher-quality outcomes in ICME, full-field resolutions are essential. Recent, work by [24] showcases the potential of Fourier neural operators [23] in conjunction with RNOs to learn and predict the full-field material response of a textured polycrystal based solely on the *average* deformation measure. The results are shown in Figure 5.3 (a) - (c). It is evident that the method still requires further refinement, however, the preliminary results show promise. The neural network correctly identifies the grains and grain boundaries as well as the stress peaks in the 2D space. The order of magnitude of the stresses is equally captured and even key areas such as grain boundaries and triple-junctions are identified correctly. Further, the operator introduced in [24] converges rapidly to an acceptable error. The presented results were obtained with limited data and a small network, hence we are confident that larger networks trained on more data will prove capable of capturing the stress distribution inside the domain. The prospects of these applications are virtually limitless, given the increase in computational speed coupled with the potential for straightforward inversion, offering entirely new avenues for materials design. Not least, such an architecture could be used to significantly enhance the computational speed of a fully coupled precipitation and hardening model, such as introduced above.

Another area for improvement that could prove fruitful lies with the inclusion of texture as a model parameter in the RNO. This would enhance the versatility of the approach presented in chapter 4 significantly. Various methods are conceivable for achieving this goal. Given that we have effectively learned the response of a strongly textured material, the RNO should also be able to learn the single crystal response. Moreover, as texture is essentially represented through grain rotations, applying the corresponding

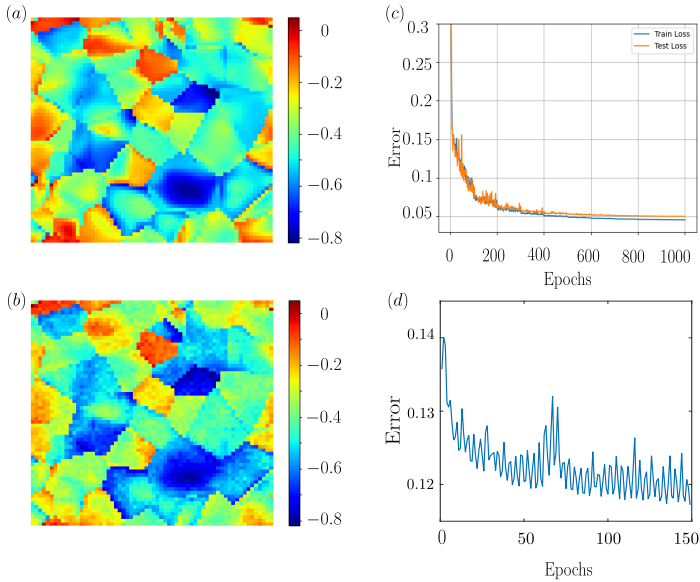


FIGURE 5.3: Ground truth (a) and prediction of an FNO network (b) of a 2D full-field simulation of a Mg polycrystal. The network is based on the work of Li et al. [23] and Wu, Hollenweger, and Liu [24]. The training performance of the network is shown in (c). These results are courtesy of Ms Rui Wu and Prof. Burigede Liu at the University of Cambridge. The training error of a transfer learning attempt of the existing RNO to a different texture is shown in (d).

deformation by rotating the deformation gradient is straightforward — and the RNO has demonstrated its capacity to accommodate arbitrary deformations. Preliminary outcomes of employing transfer learning to account for different textures are promising, as illustrated in Figure 5.3 (d).

In addition, enabling the RNO to capture rate dependence would broaden its capability to capture a wider spectrum of material behaviors. Initial findings by Bhattacharya et al. [79] indicate that expanding the RNO architecture to encompass a rate-dependent description is feasible, rendering this a potential low-hanging fruit for future research.

Finally, it remains to be acknowledged that Mg and its alloys continue to harbor numerous secrets to be unveiled and the duration of a single thesis is insufficient to comprehend them all. The potential embedded in these materials to aid us in grappling with depleting resources and climate change

remains untapped and necessitates further investigation. Additionally, the ongoing advancement of numerical methods heralds an exhilarating new era of possibilities in material design, left to future scientists to uncover.

BIBLIOGRAPHY

- [1] Suhas Eswarappa Prameela, Peng Yi, Yannick Hollenweger, Burigede Liu, Joey Chen, Laszlo Kecskes, Dennis M Kochmann, Michael Falk, and Timothy P Weihs. "Strengthening magnesium by design: integrating alloying and dynamic processing". In: *arXiv e-prints* (2021), arXiv.
- [2] J. F. Nie, K. S. Shin, and Z. R. Zeng. *Microstructure, Deformation, and Property of Wrought Magnesium Alloys*. Vol. 51. 12. Springer US, 2020, 6045.
- [3] N. Ono, R. Nowak, and S. Miura. "Effect of deformation temperature on Hall-Petch relationship registered for polycrystalline magnesium". In: *Materials Letters* 58.1-2 (2004), 39.
- [4] C. Liu, P. Shanthraj, J. D. Robson, M. Diehl, S. Dong, J. Dong, W. Ding, and D. Raabe. "On the interaction of precipitates and tensile twins in magnesium alloys". In: *Acta Materialia* 178 (2019), 146.
- [5] A Jain and SR Agnew. "Modeling the temperature dependent effect of twinning on the behavior of magnesium alloy AZ31B sheet". In: *Materials Science and Engineering: A* 462.1-2 (2007), 29.
- [6] Mariyappan Arul Kumar, Irene Jane Beyerlein, Rodney James McCabe, and Carlos N Tome. "Grain neighbour effects on twin transmission in hexagonal close-packed materials". In: *Nature communications* 7.1 (2016), 13826.
- [7] M. H. Yoo. "Slip, twinning, and fracture in hexagonal close-packed metals". In: *Metallurgical Transactions A* 12.3 (1981), 409.
- [8] E.W Kelley and W.F Hosford. "Kelley_and_Hosford.pdf". PhD thesis. University of Michigan, 1967.
- [9] Adrien Chapuis and Julian H. Driver. "Temperature dependency of slip and twinning in plane strain compressed magnesium single crystals". In: *Acta Materialia* 59.5 (2011), 1986.
- [10] B. Gurrutxaga-Lerma, D.S. Balint, D. Dini, and A.P. Sutton. "The mechanisms governing the activation of dislocation sources in aluminum at different strain rates". In: *Journal of the Mechanics and Physics of Solids* 84 (2015), 273.

- [11] Haidong Fan, Sylvie Aubry, Athanasios Arsenlis, and Jaafar A El-Awady. "The role of twinning deformation on the hardening response of polycrystalline magnesium from discrete dislocation dynamics simulations". In: *Acta Materialia* 92 (2015), 126.
- [12] A. Vidyasagar, Abbas D. Tutcuoglu, and Dennis M. Kochmann. "Deformation patterning in finite-strain crystal plasticity by spectral homogenization with application to magnesium". In: *Computer Methods in Applied Mechanics and Engineering* 335 (2018), 584.
- [13] Olga Ibragimova, Abhijit Brahme, Waqas Muhammad, Julie Levesque, and Kaan Inal. "A new ANN based crystal plasticity model for FCC materials and its application to non-monotonic strain paths". In: *International Journal of Plasticity* 144 (2021), 103059.
- [14] Burigede Liu, Margaret Trautner, Andrew M Stuart, and Kaushik Bhattacharya. "Learning macroscopic internal variables and history dependence from microscopic models". In: *arXiv preprint arXiv:2210.17443* (2022).
- [15] Wen Wang, Jinxing Liu, and Ai Kah Soh. "Crystal plasticity modeling of strain rate and temperature sensitivities in magnesium". In: *Acta Mechanica* 230.6 (2019), 2071.
- [16] Hideo Yoshinaga and Ryo Horiuchi. "Trans. JIM". In: *Trans. JIM* 4 (1963), 134.
- [17] Hideo Yoshinaga and Ryo Horiuchi. "On the nonbasal slip in magnesium crystals". In: *Transactions of the Japan Institute of Metals* 5.1 (1964), 14.
- [18] A. Akhtar and E. Teghtsoonian. "Solid solution strengthening of magnesium single crystals-ii the effect of solute on the ease of prismatic slip". In: *Acta Metallurgica* 17.11 (1969), 1351.
- [19] B C Wonsiewicz and W A Backofen. "Plasticity of Magnesium Single Crystals". In: *Trans Metall Soc AIME* 239 (1967), 1422.
- [20] Takaaki Kitahara, Shinji Ando, Masayuki Tsushida, Hiromoto Kitahara, and Hideki Tonda. "Deformation behavior of magnesium single crystals in c-axis compression". In: *Key Engineering Materials*. Vol. 345. Trans Tech Publ. 2007, 129.
- [21] T Obara, H Yoshinga, and S Morozumi. " $\{1122\} < 1123 >$ Slip system in magnesium". In: *Acta Metallurgica* 21.7 (1973), 845.

- [22] Suraj Ravindran, Zev Lovinger, Vatsa Gandhi, Michael Mello, and Guruswami Ravichandran. "Strength of magnesium at high pressures and strain rates". In: *Extreme Mechanics Letters* 41 (2020), 101044.
- [23] Zongyi Li, Nikola Kovachki, Kamyar Azizzadenesheli, Burigede Liu, Kaushik Bhattacharya, Andrew Stuart, and Anima Anandkumar. "Fourier neural operator for parametric partial differential equations". In: *arXiv preprint arXiv:2010.08895* (2020).
- [24] Rui Wu, Yannick Hollenweger, and Burigede Liu. "Learning the full-field plastic response of a 2D polycrystal".
- [25] Erica Lilleodden. "Microcompression study of Mg (0 0 0 1) single crystal". In: *Scripta Materialia* 62.8 (2010), 532.
- [26] Shinji Ando, Naoharu Harada, Masayuki Tsushida, Hiromoto Kitahara, and Hideki Tonda. "Temperature dependence of deformation behavior in magnesium and magnesium alloy single crystals". In: *Key Engineering Materials*. Vol. 345. Trans Tech Publ. 2007, 101.
- [27] BL Mordike and Tü Ebert. "Magnesium: properties—applications—potential". In: *Materials Science and Engineering: A* 302.1 (2001), 37.
- [28] Mustafa Kemal Kulekci. "Magnesium and its alloys applications in automotive industry". In: *The International Journal of Advanced Manufacturing Technology* 39.9-10 (2008), 851.
- [29] Yan Yang, Xiaoming Xiong, Jing Chen, Xiaodong Peng, Daolun Chen, and Fusheng Pan. "Research advances in magnesium and magnesium alloys worldwide in 2020". In: *Journal of Magnesium and Alloys* 9.3 (2021), 705.
- [30] Hajo Dieringa, Jan Bohlen, Norbert Hort, Dietmar Letzig, and Karl Ulrich Kainer. "Advances in manufacturing processes for magnesium alloys". In: *Essential Readings in Magnesium Technology* (2016), 19.
- [31] Alan A Luo. "Magnesium: current and potential automotive applications". In: *jom* 54 (2002), 42.
- [32] Pengyang Zhao, Thaddeus Song En Low, Yunzhi Wang, and Stephen R. Niezgod. "An integrated full-field model of concurrent plastic deformation and microstructure evolution: Application to 3D simulation of dynamic recrystallization in polycrystalline copper". In: *International Journal of Plasticity* 80 (2016), 38.
- [33] FH Froes, D Eliezer, and E Aghion. "The science, technology, and applications of magnesium". In: *Jom* 50 (1998), 30.

- [34] JT Lloyd, PA Jannotti, and TL Jones. "An overview of penetration behavior in magnesium alloys". In: *Mechanics of Materials* 162 (2021), 104038.
- [35] PA Jannotti, NJ Lorenzo, TR Walter, BE Schuster, and JT Lloyd. "Role of anisotropy in the ballistic response of rolled magnesium". In: *Mechanics of Materials* 160 (2021), 103953.
- [36] Todd C Hufnagel, Jeffrey T Lloyd, Timothy P Weihs, Laszlo J Kecskes, and Tomoko Sano. "Magnesium alloy design: Examples from the Materials in Extreme Dynamic Environments Metals Collaborative Research Group". In: *Mechanics of Materials* 165 (2022), 104136.
- [37] Debjoy D Mallick, Suhas Eswarappa Prameela, Deniz Ozturk, Cyril L Williams, Minju Kang, Gianna M Valentino, Jeffrey T Lloyd, Justin W Wilkerson, Timothy P Weihs, and KT Ramesh. "Spall strength in alloyed magnesium: A compendium of research efforts from the CMEDE 10-year effort". In: *Mechanics of Materials* 162 (2021), 104065.
- [38] Gwénaëlle Proust. "Processing magnesium at room temperature". In: *Science* 365.6448 (2019), 30.
- [39] CM Cepeda-Jiménez, M Castillo-Rodríguez, and MT Pérez-Prado. "Origin of the low precipitation hardening in magnesium alloys". In: *Acta Materialia* 165 (2019), 164.
- [40] Suhas Eswarappa Prameela and Timothy P Weihs. "Deformation driven precipitation in binary magnesium alloys". In: *Magnesium Technology 2020*. Springer. 2020, 163.
- [41] J. D. Robson. "A new model for discontinuous and continuous precipitation in AZ91 magnesium alloy". In: *Materials Science Forum* 783-786 (2014), 461.
- [42] Joseph D. Robson and Matthew R. Barnett. "The Effect of Precipitates on Twinning in Magnesium Alloys". In: *Advanced Engineering Materials* 21.4 (2019), 1.
- [43] C. R. Hutchinson, J. F. Nie, and S. Gorsse. "Modeling the precipitation processes and strengthening mechanisms in a Mg-Al-(Zn) AZ91 alloy". In: *Metallurgical and Materials Transactions A: Physical Metallurgy and Materials Science* 36.8 (2005), 2093.

- [44] Maria-Teresa Pérez-Prado, Jan Bohlen, Sangbong Yi, Dietmar Letzig, Talal Al-Samman, Joseph Robson, Matthew Barnett, Warren Poole, Chamini Mendis, Sean Agnew, et al. "Emerging hot topics and research questions in wrought magnesium alloy development". In: *Jom* 72 (2020), 2561.
- [45] S Sandlöbes, S Zaefferer, I Schestakow, S Yi, and R Gonzalez-Martinez. "On the role of non-basal deformation mechanisms for the ductility of Mg and Mg–Y alloys". In: *Acta Materialia* 59.2 (2011), 429.
- [46] SR Agnew, MH Yoo, and CN Tome. "Application of texture simulation to understanding mechanical behavior of Mg and solid solution alloys containing Li or Y". In: *Acta materialia* 49.20 (2001), 4277.
- [47] A Staroselsky and L Anand. "A constitutive model for hcp materials deforming by slip and twinning: application to magnesium alloy AZ31B". In: *International journal of Plasticity* 19.10 (2003), 1843.
- [48] Zhuoran Zeng, Jian-Feng Nie, Shi-Wei Xu, Chris HJ Davies, and Nick Birbilis. "Super-formable pure magnesium at room temperature". In: *Nature communications* 8.1 (2017), 1.
- [49] T Al-Samman and G Gottstein. "Dynamic recrystallization during high temperature deformation of magnesium". In: *Materials Science and Engineering: A* 490.1-2 (2008), 411.
- [50] Talal Al-Samman, Konstantin D Molodov, Dmitri A Molodov, Günter Gottstein, and Satyam Suwas. "Softening and dynamic recrystallization in magnesium single crystals during c-axis compression". In: *Acta materialia* 60.2 (2012), 537.
- [51] T Al-Samman, X Li, and S Ghosh Chowdhury. "Orientation dependent slip and twinning during compression and tension of strongly textured magnesium AZ31 alloy". In: *Materials Science and Engineering: A* 527.15 (2010), 3450.
- [52] Yannick **Hollenweger** and Dennis M Kochmann. "An efficient temperature-dependent crystal plasticity framework for pure magnesium with emphasis on the competition between slip and twinning". In: *International Journal of Plasticity* 159 (2022), 103448.
- [53] Zhaoxuan Wu and WA Curtin. "The origins of high hardening and low ductility in magnesium". In: *Nature* 526.7571 (2015), 62.

- [54] S Kweon and Daniel S Raja. "A study on the mechanical response of magnesium using an anisotropic elasticity twinning CP FEM". In: *Archive of Applied Mechanics* (2021), 1.
- [55] Matthew Robert Barnett, Mark D Nave, and Colleen Joyce Bettles. "Deformation microstructures and textures of some cold rolled Mg alloys". In: *Materials Science and Engineering: A* 386.1-2 (2004), 205.
- [56] MR Barnett. "Twinning and the ductility of magnesium alloys: Part II. "Contraction" twins". In: *Materials Science and Engineering: A* 464.1-2 (2007), 8.
- [57] ZR Zeng, YM Zhu, SW Xu, MZ Bian, CHJ Davies, N Birbilis, and JF Nie. "Texture evolution during static recrystallization of cold-rolled magnesium alloys". In: *Acta Materialia* 105 (2016), 479.
- [58] Laszlo J Kecskes, Nicholas M Krywopusk, Yannick **Hollenweger**, Jenna N Krynicki, Suhas Eswarappa Prameela, Peng Yi, Burigede Liu, Michael L Falk, Dennis M Kochmann, and Timothy P Weihs. "Recrystallization mechanisms, grain refinement, and texture evolution during ECAE processing of Mg and its alloys". In: *Mechanics of Materials* 162 (2021), 104067.
- [59] A. D. Tutcuoglu, A. Vidyasagar, K. Bhattacharya, and D. M. Kochmann. "Stochastic modeling of discontinuous dynamic recrystallization at finite strains in hcp metals". In: *Journal of the Mechanics and Physics of Solids* 122 (2019), 590.
- [60] Tianshui Zhou, Quanfa Zhang, Qianqian Li, Lidong Wang, Qinglin Li, and Dexue Liu. "A simultaneous enhancement of both strength and ductility by a novel differential-thermal ECAP process in Mg-Sn-Zn-Zr alloy". In: *Journal of Alloys and Compounds* 889 (2021), 161653.
- [61] LB Tong, JH Chu, WT Sun, ZH Jiang, DN Zou, SF Liu, S Kamado, and MY Zheng. "Development of a high-strength Mg alloy with superior ductility through a unique texture modification from equal channel angular pressing". In: *Journal of Magnesium and Alloys* 9.3 (2021), 1007.
- [62] Peng Yi, Taisuke Sasaki, Suhas Eswarappa Prameela, Timothy P Weihs, and Michael L Falk. "The Interplay Between Solute Atoms and Vacancy Clusters in Magnesium Alloys". In: *arXiv preprint arXiv:2112.03894* (2021).

- [63] Peng Yi. "Solute softening and vacancy generation by diffusion-less dislocation climb in magnesium alloys". In: *Scripta Materialia* 194 (2021), 113692.
- [64] Jian Feng Nie. "Precipitation and hardening in magnesium alloys". In: *Metallurgical and Materials Transactions A: Physical Metallurgy and Materials Science* 43.11 (2012), 3891.
- [65] MS Al-Haik, MY Hussaini, and H Garmestani. "Prediction of nonlinear viscoelastic behavior of polymeric composites using an artificial neural network". In: *International journal of plasticity* 22.7 (2006), 1367.
- [66] A Styczynski, Ch Hartig, J Bohlen, and D Letzig. "Cold rolling textures in AZ31 wrought magnesium alloy". In: *Scripta Materialia* 50.7 (2004), 943.
- [67] JA Chapman and DU Wilson. "Room-temperature ductility of fine-grain magnesium". In: *Journal of the Institute of Metals* 91.1 (1962), 39.
- [68] Tom Walde and Hermann Riedel. "Modeling texture evolution during hot rolling of magnesium alloy AZ31". In: *Materials Science and Engineering A* 443.1-2 (2007), 277.
- [69] Kenneth J Tam, Matthew W Vaughan, Luming Shen, Marko Knezevic, Ibrahim Karaman, and Gwénaëlle Proust. "Modelling dynamic recrystallisation in magnesium alloy AZ31". In: *International Journal of Plasticity* 142 (2021), 102995.
- [70] Binglun Yin, Zhaoxuan Wu, and WA Curtin. "First-principles calculations of stacking fault energies in Mg-Y, Mg-Al and Mg-Zn alloys and implications for c+ a activity". In: *Acta Materialia* 136 (2017), 249.
- [71] Yang Hu, Vladyslav Turlo, Irene J Beyerlein, Subhash Mahajan, Enrique J Lavernia, Julie M Schoenung, and Timothy J Rupert. "Disconnection-mediated twin embryo growth in Mg". In: *Acta Materialia* 194 (2020), 437.
- [72] C. Liu, P. Shanthraj, J. D. Robson, M. Diehl, S. Dong, J. Dong, W. Ding, and D. Raabe. "On the interaction of precipitates and tensile twins in magnesium alloys". In: *Acta Materialia* 178 (2019), 146.
- [73] Gregory B Olson. "Computational design of hierarchically structured materials". In: *Science* 277.5330 (1997), 1237.

- [74] David L. McDowell, Jitesh H. Panchal, Hae-Jin Choi, Carolyn Conner Seepersad, Janet K. Allen, and Farrokh Mistree. "Chapter 1 - Integrated Material, Product, and Process Design—A New Frontier in Engineering Systems Design". In: *Integrated Design of Multiscale, Multifunctional Materials and Products*. Ed. by David L. McDowell, Jitesh H. Panchal, Hae-Jin Choi, Carolyn Conner Seepersad, Janet K. Allen, and Farrokh Mistree. Boston: Butterworth-Heinemann, 2010, 1.
- [75] Colin Bonatti, Bekim Berisha, and Dirk Mohr. "From CP-FFT to CP-RNN: Recurrent neural network surrogate model of crystal plasticity". In: *International Journal of Plasticity* 158 (2022), 103430.
- [76] Colin Bonatti and Dirk Mohr. "One for all: Universal material model based on minimal state-space neural networks". In: *Science Advances* 7.26 (2021), eabf3658.
- [77] Mengfei Yuan, Sean Paradiso, Bryce Meredig, and Stephen R Niezgoda. "Machine learning-based reduce order crystal plasticity modeling for ICME applications". In: *Integrating Materials and Manufacturing Innovation* 7 (2018), 214.
- [78] M Mozaffar, R Bostanabad, W Chen, K Ehmann, Jian Cao, and MA Bessa. "Deep learning predicts path-dependent plasticity". In: *Proceedings of the National Academy of Sciences* 116.52 (2019), 26414.
- [79] Kaushik Bhattacharya, Burigede Liu, Andrew Stuart, and Margaret Trautner. "Learning Markovian Homogenized Models in Viscoelasticity". In: *arXiv preprint arXiv:2205.14139* (2022).
- [80] Zefeng Yu, Chenghang Han, Hang Yang, Yu Wang, Shan Tang, and Xu Guo. "Elastoplastic constitutive modeling under the complex loading driven by GRU and small-amount data". In: *Theoretical and Applied Mechanics Letters* 12.6 (2022), 100363.
- [81] Anup Pandey and Reeru Pokharel. "Machine learning enabled surrogate crystal plasticity model for spatially resolved 3D orientation evolution under uniaxial tension". In: *arXiv preprint arXiv:2005.00951* (2020).
- [82] Siddhant Kumar, Stephanie Tan, Li Zheng, and Dennis M Kochmann. "Inverse-designed spinodoid metamaterials". In: *npj Computational Materials* 6.1 (2020), 73.

- [83] Colin Bonatti and Dirk Mohr. "On the importance of self-consistency in recurrent neural network models representing elasto-plastic solids". In: *Journal of the Mechanics and Physics of Solids* 158 (2022), 104697.
- [84] A. D. Tutcuoglu, Y. Hollenweger, A. Stoy, and D. M. Kochmann. "High- vs. low-fidelity models for dynamic recrystallization in copper". In: *Materialia* 7:July (2019), 100411.
- [85] K. Huang and R. E. Logé. *A review of dynamic recrystallization phenomena in metallic materials*. 2016.
- [86] Sean R Agnew and Özgür Duygulu. "Plastic anisotropy and the role of non-basal slip in magnesium alloy AZ31B". In: *International Journal of plasticity* 21.6 (2005), 1161.
- [87] XY Lou, Min Li, RK Boger, SR Agnew, and RH Wagoner. "Hardening evolution of AZ31B Mg sheet". In: *International Journal of Plasticity* 23.1 (2007), 44.
- [88] Srihari Kurukuri, Michael J Worswick, Dariush Ghaffari Tari, Raja K Mishra, and Jon T Carter. "Rate sensitivity and tension-compression asymmetry in AZ31B magnesium alloy sheet". In: *Philosophical Transactions of the Royal Society A: Mathematical, Physical and Engineering Sciences* 372.2015 (2014), 20130216.
- [89] V. Herrera-Solaz, J. Llorca, E. Dogan, I. Karaman, and J. Segurado. "An inverse optimization strategy to determine single crystal mechanical behavior from polycrystal tests: Application to AZ31 Mg alloy". In: *International Journal of Plasticity* 57 (2014), 1.
- [90] Jian Feng Nie. "Effects of precipitate shape and orientation on dispersion strengthening in magnesium alloys". In: *Scripta Materialia* 48.8 (2003), 1009.
- [91] Zheyuan Xing, Haidong Fan, Jing Tang, Bing Wang, and Guozheng Kang. "Molecular dynamics simulation on the cyclic deformation of magnesium single crystals". In: *Computational Materials Science* 186 (2021), 110003.
- [92] Saadi A Habib, Akhtar S Khan, Thomas Gnäupel-Herold, Jeffrey T Lloyd, and Scott E Schoenfeld. "Anisotropy, tension-compression asymmetry and texture evolution of a rare-earth-containing magnesium alloy sheet, ZEK100, at different strain rates and temperatures: Experiments and modeling". In: *International Journal of Plasticity* 95 (2017), 163.

- [93] Kristián Máthis, Jan Čapek, Zuzana Zdražilová, and Zuzanka Trojanová. "Investigation of tension–compression asymmetry of magnesium by use of the acoustic emission technique". In: *Materials Science and Engineering: A* 528.18 (2011), 5904.
- [94] Sung Hyuk Park, Jeong Hun Lee, Byoung Gi Moon, and Bong Sun You. "Tension–compression yield asymmetry in as-cast magnesium alloy". In: *Journal of Alloys and Compounds* 617 (2014), 277.
- [95] Hyo Tae Jeong and Tae Kwon Ha. "Texture development in a warm rolled AZ31 magnesium alloy". In: *Journal of Materials Processing Technology* 187 (2007), 559.
- [96] DC Foley, M Al-Maharbi, KT Hartwig, I Karaman, LJ Kecskes, and SN Mathaudhu. "Grain refinement vs. crystallographic texture: Mechanical anisotropy in a magnesium alloy". In: *Scripta Materialia* 64.2 (2011), 193.
- [97] N Chetty and M Weinert. "Stacking faults in magnesium". In: *Physical Review B* 56.17 (1997), 10844.
- [98] CQ Liu, HW Chen, Nicholas C Wilson, and JF Nie. "Zn segregation in interface between Mg₁₇Al₁₂ precipitate and Mg matrix in Mg–Al–Zn alloys". In: *Scripta Materialia* 163 (2019), 91.
- [99] Dalong Zhang, Baolong Zheng, Yizhang Zhou, Subhash Mahajan, and Enrique J Lavernia. "Prism stacking faults observed contiguous to a {10-12} twin in a Mg–Y alloy". In: *Scripta Materialia* 76 (2014), 61.
- [100] M Itakura, H Kaburaki, M Yamaguchi, and T Tsuru. "Atomistic study on the cross-slip process of a screw a dislocation in magnesium". In: *Modelling and Simulation in Materials Science and Engineering* 23.6 (2015), 065002.
- [101] Rasool Ahmad, Binglun Yin, Zhaoxuan Wu, and WA Curtin. "Designing high ductility in magnesium alloys". In: *Acta Materialia* 172 (2019), 161.
- [102] Zhihua Huang. "Dislocation-Precipitate Interactions in Magnesium-Neodymium Alloys". PhD thesis. University of Michigan, 2019.
- [103] GI Taylor and W Floyd. "J. Inst. Met." In: (1938).
- [104] R Von Mises. "Mechanik der plastischen Formänderung von Kristallen". In: (1928).

- [105] GW Groves and A Kelly. "Independent slip systems in crystals". In: *Philosophical Magazine* 8.89 (1963), 877.
- [106] RE Smallman and D Green. "The dependence of rolling texture on stacking fault energy". In: *Acta Metallurgica* 12.2 (1964), 145.
- [107] Yingrui Chang and Dennis M. Kochmann. "A variational constitutive model for slip-twinning interactions in hcp metals: Application to single- and polycrystalline magnesium". In: *International Journal of Plasticity* 73 (2015), 39.
- [108] Jing Zhang and Shailendra P. Joshi. "Phenomenological crystal plasticity modeling and detailed micromechanical investigations of pure magnesium". In: *Journal of the Mechanics and Physics of Solids* 60.5 (2012), 945.
- [109] S. R. Agnew and J. F. Nie. "Preface to the viewpoint set on: The current state of magnesium alloy science and technology". In: *Scripta Materialia* 63.7 (2010), 671.
- [110] Kelvin Y Xie, Zafir Alam, Alexander Caffee, and Kevin J Hemker. "Pyramidal I slip in c-axis compressed Mg single crystals". In: *Scripta Materialia* 112 (2016), 75.
- [111] J Geng, Matthew F Chisholm, RK Mishra, and KS Kumar. "The structure of $c+a$ type dislocation loops in magnesium". In: *Philosophical Magazine Letters* 94.6 (2014), 377.
- [112] Jean François Stohr and Jean Paul Poirier. "Etude en microscopie électronique du glissement pyramidal $\{1122\} \langle 1123 \rangle$ dans le magnésium". In: *Philosophical Magazine* 25.6 (1972), 1313.
- [113] UF Kocks and DG Westlake. "The importance of twinning for the ductility of CPH polycrystals". In: *AIME Met Soc Trans* 239.7 (1967), 1107.
- [114] MH Yoo, JR Morris, KM Ho, and SR Agnew. "Nonbasal deformation modes of HCP metals and alloys: role of dislocation source and mobility". In: *Metallurgical and Materials Transactions A* 33.3 (2002), 813.
- [115] Zhaoxuan Wu, Rasool Ahmad, Binglun Yin, Stefanie Sandlöbes, and WA Curtin. "Mechanistic origin and prediction of enhanced ductility in magnesium alloys". In: *Science* 359.6374 (2018), 447.

- [116] Michael A Ritzo, Jishnu J Bhattacharyya, Ricardo A Lebensohn, and Sean R Agnew. "An investigation into the role of dislocation climb during intermediate temperature flow of Mg alloys". In: *Magnesium Technology 2020*. Springer. 2020, 115.
- [117] Bo-Yu Liu, Fei Liu, Nan Yang, Xiao-Bo Zhai, Lei Zhang, Yang Yang, Bin Li, Ju Li, Evan Ma, Jian-Feng Nie, et al. "Large plasticity in magnesium mediated by pyramidal dislocations". In: *Science* 365.6448 (2019), 73.
- [118] Feng Kang, Zheng Li, Jing Tao Wang, Ping Cheng, and Hai Ying Wu. "The activation of $\langle c+a \rangle$ non-basal slip in Magnesium alloys". In: *Journal of Materials Science* 47.22 (2012), 7854.
- [119] Bin JIANG, Zhi-hua DONG, Ang ZHANG, Jiang-feng SONG, and Fu-sheng PAN. "Recent advances in micro-alloyed wrought magnesium alloys: Theory and design". In: *Transactions of Nonferrous Metals Society of China* 32.6 (2022), 1741.
- [120] John Wyrill Christian and Subhash Mahajan. "Deformation twinning". In: *Progress in materials science* 39.1-2 (1995), 1.
- [121] A. Serra, R.C. Pond, and D.J. Bacon. "Computer simulation of the structure and mobility of twinning dislocations in H.C.P. Metals". In: *Acta Metallurgica et Materialia* 39.7 (1991), 1469.
- [122] Arijit Roy, E. S. Nani, Arka Lahiri, and M. P. Gururajan. "Interfacial free energy anisotropy driven faceting of precipitates". In: *Philosophical Magazine* 97.30 (2017), 2705.
- [123] M. R. Barnett, Z. Keshavarz, A. G. Beer, and X. Ma. "Non-Schmid behaviour during secondary twinning in a polycrystalline magnesium alloy". In: *Acta Materialia* 56.1 (2008), 5.
- [124] Balaji Selvarajou, Joong-Ho Shin, Tae Kwon Ha, In-suk Choi, Shailendra P. Joshi, and Heung Nam Han. "Orientation-dependent indentation response of magnesium single crystals: Modeling and experiments". In: *Acta Materialia* 81 (2014), 358.
- [125] Konstantin D. Molodov, Talal Al-Samman, Dmitri A. Molodov, and Günter Gottstein. "Mechanisms of exceptional ductility of magnesium single crystal during deformation at room temperature: Multiple twinning and dynamic recrystallization". In: *Acta Materialia* 76 (2014), 314.

- [126] Konstantin D. Molodov, Talal Al-Samman, Dmitri A. Molodov, and Günter Gottstein. "On the role of anomalous twinning in the plasticity of magnesium". In: *Acta Materialia* 103 (2016), 711.
- [127] J Koike, T Kobayashi, T Mukai, H Watanabe, M Suzuki, K Maruyama, and K Higashi. "The activity of non-basal slip systems and dynamic recovery at room temperature in fine-grained AZ31B magnesium alloys". In: *Acta materialia* 51.7 (2003), 2055.
- [128] Junichi Koike. "Enhanced deformation mechanisms by anisotropic plasticity in polycrystalline Mg alloys at room temperature". In: *Metallurgical and Materials Transactions A* 36 (2005), 1689.
- [129] SR Agnew, P Mehrotra, TM Lillo, GM Stoica, and PK Liaw. "Texture evolution of five wrought magnesium alloys during route A equal channel angular extrusion: Experiments and simulations". In: *Acta Materialia* 53.11 (2005), 3135.
- [130] LE Murr. "Dislocation ledge sources: dispelling the myth of Frank-Read source importance". In: *Metallurgical and Materials Transactions A* 47 (2016), 5811.
- [131] EO Hall. "The deformation and ageing of mild steel: III discussion of results". In: *Proceedings of the Physical Society. Section B* 64.9 (1951), 747.
- [132] NJ Petch. "The cleavage strength of polycrystals". In: *J. Iron Steel Inst.* 174 (1953), 25.
- [133] CH Caceres, Gemma E Mann, and JR Griffiths. "Grain size hardening in Mg and Mg-Zn solid solutions". In: *Metallurgical and Materials Transactions A* 42 (2011), 1950.
- [134] Kang Wei, Rong Hu, Dongdi Yin, Lirong Xiao, Song Pang, Yang Cao, Hao Zhou, Yonghao Zhao, and Yuntian Zhu. "Grain size effect on tensile properties and slip systems of pure magnesium". In: *Acta Materialia* 206 (2021), 116604.
- [135] N Stanford and Matthew Robert Barnett. "Solute strengthening of prismatic slip, basal slip and $\{101\ 2\}$ twinning in Mg and Mg-Zn binary alloys". In: *International Journal of Plasticity* 47 (2013), 165.
- [136] A Tehranchi, B Yin, and WA Curtin. "Solute strengthening of basal slip in Mg alloys". In: *Acta Materialia* 151 (2018), 56.
- [137] P Garg, I Adlakha, and KN Solanki. "Effect of solutes on ideal shear resistance and electronic properties of magnesium: A first-principles study". In: *Acta Materialia* 153 (2018), 327.

- [138] Jian Feng Nie, K Oh-Ishi, Xiang Gao, and K Hono. "Solute segregation and precipitation in a creep-resistant Mg–Gd–Zn alloy". In: *Acta Materialia* 56.20 (2008), 6061.
- [139] Fulin Wang, Jishnu J Bhattacharyya, and Sean R Agnew. "Effect of precipitate shape and orientation on Orowan strengthening of non-basal slip modes in hexagonal crystals, application to magnesium alloys". In: *Materials Science and Engineering: A* 666 (2016), 114.
- [140] John D Clayton and Jarek Knap. "A phase field model of deformation twinning: nonlinear theory and numerical simulations". In: *Physica D: Nonlinear Phenomena* 240.9-10 (2011), 841.
- [141] C. Liu, P. Shanthraj, M. Diehl, F. Roters, S. Dong, J. Dong, W. Ding, and D. Raabe. "An integrated crystal plasticity-phase field model for spatially resolved twin nucleation, propagation, and growth in hexagonal materials". In: *International Journal of Plasticity* 106. March (2018), 203.
- [142] Eric Ocegueda and Kaushik Bhattacharya. "Phase-Field Modeling of Deformation Twinning and Dislocation Slip Interaction in Polycrystalline Solids". In: *Magnesium Technology 2022*. Springer, 2022, 305.
- [143] Surya R. Kalidindi. "Incorporation of Deformation Twinning in Models". In: *International Journal of Plasticity* 46.2 (1998), 267.
- [144] M. Homayonifar and J. Mosler. "On the coupling of plastic slip and deformation-induced twinning in magnesium: A variationally consistent approach based on energy minimization". In: *International Journal of Plasticity* 27.7 (2011), 983.
- [145] Richard D James. "Finite deformation by mechanical twinning". In: *Archive for Rational Mechanics and Analysis* 77 (1981), 143.
- [146] John W Cahn and John E Hilliard. "Free energy of a nonuniform system. I. Interfacial free energy". In: *The Journal of chemical physics* 28.2 (1958), 258.
- [147] Yingrui Chang. "A Continuum Model for Slip-Twinning Interactions in Magnesium and Magnesium Alloys". PhD Thesis. California Institute of Technology, 2016.
- [148] Robert J Asaro and JRo375 Rice. "Strain localization in ductile single crystals". In: *Journal of the Mechanics and Physics of Solids* 25.5 (1977), 309.

- [149] James R Rice. "Inelastic constitutive relations for solids: an internal-variable theory and its application to metal plasticity". In: *Journal of the Mechanics and Physics of Solids* 19.6 (1971), 433.
- [150] R. Hill. "Generalized constitutive relations for incremental deformation of metal crystals by multislip". In: *Journal of the Mechanics and Physics of Solids* 14.2 (1966), 95.
- [151] R. E. Reed-Hill and W. D. Robertson. "The crystallographic characteristics of fracture in magnesium single crystals". In: *Acta Metallurgica* 5.12 (1957), 728.
- [152] G Proust, CN Tomé, and GC Kaschner. "Modeling texture, twinning and hardening evolution during deformation of hexagonal materials". In: *Acta Materialia* 55.6 (2007), 2137.
- [153] Michael Ortiz and EA Repetto. "Nonconvex energy minimization and dislocation structures in ductile single crystals". In: *Journal of the Mechanics and Physics of Solids* 47.2 (1999), 397.
- [154] Michael Ortiz and Laurent Stainier. "The variational formulation of viscoplastic constitutive updates". In: *Computer methods in applied mechanics and engineering* 171.3-4 (1999), 419.
- [155] Yingrui Chang, Jeffrey T. Lloyd, Richard Becker, and Dennis M. Kochmann. "Modeling microstructure evolution in magnesium: Comparison of detailed and reduced-order kinematic models". In: *Mechanics of Materials* 108 (2017), 40.
- [156] Milan Ardeljan, Irene J. Beyerlein, Brandon A. McWilliams, and Marko Knezevic. "Strain rate and temperature sensitive multi-level crystal plasticity model for large plastic deformation behavior: Application to AZ31 magnesium alloy". In: *International Journal of Plasticity* 83 (2016), 90.
- [157] Roberto B. Figueiredo, Flávia S.J. Poggiali, Cláudio L.P. Silva, Paulo R. Cetlin, and Terence G. Langdon. "The influence of grain size and strain rate on the mechanical behavior of pure magnesium". In: *Journal of Materials Science* 51.6 (2016), 3013.
- [158] Kenneth J. Tam, Matthew W. Vaughan, Luming Shen, Marko Knezevic, Ibrahim Karaman, and Gwénaëlle Proust. "Modelling the temperature and texture effects on the deformation mechanisms of magnesium alloy AZ31". In: *International Journal of Mechanical Sciences* 182.May (2020).

- [159] Qiang Liu, Anish Roy, and Vadim V. Silberschmidt. "Temperature-dependent crystal-plasticity model for magnesium: A bottom-up approach". In: *Mechanics of Materials* 113 (2017), 44.
- [160] G Sachs. "Plasticity problems in metals". In: *Transactions of the Faraday Society* 24 (1928), 84.
- [161] Robert J Asaro and Alan Needleman. "Overview no. 42 texture development and strain hardening in rate dependent polycrystals". In: *Acta metallurgica* 33.6 (1985), 923.
- [162] Tien-Yue Wu, John L Bassani, and Campbell Laird. "Latent hardening in single crystals-I. Theory and experiments". In: *Proceedings of the Royal Society of London. Series A: Mathematical and Physical Sciences* 435.1893 (1991), 1.
- [163] John L Bassani and Tien-Yue Wu. "Latent hardening in single crystals. II. Analytical characterization and predictions". In: *Proceedings of the Royal Society of London. Series A: Mathematical and Physical Sciences* 435.1893 (1991), 21.
- [164] Ekkehart Kröner. "Berechnung der elastischen Konstanten des Vielkristalls aus den Konstanten des Einkristalls". In: *Zeitschrift für Physik* 151.4 (1958), 504.
- [165] John Douglas Eshelby. "The determination of the elastic field of an ellipsoidal inclusion, and related problems". In: *Proceedings of the royal society of London. Series A. Mathematical and physical sciences* 241.1226 (1957), 376.
- [166] E Kröner. "Zur plastischen verformung des vielkristalls". In: *Acta metallurgica* 9.2 (1961), 155.
- [167] Bernard Budianski and Tai Te Wu. *Theoretical prediction of plastic strains of polycrystals*. 12. Division of Engineering and Applied Physics, Harvard University, 1961.
- [168] M Berveiller and A Zaoui. "An extension of the self-consistent scheme to plastically-flowing polycrystals". In: *Journal of the Mechanics and Physics of Solids* 26.5-6 (1978), 325.
- [169] PA Turner and CN Tomé. "A study of residual stresses in Zircaloy-2 with rod texture". In: *Acta metallurgica et Materialia* 42.12 (1994), 4143.
- [170] B Clausen, CN Tomé, DW Brown, and SR Agnew. "Reorientation and stress relaxation due to twinning: Modeling and experimental characterization for Mg". In: *Acta Materialia* 56.11 (2008), 2456.

- [171] Gwénaëlle Proust, Carlos N. Tomé, Ashutosh Jain, and Sean R. Agnew. "Modeling the effect of twinning and detwinning during strain-path changes of magnesium alloy AZ31". In: *International Journal of Plasticity* 25.5 (2009), 861.
- [172] Farhoud Kabirian, Akhtar S. Khan, and Thomas Gnäupel-Herlod. "Visco-plastic modeling of mechanical responses and texture evolution in extruded AZ31 magnesium alloy for various loading conditions". In: *International Journal of Plasticity* 68 (2015), 1.
- [173] Miroslav Zecevic, Ricardo A Lebensohn, Michael Rogers, Jacob Moore, Vincent Chiravalle, Evan Lieberman, Daniel Dunning, Galen Shipman, Marko Knezevic, and Nathaniel Morgan. "Viscoplastic self-consistent formulation as generalized material model for solid mechanics applications". In: *Applications in Engineering Science* 6 (2021), 100040.
- [174] Dennis Kochmann. *Introduction to FEA*. https://ethz.ch/content/dam/ethz/special-interest/mavt/mechanical-systems/mm-dam/documents/Notes/IntroToFEA_red.pdf. [Online; accessed 21-July-2023]. 2017.
- [175] H. Moulinec and P. Suquet. "A numerical method for computing the overall response of nonlinear composites with complex microstructure". In: *Computer Methods in Applied Mechanics and Engineering* 157.1-2 (1998), 69.
- [176] Ananthan Vidyasagar, Wei L Tan, and Dennis M Kochmann. "Predicting the effective response of bulk polycrystalline ferroelectric ceramics via improved spectral phase field methods". In: *Journal of the Mechanics and Physics of Solids* 106 (2017), 133.
- [177] Felix Fritzen and Max Hodapp. "The finite element square reduced (FE₂R) method with GPU acceleration: towards three-dimensional two-scale simulations". In: *International Journal for Numerical Methods in Engineering* 107.10 (2016), 853.
- [178] Pramila P Shinde and Seema Shah. "A review of machine learning and deep learning applications". In: *2018 Fourth international conference on computing communication control and automation (ICCUBEA)*. IEEE. 2018, 1.
- [179] Praphula Kumar Jain, Rajendra Pamula, and Gautam Srivastava. "A systematic literature review on machine learning applications for consumer sentiment analysis using online reviews". In: *Computer science review* 41 (2021), 100413.

- [180] RAFAEL A. CALVO, DAVID N. MILNE, M. SAZZAD HUSSAIN, and HELEN CHRISTENSEN. "Natural language processing in mental health applications using non-clinical texts". In: *Natural Language Engineering* 23.5 (2017), 649.
- [181] Gael Sentis, Alex Monras, Ramon Munoz-Tapia, John Calsamiglia, and Emilio Bagan. "Unsupervised classification of quantum data". In: *Physical Review X* 9.4 (2019), 041029.
- [182] Félix Michaud, Jérôme Sueur, Maxime Le Cesne, and Sylvain Hupert. "Unsupervised classification to improve the quality of a bird song recording dataset". In: *Ecological Informatics* 74 (2023), 101952.
- [183] Donald O. Hebb. *The organization of behavior: A neuropsychological theory*. New York: Wiley, 1949.
- [184] Frank Rosenblatt. "The perceptron: a probabilistic model for information storage and organization in the brain." In: *Psychological review* 65.6 (1958), 386.
- [185] Frederic E Bock, Roland C Aydin, Christian J Cyron, Norbert Huber, Surya R Kalidindi, and Benjamin Klusemann. "A review of the application of machine learning and data mining approaches in continuum materials mechanics". In: *Frontiers in Materials* 6 (2019), 110.
- [186] Erkki Oja. "Simplified neuron model as a principal component analyzer". In: *Journal of mathematical biology* 15 (1982), 267.
- [187] Terence D Sanger. "Optimal unsupervised learning in a single-layer linear feedforward neural network". In: *Neural networks* 2.6 (1989), 459.
- [188] Simon Haykin. *Neural networks: a comprehensive foundation*. Prentice Hall PTR, 1998.
- [189] Stuart J Russell. *Artificial intelligence a modern approach*. Pearson Education, Inc., 2010.
- [190] Sepp Hochreiter. "The vanishing gradient problem during learning recurrent neural nets and problem solutions". In: *International Journal of Uncertainty, Fuzziness and Knowledge-Based Systems* 6.02 (1998), 107.
- [191] Kuniyiko Fukushima. "Neocognitron: A self-organizing neural network model for a mechanism of pattern recognition unaffected by shift in position". In: *Biological cybernetics* 36.4 (1980), 193.

- [192] Kunihiko Fukushima. "Neocognitron: A hierarchical neural network capable of visual pattern recognition". In: *Neural networks* 1.2 (1988), 119.
- [193] Boukaye Boubacar Traore, Bernard Kamsu-Foguem, and Fana Tangara. "Deep convolution neural network for image recognition". In: *Ecological informatics* 48 (2018), 257.
- [194] Sepp Hochreiter and Jürgen Schmidhuber. "Long short-term memory". In: *Neural computation* 9.8 (1997), 1735.
- [195] Junyoung Chung, Caglar Gulcehre, KyungHyun Cho, and Yoshua Bengio. "Empirical evaluation of gated recurrent neural networks on sequence modeling". In: *arXiv preprint arXiv:1412.3555* (2014).
- [196] Olaf Ronneberger, Philipp Fischer, and Thomas Brox. "U-net: Convolutional networks for biomedical image segmentation". In: *Medical Image Computing and Computer-Assisted Intervention—MICCAI 2015: 18th International Conference, Munich, Germany, October 5-9, 2015, Proceedings, Part III* 18. Springer. 2015, 234.
- [197] Stefan Kollmannsberger, Davide D'Angella, Moritz Jokeit, Leon Herrmann, et al. *Deep learning in computational mechanics*. Springer, 2021.
- [198] Atsuya Oishi and Genki Yagawa. "Computational mechanics enhanced by deep learning". In: *Computer Methods in Applied Mechanics and Engineering* 327 (2017), 327.
- [199] Ehsan Haghghat, Maziar Raissi, Adrian Moure, Hector Gomez, and Ruben Juanes. "A deep learning framework for solution and discovery in solid mechanics". In: *arXiv preprint arXiv:2003.02751* (2020).
- [200] Xiaoxiao Guo, Wei Li, and Francesco Iorio. "Convolutional neural networks for steady flow approximation". In: *Proceedings of the 22nd ACM SIGKDD international conference on knowledge discovery and data mining*. 2016, 481.
- [201] Lu Lu, Pengzhan Jin, and George Em Karniadakis. "Deeponet: Learning nonlinear operators for identifying differential equations based on the universal approximation theorem of operators". In: *arXiv preprint arXiv:1910.03193* (2019).
- [202] Leah Bar and Nir Sochen. "Unsupervised deep learning algorithm for PDE-based forward and inverse problems". In: *arXiv preprint arXiv:1904.05417* (2019).

- [203] Kaushik Bhattacharya, Bamdad Hosseini, Nikola B Kovachki, and Andrew M Stuart. "Model reduction and neural networks for parametric PDEs". In: *The SMAI journal of computational mathematics* 7 (2021), 121.
- [204] Nikolaos N Vlassis, Puhao Zhao, Ran Ma, Tommy Sewell, and WaiChing Sun. "Molecular dynamics inferred transfer learning models for finite-strain hyperelasticity of monoclinic crystals: Sobolev training and validations against physical constraints". In: *International Journal for Numerical Methods in Engineering* 123.17 (2022), 3922.
- [205] WQ Shen, YJ Cao, Jian-Fu Shao, and ZB Liu. "Prediction of plastic yield surface for porous materials by a machine learning approach". In: *Materials Today Communications* 25 (2020), 101477.
- [206] Kun Wang and WaiChing Sun. "A multiscale multi-permeability poroplasticity model linked by recursive homogenizations and deep learning". In: *Computer Methods in Applied Mechanics and Engineering* 334 (2018), 337.
- [207] Yoshua Bengio, Patrice Simard, and Paolo Frasconi. "Learning long-term dependencies with gradient descent is difficult". In: *IEEE transactions on neural networks* 5.2 (1994), 157.
- [208] Robert DiPietro and Gregory D. Hager. "Chapter 21 - Deep learning: RNNs and LSTM". In: *Handbook of Medical Image Computing and Computer Assisted Intervention*. Ed. by S. Kevin Zhou, Daniel Rueckert, and Gabor Fichtinger. The Elsevier and MICCAI Society Book Series. Academic Press, 2020, 503.
- [209] Ari Frankel, Kousuke Tachida, and Reese Jones. "Prediction of the evolution of the stress field of polycrystals undergoing elastic-plastic deformation with a hybrid neural network model". In: *Machine Learning: Science and Technology* 1.3 (2020), 035005.
- [210] Diab W Abueidda, Seid Koric, Nahil A Sobh, and Huseyin Sehitoglu. "Deep learning for plasticity and thermo-viscoplasticity". In: *International Journal of Plasticity* 136 (2021), 102852.
- [211] Guobing Wei, Xiaodong Peng, Amir Hadadzadeh, Yahya Mahmoodkhani, Weidong Xie, Yan Yang, and Mary A Wells. "Constitutive modeling of Mg-9Li-3Al-2Sr-2Y at elevated temperatures". In: *Mechanics of Materials* 89 (2015), 241.

- [212] Bin Zhou. "Lean principles, practices, and impacts: a study on small and medium-sized enterprises (SMEs)". In: *Annals of Operations Research* 241.1-2 (2016), 457.
- [213] Shyong Lee, Yung Hung Chen, and Jian Yih Wang. "Isothermal sheet formability of magnesium alloy AZ31 and AZ61". In: *Journal of Materials Processing Technology* 124.1-2 (2002), 19.
- [214] H. Takuda, H. Fujimoto, and N. Hatta. "Modelling on flow stress of Mg-Al-Zn alloys at elevated temperatures". In: *Journal of Materials Processing Technology* 80-81 (1998), 513.
- [215] Hamed Mirzadeh. "Constitutive analysis of Mg-Al-Zn magnesium alloys during hot deformation". In: *Mechanics of Materials* 77 (2014), 80.
- [216] H Yoshinaga, T Obara, and S Morozumi. "Twinning deformation in magnesium compressed along the C-axis". In: *Materials Science and Engineering* 12.5-6 (1973), 255.
- [217] MH Yoo and CT Wei. "Slip modes of hexagonal-close-packed metals". In: *Journal of Applied Physics* 38.11 (1967), 4317.
- [218] EC Burke and WR Hibbard. "Plastic deformation of magnesium single crystals". In: *Jom* 4.3 (1952), 295.
- [219] O Muránsky, DG Carr, MR Barnett, EC Oliver, and P Šittner. "Investigation of deformation mechanisms involved in the plasticity of AZ₃₁ Mg alloy: In situ neutron diffraction and EPSC modelling". In: *Materials Science and Engineering: A* 496.1-2 (2008), 14.
- [220] Bo Zhou and Manling Sui. "High density stacking faults of 101 1 compression twin in magnesium alloys". In: *Journal of Materials Science & Technology* 35.10 (2019), 2263.
- [221] A Chakkedath, T Maiti, J Bohlen, S Yi, D Letzig, P Eisenlohr, and CJ Boehlert. "Contraction twinning dominated tensile deformation and subsequent fracture in extruded Mg-1Mn (Wt Pct) at ambient temperature". In: *Metallurgical and Materials Transactions A* 49.6 (2018), 2441.
- [222] Miroslav Zecevic, Irene J Beyerlein, and Marko Knezevic. "Activity of pyramidal I and II < c+ a > slip in Mg alloys as revealed by texture development". In: *Journal of the Mechanics and Physics of Solids* 111 (2018), 290.

- [223] Peng Yi, Robert C. Cammarata, and Michael L. Falk. "Solute softening and defect generation during prismatic slip in magnesium alloys". In: *Modelling and Simulation in Materials Science and Engineering* 25.8 (2017), 1.
- [224] Xin Wang, Yang Hu, Kehang Yu, Subhash Mahajan, Irene J Beyerlein, Enrique J Lavernia, Timothy J Rupert, and Julie M Schoenung. "Room Temperature Deformation-induced Solute Segregation and its Impact on Twin Boundary Mobility in a Mg-Y Alloy". In: *Scripta Materialia* 209 (2022), 114375.
- [225] C. N. Tomé, R. A. Lebensohn, and U. F. Kocks. "A model for texture development dominated by deformation twinning: Application to zirconium alloys". In: *Acta Metallurgica Et Materialia* 39.11 (1991), 2667.
- [226] Marko Knezevic, Hamad F Al-Harbi, and Surya R Kalidindi. "Crystal plasticity simulations using discrete Fourier transforms". In: *Acta materialia* 57.6 (2009), 1777.
- [227] Xiao-yang Chen, Yang Zhang, Meng-qi Cong, Ya-lin Lu, and Xiaoping Li. "Effect of Sn content on microstructure and tensile properties of as-cast and as-extruded Mg-8Li-3Al-(1, 2, 3) Sn alloys". In: *Transactions of Nonferrous Metals Society of China* 30.8 (2020), 2079.
- [228] Sudeep K Sahoo, Somjeet Biswas, Laszlo S Toth, PC Gautam, and Benoit Beausir. "Strain hardening, twinning and texture evolution in magnesium alloy using the all twin variant polycrystal modelling approach". In: *International Journal of Plasticity* 128 (2020), 102660.
- [229] Marko Knezevic, Amanda Levinson, Ryan Harris, Raja K Mishra, Roger D Doherty, and Surya R Kalidindi. "Deformation twinning in AZ31: influence on strain hardening and texture evolution". In: *Acta Materialia* 58.19 (2010), 6230.
- [230] ZS Basinski, MS Szczerba, M Niewczas, JD Embury, and SJ Basinski. "The transformation of slip dislocations during twinning of copper-aluminum alloy crystals". In: *Revue de mEtallurgie* 94.9 (1997), 1037.
- [231] Huihui Yu, Yunchang Xin, Maoyin Wang, and Qing Liu. "Hall-Petch relationship in Mg alloys: A review". In: *Journal of Materials Science and Technology* 34.2 (2018), 248.
- [232] Irene J. Beyerlein and Carlos N. Tomé. "Analytical modeling of material flow in equal channel angular extrusion (ECAE)". In: *Materials Science and Engineering A* 380.1 (2004), 171.

- [233] M Nebebe, J Bohlen, D Steglich, and D Letzig. "Mechanical characterisation of Mg alloys and model parameter identification for sheet forming simulations". In: *International Journal of Material Forming* 2 (2009), 53.
- [234] D Steglich, Y Jeong, MO Andar, and T Kuwabara. "Biaxial deformation behaviour of AZ31 magnesium alloy: Crystal-plasticity-based prediction and experimental validation". In: *International Journal of Solids and Structures* 49.25 (2012), 3551.
- [235] Joao P Nobre, U Noster, Martin Kornmeier, A Morão Dias, and Berthold Scholtes. "Deformation asymmetry of AZ31 wrought magnesium alloy". In: *Key Engineering Materials*. Vol. 230. Trans Tech Publ. 2002, 267.
- [236] AK Singh and RA Schwarzer. "Evolution of texture in pure magnesium during rolling". In: *International Journal of Materials Research* 96.4 (2022), 345.
- [237] Pauli Virtanen, Ralf Gommers, Travis E. Oliphant, Matt Haberland, Tyler Reddy, David Cournapeau, Evgeni Burovski, Pearu Peterson, Warren Weckesser, Jonathan Bright, Stéfan J. van der Walt, Matthew Brett, Joshua Wilson, K. Jarrod Millman, Nikolay Mayorov, Andrew R. J. Nelson, Eric Jones, Robert Kern, Eric Larson, C J Carey, İlhan Polat, Yu Feng, Eric W. Moore, Jake VanderPlas, Denis Laxalde, Josef Perktold, Robert Cimrman, Ian Henriksen, E. A. Quintero, Charles R. Harris, Anne M. Archibald, Antônio H. Ribeiro, Fabian Pedregosa, Paul van Mulbregt, and SciPy 1.0 Contributors. "SciPy 1.0: Fundamental Algorithms for Scientific Computing in Python". In: *Nature Methods* 17 (2020), 261.
- [238] A Khosravani, J Scott, MP Miles, D Fullwood, BL Adams, and RK Mishra. "Twinning in magnesium alloy AZ31B under different strain paths at moderately elevated temperatures". In: *International Journal of Plasticity* 45 (2013), 160.
- [239] Oleg Sitdikov and Rustam Kaibyshev. "Dynamic recrystallization in pure magnesium". In: *Materials Transactions* 42.9 (2001), 1928.
- [240] Benoit Beausir, Somjeet Biswas, Dong Ik Kim, László S Tóth, and Satyam Suwas. "Analysis of microstructure and texture evolution in pure magnesium during symmetric and asymmetric rolling". In: *Acta Materialia* 57.17 (2009), 5061.

- [241] Yunchang Xin, Maoyin Wang, Zhen Zeng, Guangjie Huang, and Qing Liu. "Tailoring the texture of magnesium alloy by twinning deformation to improve the rolling capability". In: *Scripta Materialia* 64.10 (2011), 986.
- [242] Wolfgang Sebastian, Klaus Dröder, and Sönke Schumann. "Properties and processing of magnesium wrought products for automotive applications". In: *Magnesium Alloys and their Applications* (2000), 602.
- [243] R Kaibyshev. "Dynamic recrystallization in magnesium alloys". In: *Advances in Wrought Magnesium Alloys*. Elsevier, 2012, 186.
- [244] Yannick **Hollenweger**, Dennis M Kochmann, and Burigede Liu. "Physics-Informed Crystal Plasticity RNN for Temperature-Dependent Anisotropic Plasticity in HCP Materials". In: *In preparation* (2023).
- [245] Xinxin Sun, Hongwei Li, Mei Zhan, Junyuan Zhou, Jian Zhang, and Jia Gao. "Cross-scale prediction from RVE to component". In: *International Journal of Plasticity* 140 (2021), 102973.
- [246] Annan Zhang and Dirk Mohr. "Using neural networks to represent von Mises plasticity with isotropic hardening". In: *International Journal of Plasticity* 132 (2020), 102732.
- [247] Maysam B Gorji, Mojtaba Mozaffar, Julian N Heidenreich, Jian Cao, and Dirk Mohr. "On the potential of recurrent neural networks for modeling path dependent plasticity". In: *Journal of the Mechanics and Physics of Solids* 143 (2020), 103972.
- [248] F Ghavamian and A Simone. "Accelerating multiscale finite element simulations of history-dependent materials using a recurrent neural network". In: *Computer Methods in Applied Mechanics and Engineering* 357 (2019), 112594.
- [249] Günter Klambauer, Thomas Unterthiner, Andreas Mayr, and Sepp Hochreiter. "Self-normalizing neural networks". In: *Advances in neural information processing systems* 30 (2017).
- [250] Burigede Liu, Nikola Kovachki, Zongyi Li, Kamyar Azizzadenesheli, Anima Anandkumar, Andrew M. Stuart, and Kaushik Bhattacharya. "A learning-based multiscale method and its application to inelastic impact problems". In: *Journal of the Mechanics and Physics of Solids* 158 (2022), 104668.
- [251] The LinuxFoundation. *Pytorch*. URL: <https://pytorch.org> (visited on 09/04/2023).

- [252] Adam Paszke, Sam Gross, Soumith Chintala, Gregory Chanan, Edward Yang, Zachary DeVito, Zeming Lin, Alban Desmaison, Luca Antiga, and Adam Lerer. "Automatic differentiation in pytorch". In: (2017).
- [253] Stevo Bozinovski and Ante Fulgosi. "The influence of pattern similarity and transfer learning upon training of a base perceptron b2". In: *Proceedings of Symposium Informatica*. Vol. 3. 1976, 121.
- [254] Lisa Torrey and Jude Shavlik. "Transfer learning". In: *Handbook of research on machine learning applications and trends: algorithms, methods, and techniques*. IGI global, 2010, 242.
- [255] Dipankar Ghosh, Owen T Kingstedt, and Guruswami Ravichandran. "Plastic work to heat conversion during high-strain rate deformation of Mg and Mg alloy". In: *Metallurgical and Materials Transactions A* 48 (2017), 14.
- [256] Stephen E Grunschel. "Pressure-shear plate impact experiments on high-purity aluminum at temperatures approaching melt". PhD thesis. Brown University, 2009.
- [257] Suhas Eswarappa Prameela, Yannick **Hollenweger**, Alec Davis, Steven Lavenstein, Roshan Plamthottam, Joey Chen, Joseph Robson, Jaafar El-Awady, Dennis M. Kochmann, and Timothy P. Weihs. "Unravelling complex non-equilibrium phase transformation pathways in deformed magnesium polycrystals". In: *In preparation* (2024).
- [258] Madeleine Bignon, Pratheek Shanthraj, and Joseph D Robson. "Modelling dynamic precipitation in pre-aged aluminium alloys under warm forming conditions". In: *Acta Materialia* 234 (2022), 118036.
- [259] R Kampmann and R Wagner. "Materials science and technology, vol. 5". In: *VCH, Germany* (1991).
- [260] J. Svoboda, F. D. Fischer, P. Fratzl, and Ernst Kozeschnik. "Modelling of kinetics in multi-component multi-phase systems with spherical precipitates I: Theory". In: *Materials Science and Engineering A* 385.1-2 (2004), 166.
- [261] KC Russel. *Nucleation in Solids: The Induction Period and Steady State Effects, volume 13 de Advances in Colloid and Interface Science*. 1980.

- [262] K Linga Murty, K Detemple, O Kanert, and J Th M Dehossou. "In-situ nuclear magnetic resonance investigation of strain, temperature, and strain-rate variations of deformation-induced vacancy concentration in aluminum". In: *Metallurgical and Materials Transactions A* 29 (1998), 153.
- [263] Pavel Lukáč and Jaroslav Balík. "Kinetics of plastic deformation". In: *Key Engineering Materials* 97 (1995), 307.

CURRICULUM VITAE

PERSONAL DATA

Name Yannick Hollenweger
Date of Birth November 7, 1995
Place of Birth Locarno, Switzerland
Citizen of Switzerland

EDUCATION

09/2019 Eidgenössische Technische Hochschule Zürich,
– present *Final degree: Dr. sc. (ETH)*
09/2017 Eidgenössische Technische Hochschule Zürich,
– 05/2019 *Final degree: MSc Mechanical Engineering*
08/2013 Eidgenössische Technische Hochschule Zürich,
– 02/2017 *Final degree: BSc Mechanical Engineering*
08/2009 Kantonsschule Zürich Enge
– 07/2013 *Final degree: Schweizerische Maturität (university
entrance diploma)*

EXPERIENCE

02/2022 Visiting Reseracher
– present *University of Cambridge Development of a neural opera-
tor for tempearture-dependent plastic anisotropy*
09/2015 *Akademischer Motorsportverein Zürich Design and man-
– 05/2016 ufacturing of CFRP chassis for electric racecar*

CONFERENCES

10/2019 Fall Meeting of CMEDE | Poster

- 03/2020 MACH conference 2020 (Virtual) | Presentation
- 01/2021 14th World Congress on Computational Mechanics (WCCM) and the European Community on Computational Methods in Applied Sciences (ECCOMAS) Congress 2020 – Virtual Congress | Presentation
- 6/2022 8th European Congress on Computational Methods in Applied Sciences and Engineering | Presentation

TEACHING

- 09/2022 Teaching Assistant for CM1: Intro to FEA
– 08/2019 *Eidgenössische Technische Hochschule Zürich, CH*
undergraduate level
Exam preparation and substitute lectures

PUBLICATIONS

- [1] Suhas Eswarappa Prameela, Peng Yi, Yannick **Hollenweger**, Burigede Liu, Joey Chen, Laszlo Kecskes, Dennis M Kochmann, Michael L Falk, and Timothy P Weihs. “Strengthening magnesium by design: Integrating alloying and dynamic processing”. In: *Mechanics of Materials* 167 (2022), 104203.
- [2] Laszlo J Kecskes, Nicholas M Krywopusk, Yannick **Hollenweger**, Jenna N Krynicki, Suhas Eswarappa Prameela, Peng Yi, Burigede Liu, Michael L Falk, Dennis M Kochmann, and Timothy P Weihs. “Recrystallization mechanisms, grain refinement, and texture evolution during ECAE processing of Mg and its alloys”. In: *Mechanics of Materials* 162 (2021), 104067.
- [3] Yannick **Hollenweger** and Dennis M Kochmann. “An efficient temperature-dependent crystal plasticity framework for pure magnesium with emphasis on the competition between slip and twinning”. In: *International Journal of Plasticity* 159 (2022), 103448.
- [4] Yannick **Hollenweger**, Dennis M Kochmann, and Burigede Liu. “Physics-Informed Crystal Plasticity RNN for Temperature-Dependent Anisotropic Plasticity in HCP Materials”. In: *In preparation* (2023).
- [5] Suhas Eswarappa Prameela, Yannick **Hollenweger**, Alec Davis, Steven Lavenstein, Roshan Plamthottam, Joey Chen, Joseph Robson, Jaafar El-Awady, Dennis M. Kochmann, and Timothy P. Weihs. “Unravelling complex non-equilibrium phase transformation pathways in deformed magnesium polycrystals”. In: *In preparation* (2024).